TU/e EINDHOVEN UNIVERSITY OF TECHNOLOGY

Eindhoven University of Technology

MASTER

Improvement of the modelling and control of a 6 DOF magnetically levitated spherical laser deflection system

Lemmens, J.M.

Award date:
2007

Link to publication

TU/e technische
universiteit
eindhoven

Improvement of the modelling and control of a 6 DOF magnetically levitated spherical laser deflection system

by J.M. Lemmens

Abbreviations

3D	Three Dimensional
A/D	Analog to Digital
AM	Amplitude Modulation
et al.	(Latin: et alia) and others
etc	(Latin: et cetera) and other things, and so on
CDCPS	Contactless Differential Capacitive Position Sensor
CD-ROM	Compact Disc used as Read Only Memory
c.g.	center of gravity
CTD	Central Technical Service of the TU/e
C-Sensor	Capacitive Sensor
D/A	Digital to Analog
DC	Direct Current
DOF	Degree Of Freedom
e.g.	(Latin: exampli gratia) for example
e-mail	electronic mail
EMF	Electro Motive Force
EVBP	Exact Value from Blue Prints of the prototype
EVT	Exact Value used in the Ph.D.-thesis
F-coil	Force generating coil
FEM	Finite Element Method
HCC	Horizontal Coil Core
IC	Integrated Circuit
i.e.	(Latin: id est) that is
Inc	Incorporated
LTI	Linear Time Invariant
MBS-CS	Measurement and Control Systems division of the Electrical Engineering department of the Eindhoven University of Technology
M.Sc.	Master of Science
NatLab	Physics research laboratory of the Philips company
PC	Personal Computer
PCB	Printed Circuit Board
pdf	portable document format (Digital file format of the Adobe® company)
Ph.D.	Doctor (of Philosophy)
PID	Proportional Integrating Deviating
PRGA	Performance Relative Gain Array
p.t.o.	please turn over
RGA	Relative Gain Array
SISO	Single Input Single Output
T	Value used in Thesis [1]
T-coil	Torque generating coil
TU/e	Eindhoven University of Technology
VCC	Vertical Coil Core

Physical parameters and constants

Table 1 Unit conversions.

Physical parameter	Symbol	Unit
Voltage	V	V = J/As
Electrical current	I	A = C/s
Magnetic flux	Φ	Wb = Vs
Magnetic field strength	H	A/m
Electrical capacitance	C	F (Farad) = C/V
Magnetic induction	L or M	H (Henry) = J/A^2
Mass	m	kg
Moment of inertia	J or I	kgm^2
Force	F	N = kgm/s^2
Torque	T	Nm = kgm^2/s^2 = J
Energy	E	J = Nm = kgm^2/s^2
Power	P	W = J/s = Nm/s = kgm^2/s^3 = VAs

Table 2 Physical constants.

Physical constant	Symbol	Value	Unit
Magnetic permeability of vacuum	μ_0	$4\pi \cdot 10^{-7}$	H/m = J/A^2m = kgm/A^2s^2
Gravitational acceleration	g	9.81	m/s^2
Normal atmospheric air pressure	p_0	$1.01325 \cdot 10^5$	Pa = N/m^2

Abstract

In 1997 a Ph.D.-student of the Measurement and Control Systems (MBS-CS) division of the Electrical Engineering department of the Eindhoven University of Technology (TU/e) started with the development of a new tilting mirror. He designed a topology with magnetic bearing which makes the mirror free of contact.

A prototype of this tilting mirror system has been built. The designed device with a volume of approximately 110 [cm^3] is composed of four main parts. A mirror (radius = 3 [mm]) that is attached to a **rotor** (radius = 8 [mm]), which is positioned in the center of the device. A **magnetic actuator system** that consists of two stator rings (radius = 26 [mm]) and 12 electrical coils (functioning as electromagnets) that are used to manipulate the position and orientation of the rotor, is positioned around the rotor. A capacitive **sensor system**, which measures the position and orientation of the rotor, is mainly positioned on the PCB under the rotor. A **controller** controls the magnetic actuator system based on its inputs from the capacitive sensor system. The controller has two functions:
* Bring and keep the rotor in the center of the stator, maintaining a nominal air gap distance of 0.25 [mm] between the rotor and the stator.
* Put the rotor in any wanted orientation.

The main problem of the prototype is that the magnetic levitation system is unstable. When the power of the electromagnets is turned off, the forces left in the system are caused by gravity and the permanent magnets on the rotor. These forces will pull the rotor to one side till it is "stuck to the stator". This instability is the main problem of making the device operational. The sensor system cannot be calibrated when the rotor is not stabilized and the controller that can stabilize the rotor needs a calibrated sensor system to operate. It is not possible to fully calibrate the sensor system without an external calibration device.

The Ph.D.-student did not succeed in making the device operational with a (partially) calibrated sensor- and actuator system and 5 SISO PID controllers. This graduation work is the continuation of the tilting mirror project. The main assignment was to try to make the device operational.

The work started with reviewing the Ph.D.-thesis [1] and studying the prototype. Several theoretical- and sloppy mistakes were corrected. Also some analyses were supplemented. Together these improvements resulted in a more accurate and complete modeling and calibration of the system.

Sensor calibration
The essential full (re)calibration of the capacitive sensor system has been prepared with the design and production of a calibration setup and the investigation of how to process the calibration measurement data, to obtain an optimal linear sensor model.

A simple calibration setup for the sensor of the prototype has been designed and built. It uses a clamping device to fixate the rotor. Micromanipulators can be used to perform static sensor calibration measurements for 4 sensors (u, v, z and α). For calibration of the other rotation angle (β) the device has to be reinstalled, rotated over a 90° angle around the z-axis of the stator frame. Extra features for the calibration setup are discussed. Instructions for the installation and use of the calibration setup are given. Also the maximum range (horizontal, vertical and rotation) of the rotor in the setup is calculated.

Two sets of measurement expectation values are now available for the 25 linear sensor model parameters of the prototype. The first set was calculated with the ideal sensor model in [1], the other set was extracted from the available calibration measurement data of the test setup (replica) sensor.

Position estimation tests have proven that a linear sensor model is applicable, at least for the static measurements performed on the sensor replica, which is almost identical to the sensor system of the prototype.

The sensitivity of the replica orientation sensors is too low. The orientation sensor electrodes are shaped differently in the prototype, which will probably result in a better functionality.

It was discovered that the sensitivity for vertical translations of the horizontal sensor output voltages can be used to find the horizontal coordinates of the operating point of the rotor: the center of the stator.

For the optimization of the linear sensor model that is based on the static calibration measurements, two choices must be made:
- Extract the linear sensor coupling parameters by hand or use an automatic extraction method.
- Optimize the linear sensor model for the full sensor range or only near the operating point of the rotor.

Control

A linear model approximation for the rotor in its operating point, the center of the stator, has been calculated, based on the corrected and improved ideal model of the prototype with gravity added to the system. The linear model is expressed in device parameters, which provides insight for control engineering and facilitates the implementation of improvements for possible future prototype designs. The linear model is presented in the standard State Space Model notation and shows which device parameters cause transfers between the inputs and outputs of the system.

The transfer function matrix of the linear model contains four non-diagonal elements, which represent (unwanted) couplings between the inputs and outputs of the system. These unwanted couplings have three causes:
- The optical center point of the mirror and the center of gravity of the rotor do not coincide.
- The work-lines through the points of attack of actuator forces do not cross the center of gravity of the rotor.
- The actuators that have to compensate gravity act in the direction of the normal axis of the mirror. When the rotor is tilted, this normal axis does not lie on the work-line of the gravity.

Relative Gain Array (RGA) matrices are calculated to investigate the effect of the couplings. Because the RGA matrices are almost equal to the Identity matrix for the whole frequency domain of the system, it can be concluded that the choice in [1] to consider the system as fully decoupled, was justified.

The original controllers proposed in [1] for the prototype were tested on the corrected ideal model and the expected model (based on the actuator calibration in [1] that indicated weaker actuators). The controllers seemed robust enough to cope with the possible smaller actuator gains and the added gravity. However, adaptation of the controllers resulted in faster feedback systems with less overshoot in the step-response compared to the original control results.

Overall

No crucial theoretical mistakes were found in the design and modeling of the prototype of the magnetically levitated tilting mirror presented in [1]. So in theory the system could be operational.

Despite the thorough preparations, the necessary practical execution on the prototype did not take place (by a lack of time and means). So the sensor system of the prototype hasn't been recalibrated yet and therefore the adapted controllers could not be tested on the real device. This means that the prototype still isn't operational.

Additional

This thesis doesn't contain radical suggestions for improvements of the prototype design, or the proposed calibration procedures in [1], because the emphasis of the work was on making the available prototype operational, not redesigning it.

Table of contents

Chapter 1

Introduction

In the last 15 years, various people at the Measurement and Control Systems (MBS-CS) division of the Electrical Engineering department of the Eindhoven University of Technology (TU/e), have been working on the development of a tilting mirror. This mirror can be applied as the laser deflection system in an accurate contactless three dimensional (3D) position measurement system, based on laser interferometry.

1.1 Tilting mirror application: 3D laser interferometry

A simple description of the principle of interferometry can be given as follows (see figure 1.1). A fixed laser beam, originating from an interferometer, is pointed onto the optical reflection point of a deflection mirror. This mirror has a fixed position but also the ability to rotate around its axes. The deflection mirror then is aimed at a retro reflector on a point in space that needs to be measured, for example the tip of a robotic arm. The retro reflector has the special property of reflecting the incoming light back in the same direction it came from, in this case straight back to the deflection mirror. Via the deflection mirror, the reflected beam is directed onto a half pass mirror, that splits the laser light in two directions. One part of the laser light is directed back to the interferometer. The other part of the reflected laser light is aimed at an optical tracking sensor, that provides input for the controller of the tilting angles of the deflection mirror. Now the position of the retro reflector (and so the point in space) can be calculated by using the position and orientation of the deflection mirror and the distance the laser light has traveled.
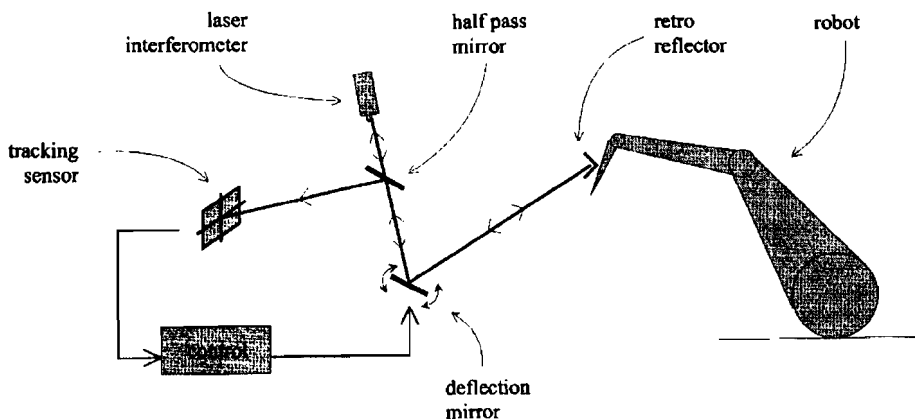
Figure 1.1
Complete 3D laser interferometer system (copied from [1, figure 1.1]).

1.2 Hovering mirror

The system described above could be realized using techniques that have been available for a long time. The scientific challenge is captured in the added demand to create a device with a deflection mirror that is free of contact with its surroundings.
In other words: the mirror has to hover. This is to reduce friction and therefore mechanical wear.

1.3 Developed hovering mirrors

The first prototype built, was a mirror supported by an air bearing. This construction is semi-contact free, because strings to three linear motors, that are used to control the position and orientation of the mirror, are connected to the mirror.

In 1997 a Ph.D.-student by the name of Victor van Acht started with the development of a new tilting mirror [1]. He designed a topology with magnetic bearing which makes the mirror truly free of contact. A prototype of this mirror system has been built (figure 1.2).
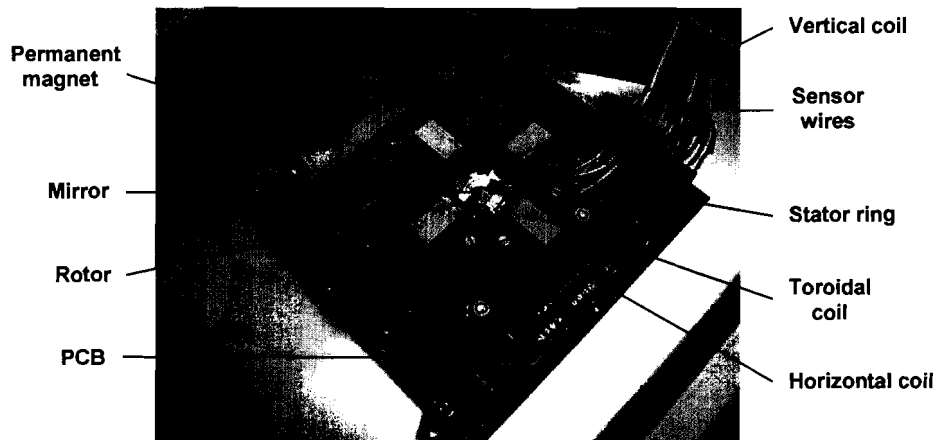
Figure 1.2
Photograph of the prototype of the magnetically levitated deflection mirror.

1.4 The prototype

The designed device (figure 1.2) is composed of four main parts. These four subsystems are named below, discussed briefly in section 2.1 and extensively in [1].

- The mirror (radius = 3 [mm]) that is attached to a **rotor** (radius = 8 [mm]) is positioned in the center of the device.

- The **magnetic actuator system** that consists of two stator rings (radius = 26 [mm]) and 12 electrical coils (functioning as electromagnets) that are used to affect the position and orientation of the rotor, is positioned around the rotor. The height of magnetic actuator system (stator) is about 20 [mm].

- A capacitive **sensor system**, which measures the position and orientation of the rotor, is mainly positioned on the PCB under the rotor.

- A **controller**, that controls the magnetic actuator system based on its inputs from the capacitive sensor system. The controller should be able to maintain the nominal air gap distance of 0.25 [mm] between the rotor and the stator (and the sensor) and it should also be able to put the rotor in any wanted orientation.

1.5 Main problem of the prototype

The main problem of the prototype is that the magnetic levitation system is unstable. When the power of the electromagnets is turned off, the forces left in the system are caused by gravity and the permanent magnets on the rotor. These forces will pull the rotor to one side till it is "stuck to the stator". This instability is the main problem of making the device operational (figure 1.3)
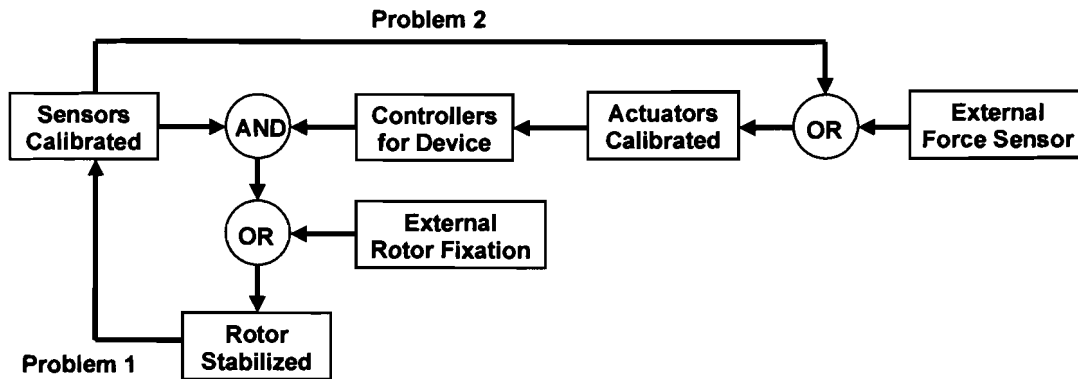
Problem 2

Figure 1.3
Condition diagram showing the two main problems, caused by the instability, that must be solved to make the prototype operational.

A controller is needed to make the device stable, i.e. let the rotor hover in the center of the prototype. This controller needs information from the capacitive position and orientation sensors. But to calibrate the sensors, the device needs to be stable and controllable (**problem 1** in figure 1.3)!

For proper controller design, the properties of the magnetic actuator system need to be known. Calibrating the actuators means determining the relation between the position and orientation of the rotor, the input currents of the electrical coils and the generated forces by the electromagnets. So again a calibrated sensor system is needed (**problem 2** in figure 1.3), which means that the device has to be stabilized before the actuators can be calibrated.

Also the use of system identification techniques is not possible as long as the device is not stabilized. Because for black box identification, sets of measurement data from the input and the output around the operating point of the system are needed.

The paradox of this double calibration problem is the order of actions to be taken, because the execution of one action is a necessary condition to be able to execute a second action and vice versa.

1.6 Status of the project

When I started to work on my assignment, I was the second person to work with the new prototype of the tilting mirror system (figure 1.2). The first person was the Ph.D.-student who designed and modeled the prototype (see section 1.3). After one month overlap time, in which he mainly finished up his Ph.D.-thesis, he left the TU/e to go working at the Philips NatLab. Contact by e-mail was still possible and necessary, because he proved to be the only one that was sufficiently informed!

At the beginning of my graduation time, the prototype was turned over to me. How the device was left, what had been achieved so far and what had been discovered about the device (e.g. the difference between the ideal design and the actual prototype that was built) can be called the status of the project. It will be described shortly in the following subsections.

1.6.1 Status of the prototype

After the device was built by the CTD (Central Technical Service of the TU/e), the subsystems of it were tested and debugged until they seemed to work properly. Although no test report is available, some results can be found in [1, section 8.3].

The sensor- and actuator system of the device haven't been properly calibrated yet. The prototype has not been successfully stabilized, so it is not operational.

1.6.2 Status of the sensor system

To test the functioning and to predict the behavior of the real sensor system in the prototype, some measurements [1, section 5.6] have been done on a mechanically stabilized replica of the sensor. It is not possible to use the replica measurement data for the real device because of the differences between it and the replica.

The only attempt in [1] to calibrate the sensors of the prototype was the execution of an automatic calibration procedure, that makes use of the four stable "stuck to the stator" positions of the rotor. The coordinates of these positions are known. With this information, the sensor data can be used to calibrate the horizontal position sensors.
An advantage of the automatic calibration procedure is that it is time and money saving because no external setup is necessary. It is also useful that the prototype can be recalibrated every time it is turned on or when the operating circumstances have changed (e.g. the temperature).

Unfortunately the automatic calibration method is inaccurate and incomplete, because it uses only four rotor positions which are not exact and solely lie in a horizontal plane. This means that the z-, α- and β-sensors and actuators are not calibrated. Also the influence of the rotor height (z) and orientation (α and β) on the horizontal position sensor outputs is not accounted for.

Another disadvantage of the "stuck to the stator" calibration method, besides the incompleteness, is the damage that the repeated rotor impacts cause to the stator. The damage sustained so far is twofold: a little chip of the magnetic iron has come off the rotor and in one of the four "stuck to the stator" positions the sensor has started to malfunction (see comments in the file identificatie.c on the CD-ROM (section 1.8)).

1.6.3 Status of the actuator system

Some measurements [1, section 8.3.1] have been done to test the functioning of the electromagnets in the prototype.

The actuator system meets the minimal demand that the electromagnets are able to pull the rotor loose from any of the four "stuck to the stator" positions. An extra layer of coating on the front side of the horizontal coil-cores helps to limit the horizontal rotor range and therefore also the maximum destabilizing force of the permanent magnets.
Measurement of the horizontal and vertical coil inductances revealed two things:
The number of coil windings has been adapted for practical manufacturing reasons. In the prototype, the vertical coils have less windings and the horizontal coils have more windings than was designed. The functioning of one vertical coil is not okay [1, section 8.3.2]. Its inductance drops more than that of the other three at high frequencies. According to [1], this fault is probably caused by damaged coating around the individual lamellae of the $-\beta$ coil-core, which causes excessive eddy currents in the coil-core. At low frequencies this evil probably won't cause any problems.

Only the horizontal actuators are calibrated by means of measuring the lift-off trajectory of the rotor between two "stuck to the stator" positions with the poorly calibrated sensor. Obviously, this leaves much room for improvement.

The rotor damage (chip of magnetic iron fell off) is expected to have a small influence on the magnetic system. However, it has influence on the total weight and the symmetrical weight distribution of the rotor.

1.6.4 Controllers

To simplify the controller design, the 6 DOF of the prototype were considered to be magnetically decoupled. The controllers proposed in [1] are five simple linear SISO PID controllers based on the ideal mathematical models in the Ph.D.-thesis. (The γ-rotation doesn't need control, because it's passively stable). The first attempt to make the rotor hover stably with the set of PID controllers failed.

This doesn't necessarily mean that these controllers were badly designed. They are just not capable of stabilizing the device with the poorly calibrated sensor- and actuator system. A small actuator modeling- or calibration error could be compensated by the controllers, but the sensor information must be accurate for the controller to function properly. Ergo, the sensor must be calibrated first, before the controllers can really be tested and tuned.

1.6.5 Future recommendation by the designer

Due to a lack of time, the Ph.D.-student wasn't able to make any more improvements. So he left the device tested, but still unstable (not operational).

The main recommendation in [1, section 9.1.1.4] is to build an external separate calibration setup for the sensor of the prototype. He is convinced that the prototype can be stabilized with five simple PID controllers when the sensor system is properly calibrated.

1.7 My work

My work started with the choice of an appropriate graduation assignment at an electrical engineering division of choice (MBS-CS). A complete description of my graduation assignment is stated in section 2.2. The assignment can be summarized as follows:
First learn about the laser deflection mirror prototype by studying the contents of the Ph.D.-thesis [1] and the SIMULINK® models belonging to the device. After that, try to fully (re)calibrate the capacitive sensors and the magnetic actuator system. Then test the designed controllers from [1] on the device and when necessary redesign them. The main goal is to make the prototype fully operational.

I decided to accept the assignment because it was in line with my main fields of interest (within electrical engineering), namely modeling of electromechanical devices, mechatronics, programming, robotics and of course measurement and control techniques.

Also working with a practical device (the prototype) instead of doing a purely theoretical assignment appealed to me. Another plus point of the assignment is that it covers more than one discipline of electrical engineering, namely electronics, (electro)magnets, digital data acquisition and processing, digital control, the use of mathematical engineering tools like MATLAB® [S1] and control engineering tools like SIMULINK® which is a part of MATLAB®.

Nevertheless, I was aware of some downsides of the assignment. The device was already designed and built, which means I was forced to work with the (non-optimal) choices made by others. Also testing of the theory on a real device means that the level of accuracy to work with has to be high. There certainly is no room for (calculation) mistakes, because a theoretical model can be simple and easy to control even with mistakes, but then it won't function in practice.

The graduation period is finished by writing a report and doing a presentation. The contents of this report is described briefly in the next section. Naturally, there is a strong link between the executed work and the contents of the report.

Although it wasn't predestined, correcting the Ph.D.-thesis [1] became a substantial part of my work. Correction of [1] was important because black box identification techniques can't be used as long as the device is unstable. This means that for a first attempt of controller design, white box models (ideal analytical models) must be used.
The errors that I found in the ideal models could be part of the reason why the device is still not operational. Ergo, they had to be corrected before it can be concluded that the white box modeling approach of stabilizing the prototype in [1] is not suitable.

1.8 This M.Sc.-thesis

Writing a M.Sc.-thesis is a compulsory part of the graduation process. In the first instance this thesis will be used to review my work, to determine whether I qualify for graduation or not. Later it can provide useful information to the people that are going to work after me on this project.

Although it was my intention to make this report an accurate reflection of my occupations, it is far from complete. Working with a real device means there are a lot of practical actions to perform, to let the device work properly. Things like how to operate the prototype, electrical connection schemes and the use of software will not be described. It is simply to much work to put it in here, considering the limited amount of available time.

This M.Sc.-thesis consists of two main parts:

PART 1: Review of the Ph.D.-work.
In principle the Ph.D.-thesis [1] was meant as an information source about the prototype. But during the reading of it and the MATLAB® files belonging to it, the verification of the presented calculations and SIMULINK® models led to the conclusion that not everything was worked out as it should have been. The most important errors that were found are displayed in part 1 of this thesis. Of course, a proposition for corrections, modifications and supplements is given too.

PART 2: Additional work.
The second part of this thesis describes the activities carried out for the continuation of the project, such as the development of an external calibration setup for the sensor, the processing of the calibration measurement data of the test setup sensor and the analysis of the control of the device. Unfortunately, the planned recalibration of the capacitive sensor system and the magnetic actuator system could not be executed.

Additional notes:
The necessary correction and supplementation of the Ph.D.-thesis [1] consumed much of my available time. Consequently, the emphasis of this report lays on the use of my analytical skills.

Terms, names and descriptions are taken from [1], even when (slightly) illogical, to keep this thesis compatible with [1] and uniform throughout the whole project.

In order to clarify my improvements (or the found mistakes) it was necessary to use a lot of references to the Ph.D.-thesis [1] or copy (parts of) calculations. This has been done to make this thesis readable on its own. It is not an attempt to copy [1] and present it as my own work.

Basic knowledge of (electrical) engineering and mathematics is needed to read this thesis. This knowledge is presumed to be present with most of the readers. Therefore, fundamental technical terms will be used without explanation.

1.9 This report is available on CD-ROM

The disc also contains:

- The created and used MATLAB® files;
- Datasheets of the ICs and force/torque sensors;
- Pictures of the device;
- Scans of blueprints of the calibration setup;
- A literature report, based on this project, with the found articles in pdf-format;
- My PowerPoint presentation;
- Some files of Victor that were not on his three CD-ROMs, but on the laptop linked to the controller of the prototype. These are controller (SIMULINK®) files, data acquisition software and measurement results.

Chapter 2

Preliminaries

This chapter contains introductory technical information about the hovering deflection mirror prototype and a self composed graduation assignment.

2.1 The prototype

The prototype is mainly a product of electrical and mechanical engineering. The picture of it in figure 1.2 is not complete. It doesn't show the sensor electronics, the power supplies for the electromagnets, the PowerPC used for data acquisition (dSPACE) and control, the desktop computer to operate and monitor the device, the electrical current- and voltage sources and the signal generator.

Also the description of the prototype in the introduction can be extended with some necessary technical information. A full description of the device can be found in [1].

2.1.1 Degrees of freedom: rotation parameter definition

For 3D measurements with only one hovering mirror, the position of the reflection point (optical center) of the deflection mirror should be controllable and measurable over three perpendicular axes (xyz). The orientation of the deflection mirror should be controllable and measurable over two perpendicular rotation axes (α around x-axis and β around y-axis). A possible rotation around the z-axis (γ) has no optical effect. Nevertheless, depending on the topology of the mirror, the γ rotation also needs to be controllable and therefore measurable. The orientation of the mirror in this thesis and in [1] is defined in figure 2.1, which is a literal copy of [1, figure 2.3].
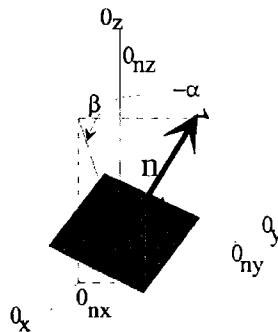
Figure 2.1
The gray square plane represents the mirror surface. Vector n is the normal axis of the mirror. Angles α and β define the orientation the mirror can have with respect to the 0-frame. This is the world fixed reference frame, which is also called the stator frame.

Throughout [1] also a second frame, the uvz-frame, is used. This is the is the xyz-frame rotated 45° around its z-axis (see figure 2.2). The rotation around the u-axis is called α^* and the rotation around the v-axis is called β^*. Both angles are defined via the same right-hand rule as was used for the xyz-frame in figure 2.1.
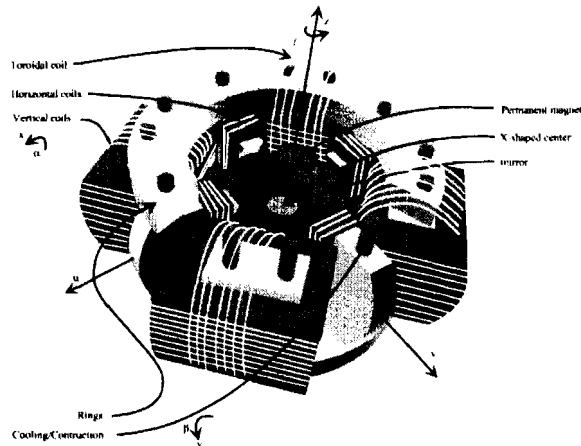
Figure 2.2
Schematic drawing of the prototype of the magnetically levitated deflection mirror (copied from [1, figure 4.8]). Note that the direction of the a-rotation arrow is not conform figure 2.1, it should be the other way around!

2.1.2 The mirror on the rotor

The mirror is flanked by magnetic material (iron with a high magnetic permeability and four permanent magnets). The magnetic material makes the mirror susceptible for manipulation with the electromagnets of the actuator system (see section 2.1.4).

An aluminum semi sphere with a radius of 8 [mm] is attached under the magnetic material and the mirror. This semi sphere functions as an electrode for the capacitive position and orientation sensor system (see section 2.1.5).

The mirror, the magnetic material and the aluminum semi sphere together form the rotor. The complete rotor is the object that is to hover and to be controlled.

Figure 2.2 shows the rotor inside the stator. The exact rotor dimensions are shown in the figures depicted throughout appendix B.

2.1.3 Prototype dimensions and rotor range

To get an idea of the size of the device, some dimensions are given: the height of the prototype is about 20 [mm], the rotor radius is 8 [mm], the rotor radius at the permanent magnets is 10 [mm], the mirror radius is 3 [mm] and the radius of the stator rings is 26 [mm].

The nominal air gap between the stator and the rotor is 0.25 [mm]. With a special coating on the horizontal coils, the horizontal rotor range in the u- and v-direction is limited to ±50 [µm]. In [1] the fact that the rotor can "slide" between the horizontal coil cores (see figure 3.5) hasn't been taken into account. This makes the rotor range in the x- and y-direction larger than 50 [µm]. The horizontal rotor range in the x- and y-direction is calculated in section 3.7 with formula (3.52). The vertical rotor range is calculated in appendix H.1. Table 2.1 gives an overview of the rotor range of the prototype.

Table 2.1 Rotor range.

Range	Parameter	Value without coating	Value with coating
Horizontal	u and v	±250 [µm]	±50 [µm]
Horizontal	x and y	> ±250 [µm]	±70 [µm]
Vertical	z	-349/+819 [µm]	-67/+185 [µm]
Rotation	a and β	±22.5°	±22.5°

2.1.4 Magnetic actuators

The magnetic actuator system has two functions. The first function is to stabilize the rotor, i.e. keep it in the middle of the stator. This position is called the neutral position or operating point of the rotor (u = v = z = 0). To enable the rotor to hover freely surrounded only by air, the magnetic actuators have to overcome gravity and other disturbing forces. The second function of the magnetic actuators is to control the orientation (and position) of the rotor, so that it can be kept steady with any orientation (α and β) within the normal rotor range (see table 2.1).

The magnetic actuator system is composed of twelve electrical coils that function as electromagnets. As figure 2.2 shows, the coils are positioned symmetrical around the rotor and provide the possible control over six degrees of freedom (6 DOF), namely 3 translations (u, v and z) and 3 rotations (α, β and γ).

There are four horizontal coils. They operate in pairs of two. The pair positioned in the u-direction is fed with the current I_u. The pair positioned in the v-direction is fed with the current I_v. Both pairs are able to generate a magnetic reluctance force that acts on the rotor and influences its horizontal position (u and v). The direction and strength of the generated force depends on respectively the polarity and the magnitude of the coil-current.

The four vertical coils have a double function. When a current is forced through one of the vertical coils, a Lorentz force is generated in the closest permanent magnet on the rotor. When all four vertical coils are fed with the same current I_z, the four generated forces all act in the same direction. Depending on the polarity of the current I_z, this is the positive or negative z-direction of the rotor. The rotor will move in the direction of the generated force.
The four vertical coils can also operate in pairs of two. The pair positioned in the x-direction is fed with the currents I_β and $-I_\beta$. The pair positioned in the y-direction is fed with the currents I_α and $-I_\alpha$. The different polarity of the currents through the opposite coils, lets them generate forces on the rotor in opposite directions. These opposite forces act as a torque on the rotor which let it rotate. With the current I_α, the rotation of the rotor around its y-axis (in the α-direction) can be controlled. With the current I_β, the rotation of the rotor around its x-axis (in the β-direction) can be controlled. The direction of the rotor rotation depends on the polarity of the currents.

The four toroidal coils can be used in two ways. When they are short circuited, the γ-rotation of the rotor becomes passively damped. When the rotor rotates around its z-axis, the moving permanent magnets induce currents in the toroidal coils. These currents generate Lorentz forces on the permanent magnets that counteract the γ-rotation of the rotor.
The γ-rotation can also be actively controlled with the toroidal coils. For this purpose, the four toroidal coils must operate in pairs of two. One pair acts as a sensor, using the induced voltage over the coil. The other pair is used as an actuator and is fed with the current I_γ. The current I_γ generates a Lorentz force on the rotor. The direction of the rotor rotation depends on the polarity of the current.

The four permanent magnets mounted on the rotor are not only used to generate the Lorentz forces in combination with the vertical and the toroidal coils. They also pre-magnetize the horizontal coils, to reduce the bias currents and so the power consumption and the generated heat in the electromagnets.

2.1.5 Capacitive sensor system

The position and orientation of the rotor are measured by an array of multiple coupled capacitive sensors. The total is called a Contactless Differential Capacitive Position Sensor System (CDCPS). The position sensor electrodes are positioned on the main PCB (Printed Circuit Board) under the rotor, which is depicted in figure 2.3. The horizontal coil-cores are used as rotation sensor electrodes.

The capacitive sensor system is composed of twelve sourcing electrodes. There also is a common sensing capacitor that is formed by the electrode in the middle on the PCB and the aluminum semi sphere with a radius of 8 [mm] on the bottom side of the rotor. A guarding electrode is added to the system to reduce the parasitic capacities between the sensor electrodes.
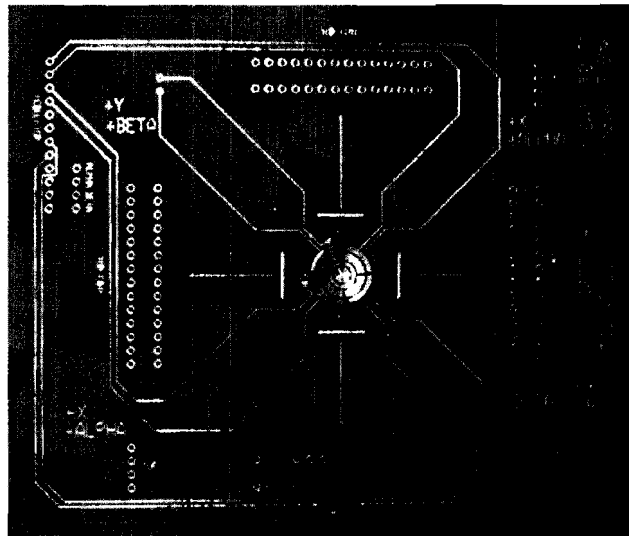
Figure 2.3
Main PCB of the prototype, at the beginning of the fabrication process. Positioned in the middle is the sensing electrode. The ring around it is the guarding electrode. The outer two rings are both divided in four equal parts, that together form the eight position sensor electrodes. The separate electrodes are electrically insulated by glue, that also holds them together. The upper surface of the electrodes is not flat, but shaped like a bowl with a radius of 8.25 [mm]. Note that the picture shows that the electrodes are not perfectly aligned with the PCB!

The basic capacitive sensor principles that are used, are based on the formula (2.1) for an ideal capacitor formed by two metal plates (electrodes).

$$C = \frac{\varepsilon_0 \varepsilon_r A}{d} \ [F]$$

(2.1)

Where A is the overlapping area of the electrodes, d is the distance between the electrodes, ε_0 is the permittivity of vacuum (= $1/(\mu_0 c^2) \approx 8.85 \cdot 10^{-12}$ [F/m]) and ε_r is the relative permittivity of the material between the plates.

The operation of all five sensors is based on the difference between two opposite positioned capacitors that arises when one of the rotor position- or orientation parameters differs from 0. For the position measurements (u, v, and z), the distance d between electrodes and the rotor electrode is the main parameter that lets the capacitor values change. For the rotation measurements (α^* and β^*), the overlapping area A of the electrodes and the rotor electrode is the main parameter that lets the capacitor values change.

Via an AM-modulation technique the difference in capacitance of the two opposite positioned sensor capacitors is translated into a DC voltage that differs from 0. This voltage is the sensor output voltage. An expression for it is given in [1, (5.17)], which is repeated below. In (2.2) V_s is a constant DC voltage.

$$V_i = V_s \frac{C_1 - C_2}{C_1 + C_2} \ [V]$$

(2.2)

The sensing capacitor is used for all five rotor position and orientation measurements (u, v, z, α^* and β^*). It is shared by means of time- and frequency multiplexing. The position sensor electrodes are modulated (and demodulated) in sequential time slots, the orientation sensor electrodes are modulated at the same time but with a different frequency.

The five sensor output voltages represent the position and orientation of the rotor. Due to the geometry of the capacitive sensor system the five output voltages are influenced by more than one parameter, which means that cross-coupling is present. Software (see 2.1.6) is used to decouple and calculate an estimation for the rotor position and orientation from the five sensor output voltages.

More detailed information about the sensor system can be found in [1, chapter 5].

2.1.6 Controllers

The controller design in [1, chapter 7] starts with the extraction of linear models of the magnetic actuators and the mechanical system from the analytical ideal models of the prototype in [1], with the neutral position of the rotor ($u = v = z = \alpha^* = \beta^* = \gamma = 0$) as operating point. The five resulting second order decoupled linear models for the actuator system are then used to design third order PID controllers for the prototype.

The controllers were designed in the continuous time domain though implemented on a digital controller of the firm dSPACE. The basis of this system is a stand alone PowerPC. The dSPACE system is also used for the data acquisition from (A/D conversion) and to (D/A conversion) the prototype. In principle the prototype has five sensor output voltages and five input voltages (for the VCCS that convert them to currents for the electromagnets), when γ is left out of consideration.

An ordinary desktop PC, can be linked to the dSPACE system. With SIMULINK® software on the PC, the controllers and the calibration (decoupling) scheme of the capacitive sensor can be programmed and transferred to the dSPACE system.

Because the controllers are implemented with software (SIMULINK®), they can be easily adapted and extended. This has been done with the prototype controllers to account for:

- Eddy currents. They are modeled by adding an extra pole (and zero) to the linear model transfer functions of the magnetic actuators.

- The non-ideal sensor behavior. First the controllers were tested with ideal sensors (transfer function = 1), which was not conform reality.

- The design of the γ-damping controller.

- Decrease of actuator strength. Calibration of the actuator system revealed that it probably is less strong than was expected based on the ideal modeling.

Due to the inefficient programming of the dSPACE PowerPC processor, the maximum sampling frequency of the digital controller is 40 [kHz]. The digital implementation introduces a delay time of one sample time, which is 25 [μs].

2.2 Graduation assignment

My Master Thesis assignment is the continuation of the work presented in [1]. The goal is to end up with an operational mirror. The following tasks and sub-assignments should lead to that goal.

❶ Study the device (hardware & software) and the Ph.D.-thesis.
Explore the current prototype for errors such as: theoretical mistakes, mistakes in calculations, interchanged electronic connections, bad design properties.
Generate recommendations for improvements of the design.

❷ Develop a way to (re)**calibrate the capacitive sensor**.
Find the relation between the position/orientation of the rotor and the output of the capacitive sensor. The influence of the magnetic topology can't be disregarded, so the calibration has to be done on the real device. Calibration must be done on a micrometer scale and that is also the manufacturing tolerance. In addition, research the sensitivity of the sensor (for different directions and orientations).

❸ **Calibrate the magnetic actuators**.
That is, extract the relation between input currents/voltages and output forces/torques (depending on the position/orientation of the rotor). This information is needed for controller design.

❹ Design a controller for static use (hovering in neutral position) of the rotor/mirror.
This has been done by Victor, based on ideal mathematical models. So now first the capacitive sensor needs to be recalibrated. Then try hovering again with controllers of Victor. The controllers might be too simple. Improve the simulations by better **modeling of the device**. This includes adjusting the controller for the more accurate modeled device (that is not magnetically decoupled).

❺ Design a controller for lift-off.
This controller pulls the rotor from the instable "stuck to (one side of) the stator" position towards the center of the device (neutral position), where the controller for static use (❹) can take over.

❻ Design a controller for dynamic use.
A controller is needed to put the mirror in a desired position/orientation, while the optical center is kept in the middle of the device. This controller can't be used unless the hovering in neutral position is already controlled (see ❹).

❼ Research and design a way for **switching between the lift-off controller and the static controller**.
Maybe the two jobs can be done by one controller but usually this means the device will become slower than with two dedicated controllers working together. During switching, the output of the controllers must have a bumpless transition and the device must retain its stability.

❽ Fine-tune the controllers for optimal performance of the device.
Depending on what specific goals must be achieved (e.g. speed, accuracy or robustness against disturbances etc), the controllers have to be adjusted.

PART 1

Review of Ph.D.-work

During the reading of the Ph.D.-thesis [1] and the MATLAB® files belonging to it, the verification of the presented calculations and SIMULINK® models led to the conclusion that not everything was worked out as it should have been. The most important errors that were found are displayed in this part of this thesis. Of course, a proposition for corrections, modifications and supplements will be given too.

The chapter- and section titles from [1] are used, to keep this part clearly structured. The six chapters that will be discussed are: Magnetic Actuator, Sensor System, Mechanics, Control, Experiments and Conclusions.

Each chapter of this part of this thesis is concluded with reviewing conclusions. Those sections contain a summarization of the most important subjects in that chapter combined with conclusions and recommendations for part 2 of this thesis.

Chapter 3

Magnetic Actuator

Chapter 4 of the Ph.D.-thesis [1] deals with the design, modeling and calibration of the magnetic actuators used for the magnetically suspended and propelled mirror system.

Reviewing [1] led to the proposition of corrections, modifications and supplements given in this chapter. The consequences of the changes to the actuator model will be researched in other chapters, mainly the ones concerning the controller design (which is primarily based on the analytical model in the Ph.D.-thesis [1]) and actuator calibration experiments.

3.1 Magnetic force [1, section 4.1.1]

The basis of the analytical modeling of magnetic actuators in [1] is stated in [1, Appendix A]. It shows the relation between the total magnetic energy (W_m) contained in a magnetic system and the force (F_x) generated in a certain direction. The main formula that was derived [1, formula (A.38)], is repeated below:

$$F_x = -\frac{\partial W_m(\Phi,x)}{\partial x} = I\frac{d\Phi_{coupled,0}}{dx} + \tfrac{1}{2}I^2\frac{dL}{dx} - \frac{dW_{m0}}{dx} \tag{3.1}$$

The first term represents the interaction between a coil (carrying current I) and permanent magnets (causing $\Phi_{coupled,0}$), resulting in a force in the x direction.
The second term describes the contribution of one coil alone (carrying a current I and having a self-inductance L) to the total force in the x direction.
The third term gives the force generated in the x direction by solely the permanent magnets.

Formula (3.1) can be used to calculate the force in the x (or any other) direction caused by the interaction between multiple (electro)magnets in a magnetic circuit.
In that case, the partial terms must be calculated for each magnetic flux source.

The second formula taken from [1] is the expression for the magnetic resistance of a beam-shaped piece of material with a cross-section A, a depth d and a relative magnetic permeability μ_r. Like [1, formula (A.44)]:

$$R = \frac{d}{\mu_0\mu_r A} \tag{3.2}$$

3.2 Magnetic topologies [1, section 4.1.5]

This section of the Ph.D.-thesis [1] investigates the possibilities of simple standard magnetic topologies with only one or two electromagnets with and without a permanent magnet present, acting as a magnetic force/displacement actuator.

Two types of actuators are examined, generating a magnetic reluctance force or a Lorentz force. To study a certain actuator topology, an analytical model was derived based on ideal components (see section 3.3). Comparing the advantages and disadvantages of the various topologies led to a suitable actuator choice for the magnetically levitated mirror system.

All presented physical analyses seem to be correct. Only the treatment of the "Reluctance force with permanent magnet pre-magnetization" configuration and the accompanying figure [1, figure 4.4] needs two remarks:

Remark 1: The direction of the magnetic coil's flux in [1, figure 4.4a] doesn't correspond with the source polarity in [1, figure 4.4b]. On itself this is no serious mistake, because it could be that the flux for a negative current through the coil is drawn.

But, later on in the thesis multiple (electro)magnets are operating in one magnetic system. The examination of the interaction of all magnets (coupling fluxes) requires an unequivocal definition of positive magnetic flux directions.

Normally, the right-hand rule is used for magnetic coils. This rule links the generated flux direction to the current direction in the coil in combination with the direction of the windings of the coil (see figure 3.1a). When the magnetic coil is modeled as a voltage source and its magnetic flux as a current in an electrical circuit, the polarity of the voltage source is determined by the magnetic flux direction for a positive current through the coil (see figure 3.1b), and vice versa. A similar agreement is applicable for the positive magnetic flux generated by a permanent magnet (see figure 3.1c).
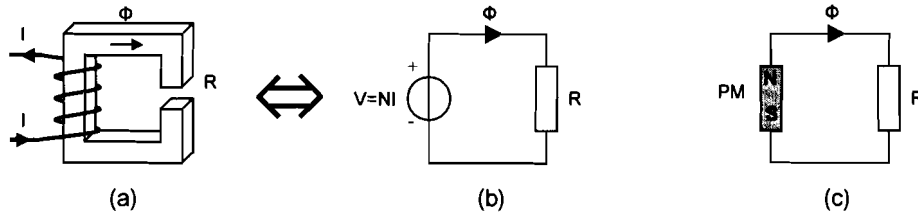
Figure 3.1
Standard sign rules for generated positive magnetic fluxes of:
a) Electromagnet with the right-hand rule applied.
b) Translation of an electromagnet (a) to an electrical circuit with corresponding voltage source signs.
c) Permanent magnet (with flux from magnetic north- to south pole).

Remark 2: The simplification of the magnetic circuit by merging the two coils [1, figure 4.4c] and the original magnetic circuit [1, figure 4.4a] are not 100% equivalent!

In the analysis it is tried to consider two separate but equal coils, working as electromagnets in the same direction, as one large coil. The trick that is used is that the analysis only looks at the flux of the permanent magnets coupled by the upper coil. Instead of calculating both coupled fluxes, the coupled flux of the two coils together is said to be 2 times the coupled flux of the upper coil alone. This last assertion is completely true for the simplified electric scheme, but not for the original. When the $\Phi_{coupled,0}$ expression in (3.3) is multiplied by 2, the result is not the same as $\Phi_{coupled,0}$ in formula (3.5) because of d_1 in the numerator.

Upper coil coupled flux:

$$\Phi_{coupled,0} = N\frac{(d_1+x)}{2d_1}J \qquad \text{and} \qquad \frac{d\Phi_{coupled,0}}{dx} = \frac{NJ}{2d_1} \tag{3.3}$$

Bottom coil coupled flux:

$$\Phi_{coupled,0} = -N\frac{(d_1-x)}{2d_1}J \qquad \text{and} \qquad \frac{d\Phi_{coupled,0}}{dx} = \frac{NJ}{2d_1} \tag{3.4}$$

Coupled fluxes of both coils together:

$$\Phi_{coupled,0} = N\frac{(d_1+x)}{2d_1}J - N\frac{(d_1-x)}{2d_1}J = N\frac{x}{d_1}J \qquad \text{and} \qquad \frac{d\Phi_{coupled,0}}{dx} = \frac{NJ}{d_1} \tag{3.5}$$

When only the derivatives of the coupled fluxes are considered, formulae (3.3)–(3.5) show that the derivative of the coupled flux of the combined coils is equal to two times the derivative of the coupled flux through one of the separate coils. So, the eventual outcome of the analysis is correct for both the original and the simplified circuit.

Remark 3: At this moment both previous remarks might seem unimportant or even nonsense, because the direct effect of both deviations in this analysis is insignificant. But, later on in [1] errors were found that could be directly linked to this analysis.

3.3 Idealized analytical modeling [1, section 4.3]

An ideal model of the real magnetic actuator system and rotor is presented in [1]. The model is called ideal, because in this model not all aspects of the real magnetic system are accounted for and are presumed to be ideal or non-existing. To get a clear picture of the ideal model, the un-modeled magnetic properties are summarized below:

- Hysteresis of the magnetic iron.
- Magnetic saturation of iron (is tried to be avoided by keeping the fluxes small).
- Leaking flux at the coils (is neglected).
- Magnetic flux spreading at the air gaps (is neglected).
- Eddy currents (is dealt with later in a separate section).
- Magnetic resistance of iron (is presumed to be zero).
- Magnetic resistance of permanent magnet material (is presumed to be infinite).

The definition of the magnetic scheme of the horizontal and vertical actuators is shown in [1, figure (4.10)]. Unfortunately, this electrical scheme and the following analysis based on it contain some mistakes that needed to be corrected. The seven corrections that I made are summed up below and explained next.

Correction ①: Un-modeled electric insulation resistance

The blue-prints of the magnetic actuator assembly [1, Figure E.1] show an electric insulation layer between the horizontal coil-cores and the upper- and bottom ring of the stator. This insulation has been placed to use the horizontal coil-cores also as capacitive rotation sensors for the angles α^* and β^*. The insulation causes un-modeled resistance to the magnetic system.

The value of one resistor can be calculated filling in formula (3.2) with the dimensions on the blue-print:

$$R_{ins} = \frac{d_{ins}}{\mu_0 \mu_r A_{ins}} = \frac{0.1 \cdot 10^{-3}}{4\pi \cdot 10^{-7} \cdot 1 \cdot (9.3 \cdot 10^{-3} \cdot 8 \cdot 0.35 \cdot 10^{-3})} = 3.06 \cdot 10^6 \ [A/Wb] \tag{3.6}$$

The height of the insulation layer is $d_{ins} = 0.1$ [mm]. The relative magnetic permeability of the insulation material $\mu_r \approx 1$. The top/bottom surface of the horizontal coil-core $A_{ins} = 2.6 \cdot 10^{-5}$ [m²] (= 9.3 [mm] long and 8 lamellae thick (= 8·0.35 [mm])).

In practice this value can be a little bit smaller because of spreading of the magnetic field. For now this resistance is presumed to be ideal, just like the others.

The magnetic insulation resistance must also be incorporated in the magnetic circuit scheme. It appears eight times in total, which is shown in figure 3.2.
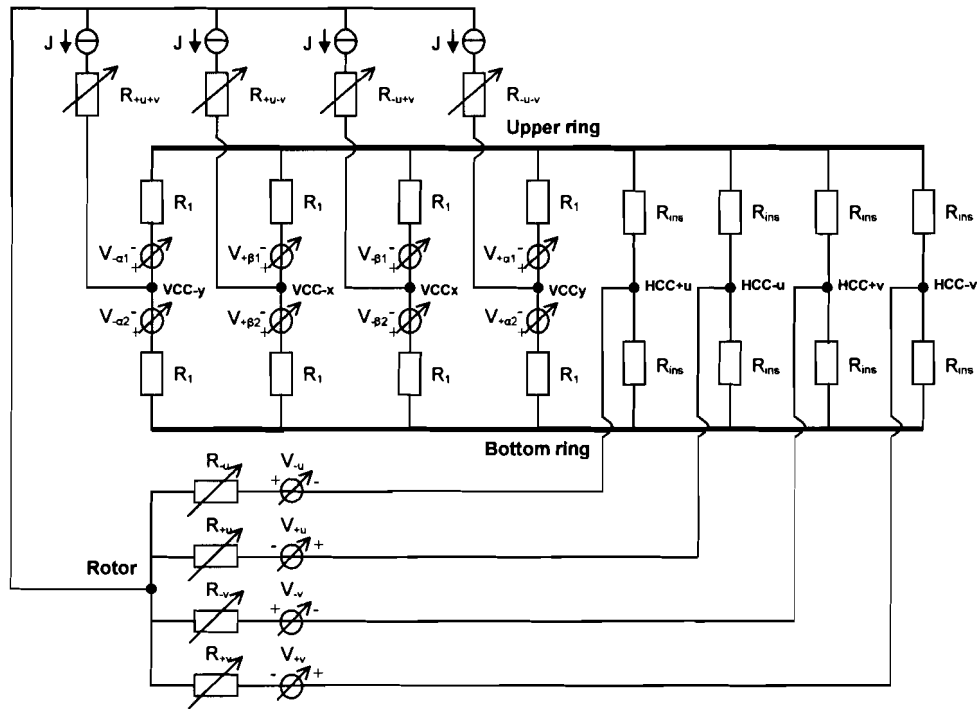
Figure 3.2
Total magnetic circuit (of stator and rotor) with insulator-resistors (R_{ins}) added.
(VCC stands for Vertical Coil-Core and HCC means Horizontal Coil-Core)

The influence of the un-modeled resistance R_{ins} can be studied by looking at the flux paths of the three types of magnetic sources (horizontal coils, permanent magnets and the vertical coils).

The magnetic flux through the complete magnetic circuit of one permanent magnet and one horizontal coil is distributed symmetrical over the upper and bottom ring of the stator. Therefore, their magnetic load circuit can be simplified as is shown in figure 3.3.

(a)   (b)
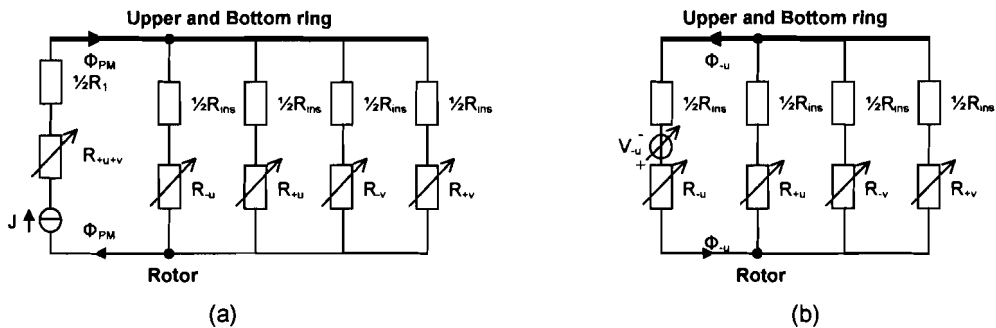
Figure 3.3
Influence of the added insulator-resistors on the magnetic load circuit of:
a) one permanent magnet (J).
b) one horizontal coil (V_{-u}).

As one can see, in both cases the insulation resistance appears (with half its value) in series with the air gap resistances of the horizontal coils. For this reason, the insulation resistance can easily be counted in the nominal air gap distance d, which is shown in formula (3.7).

$$R_{+u} + \tfrac{1}{2}R_{ins} = \frac{d+u}{\mu_0 A_{HC}} + \frac{d_{ins}}{2\mu_0\mu_r A_{ins}} = \frac{d+u+d_{ins}\left(\dfrac{A_{HC}}{2\mu_r A_{ins}}\right)}{\mu_0 A_{HC}} = \frac{d_{plus}+u}{\mu_0 A_{HC}} \tag{3.7}$$

Filling in the values of (3.6) and the nominal air gap distance d = 0.25·10⁻³ [m] gives a numerical value for d_{plus}:

$$d_{plus} = d + d_{ins}\left(\frac{A_{HC}}{2\mu_r A_{ins}}\right) = 0.25\cdot10^{-3} + 0.1\cdot10^{-3}\left(\frac{1.4\cdot10^{-5}}{2\cdot9.3\cdot10^{-3}\cdot8\cdot0.35\cdot10^{-3}}\right) =$$

$$= 2.77\cdot10^{-4}\ [m] \tag{3.8}$$

This is a virtual increase of 10.8 % of the nominal air gap d.

For the permanent magnets and the horizontal coils the influence of the un-modeled insulation rings can now be accounted for by substituting d_{plus} where the nominal air gap distance d appears in the concerning formulae in the thesis [1].

The situation for the vertical coils is more complicated, but a quick analysis of the magnetic circuit (figure 3.2) provides enough information.

The insulation layer cancels the magnetic short circuits between the upper and bottom ring of the stator, caused by the horizontal coil cores. This has no effect on the maximum force that is generated by one vertical coil, because it is a Lorentz force that depends on the magnetic field of the permanent magnet and the current through the vertical coil. These two parameters are not changed by the insulation layer.

However, the insulation layer has two main effects on the vertical coils:

Effect 1)   The magnetic resistive load of the vertical coils is increased.

Effect 2)   A flux path through the other coils (vertical and horizontal) is created. This is unwanted coupling.

Before both effects are investigated it should be mentioned that they could have been avoided. Adding an extra low magnetic resistance connection (short circuit) between the stator rings would maintain the flux paths of the vertical coils as they were originally meant, keeping the vertical coils decoupled from the rest of the magnetic circuit and each other. This extra ring-connection would not disturb the flux paths of the permanent magnets and the horizontal coils, see figure 3.3 where the rings are already virtually connected.

For this quick analysis it is necessary to know the numerical values of some magnetic resistors:

Formula (3.6) gives $R_{ins} = 3.06\cdot10^6$ [A/Wb]
[1, formula (4.135)] gives $R_1 = 12.4\cdot10^6$ [A/Wb]   (3.9)
[1, formula (4.136)] gives R_{+u} (u = v = 0) = 14.4·10⁶ [A/Wb]   (3.10)

Effect 1) Changed magnetic resistive load of vertical coil.

Instead of the short circuit, the magnetic flux of the vertical coils now must travel through all the magnetic resistances between the two stator rings. For this analysis these resistances are replaced by one resistor R_{rep} with a similar value.

When the relative high magnetic resistive flux path through the rotor (3.10) is neglected, the replacement resistor R_{rep} can be approximated by:

$$R_{rep} \approx \frac{1}{\frac{1}{2R_1} + \frac{1}{2R_1} + \frac{1}{2R_1} + \frac{1}{2R_{ins}} + \frac{1}{2R_{ins}} + \frac{1}{2R_{ins}} + \frac{1}{2R_{ins}}} = \frac{2R_1R_{ins}}{3R_{ins} + 4R_1} \qquad (3.11)$$

Substitution of (3.6) and (3.9) in (3.11) gives a numerical value for the replacement resistor:

$$R_{rep} \approx 1.27 \cdot 10^6 \ [A/Wb] \qquad (3.12)$$

By adding the insulation layer, the magnetic resistive load path of one vertical coil is changed from $2R_1$ to approximately $2R_1 + R_{rep}$. This is an increase of about $(1.27/24.8) \cdot 100\% = 5.1$ %.

Effect 2) Possible magnetic flux coupling by other coils.

The magnetic resistance of the insulation layer is relatively low compared to the other resistances (R_1 and R_{+u} etc are more than four times larger). Therefore, the major part of one vertical coil's flux will travel through the parallel connection of 4 times $2R_{ins}$. This is:

$$R_{ins}/2 = 1.53 \cdot 10^6 \ [A/Wb] \qquad (3.13)$$

Comparison of (3.13) with the approximated value of R_{rep} (3.12) shows that indeed a small part of the flux will travel through the R_1 resistances and ergo through the other three vertical coils.

In theory the insulation layer enables a flux path through the rotor and therefore through the horizontal coils. Because of the high magnetic resistance of this path it isn't very likely to have much influence.

Note that in practice the (small) coupling can be measured by forcing an AC-current through one of the vertical coils and at the same time measuring the induced voltages over the other coils in the magnetic system.

Correction ②: Air gap resistor names

The definition of the position dependant magnetic resistances [1, (4.50)] in combination with the drawing of the magnetic circuit [1, figure (4.10)] is ambiguous.
Take for example the magnetic resistance between the horizontal coil on the +u side and the rotor. This resistance is logically called R_{+u}. However, in [1, (4.50)] it is defined as $R_{+u} = (d + u)/(\mu_0 A_{HC})$ which is on itself also logical because of "+u" in the expression. But, the magnetic resistance on the +u side becomes smaller when u gets larger. So the expression for the resistor on the +u side should be $R = (d - u)/(\mu_0 A_{HC})$.

This problem can be solved in two ways by:
❶ inverting the uv-frame in the magnetic circuit [1, figure (4.10)].
❷ adjusting all signs in the magnetic resistance expressions and the calculations they were used in.

The time saving solution ❶ was chosen, with the consequence that all the concerning air gap resistors carry a name that is the opposite of its position in the stator frame. So, resistor R_{+u} is positioned at the −u side of the stator frame and so on, see figure 3.4 !!

Correction ③: Definition and position of torque actuators

The cooperation of two oppositely positioned vertical coils ($+\alpha/-\alpha$ and $+\beta/-\beta$) to act as a torque actuator is not well defined. According to [1, (4.49)] the direction of one of the opposite coils is reversed and at the same time the direction of the current through that coil is reversed. This has no net effect (with the coil winding direction left out of consideration), only one option should be used to create a torque-generating set of actuators.

To correct this, the following choices were made (to change the definitions to what I believe was meant). Keep the direction of all four vertical coils the same. Define all upper parts as 1 and the bottom parts as 2. When the four vertical coils receive the same current ($+I_z$) they will all generate a force in the same direction; the $+z$ direction.

A torque can now be generated by forcing a positive current through one of two opposite vertical coils, while the other one receives the same amount of current, only negative.

To complete the modification, formulae [1, (4.49)] need some adjustments:

$$V_{-\alpha 1} = N_{VC}(-I_\alpha + I_z)\frac{k + \alpha}{2k} \qquad \text{and} \qquad V_{-\alpha 2} = N_{VC}(-I_\alpha + I_z)\frac{k - \alpha}{2k} \qquad (3.14)$$

$$V_{-\beta 1} = N_{VC}(-I_\beta + I_z)\frac{k + \beta}{2k} \qquad \text{and} \qquad V_{-\beta 2} = N_{VC}(-I_\beta + I_z)\frac{k - \beta}{2k} \qquad (3.15)$$

Also the position of the vertical coils in the magnetic scheme [1, (4.10)] is not according to the angle definitions in [1, figure 2.3], at least when it is presumed that a positive current ($+I_\alpha$) through the $+\alpha$ coil would increase the angle α, and so on. The right positions (by this definition) of the vertical coils is depicted in figure 3.4 (and also in figure 3.2).
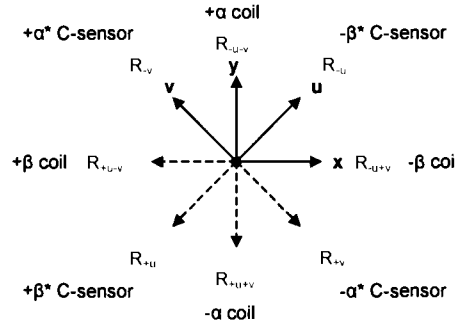
Figure 3.4
Definition of positions with respect to the stator frame of:
the vertical coils, the magnetic resistances and the capacitive angular sensors.

Correction ④: Permanent magnets coupled fluxes

Two mistakes are made regarding the coupling of the permanent magnet fluxes by the horizontal coils. The first one is that the coupling of these fluxes is only N_{HC} times by each coil, not $2N_{HC}$ times as is claimed in [1, (4.67)]. The second mistake is that the signs of the permanent magnet fluxes coupled by the horizontal coils are reversed in the calculations. As figure 3.2 and the original magnetic circuit [1, figure 4.10] show the positive permanent magnets flux flows in the same direction as the positive flux of the $-u$ and $-v$ coil. Therefore, the permanent magnets flux is positively coupled by these two coils. Logically, for the $+u$ and $+v$ coils follows that they couple the permanent magnets flux negatively. See figure 3.1 (and Remark 1 in section 3.2) for the normal flux sign definitions.

The adjusted formulae for the coupled permanent magnet fluxes by the horizontal coils are:

$$\frac{d\Phi_{coupled,0,u}}{du} = -4JN_{HC}\frac{(v^2 - d^2)(u^2 - v^2 + 2d^2)}{d(u^2 + v^2 - 2d^2)^2} \overset{u,v \ll d}{=} \frac{2JN_{HC}}{d} + O(u^2, v^2) \qquad (3.16)$$

$$\frac{d\Phi_{coupled,0,v}}{dv} = -4JN_{HC}\frac{(u^2 - d^2)(v^2 - u^2 + 2d^2)}{d(u^2 + v^2 - 2d^2)^2} \overset{u,v \ll d}{=} \frac{2JN_{HC}}{d} + O(u^2, v^2) \qquad (3.17)$$

Both expressions are parts of the first terms in the formulae describing the horizontal force actuators. Also remember that as a result of Correction ①: parameter d should be replaced by d_{plus}.

Correction ⑤: Horizontal coils coupled fluxes

In an attempt to merge the two horizontal coils for one direction into one big actuator, the magnetic fluxes of the horizontal coils are unjustly said to be coupled $2N_{HC}$ times instead of just N_{HC} times. This is the same mistake as Correction ④ and it is probably caused by the analysis talked about at Remark 2 in section 3.2.

The mistake can be easily checked by looking directly at the total magnetic energy in the complete system and then at the magnetic coil fluxes (which is done below), instead of the other way around.

The four horizontal coils (+u, -u, +v and -v) interact with themselves (4 self- inductances L) and with each other (2 times 6 mutual inductances M) by generating fluxes that are coupled via their paths through the magnetic circuit. The part of the magnetic energy in the total system caused by the set of coupled horizontal coils solely can be described by the following expression:

$$W_{m,HC} = \tfrac{1}{2}L_{+u}I_{+u}^2 + \tfrac{1}{2}L_{-u}I_{-u}^2 + \tfrac{1}{2}L_{+v}I_{+v}^2 + \tfrac{1}{2}L_{-v}I_{-v}^2 + M_{+u,-u}I_{+u}I_{-u} + M_{+u,+v}I_{+u}I_{+v} +$$

$$+ M_{+u,-v}I_{+u}I_{-v} + M_{-u,+v}I_{-u}I_{+v} + M_{-u,-v}I_{-u}I_{-v} + M_{+v,-v}I_{+v}I_{-v}$$

(3.18)

With $I_{+u} = I_{-u} = I_u$ and $I_{+v} = I_{-v} = I_v$ formula (3.18) can be written as:

$$W_{m,HC} = \tfrac{1}{2}I_u^2(L_{+u} + L_{-u} + 2M_{+u,-u}) + \tfrac{1}{2}I_v^2(L_{+v} + L_{-v} + 2M_{+v,-v}) +$$

$$+ I_uI_v(M_{+u,+v} + M_{+u,-v} + M_{-u,+v} + M_{-u,-v}) = \tfrac{1}{2}I_u^2L_u + \tfrac{1}{2}I_v^2L_v + I_uI_vL_{uv}$$

(3.19)

These terms correspond with the flux terms in the thesis [1, (4.59), (4.62) and (4.63)]. The only difference is that all these partial terms represent coils with N_{HC} windings. So the fluxes in the thesis [1] should be coupled N_{HC} times instead of $2N_{HC}$ times.

Correction ⑥: Calculation of torques $T_{\alpha/\beta}$

The presented coupled fluxes of the permanent magnets by the vertical coils [1, (4.77)] are incorrect. Simply fill in $\alpha = 0$ (or $\beta = 0$) and the coupled permanent magnet flux should be 0, which is not the case.

The correct calculation of the torque T_α is done in appendix A.5. The calculation of torque T_β is equivalent. The changes to the coil definitions (3.14) and (3.15) are also incorporated in appendix A.5.

It seems that there's no difference between (A.13) and the formula for T_α in the thesis [1, (4.79)]. But that is not the importance of this correction. If the coil definitions [1, (4.49)] are used, then I_z becomes the torque generating current and I_α the vertical force generating current! This would be devastating for the controller.

Correction ⑦: Rough calculation of torque T_γ

The presented magnetic resistive load for one permanent magnet R_{tot} [1, (4.82)] is incomplete and therefore incorrect. Apparently, it's forgotten that also a flux path through the other two horizontal magnetic resistances (air gaps between rotor and horizontal coil-cores, not drawn in [1, figure 4.11]) is possible. The magnetic resistance of the electric insulation layer (R_{ins}, see Correction ①) is also not mentioned. With these two corrections the expression for R_{tot} becomes:

$$R_{tot} = R_{VC} + \tfrac{1}{4}R_{HC} + \tfrac{1}{2}R_1 + \tfrac{1}{4}R_{ins} \text{ [A/Wb]}$$

(3.20)

Somewhat astonishing is the use of formula (3.21) for the magnetic energy (W_m) stored in an air gap with a magnetic resistance R, in the continuation of the analysis.

$$W_m = \tfrac{1}{2}\Phi^2 R$$

(3.21)

Because this is a quadratic function of the magnetic flux Φ through the resistor R, superposition of magnetic energies does not hold, even though [1, (4.91)] would like us to think so.

The way to use (3.21) correctly is shown in table 3.1. First determine the sum of the fluxes through one of the separate resistors (column 3). Then calculate the magnetic energy stored in this air gap and multiply it by the times the resistor appears in the magnetic system (column 2). Then calculate the sum of all the resistors together.

Table 3.1 Correction of stored magnetic energies.

Magnetic resistance	Appears [times]	Magnetic flux Φ [Wb]	$W_m = \frac{1}{2}\Phi^2 R$ [J]
R_1	8	$J/2$	$8 \cdot \frac{1}{2}R_1 \cdot \frac{1}{4}J^2 = J^2 R_1$
R_{VC}	4	J	$4 \cdot \frac{1}{2}R_{VC} \cdot J^2 = 2J^2 R_{VC}$
R_{HC}	4	J	$4 \cdot \frac{1}{2}R_{HC} \cdot J^2 = 2J^2 R_{HC}$
R_{ins}	8	$J/2$	$8 \cdot \frac{1}{2}R_{ins} \cdot \frac{1}{4}J^2 = J^2 R_{ins}$
		Total:	$2J^2(R_{VC} + R_{HC} + \frac{1}{2}R_1 + \frac{1}{2}R_{ins})$

The last row of table 3.1 shows that [1, (4.91)] should be:

$$W_{m0} = 2J^2(R_{VC} + R_{HC} + \tfrac{1}{2}R_1 + \tfrac{1}{2}R_{ins}) \neq 4 \cdot \tfrac{1}{2}J^2 R_{tot} \qquad (3.22)$$

Luckily this has no influence on rest of the calculation.

Note that above problems could have been avoided by a faster reasoning, namely:
All permanent magnet fluxes are directly forced through R_{VC}. So each R_{VC} receives a flux J. The only way back to the rotor is through the horizontal coil air gaps (R_{HC}). When the rotor is in its neutral positions all four R_{HC} are equal, so the fluxes of the permanent magnets will be divided equally over the four air gaps, ergo each R_{HC} receives a flux J.

Since only the dW_{m0}/dy is of interest, R_1 and R_{ins} can be neglected because they are constant (not dependant of y). Then $dW_{m0}/dy = d(2J^2(R_{VC} + R_{HC}))/dy$.

Another problem arises with the use of parameter c_{VC} in formula [1, (4.94)] and on.
This formula is given without any explanation, except that it can be compared with the previous calculation of the vertical coil force. Indeed this is true, both forces are Lorentz forces but the direction of the windings of the toroidal coils is rotated 90° (which means the direction of the force is also rotated by 90°) compared to the vertical coils. The second difference is the size of the coils (diameter, length, number of windings and wire diameter).

The generated torque by the toroidal coils can be calculated with the method in appendix A.5 which gives the same result as the direct calculation of the Lorentz force of one coil with [1, (4.43)]:

$$F_L = -BI_L I_L = -B_{PM} A_{PM} I_y \frac{N_{TC}}{I_{TC}} = -\frac{JN_{TC} I_y}{I_{TC}} \qquad (3.23)$$

Resulting in a corrected expression for the approximated magnitude of torque T_y generated by the four toroidal coils together:

$$T_y = 4R_{PM} \cdot F_L = -\frac{4R_{PM} J N_{TC}}{I_{TC}} I_y \qquad (3.24)$$

Wherein parameter I_{TC} is the length of the toroidal coil and R_{PM} is the radius of the rotor where a permanent magnet is mounted.

Comparison of (3.24) with [1, (4.96)] shows that both expressions are equal when:

$$c_{VC} \text{ is equal to } (I_{TC}/R_{PM}) \qquad (3.25)$$

When the definitions in [1] are used, it can be proven that this leads to an inconsistency. Starting with [1, (4.90)]:

$$c_{VC} = \frac{1}{(y_{max}^{VC})^2} \qquad (3.26)$$

and

$$2y_{max}^{VC} = \frac{I_{TC}}{R_{PM}} = \frac{1}{\sqrt{\frac{c_{VC}}{4}}} = \frac{2}{\sqrt{c_{VC}}} \qquad (\neq c_{VC}) \qquad (3.27)$$

Clearly, formulae (3.27) and (3.25) can't both be true at the same time (except for one specific value). There might be a reason for this irregularity. Maybe it is a correction factor for the fact that the shape of toroidal coil is not spherical, or the non-ideal flux path of the permanent magnet through the toroidal coil? These are just speculations.

For now, formula (3.24) is considered to be the correct one. The calculation of numerical values in section 3.5 will show the deviation between the corrected values and the values in the thesis [1].

3.4 Finite Element Modeling [1, section 4.4]

The finite element modeling (FEM) example in [1, section 4.4] was created to do a more realistic calculation of the electromagnetic fields in a system, to compare the FEM results with the results from idealized modeling of the system.

Four mistakes were found in the finite element modeling as presented in the thesis [1]. Two mistakes corrupt the calculation of the motor constants:

❶ The magnetic resistance (R_S) of the four small air gaps in the stator has been neglected in the calculations based on ideal modeling.

❷ Parameter l has mistakenly been interpreted as the length of the T-coil, while it is only half the length ($l = \frac{1}{2}I_{TC}$) of this coil.

Two minor mistakes are:

❸ All the x parameters in the formulae in [1, section 4.4.2] should be replaced by parameter y.

❹ The flux of the two permanent magnets together is $J = 2B_{PM}h_{PM}$ and for the coils $NI = d_c I_c J_c$. In the thesis [1] the factor 2 is wrongly placed in the last formula. Since both formulae are multiplied in all the calculations, this mistake has no effect on the final outcome.

The correction for the mistakes is done in appendix F. The results of the corrections are presented below. (Note that K_T^T is not changed by R_S because it's a Lorentz force)

$$\frac{_{FEM}K_T^T}{K_T^T} \approx \frac{-3.4 \cdot 10^{-8}}{-4.04 \cdot 10^{-8}} \approx 84\% \qquad (3.28)$$

$$\frac{_{FEM}K_F^F}{K_F^F} \approx \frac{1.3 \cdot 10^{-5}}{2.33 \cdot 10^{-5}} \approx 56\% \qquad (3.29)$$

$$\frac{_{FEM}K_F^T}{K_F^T} \approx \frac{1.5 \cdot 10^{-5}}{2.94 \cdot 10^{-5}} \approx 51\% \qquad (3.30)$$

The conclusion for this example in [1] that with ideal modeling the motor constants are calculated 2 times larger than they are calculated with FEM is still valid, but now the numbers are more in agreement with it...

Disclaimer:
The FEM analysis itself hasn't been checked. The FEM results that are presented in the thesis [1] are simply copied here and assumed to be correct. Normally this shouldn't be a problem.

3.5 Calculation of generated forces and torques
[1, section 4.6]

3.5.1 Forces by horizontal coils

In total, three changes have been made to the horizontal force actuator formulae (section 3.3):

❶ Parameter d (nominal air gap between rotor and stator) has been replaced by d_{plus} to account for the non-modeled magnetic resistance caused by the electrical insulations between the horizontal coil-cores and the upper- and bottom ring of the stator.

❷ Some magnetic fluxes were unjustly said to be coupled $2N_{HC}$ times instead of only N_{HC} times.

❸ The first term now has a positive sign.

The corrected formula for the horizontal force actuator in the u direction is:

$$F_u = \frac{2JN_{HC}}{d_{plus}}I_u + I_u^2\frac{\mu_0 A_{HC}N_{HC}^2}{d_{plus}^3}u - I_uI_v\frac{\mu_0 A_{HC}N_{HC}^2}{d_{plus}^3}v + \frac{2J^2}{\mu_0 A_{HC}d_{plus}}u \tag{3.31}$$

The formula for the actuator force in the v direction is equivalent to formula (3.31) with all u's interchanged for v's, and vice versa. Note that this simplified formula is valid for the rotor near its neutral position (u,v << d).

In appendix G the maximum horizontal actuator forces are numerically calculated. The results are repeated here followed by some derived parameters:

The maximum force generated in the u or v direction is $F_{u/v,max} = 14.38$ [N].

Only the first term of $F_{u/v}$ (3.31) is really the generated force for the neutral position of the rotor, so $F_{u/v,generated,max} = 8.66$ [N].

The maximum acceleration of the rotor in the u direction can now be calculated using the maximum force in this direction and the corrected estimated rotor mass ($m_{ROTOR} = 8.49 \cdot 10^{-3}$ [kg], see section 5.2).

$$a_{u,max} = \frac{F_{u,max}}{m_{ROTOR}} = \frac{14.38}{8.49 \cdot 10^{-3}} = 1.7 \cdot 10^3 \ [m/s^2] \approx 173 \ [g] \tag{3.32}$$

This is just a theoretical value because this maximum force can only be generated when the rotor is stuck to the stator, so it can't move (or accelerate). The practical maximum acceleration for the rotor in the neutral position (u = v = z = 0) is:

$$a_{u,generated,max} = \frac{F_{u,generated,max}}{m_{ROTOR}} = \frac{8.66}{8.49 \cdot 10^{-3}} = 1.02 \cdot 10^3 \ [m/s^2] \approx 104 \ [g] \tag{3.33}$$

The linear model for the two horizontal force actuators [1, (4.144)] is repeated below:

$$\frac{F_u}{m} = {}_uK_I \cdot I_u + {}_uK_u \cdot u$$

$$\frac{F_v}{m} = {}_vK_I \cdot I_v + {}_vK_v \cdot v \tag{3.34}$$

The corrected linear model gains can now be calculated.
The generated force by the horizontal actuators is mainly the first term in expression (3.31), so:

$$_uK_I = {}_vK_I = \frac{2JN_{HC}}{m_{ROTOR}d_{plus}} = \frac{3.47}{8.49 \cdot 10^{-3}} = 408 \ [m/s^2A] \tag{3.35}$$

The destabilizing force by the horizontal actuators is mainly the fourth term in expression (3.31), so:

$$_uK_u = {}_vK_v = \frac{2J^2}{m_{ROTOR}\mu_0 A_{HC}d_{plus}} = \frac{1.05 \cdot 10^5}{8.49 \cdot 10^{-3}} = 1.238 \cdot 10^7 \ [1/s^2] \tag{3.36}$$

3.5.2 Forces and torques by vertical coils

No changes are made to the formulae derived in [1] for the forces and torques generated by the vertical coils. However, the use of the correct formulae to get numerical values for the maxima of the forces and torques contains two mistakes:

❶ Parameter l was understandably mistaken for the length of the vertical coil, while it is defined as half the length of the vertical coil [1, figure 4.5]. This results in a maximum force in the z direction that is twice as large as is calculated in [1].

❷ The parameter D_{vc}^2 (cross-section of vertical coil wire, which is presumed to be square) is being conjured with.

To clarify the mistakes, a well-ordered summary of the calculations with the corrected values and expressions is given in appendix G. The results are repeated here followed by some derived parameters:

The maximum force generated in the z direction is $F_{z,max} = 1.92$ [N].

The maximum torque generated in the α or β direction is $T_{\alpha/\beta,max} = 9.6 \cdot 10^{-3}$ [Nm].

The maximum acceleration of the rotor in the z direction can be calculated using the maximum force in this direction and the corrected estimated rotor mass ($m_{ROTOR} = 8.49 \cdot 10^{-3}$ [kg], see section 5.2).

$$a_{z,max} = \frac{F_{z,max}}{m_{ROTOR}} = \frac{1.92}{8.49 \cdot 10^{-3}} = 226 \ [m/s^2] \approx 23 \ [g] \tag{3.37}$$

The maximum angular acceleration of the rotor in the α- or β-direction can be calculated using the maximum torque in this direction and the corrected estimated moment of inertia around the x- or y-axis of the rotor ($I_{X/Y} = 2.21 \cdot 10^{-7}$ [kgm^2], see section 5.2).

$$\dot{\omega}_{\alpha/\beta,max} = \frac{T_{\alpha/\beta,max}}{I_{X/Y}} = \frac{9.6 \cdot 10^{-3}}{2.21 \cdot 10^{-7}} = 4.34 \cdot 10^4 \ [rad/s^2] \tag{3.38}$$

The corrected gains for the linear model are:

$$_z K_I = \frac{F_{z,max}}{m_{ROTOR} I_{z,max}} = \frac{1.92}{8.49 \cdot 10^{-3} \cdot 2.5} = 90.46 \ [m/s^2 A]$$ (3.39)

$$_\alpha K_I = {_\beta K_I} = \frac{\dot\omega_{\alpha/\beta,max}}{I_{\alpha/\beta,max}} = \frac{4.34 \cdot 10^4}{-2.5} = -1.74 \cdot 10^4 \ [rad/s^2 A]$$ (3.40)

3.5.3 Torques around the z-axis (T_y)

The rough approximation for the magnitude of the torque around the z-axis of the rotor with the first term replaced by the correction (3.24) is given in (3.41).

$$T_y = -\frac{4R_{PM} J N_{TC}}{I_{TC}} I_y - \frac{4J^2 d}{\mu_0} \left(\frac{c_{VC}}{A_{PM}} + \frac{c_{HC}}{A_{HC}} \right) \gamma = {_y T_I} + {_y T_\gamma}$$ (3.41)

Filling in the parameters in appendix (G.13) in formula (3.41) results in:

$$T_y = -9.546 \cdot 10^{-4} I_y - 0.16\gamma$$ (3.42)

From (3.41) combined with the maximum inputs:
$I_{y,max} = \pm 2.5$ [A] and
$\gamma_{max} \approx \pm 0.48$ [rad]   (No longer overlap of real vertical coil pole shoes)
some extra parameters can be derived, namely:

The generated maximum torque by the coils:

$$_y T_{I,max} = 9.546 \cdot 10^{-4} \cdot 2.5 = 2.3865 \cdot 10^{-3} \ [Nm]$$ (3.43)

The first part of the maximum angular acceleration of the rotor in the y-direction can now be calculated using the maximum torque in this direction and the corrected estimated moment of inertia around the z-axis of the rotor ($I_z = 3.41 \cdot 10^{-7}$ [kgm²], see section 5.2):

$$\dot\omega_{y,coils,max} = \frac{_y T_{I,max}}{I_z} = \frac{2.3865 \cdot 10^{-3}}{3.41 \cdot 10^{-7}} = 7 \cdot 10^3 \ [rad/s^2]$$ (3.44)

The maximum stabilizing torque by the permanent magnets alone:

$$_y T_{\gamma,max} = -0.16 \cdot 0.48 = -76.8 \cdot 10^{-3} \ [Nm]$$ (3.45)

The second part of the maximum angular acceleration of the rotor in the y direction:

$$\dot\omega_{y,PM,max} = \frac{_y T_{\gamma,max}}{I_z} = \frac{-76.8 \cdot 10^{-3}}{3.41 \cdot 10^{-7}} = -2.25 \cdot 10^5 \ [rad/s^2]$$ (3.46)

It seems that the torque generated by the permanent magnets (3.45) is very dominant compared to the torque generated by the coils (3.43). In reality this is not the case, because (3.45) strongly depends on the change of magnetic resistance between the rotor and stator when the rotor is rotated over an angle γ. In the real design this effect has been minimized by overlapping of the rotor and stator pole shoes. So, the four coils generate the dominant torque for a small angle γ.

The corrected gains for the linear model are:

$$_{y}K_{I} = \frac{_{y}T_{I}}{I_{z} \cdot I_{y}} = \frac{-9.546 \cdot 10^{-4}}{3.41 \cdot 10^{-7}} = -2800 \text{ [rad/s}^2\text{A]} \tag{3.47}$$

$$_{y}K_{y} = \frac{_{y}T_{y}}{I_{z} \cdot y} = \frac{-0.16}{3.41 \cdot 10^{-7}} = -4.7 \cdot 10^{5} \text{ [1/s}^2\text{]} \tag{3.48}$$

Lastly, the influence of the correction (3.24) will be investigated. The change is that the torque generated by the coil contains a different multiplication factor. The ratio between the two factors is displayed in (3.49):

$$\frac{R_{PM}}{I_{TC}} : \frac{1}{c_{VC}} \Leftrightarrow \frac{4}{5} : \frac{1}{2.84} \Leftrightarrow 3.5 : 1 \tag{3.49}$$

So the corrected torque generated by the toroidal coils is 3.5 times larger than calculated in [1].

3.6 Modal analysis [1, section 4.7]

The section in [1] was meant to analyze some critical bending modes of the mechanical structure. It gives a rough estimation of the resonance frequencies of the system. However, the presented working out is questionable and somewhat strange. This correction might be useful to explain deviations in the expected behavior of the laser deflection system or for future designs.

The first striking thing is that the presented formula for the stiffness S is derived incorrectly from the two previous expressions in that section. (48/12 = 4, not 3). The corrected formula for S is given below.

$$S = \frac{F}{f} = \frac{48EI}{I^3} = \frac{48Ewh^2}{12I^3} = \frac{4Ewh^3}{I^3} \text{ [N/m]} \tag{3.50}$$

Evidently, the next formula (for the resonance frequency) that contains S is also wrong. This formula should be as stated in (3.50).

$$f_{res} = \frac{1}{2\pi}\sqrt{\frac{S}{m}} = \frac{1}{2\pi}\sqrt{\frac{4Ewh^3}{mI^3}} = \frac{1}{\pi}\sqrt{\frac{Ewh^3}{mI^3}} \text{ [Hz]} \tag{3.51}$$

The second notable thing is that when the formula for f_{res} is used, suddenly an extra factor 2 is added under the square root sign. Maybe this is done to calculate the bending mode for two directions at the same time? This is just a guess, because the thesis [1] doesn't give an explanation.

The third remarkable thing is that when the proposed parameter values for both calculations are entered in the formula, different outcomes from the ones presented appear. The thesis values and the corrected values of the two resonance frequencies are displayed in table 3.2.

Table 3.2 Corrected resonance frequencies.

	f_{res} [Hz] (Vertical coils)	f_{res} [Hz] (rotor PCB)
Thesis [1] value	$9 \cdot 10^3$	$20 \cdot 10^3$
Corrected thesis value	$9 \cdot 10^2$	$1.6 \cdot 10^3$
Corrected outcomes	735	1,334

It is clear that some things went wrong in this analysis. For me it's not useful to look further into this subject now.

3.7 Calibration [1, section 4.10]

In [1, section 4.10] some calibration methods for the magnetic actuators are discussed. The calibration method based on the lift-off trajectories of the rotor is the one used so far on the real device, because it identifies both $_{uv}K_i$ and $_{uv}K_{uv}$, without using extra measurement equipment. However, the description of the method [1, section 4.10.4] is incomplete and contains some errors. The problems that are caused by this are clarified in this section.

Problem 1: The "stuck to the stator" position of the rotor.

Particular attention must be paid to the "stuck to the stator" position of the rotor, because it is used on three occasions throughout the thesis [1], namely:
① The calculation of the magnetic resistance between a permanent magnet and the vertical coil-core it is facing [1, section 4.5.10.2].
② The magnetic actuator calibration [1, section 4.10 and section 8.5].
③ The capacitive sensor calibration [1, section 5.6.4 and section 8.4].

Especially the use of parameter d_{max} is ambiguous. In all three situations d_{max} is defined as the maximum distance the rotor can travel in the ±x- or ±y-direction. In figure 3.5 is shown that it is determined by the distance the rotor can travel in the ±u- and ±v-direction. So, with the coating of 200 [μm] on the contact surfaces of the horizontal coil-cores:

$$d_{max} = x_{max} = y_{max} = \sqrt{2} \cdot u_{max} = \sqrt{2} \cdot v_{max} = \sqrt{2} \cdot 50 \ [\mu m] \tag{3.52}$$

Rotor distance traveled:

$x_0 = 0$

(a)   (b)   (c)
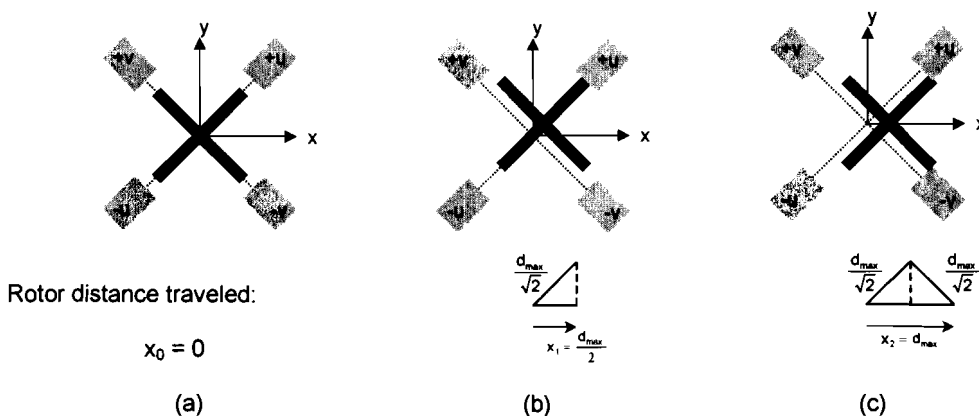
Figure 3.5
Schematic top-view of rotor (black cross) between the horizontal coils (gray blocks) in three positions:
a) Neutral position (operating point of the rotor).
b) One rotor-leg stuck to the stator ($u = u_{max}$, $v = 0$).
c) Two rotor-legs stuck to the stator ($u = u_{max}$, $v = -v_{max}$).

Two notes must be made:

Note 1) In figure 3.5 the contact surfaces of both the rotor-legs and the horizontal coil-cores are assumed to be flat. In reality these surfaces are somewhat spherical. This has only a slight effect on d_{max}.

Note 2) There also is a little problem with the coating. According to [1, section 4.9.1.6] no coating was applied between the capacitive sensors on the stator and the aluminum semi-sphere on the rotor, due to a manufacturing error. This mistake comes in handy because otherwise the bottom part of the rotor would have been blocked at a distance of 50 [μm], while the top part can travel $\sqrt{2} \cdot 50$ [μm], meaning the rotor would tilt a little (and damage the coating) while getting in the "stuck to the stator" position.

Problem 2: ∂I should be I_u in [1, formula (4.181)].

The linear transfer function of the force actuator in the u-direction is copied from [1, (4.173)] and transformed to the time domain:

$$H_u(s) = \frac{u(s)}{I_u(s)} = \frac{_uK_I}{s^2 - _uK_u} \Leftrightarrow \ddot{u}(t) = _uK_I \cdot I_u(t) + _uK_u \cdot u(t) \tag{3.53}$$

Filling in the constant current $I_u(t) = I_{u,lift-off} + \partial I_u$ guaranties lift-off of the rotor:

$$\ddot{u}(t) - _uK_u \cdot u(t) = _uK_I \cdot (I_{u,lift-off} + \partial I_u) \tag{3.54}$$

At the moment of lift-off $(t = 0)$, $(-_uK_u \cdot u = _uK_I \cdot I_{u,lift-off})$ holds. Then (3.55) remains:

$$\ddot{u}(0+) = _uK_I \cdot \partial I_u \tag{3.55}$$

This only represents the rotor acceleration at the start of lift-off (here $t = 0$).
After that $(-_uK_u \cdot u < _uK_I \cdot I_{u,lift-off})$ holds, and formula (3.54) has to be used again.

Problem 3: The presented solution for the differential equation is incomplete.

A rectification for [1, formula (4.185)] is given in (3.56). Forgotten were the minus-sign (before d_{max}) and the last part (gains and the <u>constant</u> current $I_u(t) = I_u$).

$$u(t) = \left(-\frac{d_{max}}{\sqrt{2}} + \frac{_uK_I}{_uK_u}I_u\right) \cdot \left(\frac{1}{2}e^{\sqrt{_uK_u}t} + \frac{1}{2}e^{-\sqrt{_uK_u}t}\right) - \frac{_uK_I}{_uK_u}I_u = \left(-\frac{d_{max}}{\sqrt{2}} + \frac{_uK_I}{_uK_u}I_u\right)\cosh\left(\sqrt{_uK_u}t\right) - \frac{_uK_I}{_uK_u}I_u \tag{3.56}$$

These mistakes were easily discovered by just filling in the initial conditions.

Problem 4: It is not shown how $(_uK_I / _uK_u)$ can be derived form $I_{u,lift-off}$. (It is only mentioned that it is equal to the DC-gain of the actuator).

Start with the differential equation (3.53). With the initial conditions (3.57):

$$\ddot{u}(t_{lift-off}-) = \dot{u}(t_{lift-off}-) = 0, I_u = I_{u,lift-off} \text{ and } u(0) = \frac{-d_{max}}{\sqrt{2}} \tag{3.57}$$

It results in results in:

$$0 = _uK_I \cdot I_{u,lift-off} + _uK_u \cdot \left(-\frac{d_{max}}{\sqrt{2}}\right) \Rightarrow \frac{_uK_I}{_uK_u} = \frac{d_{max}}{I_{u,lift-off} \cdot \sqrt{2}} = \frac{u_{max}}{I_{u,lift-off}} \tag{3.58}$$

Problem 5: How can the term(s) $\sqrt{_uK_u}$ (and $_uK_I$) be derived from the lift-off trajectory measurements?

This question is not explicitly answered in [1, chapter 4]. A peek at [1, section 8.5.2], where the horizontal actuator calibration experiment is executed, explains a little more.
Three methods are mentioned:

❶ Take the natural logarithm of the measured position trajectory u. The slope of the plot for $t \to \infty$ is mainly determined by the dominating term $e^{\sqrt{_uK_u}t}$. The other parameter $(_uK_I)$ can be derived from the DC-gain and the lift-off current (3.58).

❷ Black box identification. Unfortunately, this method is not good applicable for this device as long as it is unstable.

❸ Data fitting by non-linear least squares optimization. This method has been used eventually.

Because the information in [1] is quite limited, now a supplementary analysis is given including an expectation for the horizontal actuator lift-off trajectories and the derivation of (all) important lift-off parameters and linear model actuator gains.

The horizontal lift-off current is the minimal current needed to pull the rotor loose from the stator. This current can be calculated for the ideal model by rearranging formula (3.58) and filling in the already calculated ideal linear model gains
($_uK_l$ = 408 [m/s^2/A] (3.35) and $_uK_u$ = 1.24·10^7 [1/s^2] (3.36)) and u_{max} (3.52).

$$I_{u,lift-off} = \frac{_uK_u \cdot u_{max}}{_uK_l} = \frac{1.24 \cdot 10^7 \cdot 50 \cdot 10^{-6}}{408} = 1.5196078 \ [A] \tag{3.59}$$

To guarantee lift-off, this current is increased by a small amount (∂I_u):

$$I_u = I_{u,lift-off} + \partial I_u = 1.52 \ [A] \quad \text{with } \partial I_u \approx 0.39 \ [mA] \tag{3.60}$$

For now, the horizontal lift-off time Δt is defined as the time between the start of the rotor movement and the moment of impact on the other stator side. Formula (3.56) can be used to calculate Δt. It is repeated below.

$$u(t) = \left(-u_{max} + \frac{_uK_l}{_uK_u} I_u \right) \cosh\left(\sqrt{_uK_u} \ t \right) - \frac{_uK_l}{_uK_u} I_u$$

Substitution of the limiting conditions (on t = 0 ➔ u = -u_{max}, after Δt ➔ u = u_{max}) results in an expression for the horizontal lift-off time Δt.

$$u_{max} = \left(-u_{max} + \frac{_uK_l}{_uK_u} I_u \right) \cosh\left(\sqrt{_uK_u} \ \Delta t \right) - \frac{_uK_l}{_uK_u} I_u \quad \Leftrightarrow$$

$$\Leftrightarrow \ \Delta t = \frac{1}{\sqrt{_uK_u}} \cosh^{-1}\left(\frac{\left(u_{max} + \frac{_uK_l}{_uK_u} I_u \right)}{\left(-u_{max} + \frac{_uK_l}{_uK_u} I_u \right)} \right) = Acosh^{-1}(B) \ \Rightarrow$$

With the equivalent formula from [4, p149] to replace the inverse hyperbolic cosh^{-1} function, the lift-off time as function of a constant current I_u can be calculated directly:

$$\Rightarrow \ \Delta t(I_u) = A \cdot \ln[B + \sqrt{B^2 - 1}] \quad \text{for } (B \geq 1) \tag{3.61}$$

With formula (3.61) numerical values for horizontal lift-off times can be calculated for the constant actuator currents $I_{u,max}$ = 2.5 [A] and $I_{u,lift-off} + \partial I_u$ = 1.52 [A]:

$$A = 1/\sqrt{_uK_u} = 2.839809171 \cdot 10^{-4}$$

$$B(I_{u,max}) = 4.1 \qquad \Rightarrow \ \Delta t \ (I_{u,max}) = 0.59 \ [ms] \tag{3.62}$$

$$B(I_{u,lift-off} + \partial I_u) = 7751 \quad \Rightarrow \ \Delta t \ (I_{u,lift-off} + \partial I_u) = 2.74 \ [ms] \tag{3.63}$$

Formula (3.56) combined with the ideal linear model gains (3.35) and (3.36) can be used to plot the horizontal lift-off trajectories as function of a constant actuator current I_u. Figure 3.6a shows two of these plots for the maximum actuator current ($I_{u,max}$) and the minimum current needed for horizontal lift-off ($I_{u,lift-off}$). The trajectories for other currents will be similar shaped as the plotted two, only positioned somewhere in between.

Figure 3.6b shows that the needed straight slope of the natural logarithm of the lift-off trajectory is only situated in the physical range of the rotor (under the gray horizontal line) when the actuator current is chosen not too large ($I_u \gg I_{u,lift-off}$). Note that the trajectory fuction is shifted over a distance $-u_{min}$ (= u_{max} = 50 [μm]) to avoid a negative input for the natural logarithm function.
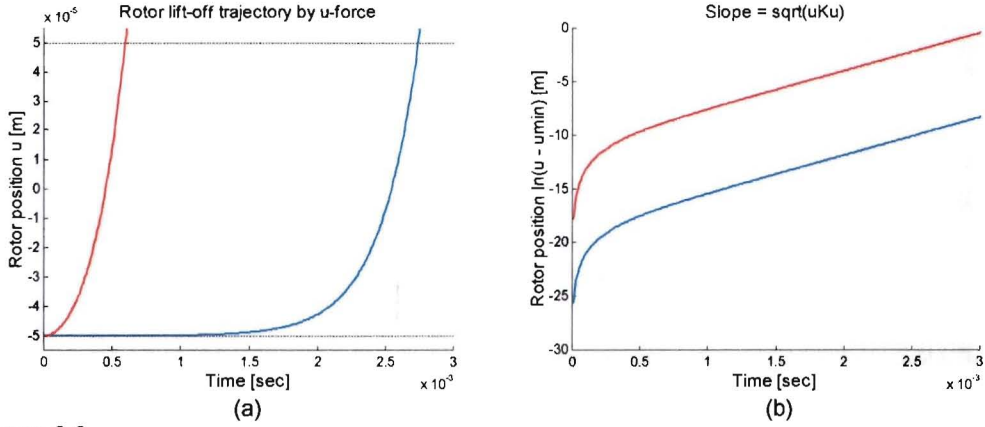
Figure 3.6
Blue line: $I_u = I_{u,max}$ = 2.5 [A]; $\Delta t_{lift-off}$ = 0.59 [ms]
Red line: $I_u = I_{u,lift-off} + \partial I_u$ = 1.52 [A]; $\Delta t_{lift-off}$ = 2.74 [ms]
Gray line: Maximum rotor positions enforced by solid physical stops.
a) Ideal lift-off trajectories for horizontal rotor movement.
b) Shifted natural logarithm function $\ln[u(t) - u_{min}]$ of the lift-off trajectory (a), to avoid negative input.

Another way to extract the gains from the lift-off trajectory is to make use of the measured horizontal lift-off time Δt. At first sight, it seems very difficult to isolate the wanted parameters (gains) in formula (3.61). This problem can be avoided by rewriting term B, using formula (3.58):

$$B = \frac{u_{max} + u_{max}\left(\dfrac{I_u}{I_{u,lift-off}}\right)}{-u_{max} + u_{max}\left(\dfrac{I_u}{I_{u,lift-off}}\right)} = \frac{I_u + I_{u,lift-off}}{I_u - I_{u,lift-off}} \tag{3.64}$$

Then (3.61) is rearranged resulting in:

$$_uK_u = \left(\frac{1}{\Delta t} \cdot \ln[B + \sqrt{B^2 - 1}]\right)^2 \quad \text{for (B} \geq 1) \tag{3.65}$$

Finally (3.58) can be rearranged and combined with (3.65), resulting in:

$$_uK_I = \frac{_uK_u \cdot u_{max}}{I_{u,lift-off}} = \frac{\left(\dfrac{1}{\Delta t} \cdot \ln[B + \sqrt{B^2 - 1}]\right)^2 \cdot u_{max}}{I_{u,lift-off}} \quad \text{for (B} \geq 1) \tag{3.66}$$

To finish, two problems with this method must be mentioned. A good determination of the starting time of the lift-off moment is necessary when the lift-off-time is to be measured. The rotor impacts, which actually should be avoided, have a damaging effect on the device. Certainly when often repeated.

Problem 6: How can this method (observing the lift-off trajectory) be used for the calibration of the z-, α- and β-actuators?

The calibration of the vertical force actuator (z-direction) via the lift-off trajectory method is in principle the same as for the horizontal force actuators (u- and v-direction, see the solution for Problem 5). However, there are some differences.
Here, only one parameter (linear model gain) is to be identified. Also, the destabilizing force is not generated by the permanent magnets but by gravity.
Besides, as already stated in [1], for the execution of this method on the vertical force actuator it is necessary that the rotor is stabilized in the horizontal directions.

The analysis starts with the four vertical coils working together as the vertical force actuator. First the linear transfer function of the vertical actuator (z-direction) is copied from [1, (4.173)] and transformed to the time domain:

$$H_z(s) = \frac{u(s)}{I_z(s)} = \frac{{}_zK_I}{s^2} \Leftrightarrow \ddot{z}(t) = {}_zK_I \cdot I_z(t) \tag{3.67}$$

In the real system, gravity works on the rotor. Therefore, the gravitational acceleration (g = 9.81 [m/s²]) needs to be added to (3.67):

$$\ddot{z}(t) = {}_zK_I \cdot I_z(t) - g \tag{3.68}$$

The solution of differential equation (3.68) with a <u>constant</u> current I_z and the initial conditions ($\dot{z}(0) = 0$ and $z(0) = z_{min}$) is given in (3.69).

$$z(t) = \tfrac{1}{2}\left({}_zK_I \cdot I_z - g\right)t^2 + z_{min} \tag{3.69}$$

The vertical lift-off current is the minimal current needed to overcome gravity. This current can be calculated for the ideal model by rearranging formula (3.68) and filling in the already calculated ideal linear model gain (${}_zK_I$ = 90.46 [m/s²/A] (3.39)).

$$\ddot{z} = 0 = {}_zK_I \cdot I_z - g \Leftrightarrow I_z = \frac{g}{{}_zK_I} = \frac{9.81}{90.46} = 0.1084457211\,[A] \tag{3.70}$$

To guarantee lift-off, this current is increased by a small amount (∂I_z):

$$I_z = I_{z,\text{lift-off}} + \partial I_z = 0.11\,[A] \qquad \text{with } \partial I_z \approx 1.55\,[mA] \tag{3.71}$$

The vertical lift-off time Δt is defined as the time between the start of the rotor movement and the moment it reaches a designated height. Combination of the limiting conditions (on t = 0 ➔ z = z_{min}, after Δt ➔ z = z_{max}) and formula (3.69) results in an expression for the vertical lift-off time Δt as function of a constant current I_z:

$$z_{max} = \tfrac{1}{2}\left({}_zK_I \cdot I_z - g\right)(\Delta t)^2 + z_{min} \Leftrightarrow \Delta t(I_z) = \sqrt{\frac{2(z_{max} - z_{min})}{{}_zK_I \cdot I_z - g}} \tag{3.72}$$

With (3.72), numerical values for vertical lift-off times can be calculated for the constant actuator currents $I_{z,max}$ = 2.5 [A] and $I_{z,\text{lift-off}} + \partial I_z$ = 0.11 [A] and z_{max} = -z_{min} = 0.25·10⁻³ [m]:

$$\Delta t(I_{z,max}) = 2 \cdot \sqrt{\frac{0.25 \cdot 10^{-3}}{90.46 \cdot 2.5 - 9.81}} = 2.15\,[ms] \tag{3.73}$$

$$\Delta t(I_{z,\text{lift-off}} + \partial I_z) = 2 \cdot \sqrt{\frac{0.25 \cdot 10^{-3}}{90.46 \cdot 0.11 - 9.81}} = 84.3\,[ms] \tag{3.74}$$

Formula (3.69) combined with the ideal linear model gain (3.39) can be used to plot the vertical lift-off trajectories as function of a constant actuator current I_z. Figure 3.7a shows two of these plots for the maximum actuator current ($I_{z,max}$) and the minimum current needed for lift-off ($I_{z,lift-off}$). The trajectories for other currents will be similar shaped as the plotted two, only positioned somewhere in between.

Figure 3.7b shows that the needed straight slope of the square root of the lift-off trajectory is always situated in the physical range of the rotor (between the gray horizontal lines). Note that the trajectory fuction is shifted over a distance $-z_{min}$ (= 67 [μm]) to avoid a negative input for the square root function.

(a)   (b)
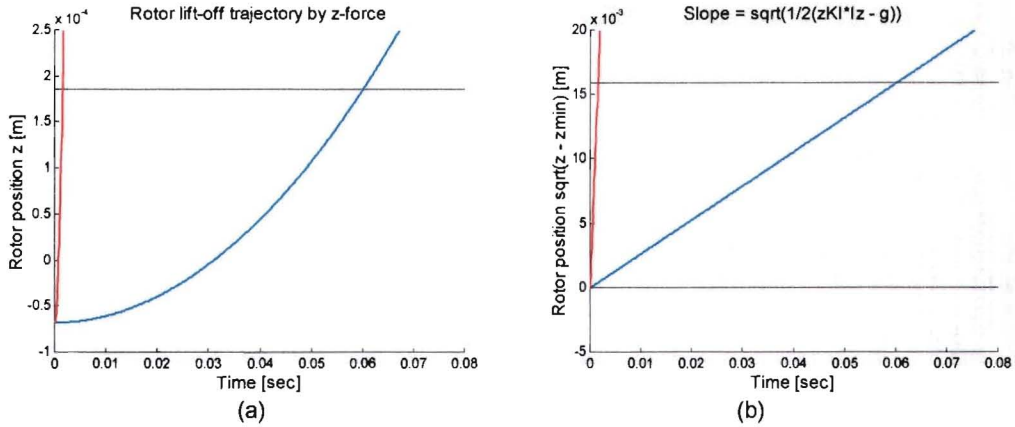
Figure 3.7
Blue line: $I_z = I_{z,max} = 2.5$ [A]; $\Delta t_{lift-off} = 2.15$ [ms]
Red line: $I_z = I_{z,lift-off} + \partial I_z = 0.11$ [A]; $\Delta t_{lift-off} = 84.3$ [ms]
Gray lines: Maximum rotor positions enforced by solid physical stops.
a) Ideal lift-off trajectories for vertical rotor movement.
b) Shifted square root function sqrt[$z - z_{min}$] of the lift-off trajectory (a), to avoid negative input.

Another way to extract the gain from the lift-off trajectory is to make use of the measured vertical lift-off time Δt. For this purpose, the wanted parameter (gain) is isolated in formula (3.72):

$$_zK_I = \frac{\left(\dfrac{2(z_{max} - z_{min})}{(\Delta t)^2} + g \right)}{I_z} \tag{3.75}$$

Two notes must be made:

Note 1) The values for z_{max} and z_{min} can be any beginning height and end height of the rotor. They also don't have to be the same. The vertical rotor range of the real device is calculated in appendix H.1. Table H.1 shows that the vertical range is limited by the coated horizontal coil-cores to $z_{min} \approx -67$ [μm] and $z_{max} \approx 185$ [μm].

Note 2) As a result of manufacturing tolerances (or mistakes) it can be that the four vertical coils that form the vertical actuator are not equally strong. When the same current (I_z) powers all four coils, this will then result in a tilting rotor. In normal operation this tilting is prevented by the α- and β-controllers. For the design of these controllers the α- and β-actuators need to be calibrated (to know their linear gains). Thus, the problem is that the calibration can't be done without the controllers and the controllers can't be properly designed without calibrated actuators!
Of course, this is a possible worst case situation. However, if assumed that the four vertical coils are fairly equal, then the α- and β-controllers won't be necessary.
Lastly, the linear model gains of the torque actuators (α- and β-rotation) must be calibrated. The torques are generated by the same four coils that form the vertical force actuator, divided in two pairs of two opposite coils. The torque is generated by forcing a differential current through two opposite positioned coils.

If assumed that the four coils are perfectly equal (see note 2 above), then the wanted gains $_\alpha K_l$ and $_\beta K_l$ are equal and can be derived from the previously extracted vertical force actuator gain $_z K_l$ (3.75).

Combining (G.7), (G.10), (3.39) and (3.40) leads to:

$$\frac{_{\alpha/\beta} K_l}{_z K_l} = \frac{\left(\frac{T_{\alpha/\beta}}{I_{\alpha/\beta} \cdot I_{x/y}}\right)}{\left(\frac{F_z}{I_z \cdot m_{ROTOR}}\right)} = \frac{JN_{VC}}{I_{x/y} \cdot k} \cdot \frac{m_{ROTOR} \cdot R_{PM} \cdot k}{2JN_{VC}} = \frac{m_{ROTOR} \cdot R_{PM}}{2I_{x/y}} \quad [rad/m] \tag{3.76}$$

The parameters in (3.76) are all constant rotor properties (see section 5.2):

$$m_{ROTOR} = 8.49 \cdot 10^{-3} \text{ [m]}, \quad R_{PM} = 10 \cdot 10^{-3} \text{ [m] and } I_{x/y} = 2.21 \cdot 10^{-7} \text{ [kgm}^2] \tag{3.77}$$

Rearranging (3.76) and substitution of (3.77) yields:

$$_\alpha K_l = _\beta K_l = 192 \cdot _z K_l \tag{3.78}$$

3.8 Reviewing conclusions

3.8.1 Idealized analytical modeling

The reason for the derivation of a model is that it is used to investigate and predict the behavior of (parts of) a real system. Often the model can't be perfect, because it is simply impossible to incorporate all properties of a real system in a model.

To end up with a model that corresponds more with the real system, the developed ideal model for the electromagnetic actuators in [1] has been improved by removing some errors and adding extra information.

A short summary of the changes made to the model and their effects on it is given below:

- The influence of the un-modeled electrical insulation layer is twofold. The horizontal force actuators lose 11% ({19.5/2 − 8.66}/(19.5/2)}·100%) of their (maximum) generated force. Besides that, the possibility of a small coupling of vertical- and horizontal coil fluxes is exposed.

- The coupling of the horizontal force-coils is two times smaller than mentioned in [1]. This results in a decrease of the (maximum) horizontal actuator force of 50%.

- The thesis starts with a clear definition in [1, section 2.2] of the position and orientation of the rotor (parameters (x, y, z, α, β, γ) and (v, u, z, α*, β*, γ)). However, the position and the analytical description of the magnetic resistors and of the α- and β-actuators was not in accordance with this definition.

- The unconventional (wrong) choice in [1] not to comply with the standard sign conventions for electrical current and magnetic flux directions from the beginning to the and of some analyses has been rectified.

Especially the last two points need some extra commentary. Besides that it is disturbing for an attentive reader, these kinds of sloppiness can have nasty side-effects on the controllers of the system, because it results in measured signals that are not representing the controller inputs they feed and controller outputs that go to the wrong actuators or have a wrong polarity.
There also is a positive side to the (extra) correctional work that has been done. It has made me aware to check the real device thoroughly for any of these problems because they might exist and be the reason why the system is still non-operational.

For controller design purposes, the model for the horizontal force actuators has already been reduced to a first order approximation, so now it is only valid for rotor positions around its neutral position (u = v = z = 0). When necessary, it is possible to test the controller on the more elaborate actuator model which is still available.

3.8.2 Finite Element Modeling

The simple finite element modeling example in [1, section 4.4] was created to compare the more realistic FEM calculations with the results from idealized modeling. The outcome of the example can be translated to the real device. A better prediction of the actuator parameters of the real device can be made by using the idealized modeling results (section 3.3) of the real device, combined with a FEM correction factor.

After the modifications (described in section 3.4) made to the ideal modeling of the example system, the differences between the FEM- and the ideal actuator gains have also changed. This is depicted in table 3.3.

Table 3.3 Correction factor between FEM- and ideal actuator modeling.

Actuator	Differences in [1, (4.111)]		Corrected differences	
	Factor Ideal → FEM	Factor FEM → Ideal	Factor Ideal → FEM	Factor FEM → Ideal
K_T^T	0.88	1.14	0.84	1.19
K_F^F	0.42	2.38	0.56	1.78
K_F^T	0.38	2.63	0.51	1.96

The conclusion for this example in [1] that with ideal modeling the motor constants are calculated maximally 2 times larger than they are calculated with FEM is still valid, but now the numbers are more in agreement with it ...

As stated in [1, section 4.4.1] the FEM analysis includes the material parameters of the weak iron and the permanent magnet (NdFeB), but not the hysteresis and eddy currents. Both phenomena can have a weakening effect on the actuator force, so in practice the difference between ideal modeling and FEM could be even larger (than a factor of about 2).

3.8.3 Maximum forces and torques

Some calculation results of section 3.5 are summarized in table 3.4.

Table 3.4 Maximum forces and torques in the ideal actuator model.

Parameter	Maximum thesis [1] value	Corrected maximum value	Factor
$F_{u/v,generated}$ [N]	19.5	8.66	2.25
$F_{u/v,destab}$ [N]	5.82	unchanged	
F_z [N]	0.96	1.92	0.5
$T_{\alpha/\beta}$ [Nm]	0.01	unchanged	
$(T_y)_vK_l$ [rad/s^{2}A]	-812	-2800	0.29

The corrected $F_{u/v,generated,max}$ is more than twice as weak as calculated in [1]. The destabilizing force is unchanged but still smaller than the actuator force on the rotor, so $F_{u/v,net}$ = 8.66 + 0.23 − 5.82 = 3.07 [N]. This means that the horizontal force actuators are still able to pull the rotor loose from the stator.

The corrected $F_{z,max}$ is two times larger than calculated in [1]. The gravity force on the rotor is $F_g = m_{ROTOR} \cdot g = 8.49 \cdot 10^{-3} \cdot 9.81 = 83.29$ [mN], so $F_{z,net} = F_{z,max} - F_g = 1.84$ [N]. So $F_{z,net} > 0$, which means that the vertical force actuators are still able to overcome the gravity force on the rotor.

The higher linear model current gain ($_yK_i$) for the torque T_y means that the unwanted rotation y is better controllable, either passively or actively.

3.8.4 Actuator calibration

Non of the four actuator calibration methods discussed in [1] (① direct force/torque measurement, ② black box identification, ③ back EMF and ④ lift-off trajectories) seems to be ideal for this application.

The problems encountered are:

- Extra hardware is needed to apply the method [① ③].

- Not all actuator gains (parameters) are identified by the method [③].

- The method highly depends on a correctly calibrated position/orientation sensor, either an external sensor or the perfectly calibrated own C-sensor (or both) [(①) ② ③ ④].

- The method damages the system, certainly when often repeated [④].

- The device needs to be stabilized to be able to execute the method [(①) ② (③ ④)].

The calibration method based on the lift-off trajectories of the rotor is the one used so far on the real device, only to identify $_{u,v}K_i$ and $_{u,v}K_{u,v}$. Because the description of the method in [1, section 4.10.4] was incomplete and contained some errors, the analysis has been extended. A full description of how all actuator gains can be extracted from the rotor lift-off trajectories is now available.

The proposed method in [1] to deduce the actuator gains from the straight slope of the manipulated lift-off plots proved not applicable on the ideal lift-off plots for large horizontal actuator currents ($I_u >> I_{u,lift-off}$), since the needed straight slope is then situated outside the physical rotor range. To overcome this problem, it is shown how the gains can still be derived from the lift-off trajectories using the lift-off time. This is the time from the start of the rotor movement until the moment of impact.

The actuator calibration experiments on the real device are described in [1, section 8.5]. First these experiments need to be reviewed. After that it might be necessary to investigate other possible (different) calibration methods.

3.8.5 Overall conclusions and recommendations

The corrected actuator gains of the ideal model don't seem to be a problem for the real device, since the actuators are still able to pull the rotor to its operation point (the neutral position: u = v = z = 0). The surplus force can be used for fast control.

Nevertheless, the controller design might be up for an improvement. In [1, chapter 7] the actuator gains are used in a SIMULINK® model. This SIMULINK® model is used to design controllers, later to be applied on the real device! Are these controllers robust enough to cope with the corrected actuator gains? This will be investigated later.

Lastly, special attention was paid to the important parameter d_{max} that is used in several analyses in [1] and is defined as the maximum distance the rotor can travel in the ±x- or ±y-direction. Throughout [1], it is assumed that the horizontal rotor range is limited to 50 [µm] in all directions. However, figure 3.5 shows that the horizontal rotor range is 50 [µm] in the ±u- and ±v-direction, the range is $\sqrt{2} \cdot 50$ [µm] in the ±x- and ±y-direction and somewhere in between for all other horizontal rotor movements in the plane z = 0.

Chapter 4

Sensor System

Chapter 5 of the Ph.D.-thesis [1] deals with the design, modeling and calibration of the 5 DOF capacitive sensor system used for the magnetically suspended and propelled mirror system. The sensor is designed to measure the position (3 DOF: u, v, and z) and orientation (2 DOF: α^* and β^*) of the hovering rotor (mirror) in the stator.

Reviewing [1] led to the proposition of corrections, modifications and supplements given in this chapter. The possible consequences, of the necessary changes made, for the controller design and the sensor calibration experiments will be studied later.

4.1 Contactless differential capacitive position sensor [1, section 5.2]

The electrode lay-out of the complete sensor is depicted in [1, figure 5.18]. Unfortunately, this figure is outdated and not conform the angle definitions in [1, figure 2.3] or the later derived formulae for the capacitances of the $\pm\alpha$ sensors [1, (5.73)] and the capacitances of the $\pm\beta$ sensors [1, (5.74)].

The first problem is probably caused by the fact that the magnetic actuator system and the position/orientation sensor are designed separately, with their own reference frame. Fusion of the actuator system and the sensor system means that the two reference frames have to match. That is, have one common reference frame: the fixed stator (world) frame. The decision to use the horizontal coil-cores as rotation sensor electrodes automatically links the two systems.

The actuator frame has already been harmonized with [1, figure 2.3]. To do the same with the sensor frame, the x-axis and the y-axis in [1, figure 5.18] must be replaced by respectively the u-axis and the v-axis. Then the measured rotations by the sensors are not α and β (around respectively the x-axis and the y-axis), but α^* around the u-axis and β^* around the v-axis.

The second problem is that the positions of the angular sensor electrodes in [1, figure 5.18] are not in accordance with the derived formulae for the capacitances of the sensors (formula [1, (5.73)] for $C_{\pm\alpha}$ and formula [1, (5.74)] for $C_{\pm\beta}$). (Yes, this is the same problem as with the definition of the actuators in section 3.3 I).
The formulae for $C_{\pm\alpha}$ and $C_{\pm\beta}$ are correct and in accordance with [1, figure 2.3]. So, the sensor names in [1, figure 5.18] must be changed, as is shown in table 4.1.

Table 4.1 Corrected angular sensor names!

Ph.D.-thesis [1] sensor name	Actual sensor function
$+\alpha$	$-\beta^*$
$-\alpha$	$+\beta^*$
$+\beta$	$+\alpha^*$
$-\beta$	$-\alpha^*$

The corrected positions (see table 4.1) of the capacitive angular sensors with respect to the stator frame are drawn in figure 3.4 in section 3.3.

A third problem is hidden in the text [1, p148] where it is declared that the α-sensor is sensitive for α and x (should be α, v and z) and the β-sensor is sensitive for β and z (should be β, u and z). The proof for this is given in [1, (5.73) and (5.74)], where x and y should be replaced by respectively u and v!

4.2 Dimensioning [1, section 5.3]

In principle the calculations presented in [1, section 5.3] are correct, except for some outcomes. They are put right in this section.

In [1, section 5.3.1] the nominal values for the sensor capacitors are calculated based on the blue-prints of the sensor bowl [1, appendix E.3]. The presented values differ somewhat from the ones calculated with formula (4.1).

$$\sin\theta = \frac{d_{edge}}{R} \Leftrightarrow \theta = \arcsin\left(\frac{d_{edge}}{R}\right)$$ (4.1)

where $R = 8.25 \cdot 10^{-3}$ [m] is the radius of the rotor plus the nominal air gap distance and d_{edge} is the distance from z-axis to the edge of the sensor electrode. The real (corrected) sensor parameters are shown in table 4.2.

Table 4.2 Corrected sensor electrode properties.

Ph.D.-thesis [1] name	Actual name	Inner edge [mm]	Outer edge [mm]	Inner angle [°]	Outer angle [°]	Capacitance [pF]
C_3^{nom}	C_3^{nom}	0	1.5	0	10.3	0.244
C_{xy-z}^{nom}	C_{uv-z}^{nom}	2.75	4.25	19.5	31.0	0.324
C_{xy+z}^{nom}	C_{uv+z}^{nom}	4.5	5.5	33.1	41.8	0.349
$C_{\alpha\beta}^{nom}$	$C_{\alpha'\beta'}^{nom}$	does not apply	total = 25▼		0.367

Another possible mistake was found in the presented values for the capacitors C_1 and C_2 of the second order low-pass filter [1, figure 5.22] of the sensor system. They are printed twice as large as calculated and used in the MATLAB® file bodestep.m, that was used for the calculation of the factor ξ (= 0.25) to model the parasitic capacities in the sensor. The correct values are $C_1 = 14.3$ [nF] instead of [1, (5.63)] and $C_2 = 2.90$ [nF] instead of [1, (5.64)].

4.3 Modeling ideal sensor behavior for simulation and control [1, section 5.4]

Except for the three easy to discover typos, the derived ideal expressions for the sensor capacitors presented in this section are correct. However, be aware of the following:

① For the derivations in [1, section 5.4] the local sensor frame has been used.
Unfortunately, this frame is consequently called the fixed world frame (0-frame). This is no longer right after the fusion with the magnetic actuator system. To correct this, the variables used in the capacitor- and sensor voltage expressions (x, y, z, α and β) should be replaced by respectively (u, v, z, α^* and β^*), to get the right formulae for the stator (world) frame. It is very unpractical that this change is only mentioned in [1, section 8.2] nearly at the end of the Ph.D.-thesis [1].

② The permittivity of vacuum ($\varepsilon_0 = 8.85 \cdot 10^{-12}$ [F/m]) has been omitted in the presented expressions. All the presented expressions for sensor capacitors should be multiplied with this constant, to obtain the right expressions. Because the capacitor equations are used in a division, this has no consequence for the sensor voltage expressions. They stay unchanged.

▼ The magnetic iron top of the rotor (part C and D in appendix B.1) is excluded from the calculation, because it was not meant to function as a sensor electrode. However, since iron is an electric conductor it is able to act as an electrode, like the horizontal coil-cores.

③ The presented expressions for the sensor capacities (and therefore the sensor output voltages) are not exact, but approximations. Three types of approximations are used, which all introduce a modeling error:

- The spherical electrode shapes are modeled by straight electrodes. The average angles λ, k_1 and k_2 are used in the calculations.

- Electric field bending hasn't been taken into account. The simple expression for an ideal capacitor (2.1) has been used:

$$C = \varepsilon_0\varepsilon_r A/d \ [F] \tag{4.2}$$

- A first order approximation is used to simplify the expressions near the operating point of the rotor, that is the neutral position ($u = v = z = 0$).

The effect of the approximations can be the subject of further research, with the goal to come up with a better sensor model. Ultimately, this could result in a better calibrated sensor system.

To end this section, some parameters used for the ideal modeling of the rotation sensors are calculated. These parameters are used in [1, (5.73)-(5.76)], but not calculated. In section 10.2.1 these parameters are needed to make an expectation for the sensor calibration measurements. The calculation will be done next. First two parameters concerning the dimensions of the rotation sensors (the horizontal coil-cores) are defined.

$$\text{Rotation sensor radius: } R_+ = R + d = 8 \ [mm] + 0.25 \ [mm] = 8.25 \cdot 10^{-3} \ [m] \tag{4.3}$$

$$\text{Width of the rotation sensor: } w_{HC} = 2.88 \cdot 10^{-3} \ [m] \tag{4.4}$$

The nominal overlap area ($A_{\alpha\beta}$) of the rotation sensors (covering 25°) is:

$$A_{\alpha\beta} = (25/180) \cdot \pi \cdot R_+ \cdot w_{HC} = (25/180) \cdot \pi \cdot 8.25 \cdot 10^{-3} \cdot 2.88 \cdot 10^{-3} = 1.036726 \cdot 10^{-5} \ [m^2] \tag{4.5}$$

The extra sensor overlap surface caused by rotation = $\alpha \cdot R_+ \cdot w_{HC} = k_{\alpha\beta} \cdot \alpha$

$$\Rightarrow k_{\alpha\beta} = R_+ \cdot w_{HC} = 8.25 \cdot 10^{-3} \cdot 2.88 \cdot 10^{-3} = 2.376 \cdot 10^{-5} \ [m^2/rad] \tag{4.6}$$

The extra sensor overlap surface caused by z-translation = $\arcsin(z/R_+) \cdot R_+ \cdot w_{HC} = k_z \cdot z$

$$\Rightarrow k_z = (\arcsin(z/R_+) \cdot R_+ \cdot w_{HC})/z \approx (z/R_+) \cdot (R_+/z) \cdot w_{HC} = w_{HC} = 2.88 \cdot 10^{-3} \ [m] \tag{4.7}$$

4.4 Implementation and manufacturing [1, section 5.5]

The capacitive sensor system, including the electronics, has been built. Although in theory the system seems operational, it could be suffering from manufacturing mistakes. The question is whether the sensor system has been built, checked and tested properly or not?

One problem, that already has come up in section 4.1, is the reference frame of the sensor system with the angle definitions of α and β. The wrong reference frame of [1, figure 5.18] is also printed on the PCB (Printed Circuit Board) of the real device. This could lead to problems for the electronics and the controller of the system.

When the inputs of the sensor electronics are connected to the sensor electrodes with the same name on the PCB (see table 4.1), based on formula (2.2), the following output voltage can be expected for the angular sensors:

$$_\alpha V_i = V_s \frac{C_{\alpha'} - C_{-\alpha'}}{C_{\alpha'} + C_{-\alpha'}} \quad \overset{becomes}{\Rightarrow} \quad _\alpha \hat{V}_i = V_s \frac{C_{-\beta'} - C_{\beta'}}{C_{-\beta'} + C_{\beta'}} = -_\beta V_i \tag{4.8}$$

$$_\beta V_i = V_s \frac{C_{\beta'} - C_{-\beta'}}{C_{\beta'} + C_{-\beta'}} \quad \overset{becomes}{\Rightarrow} \quad _\beta \hat{V}_i = V_s \frac{C_{\alpha'} - C_{-\alpha'}}{C_{\alpha'} + C_{-\alpha'}} = _\alpha V_i \tag{4.9}$$

Formula (4.8) shows that the output voltage of the $\overset{\bullet}{\alpha}$-sensor electronics becomes the negative output voltage that the $\overset{\bullet}{\beta}$-sensor should have. Similarly, formula (4.9) shows that the output voltage of the $\overset{\bullet}{\beta}$-sensor electronics becomes the output voltage that the $\overset{\bullet}{\alpha}$-sensor should have.

The testing of the sensor system has been performed by the designer of it. Unfortunately, no test report was written (for this prototype). Consulting the people involved resulted in the comment that only several power supply wires were added to some ICs on the PCB.

For now, it is assumed that the sensor electronics are tuned and working properly, otherwise it would have been told. Of course the "reference frame problem" mentioned above will be investigated. Unless there are problems using it, the sensor and electronics won't be subjected to tests.

4.5 Test setup and calibration [1, section 5.6]

A replica of the capacitive sensor (electrodes) was built in a test setup of the sensor. Using xyzα-micro-manipulation tables, some static calibration measurements were done on the test setup. The measurement results give an indication of the behavior of the sensor in the real device. The replica has also been used to test and debug the sensor electronics.

Due to the differences between the test setup and the real device (like manufacturing tolerances, <u>the angular sensors are not the horizontal coil-cores</u> and the absence of the actuator system) the calibration results of the test setup cannot be used for the real device.

4.5.1 Static measurements on the test setup [1, section 5.6.3]

The results of some static measurements on the test setup are depicted in [1, figures 5.30 – 5.37] and are already discussed in [1, section 5.6.3]. Some supplementary and more critical comments and observations are given below.

Observation ①:
The five sensor output voltages all show at least some sensitivity for the parameter that is to be measured. Besides this wanted behavior, some large cross-couplings are present.

The figures also show curved lines and planes. However, around the operating point of the rotor, the sensor outputs seem to be fairly linear within the rotor range of the real device. Therefore, an approximation of the five sensor output voltages can be described by the following set of five (linear) equations:

$$_xV_i = {}_xC_{x \cdot 0}x + {}_xC_{y \cdot 0}y + {}_xC_{z \cdot 0}z + {}_xC_{\alpha \cdot 0}\alpha + {}_xC_{\beta \cdot 0}\beta + {}_xV_0 \tag{4.10}$$

$$_yV_i = {}_yC_{x \cdot 0}x + {}_yC_{y \cdot 0}y + {}_yC_{z \cdot 0}z + {}_yC_{\alpha \cdot 0}\alpha + {}_yC_{\beta \cdot 0}\beta + {}_yV_0 \tag{4.11}$$

$$_zV_i = {}_zC_{x \cdot 0}x + {}_zC_{y \cdot 0}y + {}_zC_{z \cdot 0}z + {}_zC_{\alpha \cdot 0}\alpha + {}_zC_{\beta \cdot 0}\beta + {}_zV_0 \tag{4.12}$$

$$_\alpha V_i = {}_\alpha C_{x \cdot 0}x + {}_\alpha C_{y \cdot 0}y + {}_\alpha C_{z \cdot 0}z + {}_\alpha C_{\alpha \cdot 0}\alpha + {}_\alpha C_{\beta \cdot 0}\beta + {}_\alpha V_0 \tag{4.13}$$

$$_\beta V_i = {}_\beta C_{x \cdot 0}x + {}_\beta C_{y \cdot 0}y + {}_\beta C_{z \cdot 0}z + {}_\beta C_{\alpha \cdot 0}\alpha + {}_\beta C_{\beta \cdot 0}\beta + {}_\beta V_0 \tag{4.14}$$

Keep in mind that the local sensor frame is used in the equations above, so read uvzα*β* (instead of xyzαβ) when world frame expressions are needed!

Furthermore, in expressions (4.10)-(4.14) the parameters $_iC_i$ are the linear sensor gains, the parameters $_iC_j$ are the linear sensor couplings and the parameters $_iV_0$ are the sensor offset voltages. These three types of parameters (**30** in total) are **all** to be identified for the linear senor model of the real device.

Observation ②:

For higher rotor positions (z) the x- and y-position sensors become less sensitive. This is indicated by the almost horizontal planes in [1, figures 5.33 and 5.34].

This sensor behavior was predicted by the ideal modeling approximation formulae for the sensor voltage outputs [1, (5.71) and (5.72)]. They are repeated below:

$$_xV_i = V_s \frac{C_{+x} - C_{-x}}{C_{+x} + C_{-x}} = V_s \frac{_0^0 x \cdot \sin\lambda}{_0^0 z \cdot \cos\lambda + d} \tag{4.15}$$

$$_yV_i = V_s \frac{C_{+y} - C_{-y}}{C_{+y} + C_{-y}} = V_s \frac{_0^0 y \cdot \sin\lambda}{_0^0 z \cdot \cos\lambda + d} \tag{4.16}$$

The parameters V_s (modulator voltage = 2.5 [V]), λ (separation angle = 34.6°) and d (nominal air gap distance = 0.25 [mm]) are all constants, so the variation in these sensor output voltages is solely determined by the variation of the variable position parameters of the rotor: x/y and z.

The variable z (vertical rotor position) in the denominator of equations (4.15) and (4.16) determines the sensitivity of both sensor output voltages. When in theory z becomes infinite (or very large for that matter) the sensor outputs will become 0 for all positions x and y, which means that the sensor is completely insensitive to horizontal position variations of the rotor.

Fortunately, the vertical range of the rotor is bounded by the stator. The range is calculated in appendix H.1, where it is determined to be $-67 \le z \le 185$ [μm] (with the coated horizontal coil-cores).

In appendix H.2 is shown that there might be a distance offset of 0.2 [mm] on the z-position of the rotor, caused by manufacturing or designing tolerances.
As the above reasoning shows, this could lead to a reduction of the x- and y-sensor sensitivity. A possible z-position offset of the rotor should be revealed during the calibration of the real device.

Observation ③:

In [1, figure 5.30d] the output voltages of both angular sensors are almost not reacting to the varying angle parameter α. All five sensor output voltages show almost the same low sensitivity for the α-variation. With no labels it would be impossible to tell which line corresponds with the sensor output voltage $_\alpha V_i$, without using the offset voltages from the other plots.

According to [1, section 5.6.3.4] the sensor still performs well enough to lift the rotor and stabilize it in its operating point. However, this is stated without showing any positive research results or a fully operational device to prove it.

The angular sensors on the real device are shaped differently. This hopefully results in a more useful sensor output. A possible problem (timing, electronics, bad or interchanged connection, design, low modulation voltage V_s or something else) should be investigated, when the real angular sensors also show a low sensitivity.

Observation ④:

In section 4.1 and 4.4 has already been shown that there might be wrongly named angular sensor positions and what the consequences of this would be.

A change of angular sensor positions should be revealed by the presented plots of the measurements. In fact it seems that the output voltage $_\beta V_i$ in [1, figure 5.30d] is slightly more sensitive to the α-variation than $_\alpha V_i$. This would be in accordance with the finding that the sensor definition printed on the PCB is wrong.

On the other hand, [1, figure 5.31 and 5.36] show a linear relation between $_\alpha V_i$ and y, which is conform the expected correct dependencies. But [1, figure 5.30 and 5.37] show a linear relation between $_\beta V_i$ and x, which should be $-x$. This delimitation means that the wires from the rotation sensor electrodes

were connected to the corresponding inputs of the sensor electronics, but the wires of the β-rotation sensor were probably interchanged (the $+\beta$ electrode is connected to the $-\beta$ input and the $-\beta$ electrode is connected to the $+\beta$ input).
This problem has to be verified for the real device!

Observation ⑤:
It is notable that in [1] the collected data from measurements on the test setup of the sensor was mainly used to plot and to get a visual impression of the sensor behavior of the test setup sensor (and the almost equal sensor in the real device), while this data also provides many other research opportunities. Hence, a supplemental analysis of the measurement data is executed in chapter 10 (part 2) of this thesis. In here among other things:

- Ideal linear sensor model parameters are calculated, based on formulae in [1].

- The linear sensor model parameters for the sensor in the test setup are extracted from the measurement data of the test setup.

- The ideal and extracted parameters are compared, because both serve as a measurement expectation for the sensor of the real device.

- The extracted linear sensor model is tested and evaluated by doing some rotor position and orientation estimations based on the same data.

- It is investigated how to optimize the linear sensor model (parameters).

Besides the testing of the applicability of a linear sensor model for the real device, the analysis in chapter 10 serves two other purposes:

❶ It is an exercise for processing the data to be measured on the real device.

❷ Only in case of need, the values of extracted parameters from the test setup sensor can be used to substitute linear parameters of the sensor of the real device that cannot be extracted with the proposed automatic "stuck to the stator" calibration method in [1] (see the next section).

4.5.2 Calibration procedure for the real device [1, section 5.6.4]

To calibrate the sensors of the prototype, an automatic calibration procedure is proposed. This procedure makes use of the four stable "stuck to the stator" positions of the rotor. The rotor can easily be put in one of these four positions with open loop control of the device. The coordinates of the four positions are known. With this information, the sensor data can be used to (partially) calibrate the horizontal position sensors. The sensor calibration attempt that was carried out on the real device is described in [1, section 8.4] and evaluated in chapter 7 of this thesis.

A least squares method [1, section 5.6.4.1] is utilized to make an optimal estimation of the wanted linear sensor model parameters, based on the 5 sensor output voltages measured in the four stable positions. The resulting mathematical expressions are simple average functions.

4.5.2.1 The four stable "stuck to the stator" positions

The expression of the four stable positions in the world frame (0-frame) coordinates in [1, p183] is correct (table 4.3), except for the given value of parameter d_{max}.

Where d_{max} is the maximum distance the rotor can travel in the x- or y-direction. The correct value for d_{max} is derived in section 3.7, see figure 3.5 and equation (3.52), which is repeated below.

$$d_{max} = x_{max} = y_{max} = \sqrt{2} \cdot u_{max} = \sqrt{2} \cdot v_{max} = \sqrt{2} \cdot 50 \, [\mu m] \tag{4.17}$$

Table 4.3 Coordinates of the four stable "stuck to the stator" positions.

	O-Frame (x, y, z)	O-Frame (u, v, z)
Position 1	$(0, +d_{max}, 0)$	$(+\frac{1}{\sqrt{2}}d_{max}, +\frac{1}{\sqrt{2}}d_{max}, 0)$
Position 2	$(+d_{max}, 0, 0)$	$(+\frac{1}{\sqrt{2}}d_{max}, -\frac{1}{\sqrt{2}}d_{max}, 0)$
Position 3	$(0, -d_{max}, 0)$	$(-\frac{1}{\sqrt{2}}d_{max}, -\frac{1}{\sqrt{2}}d_{max}, 0)$
Position 4	$(-d_{max}, 0, 0)$	$(-\frac{1}{\sqrt{2}}d_{max}, +\frac{1}{\sqrt{2}}d_{max}, 0)$

Some notes must be made:

The parameter d_{max} is not accurate, see section 4.5.2.3.

The factor $(1/\sqrt{2})$ in [1, (5.80)] has to be removed.

In contradistinction to what is claimed on [1, p184], the extreme z-positions of the rotor are not $\pm d_{max}$. The real values are calculated in appendix H.1.

4.5.2.2 Rotor orientation estimation

The proposed estimation of the angles [1, (5.89)] is somewhat strange. Besides the fact that the offset voltages have been forgotten in the matrix expression, which is probably again slovenliness, the presented principle of calculation is contradictory.

In the estimation formula of α, parameter β is assumed to have no influence. This can only be when $_\alpha C_\beta$ or β is equal to 0. In the estimation formula of β, parameter α is assumed to have no influence. This can only be when $_\beta C_\alpha$ or α is equal to 0.

The calibration measurements on the test setup have proven that $_\alpha C_\beta$ (and $_\beta C_\alpha$) is not equal to 0. So in the estimation of α, the angle β is assumed to be 0. And in the estimation of β, the angle α is assumed to be 0. This means that the estimations of the angles α and β are done under the condition that both angles are equal to 0[♥]. This is a contradiction. It is caused by a lack of needed information to solve the five linear equations (4.10)–(4.14).

4.5.2.3 Limitations of the procedure

The automatic calibration method is inaccurate and incomplete, because it uses only four rotor positions which are not exact and solely lie in a horizontal plane[♥♥]. This means that the z-, α- and β-sensors and actuators are not calibrated. Also the influence of the rotor height (z) and orientation (α and β) on the horizontal sensor outputs is not accounted for. So, only 15 ($_iC_x$, $_iC_y$ and $_iV_0$, with $i = x, y, z, \alpha$ or β) of the 30 linear sensor model parameters (4.10)-(4.14) can be identified.

[♥] Property of the four stable positions is that the other parameters: $z = \alpha = \beta = 0$.

[♥♥] Gravity can pull the rotor down, since the vertical rotor position is not controlled in open loop. However, for this procedure only the end positions of the rotor are important.

The linear model parameter identification is not accurate for three reasons:

- With open loop control the rotor can only be put near one of the four "stuck to the stator" positions, so these positions are not exact.

- Parameter d_{max} depends on the thickness of the coating on the outer surface of the horizontal coil-cores. The coating thickness is not exact and can change because of wear. Also manufacturing tolerances on the positions of the horizontal coil-cores influence parameter d_{max}. So, parameter d_{max} will be different for any of the four stable positions.

- The four "stuck to the stator" positions, that lie on the outer range of the rotor, are used to calibrate the sensor near the operating point in the middle of the rotor range. This is not optimal.

Another disadvantage of the "stuck to the stator" calibration method, besides the incompleteness, is the damage that the repeated rotor impacts to the stator cause. The damage sustained so far is twofold: a little chip of the magnetic iron has come off the rotor and in one of the four "stuck to the stator" positions the sensor has started to malfunction.

4.6 Reviewing conclusions

4.6.1 Sensor names and positions

The used sensor electrode names, their positions and the angle definitions in general throughout [1], were not consistent. To correct this, everything has been harmonized with the world frame definitions in figure 2.1.

The sensor has its own reference frame with coordinates x, y, z, α and β, which is used in [1, chapter 5]. It is important to know that the sensor in the prototype is positioned such, that it actually measures the rotor positions (u, v and z) and the rotor orientations (α^* and β^*) defined in the world reference frame!

4.6.2 Modeling ideal sensor behavior

For the derivation of a physical model of the sensor system of the prototype, several approximations were made. This means that the model only gives a rough idea of the ideal sensor behavior. The modeling of the sensor system could be extended and improved when necessary.

4.6.3 Sensor wire connections

The consequences of the possible wrong sensor wire connections, based on the names printed on the prototype main PCB of the prototype, have been investigated. The angular sensors will work, but the output voltages are interchanged and a minus sign is added to the α-rotation output voltage.

4.6.4 Measurements on the test setup sensor

Static measurements on a test setup replica of the capacitive sensor revealed that near the operating point of the rotor, each of the five sensor output voltages shows a fairly linear relation with all five rotor position and orientation parameters.

Therefore, a complete linear sensor model counts 30 parameters to be identified with a calibration method, namely 25 (cross-)couplings and 5 offset voltages.

The calibration measurements also confirmed the theoretical relation between the vertical rotor position and the sensitivity of the horizontal position sensors. The sensitivity decreases when the rotor gets higher.

Furthermore, the rotation sensor output voltages show a very low sensitivity for the rotor rotation. When the measurements on the real device, which has differently shaped rotation sensor electrodes, show the same low sensitivity, this problem has to be investigated and solved.

In the plots of the measurement data, a relation was detected that is not conform the ideal sensor modeling formulae (see Observation ④ in section 4.5.1). An explanation for it could be the interchange of two sensor electrode connection wires, which probably is caused by the inconsistent use of reference frames in [1, chapter 5].

The proposed linear sensor model hasn't been tested and no numerical measurement expectations for the linear model parameters were presented in [1]. Therefore, in chapter 10 in part 2 of this thesis a supplementary analysis is done. The calibration measurement data of the test setup sensor is used to first extract the linear sensor model parameters of the test setup sensor. After that, the linear sensor model is used to do some rotor position and orientation estimations, based on the same data.

4.6.5 Automatic "stuck to the stator" calibration method

An advantage of the automatic calibration procedure is that it is time and money saving because no external setup is necessary. It is also useful that the prototype can be recalibrated every time it is turned on or when the operating circumstances have changed (e.g. the temperature).

Disadvantages of the automatic calibration method are that it is incomplete (only 15 of the 30 linear model parameters are identified), inaccurate and it causes damage to the prototype. Due to the sustained damage this method is no longer applicable!

4.6.6 Overall conclusions and recommendations

Watch out with the sensor wire connections. Make sure they are correct.

Make calibration measurement expectations for the prototype based on the ideal model formulae and the test setup measurement data.

Test the linear sensor model of test setup sensor.

Investigate if the malfunctioning sensor in one of the four stable rotor positions causes a problem with the rotor lift-off from that position.

The proposed automatic "stuck to the stator" calibration procedure seems just an academic solution for the calibration of the sensor in the prototype. Try to do calibration measurements on the sensor of the prototype with a fixated rotor as was done on the test setup sensor. That way the calibration is accurate and complete for the current circumstances.

Chapter 5

Mechanics

Chapter 6 of the Ph.D.-thesis [1] deals with the derivation of a simple 'complete' mathematical/physical/analytical model of the laser deflection system, including:

- The equations of motion of the rotor.
- Rotor parameters like mass, moments of inertia and the center of gravity.
- Actuator and sensor coordinate transformations.

Reviewing [1] led to the proposition for corrections, modifications and supplements given in this chapter. The consequences of the changes to rotor parameter values and formulae will be researched in other chapters. Mainly the ones concerning the controller design, which is primarily based on the analytical model in [1].

5.1 Equations of motion [1, section 6.2]

The equations of motion of a rigid body (the rotor) are derived in [1, Appendix C]. These calculations seem to be flawless. Only one small error was found that could give some trouble. In formula [1, (C.22)] the products of inertia are interchanged. However, this switch has no consequences because on [1, p317] it is stated that these inertias are all equal to zero.

5.2 Rotor mass and moments of inertia [1, section 6.3]

In [1, Appendix D] an approximation is made for some parameters describing the rotor, namely: the mass of the rotor, the moments of inertia around the z- and the x/y-axis of the rotor and the position of the center of gravity of the rotor.
Four types of mathematical irregularities were found.

❶ Double definition of parameters
The blue-print of the rotor [1, figure E.2 p328] shows different parameters than those used in the calculations:

Calculation:	$r_2 = 2$ [mm];	Blue-print:	$r_2 = 3$ [mm] (correct, see prototype)
Calculation:	$a = 2.74$ [mm];	Blue-print:	$a = 2.8$ [mm] (not sure yet)

❷ Wrongly calculated derived parameters
In [1, Figure D.1, p322] the parameters used to calculate the properties of the rotor are defined. According to this depiction:

Parameter $h_1 = a + r_2 \cdot \tan 15° = 3.28$ [mm]   (not 3.26 [mm] which has been used)
Parameter $h_2 = r_1 \cdot \tan 15° = 1.61$ [mm]   (not 1.55 [mm] which has been used)

Probably the sinus function has mistakenly been used in [1] instead of the tangents.
These deviations seem small in themselves, but the parameters are used multiple times in different formulae. Therefore, they could have a large effect on the total outcome.

❸ Calculation mistakes in formulae
On four occasions the calculation of a quantity started with a correct formulation of a mathematical description, that subsequently wasn't worked out to a right algebraic expression. This happened with formula [1, (D.16)] for $I_{A, x}^V$, formula [1, (D.18)] for $I_{C, x}^V$, formula [1, (D.19)] for $I_{D, x}^V$ and formula [1, (D.20)] for $I_{E, x}^V$. The corrected expressions for these quantities are stated in appendix A.

❹ Calculation errors

When a correct algebraic expression is found for a quantity, the describing parameters of the rotor have to be filled in properly to obtain the right value of that quantity.

This didn't happen on three occasions:

In formula [1, (D.7)] for m_D (later in the thesis [1, p326] the right value of m_D is used!?); In formula [1, (D.9)] for m_{rotor} (caused by fault in m_D); In formula [1, (D.24)] for I_{cg} (caused by sloppy copying of earlier calculated values in [1, (D.23)]).

⑤ The properties of rotor-part D are approximated

With the given dimensions (and a little more effort.... ♥) the properties of rotor-part D (m_D, I_D, $I_{D,}{}^V{}_z$ and $I_{D,}{}^V{}_x$) can be (exactly) calculated using cylinder-coordinates. This has been done in appendix B.

The correction of the above mentioned irregularities resulted in improved parameter values. An overview of the changes is given in table 5.1. The influence of these changes will be investigated in the following.

Table 5.1 Adjustment of rotor parameters. [Red value = miscalculation; Green value = estimated value; ? = calculation method unknown, so it can't be corrected♥♥]

Parameter	Value in Thesis	Corrected Value [Thesis]	Exact Value [Thesis]	Exact Value [Blue Print]	Δ [%] T / EVT	Δ [%] T / EVBP
m_A [kg]	$1.47 \cdot 10^{-3}$		$1.47 \cdot 10^{-3}$	$1.44 \cdot 10^{-3}$		
m_B [kg]	$9.28 \cdot 10^{-5}$		$9.30 \cdot 10^{-5}$	$2.14 \cdot 10^{-4}$		
m_C [kg]	$3.0 \cdot 10^{-3}$		$3.1 \cdot 10^{-3}$	$2.71 \cdot 10^{-3}$		
m_D [kg]	$1.3 \cdot 10^{-4}$ / $1.2 \cdot 10^{-3}$	$1.206 \cdot 10^{-3}$	$1.57 \cdot 10^{-3}$	$1.58 \cdot 10^{-3}$	+31 / -24	+32 / -24
m_E [kg]	$2.5 \cdot 10^{-3}$		$2.55 \cdot 10^{-3}$	$2.55 \cdot 10^{-3}$		
m_{ROTOR} [kg]	$7.2 \cdot 10^{-3}$	$8.27 \cdot 10^{-3}$	$8.77 \cdot 10^{-3}$	$8.49 \cdot 10^{-3}$	+22 / -18	+18 / -15
I_A [m]	$-4.3 \cdot 10^{-3}$		$-4.6 \cdot 10^{-3}$	$-4.65 \cdot 10^{-3}$		
I_B [m]	$-1.37 \cdot 10^{-3}$		$-1.37 \cdot 10^{-3}$	$-1.4 \cdot 10^{-3}$		
I_C [m]	$-0.62 \cdot 10^{-3}$	?♥♥	$-0.78 \cdot 10^{-3}$	$-0.77 \cdot 10^{-3}$	+26 / -21	+24 / -20
I_D [m]	$-0.62 \cdot 10^{-3}$	?♥♥	$-0.68 \cdot 10^{-3}$	$-0.73 \cdot 10^{-3}$	+10 / -9	+18 / -15
I_E [m]	$-0.60 \cdot 10^{-3}$		$-0.59 \cdot 10^{-3}$	$-0.65 \cdot 10^{-3}$		
I_{cg} [m]	$-1.5 \cdot 10^{-3}$	$-1.27 \cdot 10^{-3}$	$-1.35 \cdot 10^{-3}$	$-1.4 \cdot 10^{-3}$	-10 / +11	-7 / +7
$I_{A,}{}^V{}_z$ [kgm²]	$3.01 \cdot 10^{-8}$		$3.01 \cdot 10^{-8}$	$2.93 \cdot 10^{-8}$		
$I_{B,}{}^V{}_z$ [kgm²]	$1.86 \cdot 10^{-10}$		$1.86 \cdot 10^{-10}$	$9.62 \cdot 10^{-10}$		
$I_{C,}{}^V{}_z$ [kgm²]	$6.35 \cdot 10^{-8}$		$6.41 \cdot 10^{-8}$	$6.23 \cdot 10^{-8}$		
$I_{D,}{}^V{}_z$ [kgm²]	$5.56 \cdot 10^{-8}$		$7.58 \cdot 10^{-8}$	$7.66 \cdot 10^{-8}$	+36 / -27	+38 / -27
$I_{E,}{}^V{}_z$ [kgm²]	$1.72 \cdot 10^{-7}$		$1.72 \cdot 10^{-7}$	$1.72 \cdot 10^{-7}$		
I_z [kgm²]	$3.31 \cdot 10^{-7}$	$3.21 \cdot 10^{-7}$	$3.42 \cdot 10^{-7}$	$3.41 \cdot 10^{-7}$	+3.3 / -3.2	+3.0 / -2.9
$I_{A,}{}^V{}_x$ [kgm²]	$5.3 \cdot 10^{-8}$	$4.87 \cdot 10^{-8}$	$4.87 \cdot 10^{-8}$	$4.8 \cdot 10^{-8}$	-8 / +9	-9 / +10
$I_{B,}{}^V{}_x$ [kgm²]	$3.25 \cdot 10^{-10}$		$3.26 \cdot 10^{-10}$	$1.04 \cdot 10^{-9}$		
$I_{C,}{}^V{}_x$ [kgm²]	$9.19 \cdot 10^{-8}$	$3.14 \cdot 10^{-8}$	$3.80 \cdot 10^{-8}$	$3.65 \cdot 10^{-8}$	-59 / +142	-60 / +152
$I_{D,}{}^V{}_x$ [kgm²]	$9.1 \cdot 10^{-8}$	$2.69 \cdot 10^{-8}$	$4.37 \cdot 10^{-8}$	$4.43 \cdot 10^{-8}$	-52 / +108	-51 / +105
$I_{E,}{}^V{}_x$ [kgm²]	$9.0 \cdot 10^{-8}$		$9.06 \cdot 10^{-8}$	$9.08 \cdot 10^{-8}$		
I_x /I_y [kgm²]	$3.26 \cdot 10^{-7}$	$1.97 \cdot 10^{-7}$	$2.21 \cdot 10^{-7}$	$2.21 \cdot 10^{-7}$	-32 / +48	-32 / +48
I_{uv} [m]	$1.15 \cdot 10^{-3}$	$0.92 \cdot 10^{-3}$	$1.02 \cdot 10^{-3}$	$1.03 \cdot 10^{-3}$	-11 / +13	-10 / +12
I_z [m]	$0.91 \cdot 10^{-3}$	$0.68 \cdot 10^{-3}$	$0.76 \cdot 10^{-3}$	$0.75 \cdot 10^{-3}$	-17 / +20	-18 / + 21

♥ Of course an engineer will try to calculate a required quantity in a fast and reliable way. A simple approximation can help to verify a found answer or speed up a calculation.

♥♥ Parameters I_C and I_D in column 2 are the same, so it could be that they were calculated together using the formula $I_{c+D} = (I_C m_C + I_D m_D)/(m_C + m_D)$. Looking at the exact values in column 4 there must be an calculation or approximation error, because the formula is a weighted average, which is bounded by the values of I_D and I_C, see appendix C. (Note that the combined parameter should be $I_{c+D} = -0.74 \cdot 10^{-3}$ [m])

The next sum-up clarifies the table's contents:

Column 1: Calculated parameters.
Column 2: Value of parameter as calculated and used in [1].
Column 3: Value of parameter corrected for calculation mistakes in formulae (❸) and calculation errors (❹), but not for the deviation in parameter values (❶ and ❷). So, the used parameter values for this column are:
h_1 = 3.26 [mm], h_2 = 1.55[mm], r_2 = 2 [mm] and a = 2.74 [mm].
Column 4: Exact values using my own calculations (r_2 = 2 and a = 2.74 [mm]).
Column 5: Exact values using my own calculations (r_2 = 3 and a = 2.8 [mm]).
Column 6: Difference in percentage between the value used in the Ph.D.-thesis (T, column 2) and the exact value (EVT, column 4). The difference is calculated with respect to both values.
Column 7: Difference in percentage between the value used in the Ph.D.-thesis (T, column 2) and the exact value from the blue prints of the prototype (EVBP, column 5). The difference is calculated with respect to both values.

5.3 Actuator and sensor coordinate transformations [1, section 6.4]

On [1, p194] the formula for torque ${}_g^v\vec{T}_v$ contains an error. The calculation formula is correct, but two sine functions have (probably by accident) been switched for cosine functions. The concerning functions are underlined in the corrected formula (5.1).

$$
{}_g^v\vec{T}_v = {}^v R_0 \begin{pmatrix} 0 \\ 0 \\ T_v \end{pmatrix} = \begin{pmatrix} T_v(-\cos\Psi\sin\Theta\cos\Phi + \sin\Psi\,\underline{\sin\Phi}) \\ T_v(\sin\Psi\sin\Theta\cos\Phi + \cos\Psi\,\underline{\underline{\sin\Phi}}) \\ T_v(\cos\Theta\cos\Phi) \end{pmatrix} \tag{5.1}
$$

Since the rotor-parameters are calculated more accurately and correctly, the calculated position of the center of gravity has been changed. Therefore, the two parameters (used in this chapter) that are calculated relative to the center of gravity are changed also. This is shown in the last two rows of table 5.1 on the previous page.

Parameter l_{uv} is the point of attack of the horizontal forces ${}_g^v\vec{F}_u$ and ${}_g^v\vec{F}_v$. It is used to calculate the torque generated on the rotor by the horizontal forces [1, p195].

Parameter l_z is the point of attack of the vertical force ${}_g^v\vec{F}_z$. It is used to calculate the torque generated on the rotor by the vertical forces [1, p196].

The calculation of the torque generated by the vertical actuators [1, formula (6.22), p196] contains an error. The position vector of the force hasn't been transformed to the rotating rotor-frame V. This problem could have been avoided by immediately using the standard formula for calculation of a torque around the center of gravity. This is shown in appendix D where the torques ${}_g^v\vec{T}_\alpha$ and ${}_g^v\vec{T}_\beta$ are verified. The correct calculation of ${}_g^v\vec{T}_z$ is given on the next page in equation (5.2).

Now the forces of two opposite tilt-actuators are pointing in the same direction, so:

$$
{}_g^v\vec{F}_{-\alpha} = {}_g^v\vec{F}_{+\alpha} \quad \text{but} \quad {}_g^v\vec{r}_{-\alpha} \neq {}_g^v\vec{r}_{+\alpha} \quad \text{and}
$$
$$
{}_g^v\vec{F}_{-\beta} = {}_g^v\vec{F}_{+\beta} \quad \text{but} \quad {}_g^v\vec{r}_{-\beta} \neq {}_g^v\vec{r}_{+\beta}
$$

Together these four forces generate the following torque:

$$
{}^V_g \vec{T}_z = ({}^V_g \vec{r}_{+\alpha} + {}^V_g \vec{r}_{-\alpha}) \times {}^V_g \vec{F}_{+\alpha} + ({}^V_g \vec{r}_{+\beta} + {}^V_g \vec{r}_{-\beta}) \times {}^V_g \vec{F}_{+\beta} = \begin{pmatrix} 0 \\ 0 \\ 2l_z \end{pmatrix} \times \begin{pmatrix} -\frac{1}{4}F_z\sin\beta \\ 0 \\ \frac{1}{4}F_z\cos\beta \end{pmatrix} + \begin{pmatrix} 0 \\ 0 \\ 2l_z \end{pmatrix} \times \begin{pmatrix} 0 \\ \frac{1}{4}F_z\sin\alpha \\ \frac{1}{4}F_z\cos\alpha \end{pmatrix} =
$$

$$
= \begin{pmatrix} 0-0 \\ -\frac{1}{2}l_zF_z\sin\beta - 0 \\ 0-0 \end{pmatrix} + \begin{pmatrix} 0-\frac{1}{2}l_zF_z\sin\alpha \\ 0-0 \\ 0-0 \end{pmatrix} = \begin{pmatrix} -\frac{1}{2}l_zF_z\sin\alpha \\ -\frac{1}{2}l_zF_z\sin\beta \\ 0 \end{pmatrix} \tag{5.2}
$$

5.4 Reviewing conclusions

5.4.1 Equations of motion

No serious mistakes were found in the derivation of the equations of motion of the rotor as they are presented in [1]. Therefore, they appear to be ready to be utilized.

5.4.2 Rotor parameters

Looking at the parameter deviations in table 5.1, half[♥] of the parameters contain a calculation or approximation error. The deviations with the corrected values (see the last column) range from −27 % to +152 %.

The six main parameters (m_{ROTOR}, l_{cg}, I_z, I_x, I_{uv} and I_z) are all affected by errors. However, the deviations are smaller than mentioned above, because calculation mistakes in various parts can cancel each other out. Also the effect on the total of the complete rotor of a relative large calculation error in a small part of the rotor is relatively small.

So, for a better evaluation of the errors one should also look at the percentage of the error with respect to the total outcome. For this purpose, some extra information has been derived from table 5.1. It is presented in table 5.2.

Table 5.2 Influence of calculation and approximation errors on four of the main rotor parameters, expressed in percents.

Influenced parameter	Error ❶ $\Delta = (4\text{-}5)$ [%]	Error ❷ $\Delta = (3\text{-}4)$ [%]	Error ❶&❷ $\Delta = (2\text{-}3)$ [%]	Approximation part D ⑤ $\Delta = (Green\text{-}4)$ [%]	Part D omitted [%]	Total error $\Delta = (2\text{-}4)$ [%]	Total error $\Delta = (2\text{-}5)$ [%]
m_{ROTOR} [kg]	+ 3.3	- 5.7	- 12.9	- 4.15	- 18	- 17.9	- 15.2
l_{cg} [m]	- 3.6	- 5.9	+ 18.1	+ 1.75	+ 11.1	+ 11.1	+ 7.1
I_z [kgm²]	+ 0.3	- 6.1	+ 3.1	- 6.0	- 22	- 3.2	- 2.9
I_x [kgm²]	0	- 10.9	+ 65.5	- 7.6	- 20	+ 47.5	+ 47.5

The numbers after the difference symbol (Δ) refer to column numbers in table 5.1. The percentage is calculated by the equation: [(first - second) · 100 / second], since the second column is always an improvement.

♥ This actually is 7/20, because 6 parameters are composed of calculated parameters (20 in total). When the composed parameters are also counted, the proportion becomes (7 + 6)/(20 + 6) = ½.

In table 5.2, the biggest differences are displayed in the yellow cells. The error in the fourth column (❷ Calculation mistakes in formulae and ❶ Calculation errors) clearly has the main contribution to the errors in the total outcome. Two major errors can be indicated in particular, namely:

1. The miscalculation of m_D has a direct effect on both m_{rotor} and l_{cg}.

2. The miscalculation of parts of l_X results in a +65.5 % error. The other errors (❸ and ⑤) have a different sign. Nevertheless, the sum of all errors results in a +47.5 % error in the total outcome of value of l_X. Unfortunately, this parameter is used twice (also as l_Y).

The other errors contribute a few percents to the total. They are on themselves, but certainly when added, not negligible.

When all calculations in the Ph.D.-thesis [1] were executed perfectly..., only the approximation error of rotor-part D would exist (column 5). Comparison of this error and the total error (column 7) shows that the contribution of the approximation error is about ¼ part of the total error.

Since the exact values of the rotor parameters are now available, as a result of my own calculations (see appendix B), these parameters (in column 5 of table 5.1) will be used to test the designed controllers in [1]. This will be done later on.

5.4.3 Actuator and sensor coordinate transformations

Two mistakes in formulae were found in this section. The error in the formula for the torque $^V_g\vec{T}_y$ could be just a typo. The mistake in the formula for the torque $^V_g\vec{T}_z$ seems more serious. The effect of these errors depends on how the formulae are further used.

Rotor parameters l_{uv} and l_v are expressed relative to the center of gravity. Since the value of (the z-coordinate) of the center of gravity has been changed, these two values also have changed. Both distances lie relatively close to the center of gravity, so the deviation in percents is quite large.

5.4.4 Overall

The parameters and formulae contemplated in this section are part of the analytical model of the prototype, that is used for the controller design. The effect of all (unintentional) errors on the model and controller design will be investigated later.

Chapter 6

Control

Chapter 7 of the Ph.D.-thesis [1] deals with the design of controllers for the magnetic actuators of the magnetically suspended and propelled tilting mirror system. The controller design is primarily based on the analytical models of the subsystems of the prototype formed in [1].

So far, the reviewing of [1] led to the proposition of corrections, modifications and supplements for the modeling of the subsystems (see chapters 3, 4 and 5). In this chapter the SIMULINK® model itself proves to contain some extra errors.

6.1 Linear model of magnetic actuator and mechanical system [1, section 7.2]

To obtain a linear model of the prototype, first a SIMULINK® model was composed, based on the ideally modeled prototype in [1]. After that, a linear model in the operating point of the prototype was extracted. Then controllers were designed for the linear model of the prototype. Later the same SIMULINK® model was used to test the designed controllers before they were tested on the real device.

6.1.1 Contents of the SIMULINK® model

The SIMULINK® model of the prototype that was used for the linear model extraction in [1] is depicted in figure 6.1. The contents of the model is explained in [1].
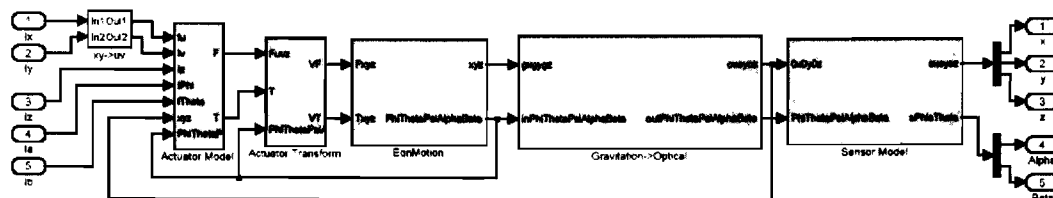
Figure 6.1
SIMULINK® model of the prototype, with (actuator) inputs [I_x, I_y, I_z, I_α and I_β] and (sensor) outputs [x, y, z, α and β].

Two notes about the model must be made:

❶ The real device's actuator inputs are [I_u, I_v, I_z, I_α and I_β] and the sensor outputs are [u, v, z, α*and β*].

❷ Not all the available modeling information was used in the SIMULINK® model.
To clarify the second note, it will be shortly named what had been incorporated in the SIMULINK® model when the linear model was extracted and what has been added to test the initially designed controllers.

The basis of the model are the ideal actuator models and the equations of motion of the rotor in [1]. The corrections already found in [1], like the FEM correction factors (about 0.5 for all actuators) or the experiment measurement results (different number of coil windings and measured maximum forces of the horizontal actuators) were not put in the model.

Obviously the corrections proposed in this thesis (see section 6.1.2) haven't been incorporated either.

Later added to the model for controller testing are: eddy currents and the non-ideal sensor behavior.

6.1.2 Corrections from other chapters

In chapter 3 of this thesis about the actuator system, some actuator modeling errors have been removed and the modeling of two neglected insulator rings was added.

In chapter 5 of this thesis about the rotor mechanics, the rotor parameters are calculated exactly and some calculation errors were removed (section 5.2). Also the formula for $^{V}_{g}\bar{T}_{z}$ (section 5.3) has been corrected.

In chapter 7 of this thesis about the executed experiments in [1], an estimation of all actuator gains (appendix G) of the real prototype has been made, based on the reviewed calibration measurements (see table 7.6 in section 7.4.1).

6.1.3 Mistakes found in the SIMULINK® model

Besides the proposed corrections that resulted from reviewing [1], summarized in the previous subsection (6.1.2), additional (probably unintended) mistakes were found in the in SIMULINK® model. These mistakes will be shortly discussed next, per block as depicted in figure 6.1.

General mux- and demux blocks
The use of mux- and demux-blocks, which respectively combine scalar or vector signals into larger vectors and split vector signal into scalars or smaller vectors, has proven to be a source of additional errors. A wrong reference number for a signal line was used four times in the SIMULINK® model.

Actuator Model
In the second term of the formula for F_v, u[3] must be replaced by u[4], because this term should contain the rotor position parameter v instead of u.

Also all the actuator gains must be adjusted, for two reasons. To correct the mistakes in the theoretical deductions in [1], which have been corrected in chapter 3 and 5. Secondly, to carry through the adjustments based on the (calibration) measurements on the magnetic actuator as presented in section 7.3.

The gravity vector acting on the center of gravity of the rotor is not mentioned in [1] or in the SIMULINK® model of the prototype! Therefore, it is shown here in (6.1), expressed in the fixed world frame (0-frame).

$$^{0}_{g}\bar{F}_{g} = \begin{pmatrix} 0 \\ 0 \\ -m_{ROTOR} \cdot g \end{pmatrix}$$

(6.1)

Where m_{ROTOR} is the mass of the rotor ($8.49 \cdot 10^{-3}$ [kg]) and g is the gravitational acceleration (9.81 [m/s^2]). To express the gravity vector in the rotating rotor frame (V-frame) it must be multiplied with the transformation matrix $^{V}R_0$ [1, (2.5)].

$$^V_g\bar{F}_g = {}^V R_0 \cdot {}^0_g \bar{F}_g = -m_{ROTOR} \cdot g \cdot \begin{pmatrix} -\cos\Psi \sin\Theta \cos\Phi + \sin\Psi \sin\Phi \\ \sin\Psi \sin\Theta \cos\Phi + \cos\Psi \sin\Phi \\ \cos\Theta \cos\Phi \end{pmatrix} \qquad (6.2)$$

Expression (6.2) should be added to the SIMULINK® model, to model the effect of gravity on the rotor.

Actuator Transform

The force transformation formulae are correct. The three torque formulae contained five errors: three incorrect reference numbers and two cos() functions that should be replaced by a sin() function.

Also the formula for T_z that wasn't expressed in the rotating rotor reference frame in [1] should be corrected in the SIMULINK® model. The correct formula for $^V_g T_z$ is shown in equation (5.2).

EqnMotion

The block for the transformation of the rotor positions expressed in the rotating rotor frame V to the fixed world frame 0 contains the wrong formulae. Although in [1, (2.6)] the correct result of consecutive rotations calculated relative with respect to the new reference frames is presented, the transformation used in the SIMULINK® model is calculated using absolute rotations with respect to the original reference frame. The calculation order of consecutive rotations determines the end result, so this mistake must be corrected.

Gravitation -> Optical

Not the coordinate transformation matrix $^V R_0$ [1, (2.5)] but $^0 R_V$ [1, (2.6)] should have been used for the calculation of the position of the optical center point of the mirror with respect to the static world frame.

Note that in later updates of the SIMULINK® model (extended with eddy currents and a controller) this mistake has been corrected.

6.1.4 Consequences of SIMULINK® model corrections

The problem with the use of mathematical software on a computer is that it will calculate anything it is programmed to do as long as it is possible and has a correct syntax. So many types of (unintended) mistakes like typos will be accepted and it is up to the user to verify the programmed assignment and double check the computation results.

It would take to much time to investigate the effect of every individual mistake or correction. Luckily, this is not necessary because the main goal is to end up with a complete and accurate model of the prototype.

Therefore the complete model will be corrected at once. This will be done in three steps. First the programming mistakes (wrong references and functions) in the SIMULINK® model (section 6.1.3) will be removed. Secondly, the theoretical mistakes (wrong formulae, omission of gravity in the model) will be corrected. Then the total effect of these two corrections will be examined. Lastly, the actuator gains will be replaced by the corrected ones of table 7.6 in section 7.4.1 and the corrected rotor parameters of table 5.1 will be substituted. Then it will be possible to test the initially designed controllers for the prototype on the corrected (more realistic) SIMULINK® model.

The first correction step clears a small problem on [1, p204]. The unexplained difference between and the appearance of the two numbers in matrix **A**, that give a coupling of a rotation around the y-axis to the orientation accelerations $\ddot{\alpha}$ and $\ddot{\beta}$, is not caused by numerical inaccuracies as is asserted in [1], but by the errors in the SIMULINK® model. These two numbers have disappeared after the corrections. Note that this problem could have functioned as a hint for the removal of programming mistakes, but obviously it didn't. Also in the **A** matrix, four zeros are changed into numbers that are related to the gravity that has been introduced in the model. The other numbers in the four state space matrices (**A, B, C** and **D**) [1, (7.5)] keep the same magnitude, but some signs change. These magnitudes will change when the actuator gains and rotor parameters are corrected in the second correction step.

6.2 Designed controllers

The design of the five simple SISO PID controllers in [1] is primarily based on the ideal analytical models of the subsystems of the prototype formed in [1], without the incorporation of the corrections already ascertained in [1], like the FEM factors and the actuator measurement results. The choice not to incorporate these actuator model corrections prior to the initial controller design, seems inefficient and could lead to at least one extra controller tuning session.

Also the use of a flawed SIMULINK® model possibly reduces the usefulness of the designed controllers. A further review on the controllers will be given in section 7.4, where the testing of the controllers on the prototype is discussed.

6.3 Reviewing conclusions

It is clear that the programmed SIMULINK® model hasn't been thoroughly checked before it was used. Besides some mistakes that were already made in the theoretical deductions in [1], the model also contained some additional programming errors. It would have been a good idea to let the model be checked by a second person. After all, (almost) every human makes mistakes.

Although some mistakes have a minor influence on the extraction of the linear model around the operating point $\overline{0}$, because then some parameters are equal to 0 and will disappear, the mistakes can have influence on the testing of the designed controllers on the (flawed) model.

Are the controllers designed in [1], based on the flawed SIMULINK® model, still suited to control the corrected model (and possibly the real device)? Is the flawed SIMULINK® model a possible reason why no set of stabilizing controllers for the prototype could be found? This can be investigated in part 2 of this thesis.

Chapter 7

Experiments

Chapter 8 of the Ph.D.-thesis [1] deals with the experiments that have been carried out on the prototype of the magnetically suspended and propelled tilting mirror system.

It describes the measurement of the resistances and inductances of the electrical coils of the magnetic actuator system, the execution of the "stuck to the stator" calibration method on the sensor system, the calibration of the horizontal force actuators and the testing of the designed controllers on the prototype.

The consequences of the changes resulting from reviewing previous chapters of [1] on the outcome of the experiments will be investigated and discussed in this chapter.

7.1 The prototype in practice

There are some differences between the original design and the actual prototype built, mostly due to manufacturing tolerances. This section contains no corrections for [1], it just shows some information that is needed in other sections.

7.1.1 Sensor orientation [1, section 8.2]

Finally it is stated that the capacitive sensor is positioned such in the prototype that it measures the rotor position and orientations [u, v, z, α^* and β^*]. Also the position of the vertical coils is described according to the reference frame of figure 2.1. This is a confirmation that the corrections proposed in the previous sections of this thesis, concerning the use of reference frames, were justified. Problem is that it doesn't guarantee that the right reference frame has been used in practice*.

7.1.2 Measured resistance and inductance of actuator coils [1, section 8.3]

The number of actuator coil windings that is used in the prototype differs from the originated number. Measurement of the inductances of the coils in the prototype has given an idea of the actual number of coil windings. In [1], the difference between the measured inductances and the designed (ideal) inductances has been fully ascribed to the deviating number of coil windings. The concluding results in [1] are presented here in table 7.1.

Table 7.1 Indirectly measured number of coil windings.

	Designed N	Measured N	Correction factor
Horizontal coil (N_{HC})	30	42	42/30 = 1.4
Vertical coil (N_{VC})	150	100	100/150 = 0.67

♥ Even when the reference frame would have been used consistently throughout [1], there would be no guarantee that it has been used correctly in practice.

7.2 Sensor calibration [1, section 8.4]

The proposed automatic sensor calibration method for the prototype and its limitations are already discussed in section 4.5.2.

The adjusted sensor orientation in the prototype (see section 7.1.1) also changes the linear sensor model parameters (30 in total) to be identified through calibration. The linear sensor model (4.10)-(4.14) is rewritten in matrix form (see section 10.1) in equation (7.1), with the truly measured rotor position and orientation parameters expressed in the world frame.

$$\begin{bmatrix} {}_uV_i - {}_uV_0 \\ {}_vV_i - {}_vV_0 \\ {}_zV_i - {}_zV_0 \\ {}_\alpha V_i - {}_\alpha V_0 \\ {}_\beta V_i - {}_\beta V_0 \end{bmatrix} = \begin{bmatrix} {}_uC_u & {}_uC_v & {}_uC_z & {}_uC_{\alpha'} & {}_uC_{\beta'} \\ {}_vC_u & {}_vC_v & {}_vC_z & {}_vC_{\alpha'} & {}_vC_{\beta'} \\ {}_zC_u & {}_zC_v & {}_zC_z & {}_zC_{\alpha'} & {}_zC_{\beta'} \\ {}_\alpha C_u & {}_\alpha C_v & {}_\alpha C_z & {}_\alpha C_{\alpha'} & {}_\alpha C_{\beta'} \\ {}_\beta C_u & {}_\beta C_v & {}_\beta C_z & {}_\beta C_{\alpha'} & {}_\beta C_{\beta'} \end{bmatrix} \begin{bmatrix} u \\ v \\ z \\ \alpha^* \\ \beta^* \end{bmatrix} \quad \Leftrightarrow \quad V = C_{coupling}X \qquad (7.1)$$

Where V = sensor output voltages minus the offset voltages; $C_{coupling}$ = linear sensor model parameters matrix; and X = true position and orientation of the rotor.

7.2.1 Correction for calibration results

The adjusted sensor orientation in the prototype (see section 7.1.1) has been incorporated correctly in the formulae of [1, section 8.4]. However, for the processing of the calibration measurement data, the wrong value for parameter d_{max} has been used. Parameter d_{max} should be $\sqrt{2} \cdot 50$ [μm] (see section 3.7) instead of 50 [μm].

The adjustment of parameter d_{max} means that the numerical values in [1, (8.6)] (${}_uC_u$, ${}_uC_v$, ${}_vC_u$ and ${}_vC_v$) all become a factor $\sqrt{2}$ smaller. The correction is displayed in (7.2).

$$\begin{bmatrix} {}_uC_u & {}_uC_v \\ {}_vC_u & {}_vC_v \end{bmatrix} = \begin{bmatrix} 7.65 \cdot 10^3 & 8.50 \cdot 10^2 \\ 7.05 \cdot 10^3 & 1.255 \cdot 10^4 \end{bmatrix} \quad [V/m] \qquad (7.2)$$

As (7.3) shows, the inverse matrix becomes a factor $\sqrt{2}$ larger.

$$\begin{bmatrix} {}_uC_u & {}_uC_v \\ {}_vC_u & {}_vC_v \end{bmatrix}^{-1} = \frac{1}{{}_uC_u \cdot {}_vC_v - {}_uC_v \cdot {}_vC_u} \begin{bmatrix} {}_vC_v & -{}_uC_v \\ -{}_vC_u & {}_uC_u \end{bmatrix} \qquad (7.3)$$

Using (7.3) on matrix (7.2) results in the corrected inverse coupling matrix (7.4).

$$\begin{bmatrix} {}_uC_u & {}_uC_v \\ {}_vC_u & {}_vC_v \end{bmatrix}^{-1} = \begin{bmatrix} 1.3942 \cdot 10^{-4} & -9.4429 \cdot 10^{-6} \\ -7.8320 \cdot 10^{-5} & 8.4986 \cdot 10^{-5} \end{bmatrix} \quad [m/V] \qquad (7.4)$$

Also the coupling between the horizontal rotor position and the rotor orientation output voltages [1, (8.9)] has to be corrected (divided) by a factor $\sqrt{2}$, so that it becomes (7.5). Note that the unit of these parameters is [V/m] and not [rad/m] as is asserted in [1].

$$\begin{bmatrix} {}_\alpha C_u & {}_\alpha C_v \\ {}_\beta C_u & {}_\beta C_v \end{bmatrix} = \begin{bmatrix} 6.50 \cdot 10^2 & 2.795 \cdot 10^4 \\ 2.84 \cdot 10^4 & -3.700 \cdot 10^3 \end{bmatrix} \quad [V/m] \qquad (7.5)$$

The fact that only 12 of the 30 linear sensor model parameters in (7.1) are identified makes that the orientation estimation is not applicable because ${}_\alpha C_{\alpha'}$ and ${}_\beta C_{\beta'}$ are not identified, the vertical rotor position (z) sensor is not calibrated and the horizontal rotor position sensors are only partially calibrated.

7.2.2 Testing the estimation of the four stable positions

Since both the sensor output voltages in the four stable "stuck to the stator" positions [1, table 8.2] and the linear sensor model coupling parameters (7.4) are now available, a quick test can be executed: estimate the four stable rotor positions with the calibration results. The estimation results via the principle of [1, (8.7)] are presented in column 4 of table 7.2. The estimation results with the corrected parameter d_{max} are presented in column 5 of table 7.2.

Table 7.2 Estimation of the four stable "stuck to the stator" positions with the partially (only horizontally) calibrated sensor system.

Stable rotor position	Coordinates	Ideal value [µm]	Estimation with wrong d_{max} (= 50 [µm]) [µm]	Estimation with correct d_{max} (= √2·50 [µm]) [µm]
1	u1	50	46.0	65.1
	v1	50	35.0	49.5
2	u2	50	25.1	35.6
	v2	-50	-35.0	-49.5
3	u3	-50	-24.7	-34.9
	v3	-50	-35.7	-50.5
4	u4	-50	-45.6	-64.4
	v4	50	35.7	50.5

Note that the ideal absolute value of the coordinates is $50/\sqrt{2} = 35.36$ [µm] when the wrong value for d_{max} (column 4) is used, as was done in [1].

This test just serves as a demonstration, because the influence of other degrees of freedom (z, α^* and β^*) is minimized in this example. Therefore, it is not representative for the functioning of the sensor over its complete range, especially around the operating point of the rotor.

Nevertheless, it will be shortly discussed what can be noticed in table 7.2 and what could have caused it. It appears that the v-position estimation is quite accurate for all four rotor positions. The absolute estimation error for the u-position in the last column is in all four rotor positions about 15 [µm] ($\hat{=}$ 30%). However, the pairs (u1 and u2) and (u3 and u4) should be equal because it is the same position, but the difference between their estimated values is about 30 [µm]!

In theory, both horizontal sensors are equal, so explanations for the differences of the coupling and cross-coupling parameters of the two sensors should be sought in possible discrepancies between the two sensors.

The first explanation is revealed by [1, table 8.2] that shows that the total u-sensor output range is about 1 [V], while for v-direction the total sensor output range is about 2 [V]. This means that the v-position sensor is more sensitive and therefore probably more dominant than the u-position sensor. This effect is also visible in the coupling matrix (7.2) that shows that $_vC_v$ is 1.64 times larger than $_uC_u$ and the cross-coupling parameter $_vC_u$ is 8.29 times larger than $_uC_v$.

Another explanation could be the air gap manufacturing tolerance which can lead to asymmetrical air gap distances. This means that the absolute values of the coordinates of the stable positions are all about 50 [µm] instead of exactly 50 [µm].

Extended testing of rotor position and orientation estimations, based on a linear sensor model, will be done in chapter 10 (part 2) of this thesis, where the calibration measurement data of the test setup sensor is used.

7.3 Actuator calibration [1, section 8.5]

The corrections made in previous sections have influence on the conclusions drawn in [1, section 8.5]. Therefore, this section starts with an overview of the corrected calculated actuator gains that serve as measurement expectations for the linear model parameters of the magnetic actuator system that is to be calibrated.

7.3.1 Overview of actuator gain corrections

In chapter 3 of this thesis, the ideal model of the magnetic actuator system in [1] has been corrected. This means that the magnetic actuator linear model parameters have been changed. The ideal model parameters that were used for the initial controller design in [1, chapter 7] are depicted in column 2 of table 7.3. The three corrections made so far to the model are shortly indicated below. Their effect on the linear actuator model parameters is also shown in table 7.3.

Column 3 shows the corrections for two modeling errors explained in section 3.3: the un-modeled electrical insulation layers between the stator rings and the horizontal coil-cores (d_{plus}) and the number of horizontal coil windings that was taken two times too large in the calculations in [1].

Column 4 shows the correction for the number of coil windings in the prototype, resulting from the coil inductance measurements (see table 7.1 in section 7.1.2).

In **Column 5**, the correction factors (column 4 in table 3.3) resulting from the Finite Element Method (FEM) modeling example are incorporated. The FEM analysis resulted in a more realistic model of a (simplified) electromagnetic actuator system, including phenomena like fringing (magnetic flux spreading), leaking flux, magnetic resistance of used materials and magnetic saturation. Note that eddy currents and hysteresis remain un-modeled.

The FEM correction factor for the destabilizing force of the permanent magnets on the rotor is unknown (marked with ?), because it is not calculated in the FEM example of [1, section 4.4]. However, a plausible value for it is derived from the comparison of the corrected ideal modeling gains and the measured gains which resulted in a FEM correction factor of 0.63 (see formula (7.16)). The deduced results are presented between brackets and in italics.

Table 7.3 Actuator gain corrections.

Parameter	Thesis [1] model values	Corrections for d_{plus} and $\frac{1}{2}N_{HC}$	Correction coil windings	Correction FEM	Total correction factor
$F_{u/v, generated}/I_{u/v}$ [N/A]	7.68	3.47	4.858	2.720	2.83
$F_{u/v, destabilizing}/(u/v)$ [N/m]	$1.16 \cdot 10^5$	$1.05 \cdot 10^5$	$1.05 \cdot 10^5$	? $(6.62 \cdot 10^4)$	? (1.75)
F_z/I_z [N/A]	0.38	0.768	0.512	0.261	1.46
$T_{\alpha/\beta}/I_{\alpha/\beta}$ [Nm/A]	$3.8 \cdot 10^{-3}$	$3.84 \cdot 10^{-3}$	$2.56 \cdot 10^{-3}$	$2.150 \cdot 10^{-3}$	1.77

The linear actuator model gains (see equations (3.34)) can be deduced from table 7.3, but need an extra rectification for the corrected rotor mass (m_{ROTOR} [kg]) and the moment of inertia around the x-axis (I_x [kgm^2]) of the rotor (see table 5.1).

The correction factor for the rotor mass:

$$\frac{\text{Thesis [1] rotor mass}}{\text{Corrected rotor mass}} = \frac{7.2 \cdot 10^{-3}}{8.49 \cdot 10^{-3}} = 0.848 \tag{7.6}$$

The correction factor for the moment of inertia around the x-axis of the rotor:

$$\frac{\text{Thesis [1] moment of inertia}}{\text{Corrected moment of inertia}} = \frac{3.26 \cdot 10^{-7}}{2.21 \cdot 10^{-7}} = 1.475 \tag{7.7}$$

The correction factors (7.6) and (7.7) are incorporated in column 3 of table 7.4. The following columns in table 7.4 contain the actuator gains of table 7.3 divided by the corrected rotor mass respectively the moment of inertia (only the last row).

Table 7.4 Linear actuator model gain corrections.

Parameter	Thesis [1] model values	Rotor mass and inertia correction	Corrections for d_{plus} and $\frac{1}{2}N_{HC}$	Correction number of coil windings	Correction FEM	Total correction factor
$_{u/v}K_l$ [m/s^{2}A]	$1.08 \cdot 10^3$	905	409	572	320	3.375
$_{u/v}K_{u/v}$ [1/s^2]	$1.61 \cdot 10^7$	$1.37 \cdot 10^7$	$1.24 \cdot 10^7$	$1.24 \cdot 10^7$	? $(7.8 \cdot 10^6)$	? (2.06)
$_zK_l$ [m/s^{2}A]	53	44.76	90.46	60.31	30.7	1.726
$_{\alpha/\beta}K_l$ [rad/s^{2}A]	$1.22 \cdot 10^4$	$1.72 \cdot 10^4$	$1.74 \cdot 10^4$	$1.16 \cdot 10^4$	$9.73 \cdot 10^3$	1.254
$_uK_l/_uK_u$ [m/A]	$6.7 \cdot 10^{-5}$	$6.6 \cdot 10^{-5}$	$3.3 \cdot 10^{-5}$	$4.6 \cdot 10^{-5}$	? $(7.3 \cdot 10^{-5})$	? (0.91)
$I_{u,lift-off}$ [A]	0.75	0.76	1.52	1.08	? (1.22)	? (0.61)

The corrected theoretical (ideal) parameter expectations are now stated in column 5 of table 7.3 and in column 6 of table 7.4. The last column of both tables shows the difference factor with the initial values used in [1].

Later (in subsections 7.3.4 and 7.3.5), the results of the actuator calibration measurements will be incorporated in the linear actuator model parameters. These parameters can then be used to update the SIMULINK® model, to test (and redesign) the controllers for the prototype.

7.3.2 Pulling the rotor of the stator [1, section 8.5.1]

Formula (3.58) shows that the horizontal rotor lift-off current is a measure for the ratio between the horizontal actuator linear model gains. Due to the previously discussed corrections, the measurement expectation for the ratio K_l/K_x of the horizontal force actuators has to be revised. The corrected gain values can be taken from column 5 of table 7.4. The revised calculated gain ratio is:

$$\left(\frac{K_l}{K_x}\right)_{expected} = \frac{572.2}{1.24 \cdot 10^7} = 4.626 \cdot 10^{-5} \quad [m/A] \tag{7.8}$$

Note that the FEM correction factors haven't been taken into account. This has been done for two reasons:
❶ The correction factor for K_x is yet unknown.
❷ The FEM correction was also not incorporated in the expectation value in [1, table 8.3], which is $6.7 \cdot 10^{-5}$ [m/A]. Not doing it here makes a comparison fair.
In practice this omission means that the FEM correction factor for K_l and K_x is presumed to be equal.

Although the magnitude of the expectation value of K_l is almost halved by the corrections, the measured ratios K_l/K_x in table [1, table 8.3] still have the same order of magnitude as the corrected ratio (7.8).

Combining (7.8) and (3.59) gives a revised magnitude of the expected horizontal lift-off current, which replaces the previous calculated value of 1.52 [A] in formula (3.59).

$$I_{u,lift-off} = \frac{K_x \cdot u_{max}}{K_l} = \frac{1.24 \cdot 10^7 \cdot 50 \cdot 10^{-6}}{572.2} = 1.08 \, [A] \tag{7.9}$$

The average absolute value of the measured horizontal lift-off current in [1, table 8.3] is:

$$|I_{lift-off}|_{horizontal,\ average} = 0.59\ [A] \tag{7.10}$$

Comparison of (7.9) and (7.10) shows that the measured value for the horizontal lift-off current is smaller than calculated. When the air gap between the rotor and the stator is presumed to be exactly 50 [μm], this means that the ratio K_x/K_l in reality is smaller than calculated. Then K_l must be relatively larger than K_x, but both gains can be smaller or larger than calculated.

Lastly, the conclusion in [1] that the leakage flux must be larger than expected should be corrected, because the number of horizontal coil windings (N_{HC}) was taken two times too large in the calculations of [1] (see section 3.3 correction ⑤). In reality N_{HC} is 0.5·1.4 = 0.7 times smaller than was used in the calculation, a reduction of 30%. This explains the measured weaker actuators!

7.3.3 Observing rotor path [1, section 8.5.2]

The gains $_{uN}K_l$ and stiffness $_{uN}K_{uN}$ are identified in [1] via the rotor lift-off path method (see section 3.7). The obtained values are copied from [1, table 8.3] and presented here in table 7.5.

Table 7.5 Measured linear actuator model gain corrections.

Parameter	Thesis [1] model values	Measured	Total correction factor
$_uK_l$ [m/s²A]	$1.08 \cdot 10^3$	131	8.24
$_uK_u$ [1/s²]	$1.61 \cdot 10^7$	$1.31 \cdot 10^6$	12.29
$_vK_l$ [m/s²A]	$1.08 \cdot 10^3$	62.5	17.28
$_vK_v$ [1/s²]	$1.61 \cdot 10^7$	$7.82 \cdot 10^5$	20.59
$_zK_l$ [m/s²A]	53	? (12.6)	? (4.21)
$_{α/β}K_l$ [rad/s²A]	$1.22 \cdot 10^4$	? ($3.99 \cdot 10^3$)	? (3.06)

The measurement results indicate that the v-actuator is almost twice as weak as the u-actuator. This difference might be caused by the poorly calibrated sensor, as is stated in [1] and confirmed by the position estimations in table 7.2.

Although it is just a detail, it is also not clear which rotor path is displayed in [1, figure 8.2]. The path is labeled with –u-v → +u-v, but according to table 7.2 it is more likely that it actually is –u+v → +u+v.

A first and fast check to verify that the numbers in table 7.5 are realistic, is to calculate the lift-off current with formula (3.58) that follows from the measured gain and stiffness values.

$$I_{u,lift-off} = \frac{_uK_u \cdot u_{max}}{_uK_l} = \frac{1.31 \cdot 10^6 \cdot 50 \cdot 10^{-6}}{131} = 0.5\ [A] \tag{7.11}$$

$$I_{v,lift-off} = \frac{_vK_v \cdot v_{max}}{_vK_l} = \frac{7.82 \cdot 10^5 \cdot 50 \cdot 10^{-6}}{62.5} = 0.6256\ [A] \tag{7.12}$$

These two currents agree well with the measured lift-off currents presented in [1, table 8.3], which have an average absolute value of 0.59 [A] (see (7.10)).

There is not only a difference between the measured strength of the two horizontal force actuators. The measured gains also differ from (are smaller than) the expectation values. The following analysis is an attempt to recover the cause of this. The results can be used to fill in the missing numbers in table 7.3 and 7.4 and to scale the calculated ideal z-, α- and β-actuator parameters to realistic expectation values (see the next sections).

The calculations will be based on the u-actuator measurements and the following hypothesis: In appendix F, the FEM correction factors for the actuator gains are calculated. These factors mainly make the modeling of the various magnetic resistances in the actuator system more realistic. It seems reasonable to suppose that the measurement difference is caused by the only other parameter that could be different in reality: the effective permanent magnet flux J [Wb], for instance due to weaker permanent magnets, flux spreading, leaking flux or counteracting magnetic fluxes by eddy currents.

So the correction factor between the corrected ideal modeling expectation values and the measured values is linked to the modeling of the permanent magnet flux. The correction factor for it is called factor$_{PM}$ and is defined in equation (7.13).

$$J_{real} = factor_{PM} \cdot J_{ideal} \quad [Wb] \tag{7.13}$$

To calculate the numerical value of factor$_{PM}$, the values of row 2 and 3 of table 7.4 and table 7.5 are used. The u-actuator **gain** expression (the first term of equation (G.1) divided by m_{ROTOR}) contains the PM-flux J in the numerator. Applying the correction factor (7.13) results in equation (7.14).

$$320 \cdot factor_{PM} = 131 \quad \Rightarrow \quad factor_{PM} = \frac{131}{320} = 0.409 \tag{7.14}$$

The u-actuator **stiffness** expression (the fourth term of equation (G.1) divided by m_{ROTOR}) contains the quadratic PM-flux J^2 in the numerator, but also needs to be scaled with an unknown FEM correction factor. Applying both correction factors results in equation (7.15).

$$1.24 \cdot 10^7 \cdot factor_{FEM} \cdot (factor_{PM})^2 = 1.31 \cdot 10^6 \tag{7.15}$$

Combining (7.14) and (7.15) gives:

$$factor_{FEM} = \frac{1.31 \cdot 10^6}{1.24 \cdot 10^7 \cdot (factor_{PM})^2} = \frac{1.31 \cdot 10^6}{1.24 \cdot 10^7 \cdot (0.409)^2} = 0.63 \tag{7.16}$$

This is a possible value, compared to the other three FEM correction factors (0.56, 0.51 and 0.84), see table 3.3. Equation (7.16) can now be used to fill in the missing numbers in tables 7.3 and 7.4.

7.3.4 Calibration of z-, α-, and β-actuators [1, section 8.5.3]

Because direct calibration of the vertical force actuators was not possible with the available methods, a reasoning was presented in [1, section 8.5.3] to come up with a prediction for the actual z-, α-, β-actuator linear model gains. The prediction is based on the calibration measurement results of only the horizontal force actuators, the ideally modeled vertical actuator and the measured coil inductions.

Although the reasoning itself as presented in [1] is correct, it needs some revision because of two modeling errors that were found (the number of horizontal coil windings that is twice as small and the vertical actuator strength that is two times higher, see chapter 3). The revision won't be given here, because in this thesis all the corrections are explicitly incorporated in the actuator models and directly translated into numerical values, as the tables in this chapter show.

The calibration of the horizontal actuators makes it plausible to expect a similar deviation between the predicted values via (the corrected) ideal vertical actuator models and the vertical actuator gain values of the real device. Although the vertical actuators make use of another force principle (Lorentz force instead of reluctance force), the formulae for the force F_z (G.7) and the torques $T_{\alpha/\beta}$ (G.10) both contain the permanent magnet flux J in the numerator. Applying the same PM-flux correction factor factor$_{PM}$ (7.14), which was introduced in the previous section, means that both terms must be multiplied with factor$_{PM}$, to get an estimation of the expectation values for the vertical actuator gains.

The actual numerical expectation values for the gains will be calculated in the next section. These values can then be used to fill in the missing numbers in table 7.5.

7.4 Control [1, section 8.6]

The controllers that were initially tested on the prototype were designed based on the ideal actuator model without any correction factors applied and using a flawed SIMULINK® model (see section 6.1).

Since the actuator model has been corrected and revised, an update is needed for the numerical values of the actuator gains in the SIMULINK® model. The updated model can then be used to tune and test the (re)designed controllers for the prototype.

7.4.1 Revised actuator model

Now that all the correction factors are available, the revised numerical values for the actuator gains in the SIMULINK® model can be calculated.

Horizontal force actuators:

$$F_{u,generated} = {}_uK_I \cdot m_{ROTOR} \cdot I_u = 131 \cdot 8.49 \cdot 10^{-3} \cdot I_u = 1.11219 \cdot I_u \ [N] \tag{7.17}$$

$$F_{u,destabilizing} = {}_uK_u \cdot m_{ROTOR} \cdot u = 1.31 \cdot 10^6 \cdot 8.49 \cdot 10^{-3} \cdot u = 1.11219 \cdot 10^4 \cdot u \ [N] \tag{7.18}$$

$$F_{v,generated} = {}_vK_I \cdot m_{ROTOR} \cdot I_v = 62.5 \cdot 8.49 \cdot 10^{-3} \cdot I_v = 0.531 \cdot I_v \ [N] \tag{7.19}$$

$$F_{v,destabilizing} = {}_vK_v \cdot m_{ROTOR} \cdot v = 7.82 \cdot 10^5 \cdot 8.49 \cdot 10^{-3} \cdot v = 6.639 \cdot 10^3 \cdot v \ [N] \tag{7.20}$$

The two middle terms of equation (G.1), that represent the force generated by the electromagnetic coils alone, are almost negligible (2.7%) compared to generated force by the coils and permanent magnets working together (equation (7.17)). Because it is not known how to scale the single parameters in these expressions, an arbitrary scaling factor of 4 will be applied on the value in (G.3), which results in a gain of:

$$745/4 = 185 \ [N/A^2m] \tag{7.21}$$

Vertical force actuator:

$$F_z = {}_zK_{I,FEM} \cdot factor_{PM} \cdot m_{ROTOR} \cdot I_z = 30.7 \cdot 0.41 \cdot 8.49 \cdot 10^{-3} \cdot I_z = 0.107 \cdot I_z \ [N] \tag{7.22}$$

Torque actuators:

$$T_{\alpha/\beta} = {}_{\alpha/\beta}K_{I,FEM} \cdot factor_{PM} \cdot I_x \cdot I_{\alpha/\beta} = 9.73 \cdot 10^3 \cdot 0.41 \cdot 2.21 \cdot 10^{-7} \cdot I_{\alpha/\beta} =$$

$$= 0.882 \cdot 10^{-3} \cdot I_{\alpha/\beta} \ [Nm] \tag{7.23}$$

The numerical actuator gain values (7.17)-(7.23) are summarized in column 3 of table 7.6. The table is expanded with column 4, which shows the difference factor between the initial thesis [1] model values and the (expected) measurement results.

Table 7.6 Actuator gain corrections based on measurements.

Parameter	Thesis [1] model values	Measured or estimated	Total correction factor
$F_{u, generated}/I_u$ [N/A]	7.68	1.112	6.9
$F_{u, destabilizing}/u$ [N/m]	$1.16 \cdot 10^5$	$1.112 \cdot 10^4$	10.4
$F_{v, generated}/I_v$ [N/A]	7.68	0.5306	14.5
$F_{v, destabilizing}/v$ [N/m]	$1.16 \cdot 10^5$	$6.639 \cdot 10^3$	17.5
EM coil force [N/A²m]	$2.026 \cdot 10^3$	{185}$^\blacktriangledown$	11
F_z/I_z [N/A]	0.38	? *(0.107)*	? *(3.55)*
$T_{\alpha\beta}/I_{\alpha\beta}$ [Nm/A]	$3.8 \cdot 10^{-3}$	? *(0.882 \cdot 10^{-3})*	? *(4.31)*

It appears that all actuator gains in the initial thesis model [1] were calculated too large, ranging from a factor 3.5 to even 17.5.

7.4.2 Controller tuning

The previous section (7.3) shows that when the modeling corrections are applied, a correction factor of about 2 can be expected for the actuator gains (see table 7.2). When also the horizontal actuator calibration results are included, the total correction factor for all actuators becomes about 10 (see table 7.6). This means that the actual actuators are about 10 times weaker than they are ideally modeled.

In [1, section 7.3.4] it was concluded from testing the controllers on the SIMULINK® model$^{\blacktriangledown\blacktriangledown}$, that for a actuator gain deviation of K<1/6 the system becomes unstable. So it shouldn't have been a surprise that with the presented gains in [1, table 9.1 and table 9.2], that also indicate a deviation factor smaller than 1/10, the prototype remains unstable with the initially designed controllers.

Since the proposed controllers in [1, chapter 7] were not able to stabilize the prototype, it was decided to tune them. Unfortunately, there is no report available on the tuning of the controllers for the device, except for the very short description in [1, section 8.6.1]. Because the tuning attempts remained unsuccessful, even for one isolated horizontal direction, the poorly calibrated sensor system (section 7.2) was mentioned as the main cause of the failure to stabilize the prototype.

7.5 Reviewing conclusions

7.5.1 Sensor calibration

Because the automatic but incomplete "stuck to the stator" calibration method (see section 4.5.2) was used on the prototype, only the horizontal position sensors are calibrated. This means that the sensor only provides valid information under the condition that the rotor parameters z, α^* and β^* are all kept equal to 0. Any deviation of one of these three parameter from 0 will directly result in an estimation error of the horizontal rotor positions and therefore act as measurement disturbance (10.22).

The effect of the wrong value used for parameter d_{max} (should be a factor $\sqrt{2}$ larger than was used in [1]) in the processing of the calibration measurement data, became visible in table 7.2, where the horizontal rotor positions (u and v) are estimated a factor $\sqrt{2}$ too small.

$\blacktriangledown$ Guessed value, see formula (7.21).
$\blacktriangledown\blacktriangledown$ Unaware of the SIMULINK® model being flawed, see section 6.1.

Table 7.2 also reveals the large difference between the estimation errors of both sensors. It seems that the more sensitive sensor produces the most accurate estimation results. When the sensitivity of both sensors are equal (as it was designed), the estimation errors of the sensors are expected to be equal as well.

7.5.2 Actuator calibration

Despite the limiting condition for the utilization of the poorly calibrated sensor system, only for rotor positions in the horizontal plane through the operating point (see section 7.5.1), the functioning of the sensor system should be adequate to use the sensor for the horizontal actuator calibration via the rotor lift-off trajectories method (see section 3.7).

The results from application of this method indicate that all actuator gains in the initial thesis model [1] were calculated too large, ranging from a factor 3.5 to 17.5. Even when all corrections to the model (including the removal of the errors in [1]) are carried out, there still remains a difference between the ideally modeled actuator system and the deduced actuator gains from the calibration measurements. To explain this difference, an extra factor (factor$_{PM}$ (7.14)) has been introduced. The factor$_{PM}$ was subsequently used to make a prognoses for the vertical actuator gains of the prototype, which couldn't be measured.

Note that the used position sensors are poorly calibrated and therefore not 100% accurate and that the correction factor $\sqrt{2}$ for parameter d$_{max}$ hasn't been incorporated in the measured gains that were simply copied from [1].

Also note that the part in the lift-off trajectory plot [1, figure 8.2] that has been marked as unreliable data, could be caused by a varying z-position of the rotor during its journey. Especially in the middle of the trajectory, the rotor can be pulled down by gravity because there the air gap between the sensor bowl and the rotor is the largest. The horizontal position sensors are not calibrated for z-position changes, so the horizontal position measurements will be disturbed by it, which is visible in the plot.

7.5.3 Controller testing and tuning

As already stated in [1, section 8.6.1], controller testing is hard because all controllers have to work at the same time stabilizing the rotor. Also an accurate sensor system is necessary for the controllers to function properly.

It is likely that, next to the poorly calibrated sensor system, the errors in the SIMULINK® model (see section 6.1) are also part of the reason why no stabilizing controllers for the prototype could be found in [1].

Chapter 8

Conclusions of PART 1

This final chapter of part 1 of this M.Sc.-thesis contains the main conclusions resulting from reviewing the Ph.D.-thesis [1]. The reviewing conclusions per subject can be found in each last section of chapters 3 till 7. Based on those reviewing conclusions is decided how to continue this project.

8.1 The Ph.D.-thesis [1]

The main information source about the executed work on the latest prototype of the tilting mirror project (see section 1.4), so far, is the Ph.D.-thesis [1]. It is clearly structured and therefore easy to read. However, its contents is not perfect.

In general, the basis of the calculations presented in [1] is correct*. The presented analyses are mostly clear enough to understand what is meant. However, the execution of some computations is not flawless (is it ever?).

The presented analyses contain typos, ambiguous definitions (e.g. reference frames), incorrect assumptions, sloppy calculation mistakes, unjustly omitted model properties or are incompletely presented. Some (very small) parts are even incompatible with mathematical rules or electrical engineering basics.

All this has been rectified and improved without doing any further research, just by checking, reviewing and supplementing what has been presented in the Ph.D.-thesis [1] and the software belonging to the project.

8.2 Main reviewing conclusion

The main conclusion in [1] is that no stabilizing controllers were found with the poorly calibrated sensor system. Therefore, the main recommendation to make the prototype operational is to develop an external sensor calibration system.

It is clear that an accurately and completely calibrated sensor system is the most important condition for the prototype to become operational. In addition to the sensor calibration, other things that could prevent the system from proper functioning were discovered while reviewing [1]:

- The sensor frame printed on the main PCB could lead to faulty wire connections.

- The theoretical- and programming mistakes in the SIMULINK® model not only disrupt the controller design (and testing), also the robustness margin of the designed controllers, that was reserved to cope with the difference between the ideally modeled device and the real prototype, could be consumed.

♥ Obviously, because a Ph.D.-thesis should be scientific.

8.3 Uncertainties and missing Information

There are still some uncertainties about the modeling and functioning of the real prototype. Some of the things that remain uncertain are summed up below.

● There is no proof that the functioning of the real sensor system is good.
The replica of the sensor has been used for the measurements presented in [1]. These measurements prove that the principle of operation of this type of sensor is fine and that the processing electronics work. It doesn't guarantee a proper functioning of the sensor in the prototype.

● Has the functioning of the twelve separate magnetic actuators in the prototype been checked?
The difference in strength between the u- and the v-actuator measured in [1], could be caused by the poorly calibrated sensor system. The four vertical actuators, that haven't been calibrated at all, also don't have to be equally strong. This can both influence the working of the vertical force actuator as well as the tilting torque actuators.

● It hasn't been proven that the initially designed controllers are not applicable on the prototype.
The fact that the actuator gains of the real device are probably modeled a factor 10 too large and the flawed SIMULINK® model that was used in [1] for controller design and testing, certainly asks for a reconsideration of the set of controllers to be used. But, the poorly calibrated sensor system could be the main reason why no set of controllers is able to stabilize the prototype, because an accurate sensor is a primary condition for the device to become operational. Therefore, it cannot be concluded that the simple approach (linear model and 5 SISO PID controllers) is not applicable on the prototype.

● Has the tuning of the controllers really been executed?
There is no report on what alternative controllers are tested on the prototype or what tuning strategy has been followed. Has the flawed SIMULINK® model been used for the controller redesign?

● Has the difference between the ideal actuator model and the measured horizontal actuator gains properly been translated to the vertical actuators that couldn't be calibrated?
In [1, section 8.5.3] it was assumed that same the difference as was measured for the horizontal coils could be expected for the vertical coils.
In section 7.3.3 of this thesis the difference was linked to the flux of the permanent magnet, with a factor called $factor_{PM}$. Using this factor resulted in closely-reasoned calculations, but there could be other reasons[*] for the measured differences then just the $factor_{PM}$, which also doesn't has to be a constant.

● Is the prototype damaged too much?
In [1, section 9.3.1] it is stated that the damage to the prototype should be repaired before it can become operational. The repairing involves gluing the piece of lamella back on the rotor, replacing the damaged coating on the tilting sensor electrodes and putting the mistakenly forgotten coating on the position sensor electrodes (sensor bowl). Although these three evils all influence the operation of the prototype to some unknown extend, they are no primary conditions for operation of the device.
To repair the device, it must be almost completely dismantled, which is difficult, time consuming and therefore expensive. So, first will be tried to make the device operational without the damage repaired.

---

[*] Like the poorly calibrated sensor, that was used for the calibration measurements.

8.4 Project continuation strategy

The corrected SIMULINK® model could be used immediately for controller redesign. However, it seems better to wait for the sensor recalibration (this is also a requirement for the controllers), then recalibrate the actuator and incorporate this more reliable and complete information into the PID-controller redesign.

Of course, it must be checked that the electrical wires are connected to the right sensors and actuators of the prototype, and that all actuators and sensors of the prototype are functioning properly.

When subsequently a next attempt to stabilize the prototype also is unsuccessful, it will be necessary to improve the modeling of the device (actuator and sensor behavior) and/or use other (non-linear) control techniques.

8.5 Account for work presented in PART 1

What started as the introductory reading of the Ph.D.-thesis [1] led to the suggestions of improvements for [1], as reported in part 1 of this thesis. The question is whether it is useful to correct every mistake, even when it involves a lot of work?
Unfortunately, this often can only be determined after the correction has been done. The same reasoning goes for the checking of calculations that eventually proved to be right. Is this a waste of time?

Well, for me it has been an extra training and it provided a deeper understanding of the used techniques. It also showed that I am capable of reading scientific material with a critical view. More important is that the faults in [1] wouldn't be discovered when not everything was checked thoroughly.

Of course the contents of [1] is not part of my responsibility. But I am responsible when I use other people's work, without making sure it is correct. The fact that the build prototype has to become operational, increases the demands on the system.
Because now the device is no longer purely theoretical, words like *proposal*, as often used in [1], are no longer sufficient in the practical situation. This could be concluded from the fact that the system still hasn't been fully operational!

A final note must be made about the maximum forces, torques, accelerations and angular accelerations presented in chapter 3 of this thesis. The values of these device parameters are the corrected theoretical ideal values. The actuator calibration measurements in chapter 7 have shown that much smaller values are expected for the real device. The actuator gains in chapter 7, could be used immediately to recalculate the device parameters. Because it is expected that recalibration of the sensors and actuators will result in yet other actuator gains, the real parameters of the prototype will be determined when this new information is available.

PART 2

Additional work

Part 2 of this thesis contains a report on the work that has been executed, besides the reviewing and correcting of the Ph.D.-thesis [1], to continue the tilting mirror project.

It describes:

- *The processing of the calibration measurement data of the test setup sensor in order to obtain an optimal linear sensor model.*

- *The development of an external calibration setup for the capacitive sensor system of the prototype.*

- *The derivation of the linear model of the tilting mirror prototype in its operating point, expressed in design parameters.*

- *A Relative Gain Array matrix analysis executed to investigate the diagonal dominace of the transfer function matrix of the linearized system.*

- *The adaptation of the controllers for the prototype.*

Chapter 9

Possible follow up activities

In part 1 of this thesis, a project continuation strategy (section 8.4) proceeded from reviewing the tilting mirror prototype and its documentation [1]. The work in part 1 resulted in corrections and supplements for the presented analyses, not in improvements for future designs, the other part of the first point of the graduation assignment (section 2.2). Also the seven other points of the assignment haven't had any attention yet.

A further evaluation of the prototype could be helpful to make the device operational or to prove that this can't be done with the means currently available. Useful activities could be:
- Improving the analytical modeling of the device (sensor and actuator).
- Investigating the (weak) properties of the prototype, like the digital implementation of the controllers or the influence of surroundings properties like the temperature (see below).

A quick analysis shows that the influence of the surroundings temperature on the device is not negligible.

The linear expansion coefficients [5] of the materials mainly used in the prototype are:

For iron:	$\gamma_{lec} = 11.7 \cdot 10^{-6}$ [K^{-1}]	(9.1)
For aluminum:	$\gamma_{lec} = 23.2 \cdot 10^{-6}$ [K^{-1}]	(9.2)

These numbers indicate the relative expansion in one particular direction, here called x [m]. The linear expansion coefficient γ_{lec} should be used as in formula (9.3).

$$\frac{\Delta x}{x} = \gamma_{lec} \cdot \Delta T \quad \Leftrightarrow \quad \Delta x = \gamma_{lec} \cdot \Delta T \cdot x \quad [m] \tag{9.3}$$

Where ΔT [K] is the absolute temperature difference between two situations, causing the change of length Δx [m].

> For example:
> The rotor diameter at the iron top is $d_{rotor} = 16$ [mm]. This means that the size of the rotor can change with $\Delta d_{rotor} = 11.7 \cdot 10^{-6} \cdot 16 \cdot 10^{-3} = 0.18 \cdot 10^{-6}$ [m/K].

The stator will also be affected by the temperature change and the sensor bowl as well. The temperature effects on the actuator system operation (change of air gap sizes) and the operating of the sensor system could both be investigated.
Since the reviewing in part 1 indicated that there is room for improvement without doing additional research, first will be focused on activities that are necessary or might help to make the prototype operational:

- The design of a calibration setup for the sensor of the prototype has the highest priority and is described in chapter 11.

- The sensor calibration measurement is prepared in chapter 10.
  First a theoretical and experimental set of measurement expectations are calculated for the linear sensor model. After that, the linear sensor model is tested and it is investigated how it can be optimized.

- In chapter 12, the five original controllers for the prototype are adjusted, based on the corrections proposed in part 1.
  First a linear model of the prototype in its operating point is calculated. Then the adjusted controllers are tested on the corrected and supplemented SIMULINK® model of the prototype. The controllers can't be tested on the prototype as long as its sensor isn't properly calibrated.

- In section 14.2 the results of a obligatory literature survey are presented.
  The survey focused on finding information about the modeling and control of similar devices and the implementation of switching between several controllers (point ❷ of the graduation assignment).

Chapter 10

Processing the calibration measurement data of the test setup sensor

In [1, section 5.6.3] the collected data from measurements on the test setup (replica) of the sensor system was mainly used to plot and to get a visual impression of the sensor behavior of the test setup sensor (and the almost equal sensor in the real device). Because this data also provides some other research opportunities, a supplemental analysis of the measurement data is executed in this chapter.

This chapter starts with the definition of the linear sensor model in matrix notation with the local test setup frame used. Then the ideal linear sensor model parameters are calculated, based on formulae in [1]. Subsequently, the linear sensor model parameters for the sensor in the test setup are extracted manually from the measurement data of the test setup. The ideal and extracted parameters are compared, because both serve as measurement expectations for the sensor of the real device. The extracted linear sensor model is tested and evaluated by doing some rotor position and orientation estimations based on the same data. Lastly, it is investigated how to optimize the linear sensor model (parameters).

Besides the testing of the applicability of a linear sensor model for the real device, the analyses presented here serve two other purposes:

❶ It is an exercise for processing the data to be measured on the real device.
It could indicate what to reckon with when the calibration of the real sensor system is executed and possibly results in improvement of the data to be collected.

❷ Only in case of need, the values of extracted parameters from the test setup sensor can be used to substitute linear parameters of the sensor of the real device that couldn't be extracted with the proposed automatic "stuck to the stator" calibration method in [1].

10.1 The linear sensor model in matrix notation

The linear sensor model (4.10)-(4.14) can be written in matrix form, as was shown in section 7.2, only here (in (10.1)) the local setup sensor reference frame is used!

$$
\begin{bmatrix} _xV_i - _xV_0 \\ _yV_i - _yV_0 \\ _zV_i - _zV_0 \\ _aV_i - _aV_0 \\ _\beta V_i - _\beta V_0 \end{bmatrix} = \begin{bmatrix} _xC_x & _xC_y & _xC_z & _xC_a & _xC_\beta \\ _yC_x & _yC_y & _yC_z & _yC_a & _yC_\beta \\ _zC_x & _zC_y & _zC_z & _zC_a & _zC_\beta \\ _aC_x & _aC_y & _aC_z & _aC_a & _aC_\beta \\ _\beta C_x & _\beta C_y & _\beta C_z & _\beta C_a & _\beta C_\beta \end{bmatrix} \begin{bmatrix} x \\ y \\ z \\ \alpha \\ \beta \end{bmatrix} \Leftrightarrow V = C_{coupling}X \tag{10.1}
$$

Where:
V = Sensor output voltages minus the offset voltages.
$C_{coupling}$ = Linear sensor model parameter matrix.
X = True (exact) position and orientation of the rotor.

With a calibration method the 25 parameters in the coupling matrix and the five offset voltages must be determined. When all these parameters are known, the five sensor output voltages can be used to estimate the position and orientation of the rotor.
The principle for doing this is displayed in formula (10.2).

$$\hat{X} = C_{decoupling}V \Leftrightarrow \begin{bmatrix} \hat{x} \\ \hat{y} \\ \hat{z} \\ \hat{\alpha} \\ \hat{\beta} \end{bmatrix} = \begin{bmatrix} {}_xC_x & {}_xC_y & {}_xC_z & {}_xC_\alpha & {}_xC_\beta \\ {}_yC_x & {}_yC_y & {}_yC_z & {}_yC_\alpha & {}_yC_\beta \\ {}_zC_x & {}_zC_y & {}_zC_z & {}_zC_\alpha & {}_zC_\beta \\ {}_\alpha C_x & {}_\alpha C_y & {}_\alpha C_z & {}_\alpha C_\alpha & {}_\alpha C_\beta \\ {}_\beta C_x & {}_\beta C_y & {}_\beta C_z & {}_\beta C_\alpha & {}_\beta C_\beta \end{bmatrix}^{-1} \begin{bmatrix} {}_xV_i - {}_xV_0 \\ {}_yV_i - {}_yV_0 \\ {}_zV_i - {}_zV_0 \\ {}_\alpha V_i - {}_\alpha V_0 \\ {}_\beta V_i - {}_\beta V_0 \end{bmatrix} \qquad (10.2)$$

Where:

V = Sensor output voltages minus the offset voltages.

$C_{decoupling} = C_{coupling}^{-1}$ = Inverse of the linear sensor model parameter matrix.

$\hat{X}$ = Estimated position and orientation of the rotor.

In formula (10.2) the inverse of the linear sensor model parameter matrix $C_{decoupling}$ $(= C_{coupling}^{-1})$ is used. This inverse matrix can be calculated both numerically and analytically with MATLAB®.

10.2 Measurement expectations

A measurement expectation for the linear sensor model parameters can be calculated based on the ideal model of the sensor of the real device [1, section 5.4]. Expectation values for the 25 linear parameters in the 5x5 coupling matrix $C_{coupling}$ in (10.1) can be calculated by making a first order linear model approximation of the capacitive position and orientation sensor near the operating point of the rotor ($X = \overline{0}$).

10.2.1 Expected linear sensor model parameters

Each linear model parameter can be calculated with formula (10.3), which uses the first partial derivative of one of the five sensor output voltages V_i.

$$_jC_k = \left. \frac{\partial_j V_i}{\partial k} \right|_{X = \overline{0}} \qquad (10.3)$$

To obtain numerical values for the expected linear model parameters, some sensor parameters must be known: the modulation voltage $V_s = 2.5$ [V], the sensor separation angle $\lambda = 34.6°$, the nominal air gap distance $d = 0.25$ [mm], the average sensor electrode angles $k_1 = 25.25°$ and $k_2 = 37.45°$ and the rotation sensor overlapping area parameters $A_{\alpha\beta} = 1.036726 \cdot 10^{-5}$ [m²] (4.5) and $k_{\alpha\beta} = 2.376 \cdot 10^{-5}$ [m²/rad] (4.6).

Presented next are the predictions of the linear sensor model parameters that differ from 0. The other parameters are either not modeled (like $_\alpha C_\beta$ and $_\beta C_\alpha$) or equal to 0 in the operating point.

$$_xC_x = \left. \frac{\partial_x V_i}{\partial x} \right|_{X = \overline{0}} = \frac{V_s \sin\lambda}{d} = \frac{2.5 \sin(34.6°)}{0.25 \cdot 10^{-3}} = 5678 \text{ [V/m]} \qquad (10.4)$$

$$_y C_y = \frac{\partial_y V_i}{\partial y}\bigg|_{x=\bar{0}} = \frac{V_s \sin\lambda}{d} = \frac{2.5\sin(34.6°)}{0.25\cdot10^{-3}} = 5678 \text{ [V/m]} \tag{10.5}$$

$$_z C_z = \frac{\partial_z V_i}{\partial z}\bigg|_{x=\bar{0}} = \frac{V_s(\cos k_1 - \cos k_2)}{2d} = \frac{2.5(0.90 - 0.79)}{2\cdot0.25\cdot10^{-3}} = 550 \text{ [V/m]} \tag{10.6}$$

$$_a C_y = \frac{\partial_a V_i}{\partial y}\bigg|_{x=\bar{0}} = \frac{V_s}{d} = \frac{2.5}{0.25\cdot10^{-3}} = 10^4 \text{ [V/m]} \tag{10.7}$$

$$_a C_a = \frac{\partial_a V_i}{\partial a}\bigg|_{x=\bar{0}} = \frac{V_s k_{a\beta}}{A_{a\beta}} = 2.5\cdot\frac{1}{25} = 0.1 \text{ [V/°]} \approx 5.72958 \text{ [V/rad]} \tag{10.8}$$

$$_\beta C_x = \frac{\partial_\beta V_i}{\partial x}\bigg|_{x=\bar{0}} = -\frac{V_s}{d} = -\frac{2.5}{0.25\cdot10^{-3}} = -10^4 \text{ [V/m]} \tag{10.9}$$

$$_\beta C_\beta = \frac{\partial_\beta V_i}{\partial \beta}\bigg|_{x=\bar{0}} = \frac{V_s k_{a\beta}}{A_{a\beta}} = 2.5\cdot\frac{1}{25} = 0.1 \text{ [V/°]} \approx 5.72958 \text{ [V/rad]} \tag{10.10}$$

Substitution of (10.4)-(10.10) in (10.1) results in an expression for the complete coupling matrix of the sensor of the real device to be expected.

$$C_{coupling\_ideal} = \begin{bmatrix} 5678 & 0 & 0 & 0 & 0 \\ 0 & 5678 & 0 & 0 & 0 \\ 0 & 0 & 550 & 0 & 0 \\ 0 & 10^4 & 0 & 0.1 & 0 \\ -10^4 & 0 & 0 & 0 & 0.1 \end{bmatrix} \tag{10.11}$$

The first three columns of (10.11) are expressed in [V/m], the last two in [V/°].

10.2.2 Finding the operating point

From the analysis above, a property of the sensor that might be interesting to use has come up. It started with the calculation of the linear sensor model parameter that couples the z-position of the rotor to the output voltage of the x-sensor.

$$_x C_z = \frac{\partial_x V_i}{\partial z}\bigg|_{x=\bar{0}} = -\frac{V_s \cdot x \cdot \sin\lambda\cdot\cos\lambda}{d^2}\bigg|_{x=\bar{0}} = 0 \text{ [V/m]} \tag{10.12}$$

As (10.12) shows, the z-translation doesn't influence the x-sensor output voltage, when the x-position of the rotor is kept equal to 0. The same reasoning goes for the y-sensor output voltage, which has an equivalent expression, when the y-position of the rotor is kept equal to 0.

When the rotor is slightly moved in the x-direction, for example 1 [μm], the x-sensor output voltage becomes sensitive for a rotor translation in the z-direction. This is shown in (10.13).

$$_x C_z = \frac{\partial_x V_i}{\partial z}\bigg|_{x=[10^{-6},0,0,0]^T} = -\frac{2.5\cdot10^{-6}\cdot\sin34.6°\cdot\cos34.6°}{(0.25\cdot10^{-3})^2} = -18.7 \text{ [V/m]} \tag{10.13}$$

In fact, formula (10.12) shows that the more the x-position of the rotor differs from 0, the more sensitive the x-sensor output voltage becomes for a translation of the rotor in the z-direction. As already said, the same coupling is present between the y-position and the sensitivity of the y-sensor output voltage for a rotor translation in the z-direction.

It seems that the property described above can be used to find the x- and y-position of the operating point of the rotor by minimizing the cross couplings for the z-translation of the rotor to the x- and y-sensor output voltages.

10.3 Testing of the linear sensor model

In [1], the collected data from the measurements on the test setup of the sensor was mainly used to plot and to get a visual impression of the sensor behavior of the test setup sensor and the almost equal sensor in the real device.

The available calibration measurement data of the test setup also provides the opportunity to investigate the applicability of a linear sensor model for the sensor in the real device. To do this, first the data is used to extract the linear sensor model parameters for the sensor in the test setup. After that the linear sensor model is tested and evaluated with the same data.

The available data is stored in the MATLAB®-file data.m (CD-ROM (section 1.8)), made by the author of [1]. This file contains the measurements taken on a virtual grid with steps of 50 [μm] over a range of ±200 [μm] in the horizontal x- and y-direction for four different rotor heights (z-positions), namely: −0.1, 0, 0.1 and 0.2 [mm].
According to [1, section 5.6.3.2] the accuracy with which the rotor can be positioned is approximately 5...10 [μm]. This is a property of the used positioning tables.

The data-file also contains measurements for the angular sensor in grid steps of 5 degrees over a range of ±15 degrees for only one of the two measurable rotations. Therefore, these results will be used for both sensors, because in theory they should be almost the same (except for some signs).

The following evaluation of the measurements is done in the MATLAB®-file sensorcaldata.m. This evaluation serves multiple purposes:

- It is a practice for the processing of the data from measurements to be taken on the sensor of the real device.

- A realistic (non-ideal) expectation for measurements on the real device is created.

- It is checked if a linear sensor model is applicable on the real device.
  For instance: is a linear sensor model always accurate enough?

Another option is to compare the performance of the fully calibrated linear sensor model with the rotor position and orientation estimation done based on only the linear sensor model parameters that can be extracted with the incomplete "stuck to the stator" sensor calibration method. Also see the next section and [1, section 5.6.4.1 and section 8.4], where the "stuck to the stator" calibration method is explained.

10.3.1 Linear sensor model parameter extraction

The measurement data in data.m has been used to extract linear sensor model parameters for the sensor in the test setup. Based on the straight lines in the plots of [1, figure 5.30], especially within the rotor range of the real device, it seemed reasonable to first use a simple linear approximation technique. When necessary, the linear model parameters (the coupling matrix and the offset voltages) could be tuned in an attempt to get better estimation results.

For a first try, the sensor output voltage graphics are approximated by straight lines between the two (measurement) points on the edge of the rotor range of the real device. Formulae (10.14) and (10.15) show how this technique was used to extract the linear sensor coupling parameters.

For varying position parameter j = (x, y or z) and k = (x, y, z, α or β):

$$_kC_j = \frac{\text{average value } _kV_i(50 \cdot 10^{-6}) - \text{average value } _kV_i(-50 \cdot 10^{-6})}{10^{-4}} \quad [\text{V/m}] \tag{10.14}$$

For varying rotation parameter j = (α) and k = (x, y, z, α or β):

$$_kC_j = \frac{\text{average value } _kV_i(15°) - \text{average value } _kV_i(-15°)}{30°} \quad [\text{V/°}] \tag{10.15}$$

Formulae (10.14) and (10.15) are used for all possible combinations of j and k. The 20 resulting linear sensor model coupling parameters are presented in (10.16). Measurement data for the β-rotation is not available, so the values in the fifth column were derived (and copied) from the α-sensor coupling values (column 4).

Note that all parameters are extracted from the MATLAB® figures with an accuracy of 0.001 [V/m]. The zoom-in function was used to get the necessary accuracy, and multiple measurements were averaged.

$$C_{coupling\_setup} = \begin{bmatrix} 5320 & 1192.5 & -1501.5 & 7.609 \cdot 10^{-3} & 7.609 \cdot 10^{-3} \\ 2210.75 & 3165 & -5760 & 9.0467 \cdot 10^{-3} & 9.0467 \cdot 10^{-3} \\ -232 & -302 & 4856 & -6.0533 \cdot 10^{-3} & -6.0533 \cdot 10^{-3} \\ -84.5 & 9065 & 3671.25 & -3.1867 \cdot 10^{-3} & -7.8067 \cdot 10^{-3} \\ 9136 & -314.5 & 2573 & -7.8067 \cdot 10^{-3} & -3.1867 \cdot 10^{-3} \end{bmatrix} \tag{10.16}$$

The first three columns of (10.16) are expressed in [V/m], the last two in [V/°].

The dominating linear parameters in the first three columns of (10.16) are all of the same order of magnitude $\approx 10^3$ [V/m]. This means that the:

Sensor translation sensitivity $\approx 10^3$ [V/m] $\triangleq 10^{-3}$ [V/μm] \hfill (10.17)

The linear parameters in the last two columns of (10.16) are extracted from one figure and used for both rotation sensors. All parameters seem to be of the same order of magnitude $\approx 10^{-2}$ [V/°]. This means that the:

Sensor rotation sensitivity $\approx 10^{-2}$ [V/°] \hfill (10.18)

The offset voltages of the five sensors are also part of the linear model of the test setup sensor. The second column of table 10.1 shows the offset voltages that were obtained from [1, figure 5.30] in MATLAB®. These offset voltages can be taken from any of the four plots, because on the vertical middle line (were the varying parameter is 0) all the five position and orientation parameters are equal to 0. Therefore, on the vertical axis of all four plots, the five sensor output voltages are the offset voltages.

For the estimation of the position and orientation of the rotor as is done in (10.2), the inverse of the coupling matrix (10.16) is needed. Equation (10.19) shows the numerical decoupling matrix of the test setup sensor. It is calculated with MATLAB®.

$$C_{decoupling\_setup} = C^{-1}_{coupling\_setup} =$$

$$= \begin{bmatrix} 1.6305 \cdot 10^{-4} & -3.5003 \cdot 10^{-4} & -4.7780 \cdot 10^{-4} & 8.7895 \cdot 10^{-5} & 8.7895 \cdot 10^{-5} \\ -1.4802 \cdot 10^{-4} & 4.4090 \cdot 10^{-4} & 4.8774 \cdot 10^{-4} & -8.1875 \cdot 10^{-6} & -8.1875 \cdot 10^{-6} \\ 6.5283 \cdot 10^{-5} & 3.0455 \cdot 10^{-4} & 7.0898 \cdot 10^{-4} & -9.4582 \cdot 10^{-5} & -9.4582 \cdot 10^{-5} \\ 3.3195 \cdot 10^{2} & -7.1518 \cdot 10^{2} & -8.5740 \cdot 10^{2} & 1.7607 \cdot 10^{2} & -4.0380 \cdot 10^{1} \\ -2.7844 \cdot 10^{2} & 9.5092 \cdot 10^{2} & 1.2549 \cdot 10^{3} & -2.5490 \cdot 10^{2} & -3.8454 \cdot 10^{1} \end{bmatrix} \quad (10.19)$$

The first three columns of (10.19) are expressed in [m/V], the last two in [°/V].

10.3.2 Comparison of the ideal and extracted linear sensor model

The extracted linear model (coupling) parameters for the test setup sensor in $C_{coupling\_setup}$ (10.16) can be compared with the ones derived with the ideal sensor model in $C_{coupling\_ideal}$ (10.11).

The ideal coupling matrix contains seven non-zero elements ($_xC_x$, $_yC_y$, $_zC_z$, $_\alpha C_\alpha$, $_\beta C_\beta$, $_\alpha C_y$ and $_\beta C_x$). Only three parameters ($_xC_x$, $_yC_y$ and $_\alpha C_y$) show matching magnitudes and signs. The deviating parameters, which are an indication for a possible practical problem, are discussed below:

❶ Parameter $_\beta C_x$ was expected to be -10^4 [V/m] but the extracted value from the setup measurements is 9136 [V/m]. The magnitude is matching, but not the sign.
This problem was already found in section 4.5.1 at observation ④, where it was concluded that the wires of the β-rotation sensor electrodes must be interchanged.

❷ The magnitude and the sign of the measured parameter $_\alpha C_\alpha$ seem incorrect. The ideal value of $_\alpha C_\alpha$ is 0.1 [V/°] and the measured value is –0.0031867 [V/°]. So the measured value is approximately –31 times smaller than the expected one. This large difference cannot be explained by the difference in shape of the rotation sensor electrodes in real device (ideal model) and the electrodes of the test setup sensor.
Moreover, in the fourth column of $C_{coupling\_setup}$ (10.16), representing the influence of the α-rotation on the five sensor output voltages, the parameter $_\alpha C_\alpha$ has the smallest magnitude, while it should have the largest. In fact, the other three parameters ($_xC_\alpha$, $_yC_\alpha$ and $_zC_\alpha$) should be equal to 0 or at least very small, because the device was designed such that the translation sensor output voltages are rotation independent!
Note that the influence of the α-rotation on $_\beta V_i$ has not been taken into account in the ideal sensor model ($_\beta C_\alpha = 0$), while in reality it will be present.

The magnitudes of parameters $_xC_\alpha$, $_yC_\alpha$ and $_zC_\alpha$ (all smaller than 0.0091 [V/°]) seem reasonable compared to the expected value of $_\alpha C_\alpha$ (0.1 [V/°]). The fact that they are not equal to 0, could have been caused by an imperfect spherical rotor shape or by a small eccentric misalignment of the sensor electrodes and the rotor.
It is hard to recover what exactly and if something went wrong with the measurements concerning the varying α-rotation, from which the parameter $_\alpha C_\alpha$ has been extracted.

Looking solely at parameter $_\alpha C_\alpha$, it could be that the measured $_\alpha V_i$ is actually $_{-\beta} V_i$ as is shown in (4.8). This would perfectly explain the minus sign and also the very small magnitude of $_\alpha C_\alpha$. On the other hand, $_\beta V_i$ in [1, fig 5.30d] should probably show a higher sensitivity for the α-rotation, because this would then actually be $_\alpha V_i$.
Apparently, this is not the case.

Other possibilities are that:
- the measurements are done by hand, so maybe the positive and negative α-rotation direction have been mixed up.

- the sensor wires were interchanged in between the measurements that were taken for the different plots in [1, figure 5.30].

- something is wrong with the rotation electrodes or the processing electronics.

Unfortunately no measurement results for the β-rotation sensor are available, so it is not known if this sensor shows the same sort of behavior.

The explanations given above are just speculations, because the circumstances during the taking of the measurements cannot be checked anymore. Therefore, I have chosen for the following strategy.

First the calibration measurements will be done on the real device, paying extra attention to the connection of the sensor electrode wires. When the same problems as described above occur, they can be investigated directly.

⬤ The magnitudes of the measured $_7C_z$ parameters are very large and $_zC_z$ is nine times bigger than expected (4856 instead of 550 [V/m]). This cannot be explained by the off-center parameter influence demonstrated in (10.12), as is shown below:

$$\text{With} \quad {}_xC_z = -1505.1 \quad \Rightarrow \quad \text{x-offset} = 80,31 \text{ [µm]} \tag{10.20}$$

$$\text{With} \quad {}_yC_z = -5760 \quad \Rightarrow \quad \text{y-offset} = 308,08 \text{ [µm]} \tag{10.21}$$

The large values of the parameters $_7C_z$ mean that the z-position of the rotor has a dominating effect on the five sensor output voltages.

10.3.3 Estimation of some rotor positions and orientations

To test the linear model of the test setup sensor, some exactly[▼] known rotor positions with their corresponding measured sensor output voltages are required. The sensor output voltages are used together with the decoupling matrix (10.19) and the sensor offset voltages to estimate the rotor position (and orientation) that goes with the sensor output voltages, via the principle of (10.2). Comparison of the estimated rotor position and the known rotor position provides information about the quality and the applicability of the linear sensor model.

10.3.3.1 Selected rotor positions for estimation testing

In this section the linear sensor model will be tested with seven selected positions of the rotor. Six positions near the edge of the rotor range were chosen:

- The highest and the lowest position that the rotor can reach in the real device, based on the calculation of the vertical rotor range in appendix H.1. The sensor output voltages for the top- and bottom-position of the rotor were read from [1, figure 5.30c] in MATLAB®.

- The four "stuck to the stator" positions, or in this case the four positions among the measurement points closest to them. The sensor output voltages for the four positions were directly taken from the file data.m

The other position was chosen near the operating point of the rotor in the middle of the rotor range. The sensor output voltages for this point (the closest point to the operating point of the rotor) were also directly taken from data.m.

Notice that at all seven positions the angles α and β are always equal to zero, simply because no measurement data is available where the translation parameters (x, y, and z) and the rotation parameters (α and β) are varied simultaneously.

▼ Due to the inaccuracy of the used positioning tables, the rotor position is not exactly known. The rotor can be positioned with an accuracy of 5...10 [µm].

The five sensor output voltages for all seven positions are displayed in table 10.1 together with the offset voltages of the sensors (second column).

Table 10.1 Sensor output voltages derived from measurements on the test setup.

Sensor voltage	Offset voltage [V]	Top position [V]	Bottom position [V]	Near neutral [V]	Stuck 1 position [V]	Stuck 2 position [V]	Stuck 3 position [V]	Stuck 4 position [V]
$_xV_i$	-0.19495	-0.42035	-0.0893	-0.26630	0.0474	-0.0844	-0.43950	-0.31260
$_yV_i$	-3.53975	-4.2804	-3.1175	-3.6237	-3.3083	-3.6357	-3.7305	-3.4180
$_zV_i$	2.0944	2.722765	1.6990	2.0754	2.0610	2.0911	2.1333	2.1083
$_\alpha V_i$	0.742067	1.4326	0.46705	1.1470	1.5862	0.66200	0.8954	1.7658
$_\beta V_i$	0.8812	1.36245	0.6760	0.68630	1.1609	1.1814	0.2597	0.2331

10.3.3.2 Coupling matrix adaptation

In principle, the complete coupling matrix (10.16) and decoupling matrix (10.19)
should be used for the estimation of the position and orientation of the rotor. Throughout this section this is done in the situation called **B**.

In situation **V**, only the linear sensor model parameters that can be identified with the "stuck to the stator" calibration method are used for the estimation of the position and orientation of the rotor.

The estimation results in situation **B** show some extremely large estimated rotation angles. They should all be 0, but the estimated angles mostly lie far out of the real range (±22.5°) of the rotor. This problem is most likely caused by the small magnitudes of the couplings from the rotations to the output voltages of the two rotation sensor. Consequently, there is also a small difference between the couplings from the rotations to the output voltages of the two rotation sensors and the couplings from the rotations to the output voltages of the three translation sensors.

To investigate the effects of (presumably) too small couplings from the rotor rotations to the sensor output voltages, two more situations were created: situation **A** and situation **C**.

Table 10.2 Full description of the four different coupling matrices that were used for testing.

Situation	Coupling matrix adaptation
V	In situation V, only the parameters that can be identified with the "stuck to the stator" calibration method proposed in [1, section 5.6.4.1] are used for the position and orientation estimation from the five sensor voltages, see [1, section 8.4]. For the x-position only $_xC_x$, $_xC_y$ and $_xV_0$ are used and for the y-position only $_yC_x$, $_yC_y$ and $_yV_0$ are used. The z-position can't be estimated without $_zC_z$.. In principle, also the angles cannot be estimated without $_\alpha C_\alpha$ and $_\beta C_\beta$, but for the test setup sensor they are available, so: for the α-rotation $_\alpha C_x$, $_\alpha C_y$, ($_\alpha C_\alpha$) and $_\alpha V_0$ are used and for the β-rotation $_\beta C_x$ and $_\beta C_y$, ($_\beta C_\beta$) and $_\beta V_0$ are used.
A	In situation A, the linear sensor parameters $_xC_\alpha$, $_xC_\beta$, $_yC_\alpha$, $_yC_\beta$, $_zC_\alpha$ and $_zC_\beta$ are all presumed to be equal to 0, as they are supposed to be. The other 19 parameters are used with the values as in (10.16).
B	In situation B, the complete coupling matrix (10.16) for the sensor of the test setup is used. Remember that the last column (β-rotation) consists of values copied form the α-rotation measurements, simply because the necessary data is not available.
C	In situation C, the lack of sensitivity of the α/β-rotation sensors is compensated by enlargement of the parameters $_\alpha C_\alpha$, $_\alpha C_\beta$, $_\beta C_\alpha$ and $_\beta C_\beta$ by a factor 10, to a value that they were supposed to have (see (10.11)).

10.3.3.3 Position and rotation estimation results

The measured sensor output voltages in table 10.1 of seven points have been used to test the extracted linear sensor model, via the calculation in (10.2). Four different (de)coupling matrices, all described in table 10.2, have been used for this testing.
The estimation results are shown in table 10.3-10.9.

Table 10.3 Estimation of the top position of the rotor.

Parameter	Measured position / orientation	Estimated position / orientation			
		Situation V	Situation A	Situation B	Situation C
x [μm]	0	11.959	-7.3367	25.260	-3.6325
y [μm]	0	-242.37	6.7312	3.6947	6.3861
z [μm]	185	?	129.47	94.391	125.48
α [°]	0	-906.45	-23.76	18.268	-1.8984
β [°]	0	-92.814	-9.9748	-47.505	-1.4240

Table 10.4 Estimation of the bottom position of the rotor.

Parameter	Measured position / orientation	Estimated position / orientation			
		Situation V	Situation A	Situation B	Situation C
x [μm]	0	-11.911	0.37872	16.139	2.1697
y [μm]	0	141.73	-16.920	-18.388	-17.087
z [μm]	-67.2	?	-82.459	-99.419	-84.386
α [°]	0	489.79	11.643	31.964	1.3952
β [°]	0	16.258	-27.954	-46.100	-3.0016

Table 10.5 Estimation of a position near the operating point.

Parameter	Measured position / orientation	Estimated position / orientation			
		Situation V	Situation A	Situation B	Situation C
x [μm]	10	-8.8521	-7.9115	45.291	-1.8657
y [μm]	-20	-20.341	-32.483	-37.439	-33.047
z [μm]	0	?	-6.3108	-63.561	-12.817
α [°]	0	-184.70	63.216	131.81	7.1011
β [°]	0	37.790	-118.28	-179.53	-12.524

The four "stuck to the stator" positions of the real device are all on the boundary of the horizontal rotor range and therefore interesting to use as testing points. Because the four positions do not exactly match any of the measurement points in the data file, measurement data from points nearest to the four "stuck to the stator" positions is used. Using an interpolation technique is unnecessary since this is only a fast check.

The five measured sensor output voltages at the four positions are shown in table 10.1. In tables 10.6-10.9 the estimation results are presented. For columns 3 the complete coupling matrix is used (situation B). Columns 4 shows the estimation errors for situation B. In columns 5, 6 and 7 the estimation is done with an artificially adapted coupling matrix (see table 10.2).

Table **10.6** Estimation of "stuck to the stator" position 1.

Parameter	Exact value	Estimated value (B)	Difference (error)	Situation V	Situation A	Situation C
x [μm]	60	73.237	13.237	34.576	34.942	39.294
y [μm]	30	40.683	10.683	48.976	44.250	43.844
z [μm]	0	-43.665	-43.665	?	-2.4567	-7.1395
α [°]	0	80.888	80.888	-126.49	31.513	3.7124
β [°]	0	-115.23	-115.23	6.5225	-71.144	-7.6155

Table **10.7** Estimation of "stuck to the stator" position 2.

Parameter	Exact value	Estimated value (B)	Difference (error)	Situation V	Situation A	Situation C
x [μm]	60	72.536	12.536	32.695	33.102	37.583
y [μm]	-70	-62.080	7.9201	-53.153	-58.407	-58.824
z [μm]	0	-45.165	-45.165	?	-2.7305	-7.5526
α [°]	0	81.929	81.929	-126.94	31.085	3.6862
β [°]	0	-117.30	-117.30	4.7743	-71.896	-7.7055

Table **10.8** Estimation of "stuck to the stator" position 3.

Parameter	Exact value	Estimated value (B)	Difference (error)	Situation V	Situation A	Situation C
x [μm]	-40	-32.840	7.1598	-38.484	-39.172	-38.452
y [μm]	-70	-25.098	44.902	-33.387	-24.508	-24.575
z [μm]	0	-2.1984	-2.1984	?	4.6150	3.8408
α [°]	0	73.984	73.984	-142.07	65.820	6.6748
β [°]	0	-79.663	-79.663	87.994	-72.373	-7.3201

Table **10.9** Estimation of "stuck to the stator" position 4.

Parameter	Exact value	Estimated value (B)	Difference (error)	Situation V	Situation A	Situation C
x [μm]	-40	-35.424	4.5760	-36.443	-37.299	-37.086
y [μm]	30	74.798	44.798	63.923	74.973	74.953
z [μm]	0	3.7252	3.7252	?	5.7431	5.5138
α [°]	0	68.374	68.374	-138.45	65.956	6.6231
β [°]	0	-70.056	-70.056	92.588	-67.897	-6.8142

Situation B

Most notable about the estimations obtained with the complete linear decoupling matrix of the sensor (10.19) is that the estimated rotor angles are much too large. They should be equal to zero.

Situation A

Setting the linear sensor parameters $_xC_\alpha$, $_xC_\beta$, $_yC_\alpha$, $_yC_\beta$, $_zC_\alpha$ and $_zC_\beta$ all to 0 has a limited though mostly positive effect on the estimations.
Limited because the parameters that were set to 0 were already very small.
Positive because the ratio between $_\alpha C_\alpha$ and $_\beta C_\beta$ and the 0-parameters was increased

Situation C

The artificial enlargement (10 times larger than actually measured) of the linear sensor model parameters of the rotation sensors not only has a positive effect on the estimation of rotation angles α and β, also the rotor position estimations are improved.

The estimated rotor position and orientation in situation C are clearly the most in accordance with the real position and orientation of the rotor.

Situation V

The omission of the unidentified linear sensor model parameters in the estimation of the horizontal rotor position produces an extra estimation error (Δx, Δy) as is shown in equation (10.22).

$$\begin{pmatrix} \Delta x \\ \Delta y \end{pmatrix} = \begin{pmatrix} {}_xC_x & {}_xC_y \\ {}_yC_x & {}_yC_y \end{pmatrix}^{-1} \begin{pmatrix} \Delta_xV_i \\ \Delta_yV_i \end{pmatrix} = \frac{1}{{}_xC_x{}_yC_y - {}_xC_y{}_yC_x} \begin{pmatrix} {}_yC_y & -{}_xC_y \\ -{}_yC_x & {}_xC_x \end{pmatrix} \begin{pmatrix} {}_xC_zz + {}_xC_\alpha\alpha + {}_xC_\beta\beta \\ {}_yC_zz + {}_yC_\alpha\alpha + {}_yC_\beta\beta \end{pmatrix} \quad (10.22)$$

The effect of equation (10.22) is demonstrated in the estimation of the top- and bottom position of the rotor (respectively table 10.3 and 10.4) where the vertical position of the rotor (z-position) differs from 0.

10.4 Optimization of the linear sensor model

Optimization of the linear sensor model means minimizing the estimation error of all five position- and orientation parameters for the complete range of the rotor, but especially around the operating point.

When the position and orientation sensor is to be used for the actuator calibration measurements, it is necessary that the sensor is accurate over its complete range. For normal operation of the tilting mirror device, the sensor must be accurate around the operating point of the rotor. Far away from the operating point, the controllers of the device should be able to bring the rotor back to its operating point even with only a rough estimation of the rotor position available.

In this subsection two optimization methods will be discussed. The first optimization attempt is done manually and is called the pragmatic approach. The second method does a least squares fit via the Multiple Regression function in MATLAB®.

10.4.1 Pragmatic approach

In section 10.3.1 the sensor calibration measurement data was approximated with linear lines fitted manually. Such a line is described by two parameters: the offset (voltage) and the slope of the line. The slopes of the lines are the linear parameters in coupling matrix of the sensor (10.16).

Figure 10.1 on the next page shows plots of the estimation errors of the rotor position (x, y and z). The plots are created by using the sensor calibration measurement data with only one parameter varied [1, figure 5.30] combined with equation (10.2).

Looking at the estimation errors in figure 10.1.a two things can be done to make the estimation error equal to zero, especially around the operating point of the rotor:
① The difference at the operating point (0 parameter value) can be compensated by adjusting the offset voltage of the respective sensor.
② The (curved) slopes further away from the operating point can be compensated by adjusting the linear parameters in the coupling matrix of the linear sensor model.

For figure 10.1b the earlier determined offset voltages (column 2 of Table 10.1) were slightly changed, based on the estimation errors in figure 10.1a:
- *delta x* is too large in all the a-plots; compensation by enlarging $_xV_0$.
- *delta y* is too small in all the a-plots; compensation by making $_yV_0$ smaller.
- also *delta z* is too small in all the a-plots; compensation by making $_zV_0$ smaller.

The alteration of one offset voltage influences the estimation of all five rotor position and orientation parameters, therefore it was done simultaneously. Keeping in mind the sensitivities of the position sensors (10.17), the new sensor offset voltages become:

$$V_0 = V_{0\_old} + [0.050; -0.050; -0.020; 0; 0] \text{ [V]} \tag{10.23}$$

The alteration of the offset voltages (10.23) has three effects (see figure 10.1 and table 10.10):
❶ The rotor position estimation near operating point is improved. Also the estimation error range is made smaller for the x- and y-position.
❷ The estimation of the z-position has become worse.
❸ The estimation of the seven rotor testing positions (Top position, Bottom position, Operating point and "Stuck to the stator" positions 1-4) in general gets worse.

Table 10.10 Rotor positions estimation errors in figure 10.1.

Position error [μm]	Position x varied				Position y varied				Position z varied			
	0 a.x	0 b.x	Range a.x	Range b.x	0 a.y	0 b.y	Range a.y	Range b.y	0 a.z	0 b.z	Range a.z	Range b.z
Δx	+30	-5	20/38	-15/3	+35	0	34/37	-2/2	+10	-22	0/20	-35/-13
Δy	-40	0	-48/-32	-9/9	-15	24	-22/-10	18/28	-24	20	-34/0	7/38
Δz	-33	-8	-32/-25	-8/0	-42	-16	-44/-40	-18/-13	-10	15	-35/5	-10/30

10.4.2 Least squares linear model fit

A more scientifically based method to make a linear model fit the sensor calibration measurement data, is the least squares method. The Multiple Regression function in MATLAB® [6, 6-19)] can be used to perform a least squares fit.

When each sensor output voltage $_?V_i$ is considered to be a function of five independent variables [x, y, z, α and β], the Multiple Regression function identifies the five linear sensor model parameters [$_?C_x$, $_?C_y$, $_?C_z$, $_?C_α$ and $_?C_β$] (10.1) and the offset voltage $_?V_0$ belonging to that single sensor output voltage.

The Multiple Regression function can be used over the complete rotor range. For a more accurate linear sensor model around the operating point of the rotor, only the calibration measurement data from a small range around the operating point of the rotor should be processed.

10.5 Conclusions

This last section contains a short summarization of chapter 10 and some conclusions.

10.5.1 Test setup sensor calibration measurement

Because expectation values for the linear sensor model of the real prototype were not yet available, no fewer than two sets were obtained in this chapter. The first model was calculated with the ideal sensor model presented in [1]. The second model came from processing the sensor calibration measurement data of the test setup sensor.

Comparison of the ideal linear sensor model and the model extracted from the calibration measurement data of the test setup sensor exposed some deviations.
Especially the extremely low sensitivity of the of the rotation sensor ($_αC_0$ is 31 times too small) cannot be explained and is a problem.

Equation (10.12) shows that the z-translation sensitivity of the horizontal positions sensor output voltages can be used to find the x- and y-coordinates of the operating point of the rotor.

(a.x)

(b.x)

(a.y)

(b.y)

(a.z)

(b.z)
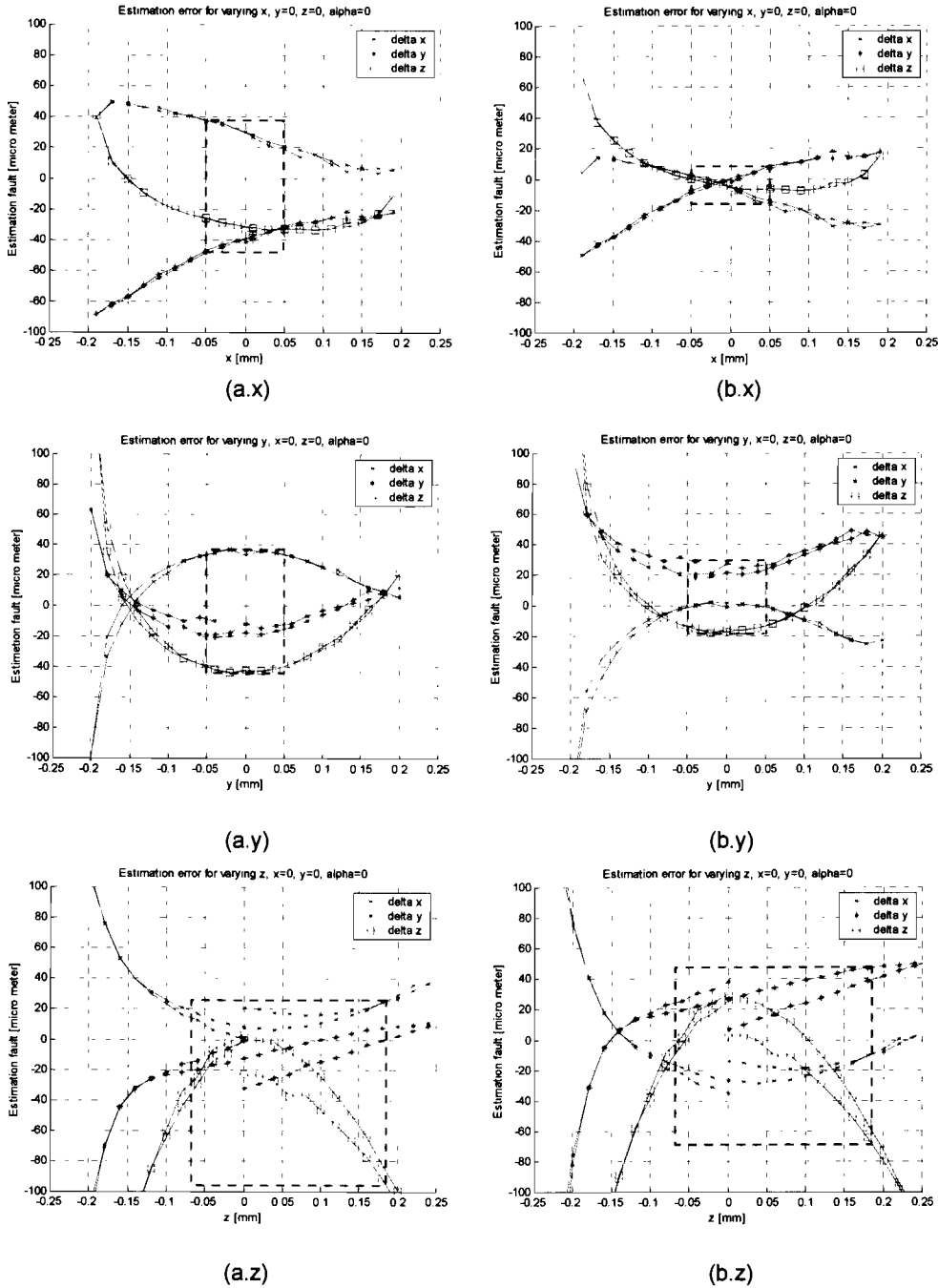
Figure 10.1
Position estimation errors for data of [1, figure 5.30abc].
The area within the red dotted quadrangles represents the real rotor range.
a) Estimation done with the complete $C_{decoupling}$ (10.19) and sensor offset voltages V_0.
b) Estimation done with slightly adjusted offset voltages in an attempt to reduce the estimation errors.
Here $V_0 = V_{0\_old} + [0.050; -0.050; -0.020; 0; 0]$ (10.23).

10.5.2 Linear sensor model testing

Although the linear sensor model testing presented in this chapter has an investigative character, because the used test setup sensor calibration measurement data was incomplete (no β-rotation) and only seven test points were used, it revealed that the estimation of the rotor rotation angles contained an extremely large error.

This problem is most likely caused by the measured low sensitivity of the rotation sensor, which was also used for the β-rotation sensor. An artificial enhancement of the parameters $_aC_a$, $_aC_\beta$, $_\beta C_a$ and $_\beta C_\beta$ (by a factor of 10) improved both the orientation and the position estimations of the sensor.

An attempt to redo the calibration measurements on the test setup sensor, to check the sensitivity and functioning of both rotation sensors, failed. So, this has to be done on the prototype when a calibration setup (chapter 11) is available for it.

10.5.3 Optimization of the linear sensor model

The pragmatic approach (section 10.4.1) for optimizing the sensor offset voltages resulted in theoretical improvement of the estimation results, but when tested on the seven test points it resulted in worse estimations. Changing the offset voltage of one sensor also influences the estimation results of the other sensors. The process of simultaneously optimizing 30 linear sensor model parameters is hard to perform manually.

Automatic optimization can be done by means of a least squares linear model fit (section 10.4.2), for example with the Multiple Regression function in MATLAB®. Depending on the chosen range, the linear sensor model can be optimized around the operating point of the rotor or over the complete range of the sensor.

10.5.4 Overall

It has been shown that a linear sensor model is applicable for the test setup sensor, even though the used calibration measurement data was incomplete and corrupted.

To minimize potential negative effects on the sensor of the prototype, the extraction of its linear sensor model should comply with the following (obvious) conditions:

- A complete sensor calibration measurement must be executed on the real device. This can be done in the same way as was presented [1], including both rotation sensors.

- The linear sensor model parameters must be determined accurately. For example with an automatic least squares data fit.

- Special attention must be paid to the rotation sensors. The rotation sensor electrodes in the real device are shaped differently than those of the test setup and will therefore probably work better. Hopefully, the sensitivity of these rotation sensors will be more in accordance with the expected ones. When this proves not to be the case, the rotation sensor electronics should be checked for malfunctioning.

Chapter 11

Design of a calibration setup for the prototype

The main conclusion in [1] and part 1 of this thesis was to use an external calibration setup to calibrate the sensor (and actuator) system of the prototype. This chapter describes some parts and aspects of the development of such a setup.

11.1 Rotor fixation

To attach an external measurement or calibration device to the rotor, a connection must be made with it. The rotor doesn't seem to be specially equipped or suited to make a connection. Even the promised special holes in the rotor [1, section 9.3.1 and figure E.1] to grab it, are not present.

Still, a connection with the rotor must be developed to be able to keep the rotor in a certain position and orientation inside the stator while calibration measurements are done. Only the top-side of the rotor is freely accessible and therefore suited to make the connection. An extra difficulty is that, unlike the test setup, the rotor cannot be taken out of the stator, unless the stator is disassembled.

11.1.1 Technical demands

Some important technical demands to create an ideal connection with the rotor are:

- The fixation must be in force for all six degrees of freedom of the rotor.

- No movability or flexibility of the connection is allowed. A slightly moved connection results in necessary recalibration. A flexible connection means that the position and orientation of the rotor is not certain within a (small) range, which results in a calibration uncertainty. In practice this means that the connection should be able to withstand (actuator) forces in all possible directions.

- The actuator system and the sensor system of the device should not be disturbed by the connection, because they both need to be calibrated as they are in the original state.

- The total system should not sustain permanent damage by the making or the removing of the connection. After calibration, the system must be restored to its original state.

- The connection must be (easily) detachable.

11.1.2 Fixation methods

Next, a number of common connection or fixation methods and their feasibility on the rotor will be discussed. The methods that seemed to be the most appropriate for this application (vacuum suction and clamping) are investigated more elaborately.

11.1.2.1 Glue

The advantages of a glued connection are that it can be super strong and glue can easily be applied. Ultrasonic sound is used to break the glued connection.
A possible problem with the application of glue on the rotor is that the rotor itself consists of parts that are glued together. When ultrasonic sound is used to break the glued connection, it would also loosen the several rotor parts, which makes the rotor fall apart. That would certainly be permanent damage.

11.1.2.2 Magnetic

A magnetic force could be used to make the rotor connection, because the rotor partially consists of magnetic iron (iron with a high magnetic permeability). A strong enough magnetic source (electromagnet or permanent magnet) to fixate the rotor in all directions must be found.
A possible problem is that the extra magnetic fields can disturb the magnetic actuator system of the device and therefore the calibration of it. However, this still might be an option for only the capacitive sensor calibration.

11.1.2.3 Screw

Another connection method is to make use of screws.
A possible problem with this method is that it is difficult to precisely drill holes and make screw-thread in the loose unsupported rotor. Besides that, the screw-holes can be regarded as damage to the rotor, which is not allowed by the owners of the device (TU/e) as long as another non-damaging method can be used instead. A third problem is that the properties of the system are changed by the screw-holes. This means that the model, and possibly the controllers, of the system have to be adapted also.

To keep the influence of the changes to the system as small as possible, it is important to maintain a symmetrical rotor. This must be kept in mind when the positions of screw-holes are determined. It might be an option to cut a screw-thread on the vertical wall of the cylinder shaped cavity above the mirror. The cavity then becomes one screw hole with a radius of 3 [mm] (size M6) and a height of 0.8 [mm].

11.1.2.4 Weld

A connection with the rotor could be made by welding some metal to the iron top of the rotor. Making the connection should not be a problem. Removal of the connection and bringing the rotor back in the original state without any damage can be difficult.

11.1.2.5 Vacuum

In normal operating conditions the prototype is surrounded by air. On a macroscopic scale the air pressure on the surface of the device results in a pushing force on that surface. This pushing force can be used to make a connection with the rotor by means of a vacuum pump. How this can be done is investigated next.

The principle of vacuum force is based on air pressure and the removal of the air* on one side of an object wall. A vacuum pump can remove air molecules from a confined space, thereby lowering the air pressure. The quality of the pump determines the quality of the vacuum and the minimal obtainable air pressure. The difference in air pressure between the two sides of the object wall results in a force acting on that wall from the high air pressure side to the low air pressure side.

As a calculation example, the box with the gray loose lid in figure 11.1, that serves as a confined space, is contemplated next.

The magnitude of the resulting vacuum force is calculated in formula (11.1).

$$F_{vacuum} = (p_{out} - p_{in}) \cdot A = \Delta p \cdot A \quad [N] \tag{11.1}$$

Where A is the effective area of the gray lid [m^2] and Δp is the difference in air pressure inside and outside the box [N/m^2].

▼ Or any other gas, but the prototype of the tilting mirror is surrounded by normal air.

(a)   (b)   (c)
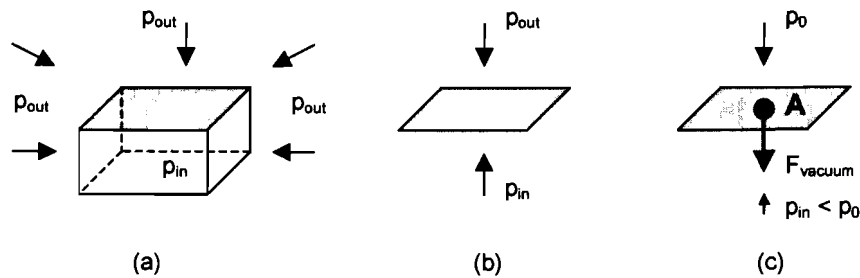
Figure 11.1
a) Simple display of the (homogeneous air) pressure inside (p_{in}) and outside (p_{out}) a box with a gray loose lid.
b) View of the gray lid alone. The two arrows symbolically show the air pressure inside and outside the box. When these two are the same (e.g. both p_0 (11.2)), there is no resulting force on the lid (when gravity is omitted).
c) With vacuum inside the box, ($p_{in} \approx 0$) < ($p_{out} = p_0$) [N/m²]. This situation results in a force on the lid, pushing it on the box.

The numerical value for normal air pressure (p_0) is taken from [5]:

$$p_0 = 1.01325 \cdot 10^5 \text{ [N/m}^2\text{]} \triangleq 10.1 \text{ [N/cm}^2\text{]} \tag{11.2}$$

This is the maximum force that can be exerted by the normal atmospheric air pressure and goes for 100% vacuum ($p_{in} = 0$ [N/m²]).

As formula (11.1) shows, there are two ways to increase the maximum vacuum force:
• artificially increase the air pressure outside the confined vacuum space.
• maximize the effective area A.

The basic horizontal cross-section shape of the rotor is a circular disc, so it seems a logical choice to use a circular shaped vacuum suction area with a radius r_s (see figure 11.2) to connect a vacuum pump to the rotor.
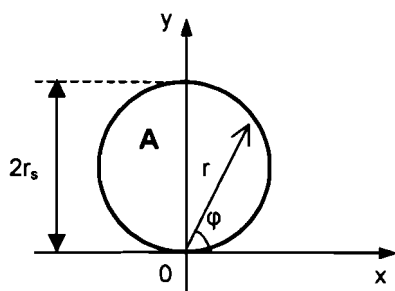
Integration parameters:

$r = \sqrt{(x^2 + y^2)}$
$x = r\cos\varphi$
$y = r\sin\varphi$

$$\tag{11.3}$$

Total area A: $x^2 + (y - r_s)^2 \leq r_s^2$

Figure 11.2
Circular shaped vacuum suction area with a radius r_s. Also depicted are a reference frame and cylinder coordinate parameters that are used for integration.

By using (11.1), the magnitude of the vacuum force on the center of gravity (middle) of the virtual disc is expressed in (11.4).

$$F_{vacuum} = \Delta p \cdot \pi r_s^2 \text{ [N]} \quad \Leftrightarrow \quad r_s = \sqrt{\frac{F_{vacuum}}{\pi \cdot \Delta p}} \text{ [m]} \tag{11.4}$$

The magnitude of the generated vacuum torque on the edge of the disc can be calculated by multiplying the vacuum force (11.4) with the radius of the disc.

$$T_{vacuum} = F_{vacuum} \cdot r_s = \pi \Delta p r_s^3 \quad [Nm]$$ (11.5)

To verify equation (11.5), the magnitude of the generated vacuum torque will also be calculated by means of integration. For this purpose, the border of area A is expressed in integration parameters:

$$x^2 + (y - r_s)^2 = r_s^2 \quad \Rightarrow \quad x^2 + y^2 - 2r_s y + r_s^2 = r_s^2 \quad \Rightarrow \quad x^2 + y^2 = 2r_s y \quad \Rightarrow$$

$$\Rightarrow \quad r^2 = 2r_s r \sin\varphi \quad \Rightarrow \quad r = 2r_s \sin\varphi$$ (11.6)

The integration borders of area A are:

$$0 \le \varphi \le \pi$$
$$0 \le r \le 2r_s \sin\varphi$$ (11.7)

Combining (11.3), (11.6) and (11.7) and integrating over (half of) the total area A results in an expression for the magnitude of the generated vacuum torque:

$$T_{vacuum} = \iint_S y \cdot \Delta p \, dA = \iint_S r\sin\varphi \cdot \Delta p \, r \, dr \, d\varphi = \Delta p \int_{\varphi=0}^{\varphi=\pi} \left[\sin\varphi \int_{r=0}^{r=2r_s\sin\varphi} r^2 \, dr \right] d\varphi =$$

$$= \Delta p \int_{\varphi=0}^{\varphi=\pi} \sin\varphi \left[\tfrac{1}{3}r^3\right]_{r=0}^{r=2r_s\sin\varphi} d\varphi = \Delta p \int_{\varphi=0}^{\varphi=\pi} \tfrac{8}{3}r_s^3 \sin^4\varphi \, d\varphi = \tfrac{8}{3}\Delta p r_s^3 \cdot 2 \cdot \int_{\varphi=0}^{\varphi=\frac{\pi}{2}} \sin^4\varphi \, d\varphi =$$

$$= [3, Standard integral (t.29)] = \tfrac{16}{3}\Delta p r_s^3 \cdot \tfrac{3}{4} \cdot \tfrac{1}{2} \cdot \tfrac{\pi}{2} = \pi \Delta p r_s^3 \quad [Nm]$$ (11.8)

When an almost perfect vacuum is reached inside the vacuum pump and there is an atmospheric air pressure of p_0 outside the pump, Δp in the formulae above can be replaced by p_0 (11.2).

Ideas for practical implementation of rotor connection with vacuum force

A first option is to connect a tube (strong enough not to be deformed when it is used) to a vacuum pump and hold it to the top-side of the rotor to make the vacuum connection. In principle this vacuum connection can then only directly compensate for forces exerted on the rotor in its z-direction. So in this simple situation, the vertical rotor fixation is attained by air pressure.

At the same time, a weaker horizontal rotor fixation is realized by the friction between the contact surfaces of the tube and the rotor. It is hard to determine the maximum friction force (see subsection 11.1.2.6) exactly. A possible rotation in the y-direction is also prevented by the fiction force.

A second option is to make the tube fit tightly in the cylinder shaped cavity above the mirror on the rotor ($r_2 = 3$ [mm], height = 0.8 [mm] see figure and table B.1). The tube then mechanically helps to block rotor rotations and horizontal translations. In this situation, the effective vacuum force area A is limited by $r_s < r_2$.

A third option is to add a suction cup to increase the total effective suction area A.
The suction cup enlarges the effective area A ($r_s < 8$ [mm]) as is demonstrated in figure 11.3.

To investigate the feasibility of a vacuum connection, practical data (see figure 11.4) is gathered from the Internet site of the suction cup and vacuum systems manufacturer **Festo** [W1].

This information indicates limitations of using a vacuum suction cup:

• The effective size (area A) is always smaller than the size of the suction cup.

• The size of the work piece (here the rotor) must be larger than the suction cup.

• The breakaway force (given for 70% vacuum) is smaller than the ideally calculated one (about 20%, as is shown in (11.10)).
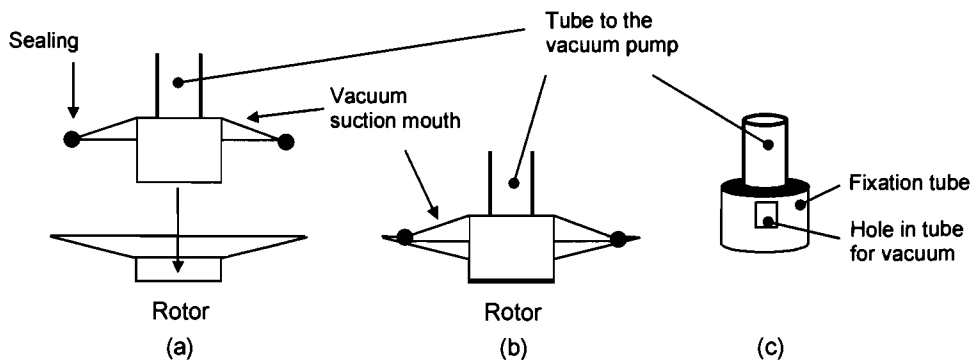
Figure 11.3
Rough vacuum suction mouth design to support the horizontal rotor fixation, by using the vertical wall of the cylinder shaped cavity above the mirror.
a) Vertical cross-section of the rotor and the vacuum suction mouth.
b) Vertical cross-section of the vacuum suction mouth positioned on the rotor. The edge of the mouth is sealed and the fixation tube is inserted in the mirror cavity.
c) 3D sketch of the vacuum tube connected to the fixation tube with special holes that enables vacuum suction under the whole vacuum suction mouth. The hole in the tube is not necessary when only the surface of the mirror is used as effective area A.

The suction cup information displayed in figure 11.4 makes it possible to compare the breakaway force of this practical suction cup with the maximum magnitude of the vacuum force (11.4).
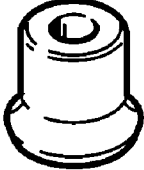
Suction cup 189282 ESS-8-SF		
	Min. workpiece radius	20 [mm]
	Nominal size	2 [mm]
	suction cup diameter	8 [mm]
	suction cup volume	0.03 [cm^3]
	Effective suction diameter	7.2 [mm]
	Design structure	round, standard
	Operating medium	Atmospheric air
	Breakaway force at 70% vacuum	2.3 [N]

Figure 11.4
A selection of practical information about one of the vacuum suction cups of the company Festo AG & Co. KG.

First the air pressure for 70% vacuum must be determined. A 70 % vacuum means that 70% of the air particles is removed from the confined space. The resulting air pressure can be calculated with the general gas-law [5]:

$$\frac{pV}{nT} = R \quad \Rightarrow \quad \left.\frac{p_1 V_1}{n_1 T_1}\right|_{p_1 = p_0} = \frac{p_2 V_2}{n_2 T_2} \qquad (11.9)$$

Where situation 1 is the starting situation (before the vacuum suction process has started) and situation 2 is the situation of the gas during the vacuum suction process.

The volume V, the temperature T and the gas constant R (= 8.3145 $[Jmol^{-1}K^{-1}]$ not needed here) are (almost) the same for both situations (1 and 2), so constant. From (11.9) then follows that p_2 = $p_0(n_2/n_1)$, so the air pressure (p) changes with the same ratio as the number of air particles, during the vacuum suction process.

Using (11.4), (11.9) and filling in p_0 (11.2) and the effective radius r_s (figure 11.4), gives the theoretical maximum magnitude of the vacuum force:

$$F_{vacuum} = \Delta p \cdot \pi r_s^2 = (0.7 \cdot p_0) \cdot \pi \cdot (3.6 \cdot 10^{-3})^2 = 2.88 \quad [N] \tag{11.10}$$

This value is a little bit larger than the typical value supplied by the manufacturer of the suction cup, which is 2.3 [N], probably due to a safety margin.

Besides the practical limitations contemplated above, also some practical problems are expected when a vacuum suction connection is to be used:

- It has to be investigated if a vacuum connection with the rotor can withstand all the forces and torques exerted on the rotor during the sensor (and actuator) calibration process. This will be done in section 11.1.3.

- The suction cup might be flexible, which can result in an unwanted position and orientation tolerance of the rotor.

- The fixation tube designed to provide extra mechanical fixation might be hard, if not impossible, to integrate inside a relatively small suction cup.

- An easy way has to be figured out to reconnect the suction cup each time the device needs (re)calibration. How can possible position or orientation offsets (most likely y-rotation) be avoided or compensated.

11.1.2.6 Clamp

The basic idea for a clamping connection with the rotor comes from [1]. Because there is no space to grab around the whole rotor, it is proposed to use the cylinder shaped cavity above the mirror (figure 11.5).

(a)   (b)
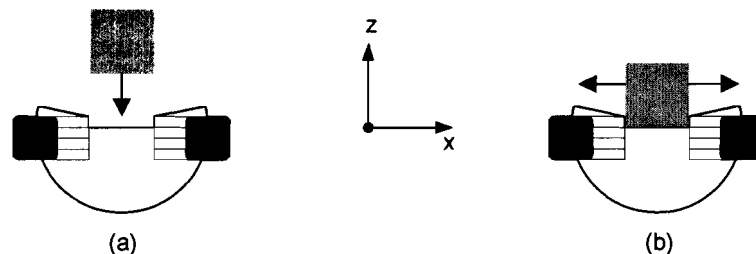
Figure 11.5
Grabbing the rotor by clamping to the upright cavity wall above the mirror.
a) Insertion of the fixation device in the cylinder shaped mirror cavity.
b) Expansion of the fixation device.

Figure 11.5 shows an expandable peg fitting tightly in the mirror cavity. When the peg expands, it applies forces to the upright cavity wall. These contact forces are absorbed by elastic deformation and oppose a sliding motion of the rotor in its vertical direction. Also translation in horizontal directions as well as rotation of the rotor around a horizontal axis are mechanically blocked. Rotation around the z-axis (y-direction) is opposed by the dry friction force between the contacting surfaces, that is caused by the expansion force.

In figure 11.5, the expansion force is pointing perpendicular to the z-axis of the rotor in every horizontal direction away from the z-axis. The resulting force generated by the pressed iron of the rotor is the normal force pointing to the z-axis.

The maximum magnitude of the dry friction force is described by Coulomb's law [8], which was found through experience:

$$F_{friction,max} = \mu_{stat} \cdot F_n \quad [N] \tag{11.11}$$

Where μ_{stat} is the dimensionless coefficient of static friction (typical value $\approx$ 0.15), depending on the two materials making contact and the state (roughness) of their contact surfaces. F_n is the magnitude of the normal force which is a reaction force to the expansion force ($F_{expansion}$), equal in size but acting in the opposite direction.

The maximum friction surface is the surface of the cavity wall above the mirror (see appendix B.1 for rotor dimensions):

$$S = 2\pi \cdot r_{mirror} \cdot h_{cavity} = 2\pi \cdot r_2 \cdot h_2 = 2\pi \cdot 3 \cdot 10^{-3} \cdot 8 \cdot 10^{-4} = 15.08 \ [mm^2] \tag{11.12}$$

Note that the mirror surface itself must be protected and should not be used as friction force surface.

Idea for practical implementation of a clamped rotor connection

The clamping device that has been designed and manufactured for the real prototype is described elaborately in section 11.3. The used expansion principle does not distribute the expansion force equally over the total surface of the cavity wall. That is, closer to the mirror the forces are larger as is exaggeratedly depicted in figure 11.6.

(a)   (b)
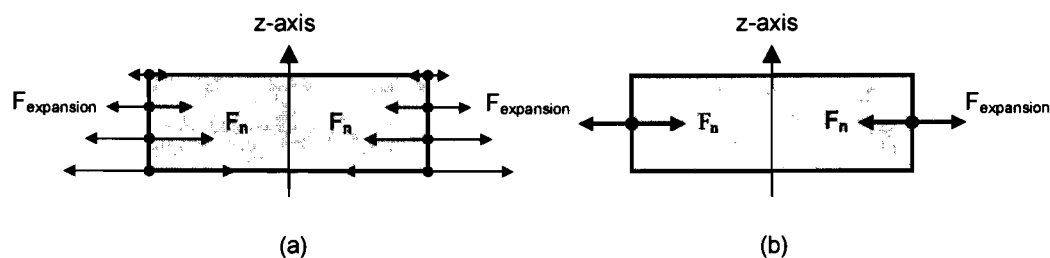
Figure 11.6
Vertical cross-section of mirror cavity showing the expansion force distribution.
a) Expansion force not equally distributed over the total surface of the cavity wall.
b) Average forces, that can be used for calculations.

Some possible practical problems of clamping the rotor inside the mirror cavity are:

- The glued connections between the rotor lamellae must be strong enough to withstand the expansion force in combination with other forces acting on the rotor, like the actuator forces and gravity.

- The maximum expansion forces should not exceed the non-elastic deformation limit of the used materials for the rotor (iron) and expansion peg (still to design).

- The total friction surface (11.12) is very small. Can it prevent the rotor from shifting a little, or even come loose, by the (actuator) forces acting on it during calibration?

11.1.3 Maximum forces and torques to withstand

The rotor connection should be able to withstand the maximum forces (and torques) exerted on the rotor. There are two ways to analyze this: Calculate the minimal connection forces (F_{vacuum} and $F_{expansion}$) needed to maintain the rotor connection during the calibration processes. Or calculate the maximum forces and torques the two connections can withstand for a given connection force (F_{vacuum} or $F_{expansion}$).

The connection to the rotor must compensate the exerted forces and torques on the rotor with reaction forces and torques, otherwise the rotor will move. This condition to keep the rotor in a static equilibrium is shown in the force and torque balances.

Force balance: $$\sum \vec{F}_{rotor} = \vec{F}_g + \sum \vec{F}_{actuators} + \sum \vec{F}_{reaction} = \bar{0}$$ (11.13)

Torque balance: $$\sum \vec{T}_{rotor} = \vec{T}_g + \sum \vec{T}_{actuators} + \sum \vec{T}_{reaction} = \bar{0}$$ (11.14)

11.1.3.1 Calibration situations

For (external) sensor calibration, the electromagnetic actuators of the prototype are off ($I_u = I_v = I_z = I_\alpha = I_\beta = 0$ [A]), so in that situation only two types of forces act on the rotor: the force exerted by gravity $\vec{F}_g$ and the force generated by the permanent magnets $\vec{F}_{u/v,PM}$.

For actuator calibration with a Force/Torque sensor (section 11.2.2), first the rotor is kept in the operating point ($u = v = z = 0$ [m] and $\alpha = \beta = \gamma = 0°$). Then the actuators are activated one by one while the force/torque-sensor measures the exerted forces and torques on the rotor.
As an option this procedure can be repeated with the rotor in any other position than the operating point, to examine the influence of this deviation from the ideal position. Provided that a suited Force/Torque sensor is available and integrated in the measurement setup.

11.1.3.2 Maximum magnitudes of actuator torques

The maximum values of the actuator torques can be derived from the ideal actuator model in [1].

From [1, (6.16)]: $$\left| {}^v_g\vec{T}_u \right| = \sqrt{\tfrac{1}{2}I_{uv}^2 F_u^2 + \tfrac{1}{2}I_{uv}^2 F_u^2} = \sqrt{I_{uv}^2 F_u^2} = I_{uv}F_u$$ (11.15)

From [1, (6.17)]: $$\left| {}^v_g\vec{T}_v \right| = \sqrt{\tfrac{1}{2}I_{uv}^2 F_v^2 + \tfrac{1}{2}I_{uv}^2 F_v^2} = \sqrt{I_{uv}^2 F_v^2} = I_{uv}F_v$$ (11.16)

From [1, (6.16/17)]: $$\left| {}^v_g\vec{T}_u + {}^v_g\vec{T}_v \right| = \sqrt{\left(\frac{-I_{uv}}{\sqrt{2}}(F_u + F_v) \right)^2 + \left(\frac{I_{uv}}{\sqrt{2}}(F_u - F_v) \right)^2} = I_{uv}\sqrt{F_u^2 + F_v^2}$$ (11.17)

From (5.2), which is a correction for [1, (6.22)]:

$$\left| {}^v_g\vec{T}_z \right| = \sqrt{(-\tfrac{1}{2}I_z F_z \sin\alpha)^2 + (-\tfrac{1}{2}I_z F_z \sin\beta)^2} = \tfrac{1}{2}I_z F_z \sqrt{(\sin^2\alpha + \sin^2\beta)}$$ (11.18)

These are all torques with their rotation axis in the xy-plane, so they can be used for a 2D analysis.

11.1.3.3 Vertical rotor fixation with a vacuum connection

The most critical to investigate is the vacuum connection and especially its vertical rotor fixation. The vacuum force connection should be able to withstand the forces on the rotor in the prototype. These forces are caused by gravity, the permanent magnets and the electromagnetic coils. To investigate this demand, a 3D force vector analysis (as described in [1, chapter 6]) is necessary for all rotor positions within the rotor range.

To avoid unnecessary complicated calculations, first will be started with a simple 2D force analysis with the rotor in its operation point. Because when the vacuum force connection does not hold in this situation, it is not feasible at all.

For sensor calibration, the electromagnetic actuators of the prototype are off, so in that situation only two types of forces act on the rotor: the gravity force and the force generated by the permanent magnets.

In the ideal case, the permanent magnet forces will equalize each other when the rotor is in its operating position. The magnitude of the gravity force can be calculated with the gravitational acceleration $g = 9.81$ [m/s^2] and the mass of the rotor (table 5.1).

$$F_g = m_{ROTOR} \cdot g = 8.49 \cdot 10^{-3} \cdot 9.81 = 83.29 \text{ [mN]} \tag{11.19}$$

In the operating point of the rotor, this gravity force acts on the work-line through the center of the suction disc area. When also the actuator system is to be calibrated, via for example a Force/Torque sensor (see section 11.2.2), the vacuum connection must be able to withstand the maximum actuator forces together with gravity. An ideal theoretical value for the maximum vertical actuator force $F_{z,max} = 1.92$ [N] (G.9) has been calculated. However in chapter 7 of this thesis, the processing of the available (inaccurate and flawed) sensor- and actuator calibration measurements resulted in a smaller expectation value for the maximum vertical actuator force:

$$F_{z,max,expected} = 0.107 \cdot 2.5 = 0.27 \text{ [N] (see table 7.6).} \tag{11.20}$$

The minimal surface radius to withstand the maximum vertical actuator forces and gravity (11.19) can be calculated with formula (11.4) as is shown in (11.21).

$$F_{vacuum} = \Delta p \cdot \pi r_s^2 = F_{z,total} \quad \Leftrightarrow \quad r_{s,min} = \sqrt{\frac{F_{z,total}}{\pi \cdot \Delta p}} = \sqrt{\frac{F_{z,max} + F_g}{\pi \cdot \Delta p}} \quad \text{[m]} \tag{11.21}$$

The vertical actuators can also be used as torque actuators. A large torque force on the rotor could pull it loose from the vacuum pump, see figure 11.7.

(a)   (b)
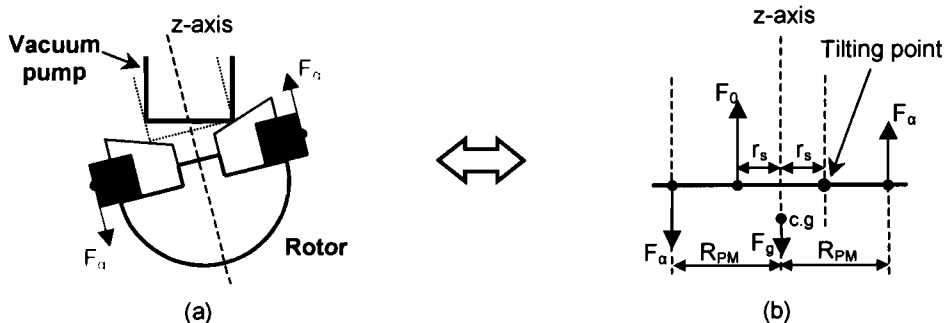
Figure 11.7
a) Schematic vertical cross-section of rotor and vacuum pump. The rotor is pulled loose from the pump by the torque actuator T_a.
b) Force diagram for situation (a), showing the two actuator forces F_a, the tilting point and the torque force F_0 "generated" by the vacuum pump.

The magnitude of the gravity torque with respect to the tilting point in figure 11.7b can be calculated using the magnitude of the gravity force F_g (11.19).

$$T_g = r_s \cdot F_g \quad [Nm] \tag{11.22}$$

An ideal theoretical value for the maximum torque of one actuator $T_{\alpha/\beta,max} = 9.6 \cdot 10^{-3}$ [Nm] (G.12) has been calculated. However in chapter 7 of this thesis, the processing of the available (inaccurate and flawed) calibration measurements resulted in a smaller expectation value for the maximum actuator torque:

$$T_{\alpha/\beta,max,expected} = 0.882 \cdot 10^{-3} \cdot 2.5 = 2.21 \cdot 10^{-3} \text{ [Nm] (see table 7.6)}. \tag{11.23}$$

Figure 11.8 shows that when the two rotation actuators are used simultaneously, the torque is doubled, but the effective arm decreases with a factor $\frac{1}{2}\sqrt{2}$, so the maximum torque magnitude of the two actuators together is:

$$T_{\alpha+\beta} = \frac{1}{2}\sqrt{2} \cdot 2 \cdot T_{\alpha/\beta} = \sqrt{2} T_{\alpha/\beta} \quad [Nm] \tag{11.24}$$
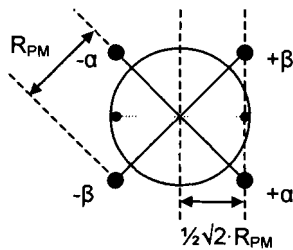
Figure 11.8
Top-view of the rotor, showing the effective torque arm (red) when both rotation actuators (α and β) are working in the same direction, at the same time.

The minimal surface radius $(r_{s,min})$ to withstand the maximum vertical actuator torques and gravity (11.19) can be calculated with formula (11.5) as is shown in (11.25).

$$T_{vacuum} = \pi \cdot \Delta p \cdot r_s^3 = T_{total,max} \Leftrightarrow r_{s,min} = \sqrt[3]{\frac{T_{total,max}}{\pi \cdot \Delta p}} = \sqrt[3]{\frac{(T_{actuator,max} + T_g)}{\pi \cdot \Delta p}} \quad [m] \tag{11.25}$$

The magnitude of the maximum vacuum force F_0 on the edge of the circular shaped suction area can be derived from (11.5).

$$F_0 = \frac{T_{vacuum}}{2r_s} = \frac{\pi \cdot \Delta p \cdot r_s^3}{2r_s} = \frac{\pi}{2} \Delta p \cdot r_s^2 \quad [N] \tag{11.26}$$

The previously derived formulae can be used in two ways:
❶ Directly calculate the minimum radius r_s that is necessary to withstand gravity and the actuator forces.
❷ Choose a suitable radius r_s for the suction mouth of the vacuum pump. Calculate the maximum (actuator) forces and torques that a connection with this radius can withstand. Make sure that during utilization of the vacuum force connection these maximum values are not exceeded.

11.1.4 Choice of the rotor fixation method

After the short orienting investigation in the previous subsections, a clamp connection to fixate the rotor is preferred to a vacuum connection for the following reasons:
- A clamp connection seems the most simple to design, manufacture and use.
- No permanent extra devices (like a vacuum pump and suction cup) are needed.
- It can be build and installed by the Technical Service of the E-department.
- A clamp connection is more likely to provide a non-flexible rotor fixation.
- The available rotation micro-manipulator provides a limited amount of vertical space between it and the rotor (36 [mm]).

11.2 Possible calibration setup features

11.2.1 Link to the measurement device

The link between the rotor and the calibration setup can have several functions, depending on its construction.

A **rigid link** can be used for the capacitive sensor calibration.

A **flexible link in one direction** can be used for the horizontal actuator calibration with the back EMF method [1, 4.10.3]. A practical implementation of this link could be a vertical thin plate that is (limited) bendable in the u-direction and is stiff in the v-direction or vise versa.

For controller testing a link that provides **free movement in one (or more) direction while blocking (stabilizing) the other DOF** could be useful.

11.2.2 Force/Torque sensor integration

The use of an Force/Torque sensor is an interesting option because it not only enables the calibration of the complete actuator system, it also makes it possible to measure the forces generated by each individual electromagnetic coil.

The Internet web-site Sensor Show [W2] contains links to manufacturers of several sensor systems. The links are sorted by sensor type. The available force sensors are reviewed for important properties like their size, range, number of axis, Force and Torque measurement, resolution, accuracy, sensitivity, stiffness, repeatability, (non)linearity, overload capacity, bandwidth, speed, compensation for temperature effects and whether it is easy to mount.

Only two of the found manufacturers seem to produce appropriate sensors:

Bokam Engineering Inc. [W3]
Product: F-sensors that can measure three perpendicular forces (F_x, F_y and F_z).
Price: $ 500 (sensor alone)

Actuator torques can't be measured with these sensors. Though it is possible to measure the force of the rotation actuators in pairs of two (exited in the same direction) and calculate the generated torque from this measurement.

ATI Industrial Automation [W4]
Product: F/T-sensors (transducers) that can measure three forces and three torques (F_x, F_y, F_z, T_x, T_y and T_z). The sensors are all cylinder shaped. The smallest one is of the type Nano17. It measures ($\varnothing$ 17 [mm], height = 14.5 [mm]). The sensor is available in different ranges that are all covered by the 16-bits of the data acquisition system, which means that the sensor with the smallest range has the highest resolution.

To choose the sensor with the appropriate specifications, it is necessary to know the maximum forces and torques that are to be measured. Table 7.6 combined with the maximum actuator currents I_{max} = 2.5 [A] and the maximum rotor position u_{max} = 50 [µm] gives the maximum forces and torques that are expected to be measured based on the actuator calibration attempt in [1].
Appendix G provides the maximum forces and torques that are calculated based on the corrected ideal actuator model (chapter 3).

The datasheet of the Nano17 multi-axis Force/Torque sensor of ATI is printed in appendix K. Although expected to be smaller, the modeled forces ask for the sensor with the second smallest range (SI-25-0.25), which still has sufficient resolution. Table 11.1 gives an overview.

Table 11.1 Actuator forces and F/T sensor (Nano17 SI-25-0.25) properties.

Parameter	Maximum actuator outputs		Sensor inputs (DAQ)	
	Modeled	"Measured"	Maximum	Resolution
$F_{u,genrated}$ [N]	8.66	2.78	25	1/320
$F_{u,destab}$ [N]	5.25	0.556	25	1/320
F_z [N]	1.92	0.268	35	1/640
$T_{\alpha/\beta}$ [Nmm]	9.6	2.205	250	1/128
T_y [Nmm]			250	1/128

There are some aspects about the use of this sensor:

* The price of a complete package including a transducer interface, cables, a data acquisition PC-card, software and documentation is: $ 6175 + $350 for the temperature compensation option (transportation, insurance and import taxes not included). This means that it is not economically responsible to purchase the sensor and accessories for only a one time use on this project. It might be useful to check if some similar sensor is already available somewhere on the TU/e campus.

* The delivery time is normally 4-6 weeks (could be faster).

* It is not clear if the nearest associated company (Schunk Intec, Germany) can provide technical assistance.

Note that this information dates from the beginning of the year 2002. Nowadays, developments may have led to better and cheaper sensors being available.

11.2.3 Rotor release mechanism

The basic function of the sensor calibration setup, to stabilize the rotor, could be used to avoid the lift-off problem of the rotor at the start-up of the prototype. The idea is to use the calibration setup to hold the rotor in its operating point, activate the sensors and controllers of the device and then somehow disconnect the rotor from the calibration setup, leaving it free of contact, while the device is active. This way it can be checked if the controllers are able to keep the rotor in its operating point, without first having to pull it loose from the stator. A special rotor release mechanism should be designed for this purpose.

11.3 The expansion-gripper

In subsection 11.1.4 it was decided to first try to implement a clamp connection with the rotor that stabilizes it inside the stator by exerting an expansion force (section 11.1.6) on the wall of the cavity above the mirror on the rotor with a 3 [mm] radius and a height of 0.8 [mm]. In this section the design of an expansion-gripper and its integration in a calibration setup for the sensor of the prototype is presented.

11.3.1 The design

The original thought was to design a setup for the complete calibration of the sensor and actuators of the prototype and incorporate all the possible features (section 11.2), like the optional flexible link, a Force/Torque sensor, a rotor release mechanism and a special double rotation table, which enables the calibration of both rotation directions without having to re-install the rotor fixation.

The designing started with the connection, the most important aspect. The designed clamp connection is based on the one that is commonly used for the handle-bar of a bicycle. The micro-manipulators of the test setup sensor, which had the basic (minimal) function of two horizontal translations, one vertical translation and one rotation, were still available. The idea was to start with this setup and try to further expand and adjust the design to accommodate the extra features. Unfortunately, due to the limited means: available equipment, (human) resources, time and mechanical engineering experience, the extra features could not be realized.
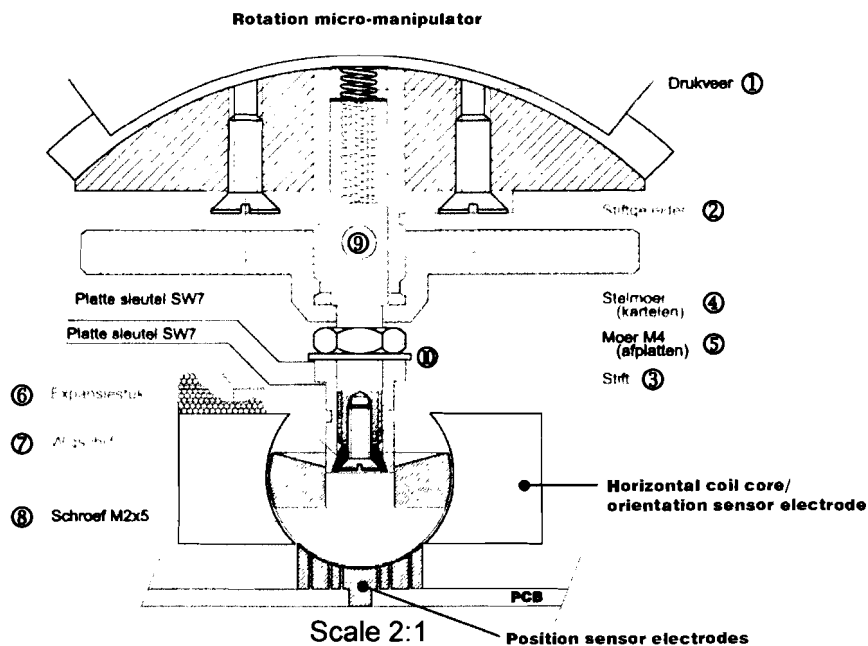
Figure 11.9
Vertical cross-section view of the designed expansion-gripper, installed between the rotation micro-manipulator (top) and the rotor inside the prototype (bottom).
In Dutch, see table 11.2 for English naming for the corresponding part numbers.

Figure 11.9 shows the final expansion-gripper design as part of the sensor calibration setup for the prototype. A detailed view of the parts of the expansion-gripper and the complete sensor calibration setup can be found in the blue-prints in appendix I. An overview of the separate parts and their function is given in table 11.2.

Table 11.2 Parts of the expansion-gripper and their function.

Part number	Part name	Function
①	Coil spring	Holds the pin (③) in place.
②	Pin-guider	Fixates the main pin (③) in the horizontal rotor directions (u and v) and enables it to slide in the vertical rotor direction (z).
③	Pin	Connection rod between the rotor and the micro-manipulator.
④	Adjustment wheel	Adjusts the length of the total expansion-gripper device to make it equal to the rotation radius of the micro-manipulator, which is 36 [mm]. It compensates for the length increase when the expansion nut (⑤) is screwed down.
⑤	M4 7mm Nut	Controls the expansion force applied on the rotor. Turning it down (counter clockwise) increases the expansion. Turning it up (clockwise) decreases the expansion.
⑥	Expansion piece	When this part is pushed down by the nut (⑤), its separated expansion legs are pushed outwards by the wedge-disc inside it. This way, the expansion-gripper clamps to the vertical wall of the cavity above the mirror on the rotor. The top of this part is also a six sided 7 [mm] nut head, which can be used to hold this part in place with a picklock during installation.
⑦	Wedge-disc	Conical shaped piece that drives the legs of the expansion piece (⑥) outwards.
⑧	M2x5 Screw	Screw that connects the wedge-disc to the main pin, so that parts ③, ⑦ and ⑥ become one part. This construction is necessary to manufacture and install the expansion-gripper.
⑨	Range blocking pin	Limits the vertical range to ±1 [mm] and avoids rotation around the z-axis of the rotor.
⑩	Washer	Smoothens the tightening of the nut (⑤) that controls the expansion force.

11.3.2 Dimensioning of the design

Because of the low level of complexity of the design, the dimensioning of it was done at sight. This means that it must be checked if the total calibration setup functions properly, so that necessary corrections can be made before the expansion-gripper is manufactured. The installation and assembly of the calibration setup must be possible and it must have sufficient range to calibrate the capacitive sensor system of the prototype.

Installation

Only two parts don't have dimensions in appendix figure I.2: the height of the washer (⑩) and the M4 7mm Nut (⑪) together must not exceed 3 [mm].

Horizontal range

The horizontal rotor range is $d_{max} = \sqrt{2} \cdot 50$ [μm] (4.17), which is far less than the available space between the expansion piece (⑥) and the horizontal coil-cores (see figure 11.9). So horizontal rotor movements are not restricted by the calibration setup.

Vertical range

The range of the rotor in its vertical direction is not limited by the calibration setup. The vertical rotor range of the prototype is calculated in appendix H.

Rotation range

The rotor rotation could possibly be blocked by three contact points (figure 11.10). Based on the dimensions of the calibration setup (appendix I), these points are calculated using geometry and (inverse) circular functions.
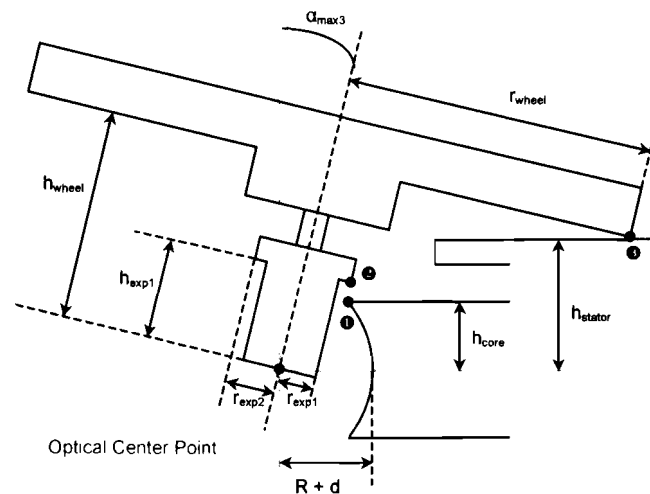
Figure 11.10
Sketch of the calibration setup showing three possible contact points (❶, ❷ and ❸) that limit the rotation range of the rotor around the Optical Center Point.

The numerical values for the parameters in figure 11.10 are taken from appendix I: $h_{exp1} = 8$ [mm], $h_{core} = 5.5$ [mm], $r_{exp1} = 3$ [mm], $r_{exp2} = 3.5$ [mm], rotor radius $R = 8$ [mm], the nominal air gap $d = 0.25$ [mm], $h_{stator} = 10$ [mm], $r_{wheel} = 25$ [mm] and $h_{wheel} = 17$ [mm].

Contact point ❶: the base of the expansion piece (⑥) contacts the horizontal coil-core.

$$\alpha_{max1} = 90° - \arcsin\left(\frac{r_{exp1}}{R+d}\right) - \arcsin\left(\frac{h_{core}}{R+d}\right) = 26.87° \tag{11.13}$$

This contact point is positioned at a height of $h_{contact}$ above the mirror surface:

$$h_{contact} = \sqrt{(R+d)^2 - r_{exp1}^2} = 7.69 \text{ [mm]} \tag{11.14}$$

Contact point ❷: the top of the expansion piece (⑥) contacts the top-side of the horizontal coil-core.

$$\alpha_{max2} = 90° - \arctan\left(\frac{r_{exp2}}{h_{exp1}}\right) - \arcsin\left(\frac{h_{core}}{\sqrt{h_{exp1}^2 + r_{exp2}^2}}\right) = 27.33° \tag{11.15}$$

Contact point ❸: the adjustment wheel (④) contacts the top-ring of the stator.

$$\alpha_{max3} = 90° - \arcsin\left(\frac{h_{stator}}{\sqrt{r_{wheel}^2 + h_{wheel}^2}}\right) - \arcsin\left(\frac{r_{wheel}}{\sqrt{r_{wheel}^2 + h_{wheel}^2}}\right) = 14.9° \tag{11.16}$$

It is clear that the radius of the adjustment wheel determines the maximum rotation range and that the top of the expansion piece (⑥) cannot contact the top-side of the horizontal coil-core (situation ❷), because $\alpha_{max3} < \alpha_{max1} < \alpha_{max2}$. The radius of the adjustment wheel (④), $r_{wheel} = 25$ [mm], was chosen because the wheel must be large enough to be turned by hand. The wheel limits the calibration rotation range to approximately 15°, which is enough.

Note that the rotation range becomes smaller when a horizontal translation is executed at the same time.

11.3.3 Assembly and Installation of the expansion-gripper

The sensor calibration setup with the expansion-gripper is depicted in appendix figure I.1 and figure 11.9. This subsection contains instructions how to assemble and install the expansion-gripper in the calibration setup.

Assembly program/order:

- First turn the z-position micro-manipulator up to its maximum position, to make enough space to install the separate pieces. Then detach the corner-support, with the rotation micro-manipulator attached to it, from the z-position micro-manipulator.

- Attach the pin-guider (②) with the two screws to the rotation micro-manipulator.

- Put in the coil spring (①) and also insert the main pin (③) in the pin-guider.

- Position the main pin such that the hole for the range blocking pin (⑨) is aligned with the slot for it in the pin-guider.

- Insert the range blocking pin (⑨).

- Now the main pin cannot get out of the pin-guider, although it is pushed by the coil spring to the maximum range of +1 [mm].

- Put on the adjustment wheel (④) and turn it till the range blocking pin is in the middle of its range (-1,+1) [mm].

- Turn the expansion nut (⑤) on the main pin as far as possible.

- Slide the washer (⑩) on the tip of the main pin, followed by the expansion piece (⑥).

- Lastly, screw (⑧) the wedge-disc (⑦) onto the main pin.

Now the expansion nut (⑤) can be turned down a little bit till there is no space left between it and the expansion piece, without letting the expansion piece expand. Mount the corner-support, with the rotation micro-manipulator, and now also the expansion-gripper attached to it, back on the z-position micro-manipulator.

When the expansion-gripper is assembled it is ready for installation:

First turn the z-micro-manipulation table of the calibration setup down, and align the tip of the expansion-gripper with the cavity above the mirror on the rotor. Then gently insert the tip of the expansion-gripper into the cavity. Make sure it touches the mirror and that it is positioned perpendicular to the mirror. Now tighten the expansion nut (⑤) by turning it clockwise with a picklock, while holding the expansion piece (⑥) in place with another picklock, to avoid rotation around the z-axis of the rotor.

Disassembly:

Execute the assembly program in reverse order.

11.3.4 Points of attention

Some practical problems are expected when this clamp connection is to be used:

- The expansion nut (⊚) must be tightened very carefully, because it is hard to determine when the expansion force is sufficient and the surplus force starts to deform the materials.

- Rotor movements must be blocked during the installation of the expansion-gripper. Maybe a special tool must be developed to accomplished this.

Chapter 12

Control

Reviewing [1] in part 1 of this thesis revealed that next to the lacking (and essential) sensor calibration some other problems (electrical wires to sensors and/or actuators might be wrongly connected and the controllers were tested on a flawed and incomplete (no gravity) SIMULINK® model) might also have contributed to the fact that the instability problem of the tilting mirror prototype was not solved.

The combination of these three problems makes that the chosen control strategy (part 1 section 6.2) can't be written off yet, which is also confirmed by literature (see the additional literature list in section 14.2.1) wherein the classical PID control approach is successfully applied to similar magnetic devices.

This chapter starts with the calculation of the linear model approximation of the device with the rotor in its operating point: the center of the stator. In [1] the linear model is presented in numerical form. Here, gravity is added to the model and the flaws (Part 1) are removed from the model. The model will be expressed in device parameters.

Secondly, as part of a MIMO systems analysis, the Relative Gain Array (RGA) is calculated to investigate if the actuator system was justly considered fully decoupled in [1]. In principle the actuators of the device were designed to function decoupled. Unfortunately, the center of gravity does not coincide with the optical center point and not with some points of attack of actuator forces. Also the introduction of gravity to the model gives some unwanted coupling between the vertical actuators and the horizontal rotor positions. These effects are represented as non-diagonal terms in the transfer function matrix G(s) op the linearized system.

Lastly the controllers for the device [1] are adapted, based on the corrected actuator gains (Part 1). Because there is no report on the tuning of the controllers in [1], this will be tried first (section 12.4) before using other control techniques. In the first instance the controllers from [1] are adapted (not fully redesigned) based on the linear model that is calculated in section 12.1. Of course, the other problems must be solved before the adapted controllers can be tested on the real device. Therefore, the adapted controllers are tested on the corrected and supplemented SIMULINK® model first.

12.1 Linear model calculation

Based on the corrected actuator models (Part 1, chapter 3) and the equations of motion [1, (6.1)-(6.3)] of the rotor, a linear model approximation of the non-linear tilting mirror prototype can be calculated. The linear model will be expressed in device parameters, which provides insight for control engineering and facilitates the implementation of improvements for possible future prototype designs.

12.1.1 Notation

Throughout this chapter, the notation for the force/torque vectors ($_2^1\bar{F}_3$) and the position/orientation

parameters ($_2^1x_3$) from [1] is used.

The prefix and suffix in this notation have the following meaning:
1: Vector/parameter expressed in the static stator frame (0) or rotating rotor frame (V).
2: The center of gravity of the rotor (g) or the optical center point of the mirror (o).
3: Name of the parameter.

12.1.2 System description

An elaborate description of the tilting mirror prototype can be found throughout this thesis and in [1]. In this chapter the prototype is regarded as a plant (or system) with five outputs (12.2) that are to be controlled via its five inputs (12.1). The sixth DOF, the y-rotation around the z-axis, is omitted because this DOF is presumed to be passively damped.

For a (linear) state variable model description, the system must be described with three sets of variables, namely the inputs, states and outputs of the system. The inputs of the system are the actuator currents:

Inputs: $\bar{u} = (I_x, I_y, I_z, I_\alpha, I_\beta)^T$ (12.1)

The outputs of the system are the position and orientation of the optical center point of the mirror, which is positioned above the center of gravity:

Outputs: $\bar{y} = ({}^0_0x, {}^0_0y, {}^0_0z, {}^0_0\alpha, {}^0_0\beta)^T$ (12.2)

The states of the system are the position, orientation and speed of the center of gravity of the rotor:

States: $\bar{x} = ({}^0_gx, {}^0_gy, {}^0_gz, {}^0_g\alpha, {}^0_g\beta, {}^0_g\dot{x}, {}^0_g\dot{y}, {}^0_g\dot{z}, {}^0_g\dot{\alpha}, {}^0_g\dot{\beta})^T$ (12.3)

Normal operation of the device means that the optical center point of mirror must be kept in center of stator:

$$({}^0_0x = 0; {}^0_0y = 0; {}^0_0z = 0)$$ (12.4)

The mirror tilting angles are variable to set the deflection angles of the mirror to any value within the range [-22.5°, +22.5°]:

$$({}^0_0\alpha = \alpha_{target}; {}^0_0\beta = \beta_{target})$$ (12.5)

Throughout this subsection some device parameters are used in the linear model functions. For convenience they are repeated below in table 12.1. The values for the rotor parameters are the corrected ones taken from table 5.1.

Table 12.1 Device parameters that are used in this subsection.

Parameter	Function	Value
J [Wb] or [Vs]	Permanent magnet flux	$1.6 \cdot 10^{-5}$
N_{HC} [turns]	Number of horizontal coil turns	42
d_{plus} [m]	Nominal air gap with insulation rings (eq. (3.8))	$2.77 \cdot 10^{-4}$
μ_0 [H/m]	Permeability of vacuum	$4\pi \cdot 10^{-7}$
A_{HC} [m²]	Horizontal coil core cross-section surface	$2.88 \cdot 4.8 \cdot 10^{-6}$
N_{VC} [turns]	Number of vertical coil turns	150
l_{VC} [m]	Length of one vertical coil	$12.9 \cdot 10^{-3}$
R [m]	Rotor radius (at Permanent Magnet)	$10 \cdot 10^{-3}$
g [m/s²]	Gravitational acceleration	9.81
l_{cg} [m]	Vertical position of center of gravity of the rotor with respect to the optical center point of the mirror	$-1.4 \cdot 10^{-3}$
l_{uv} [m]	Distance between point of attack of the horizontal force actuators and the center of gravity of the rotor	$1.03 \cdot 10^{-3}$
l_z [m]	Distance between point of attack of the vertical force actuator and the center of gravity of the rotor	$0.75 \cdot 10^{-3}$
m_{ROTOR} [kg]	Mass of the rotor	$8.49 \cdot 10^{-3}$
J_x [kgm²]	Moment of inertia around the rotor x-axis	$2.21 \cdot 10^{-7}$
J_y [kgm²]	Moment of inertia around the rotor y-axis	$2.21 \cdot 10^{-7}$

12.1.3 Operating point

In addition to the demand that the rotor is kept in the middle of the stator during normal operation of the device (12.4), for the operating point the tilting angles are chosen to be also equal to 0 (so that the mirror is orientated horizontally).

So, the **operating point** is chosen to be:

$$\overline{y}_{op} = (^0_0x, {}^0_0y, {}^0_0z, {}^0_0\alpha, {}^0_0\beta)^T = \overline{0} \tag{12.6}$$

Note that (12.6) also sets the position and orientation of the center of gravity of the rotor.

12.1.4 Approximations near the operating point

In the operating point (12.6), the reference frame of the moving rotor (V-frame) and the world fixed reference frame (0-frame) coincide.

So then $^0_g\overline{F} = {}^V_g\overline{F}$ and $^0_g\overline{T} = {}^V_g\overline{T}$ (see equations (J.1) and (J.5)) $\tag{12.7}$

The conversion of the Bryant angles (Φ, θ, Ψ) [1, chapter 2] to the mirror tilting angles (α, β) for small angles is given by:

$$\Phi = \alpha \tag{12.8}$$
$$\theta = \arctan(\tan\beta\cos\alpha) \approx \arctan(\tan\beta) = \beta \quad \text{(with } \alpha \approx 0 \text{ then } \cos \alpha \approx 1) \tag{12.9}$$
$$\Psi = 0 \text{ (The rotation around the z-axis of the rotor will be neglected in this analysis)}$$

12.1.5 Equilibrium conditions

To obtain an equilibrium in the operating point, the following must hold:
The speed, acceleration, angular speed and angular acceleration of the rotor must be equal to 0 in the fixed world frame (0-frame).

Substitution of these conditions in the *Euler Equations of Motion* [1, (6.1)-(6.3)] leaves one resulting equation: (12.10). This equation shows that in the ideal device only the gravity force has to be counteracted by the actuator system (z-force actuator) to keep the rotor in its operating point:

$$F_z = D_1 I_z = F_g = m_{ROTOR}\cdot g \quad \Rightarrow \quad I_{z0} = \frac{m_{ROTOR}\cdot g}{D_1} = \frac{g}{{}_I K_z} \tag{12.10}$$

To meet the equilibrium conditions and keep the rotor in the operating point, the input currents of the prototype must be:

$$\overline{u}_{op} = (I_{x0}, I_{y0}, I_{z0}, I_{\alpha0}, I_{\beta0}) = (0, 0, I_{z0}, 0, 0) \tag{12.11}$$

Where I_{z0} (12.10) is the vertical actuator current necessary to overcome gravity.

12.1.6 Equations of motion for the center of gravity of the rotor

The *Euler Equations of Motion* [1, (6.1) – (6.3)] describe the resulting movement of the center of gravity of the rotor, caused by the actuator forces (J.1), actuator torques (J.5) and gravity (J.4) acting on it. Filling in that the initial rotor translation- and rotation speeds are all equal to 0, which is the equilibrium condition (section 12.1.4) for the operating point (section 12.1.2) of the rotor, reduces the equations of motion to:

$$
\begin{pmatrix} {}_g^0\ddot{x} \\ {}_g^0\ddot{y} \\ {}_g^0\ddot{z} \end{pmatrix} = \frac{1}{m_{ROTOR}}\left({}_g^0\vec{F}\right) = \frac{1}{m_{ROTOR}}\left({}^0R_V \cdot {}_g^V\vec{F}_{act} + {}_g^0\vec{F}_g\right) = \frac{1}{m_{ROTOR}} \cdot \begin{pmatrix} {}_g^0F_x \\ {}_g^0F_y \\ {}_g^0F_z \end{pmatrix} \quad \text{[m/s}^2\text{]}
\tag{12.12}
$$

$$
\begin{pmatrix} {}_g^0\ddot{\alpha} \\ {}_g^0\ddot{\beta} \\ {}_g^0\ddot{\gamma} \end{pmatrix} = {}_g^0\vec{T} \cdot \begin{pmatrix} 1/J_x \\ 1/J_y \\ 1/J_z \end{pmatrix} = {}^0R_V \cdot {}_g^V\vec{T}_{act} \cdot \begin{pmatrix} 1/J_x \\ 1/J_y \\ 1/J_z \end{pmatrix} = \begin{pmatrix} {}_g^0T_x/J_x \\ {}_g^0T_y/J_y \\ {}_g^0T_z/J_z \end{pmatrix} \quad \text{[rad/s}^2\text{]}
\tag{12.13}
$$

12.1.7 System outputs: position of optical center point

The prototype of the tilting mirror system is designed such that the position of the optical center point of the mirror, which is measured, doesn't coincide with the center of gravity of the rotor. Transformation [1, (6.23)] can be used backwards to calculate the position of the optical center point of the mirror by combining the position of the center of gravity of the rotor and the orientation of the rotor:

$$
{}_o^0\bar{y} = {}_g^0\bar{x} - {}^0R_V\bar{l}_{cg} = {}_g^0\bar{x} - {}^0R_V\begin{pmatrix} 0 \\ 0 \\ l_{cg} \end{pmatrix} \quad \text{with } (l_{cg} < 0)
\tag{12.14}
$$

A linear approximation of the system outputs (12.14) can be calculated by using the transformation matrix ${}^0R_V$ [1, (2.6)], the Bryant angle conversions for small angles (12.8) and (12.9) and the small angle approximation formulae for the circular functions sine and cosine:

$$
\sin(k) \approx k \text{ and } \cos(k) \approx 1 \qquad \text{for parameter } k \approx 0
\tag{12.15}
$$

Then:

$$
{}_o^0x = {}_g^0x - l_{cg}\sin\theta \approx {}_g^0x - l_{cg}\sin\beta \approx {}_g^0x - l_{cg}\beta
\tag{12.16}
$$

$$
{}_o^0y = {}_g^0y - l_{cg}(-\cos\theta\sin\varphi) \approx {}_g^0y + l_{cg}\cos\beta\sin\alpha \approx {}_g^0y + l_{cg}\alpha
\tag{12.17}
$$

$$
{}_o^0z = {}_g^0z - l_{cg}(\cos\theta\cos\varphi) \approx {}_g^0z - l_{cg}\cos\beta\cos\alpha \approx {}_g^0z - l_{cg}
\tag{12.18}
$$

The orientation of the optical center point is the same as that of the center of gravity of the rotor, since the difference between these two points is only a translation along the z-axis of the rotor (over a distance $-l_{cg}$), so:

$$
{}_o^0\alpha = {}_g^0\alpha
\tag{12.19}
$$

$$
{}_o^0\beta = {}_g^0\beta
\tag{12.20}
$$

12.1.8 Linearization by first order Taylor series approximation

In general the equations of motion to be linearized are non-linear functions of the position and orientation of the rotor and the actuator input currents:

$$
f(x, y, z, \alpha, \beta, I_x, I_y, I_z, I_\alpha, I_\beta) = f(\bar{y}, \bar{u})
\tag{12.21}
$$

The first order Taylor series approximation [9] of the function f (12.21) around the operating point ($\bar{y}_{op}$ (12.6) and $\bar{u}_{op}$ (12.11)), for the small deviations $\Delta\bar{y} = (\Delta x, \Delta y, \Delta z, \Delta\alpha, \Delta\beta)$ and $\Delta\bar{u} = (\Delta I_x, \Delta I_y, \Delta I_z, \Delta I_\alpha, \Delta I_\beta)$, is given by:

$$\hat{f}(\overline{y}_{op} + \Delta\overline{y}, \overline{u}_{op} + \Delta\overline{u}) = f(\overline{y}_{op}, \overline{u}_{op}) + \left.\frac{\partial f}{\partial x}\right|_{\substack{\overline{y}=\overline{y}_{op}\\ \overline{u}=\overline{u}_{op}}} \Delta x + \left.\frac{\partial f}{\partial y}\right|_{\substack{\overline{y}=\overline{y}_{op}\\ \overline{u}=\overline{u}_{op}}} \Delta y + \left.\frac{\partial f}{\partial z}\right|_{\substack{\overline{y}=\overline{y}_{op}\\ \overline{u}=\overline{u}_{op}}} \Delta z + \left.\frac{\partial f}{\partial \alpha}\right|_{\substack{\overline{y}=\overline{y}_{op}\\ \overline{u}=\overline{u}_{op}}} \Delta\alpha +$$

$$+ \left.\frac{\partial f}{\partial \beta}\right|_{\substack{\overline{y}=\overline{y}_{op}\\ \overline{u}=\overline{u}_{op}}} \Delta\beta + \left.\frac{\partial f}{\partial I_x}\right|_{\substack{\overline{y}=\overline{y}_{op}\\ \overline{u}=\overline{u}_{op}}} \Delta I_x + \left.\frac{\partial f}{\partial I_y}\right|_{\substack{\overline{y}=\overline{y}_{op}\\ \overline{u}=\overline{u}_{op}}} \Delta I_y + \left.\frac{\partial f}{\partial I_z}\right|_{\substack{\overline{y}=\overline{y}_{op}\\ \overline{u}=\overline{u}_{op}}} \Delta I_z + \left.\frac{\partial f}{\partial I_\alpha}\right|_{\substack{\overline{y}=\overline{y}_{op}\\ \overline{u}=\overline{u}_{op}}} \Delta I_o + \left.\frac{\partial f}{\partial I_\beta}\right|_{\substack{\overline{y}=\overline{y}_{op}\\ \overline{u}=\overline{u}_{op}}} \Delta I_\beta \qquad (12.22)$$

This is only a first order approximation, which means that the higher order terms are neglected.

12.1.9 Linearization of the equations of motion

12.1.9.1 Differentiation of multiplied matrices: the chain rule

The chain rule for differentiation of a vector product, $\overline{a} \cdot \overline{b}$, is [4]:

$$\frac{d}{dt}(\overline{a} \cdot \overline{b}) = \frac{d\overline{a}}{dt} \cdot \overline{b} + \overline{a} \cdot \frac{d\overline{b}}{dt} \qquad (12.23)$$

This rule can be used for matrices which can be seen as a stack of vectors, as is shown in (12.25). First consider the 3x3 matrix R and the 3x1 vector $\overline{b}$ as stated in (12.24):

$$\text{If} \qquad R = \begin{pmatrix} R_{11} & R_{12} & R_{13} \\ R_{21} & R_{22} & R_{23} \\ R_{31} & R_{32} & R_{33} \end{pmatrix} = \begin{pmatrix} \overline{r}_1 \\ \overline{r}_2 \\ \overline{r}_3 \end{pmatrix} \qquad \text{and} \qquad \overline{b} = \begin{pmatrix} b_1 \\ b_2 \\ b_3 \end{pmatrix} \qquad (12.24)$$

$$\text{Then:} \qquad \frac{d(R \cdot \overline{b})}{dk} = \frac{d\begin{pmatrix} \overline{r}_1 \cdot \overline{b} \\ \overline{r}_2 \cdot \overline{b} \\ \overline{r}_3 \cdot \overline{b} \end{pmatrix}}{dk} = \begin{pmatrix} \dfrac{d\overline{r}_1}{dk} \cdot \overline{b} + \overline{r}_1 \cdot \dfrac{d\overline{b}}{dk} \\ \dfrac{d\overline{r}_2}{dk} \cdot \overline{b} + \overline{r}_2 \cdot \dfrac{d\overline{b}}{dk} \\ \dfrac{d\overline{r}_3}{dk} \cdot \overline{b} + \overline{r}_3 \cdot \dfrac{d\overline{b}}{dk} \end{pmatrix} = \frac{dR}{dk} \cdot \overline{b} + R \cdot \frac{d\overline{b}}{dk} \qquad (12.25)$$

12.1.9.2 Linear approximation of the force vector

The chain rule (12.25) can be applied to calculate the first order derivatives of the force vector (J.1):

$$\frac{\partial_g^0 \overline{F}}{\partial k} = \frac{\partial(^0 R_v \cdot {}_g^v \overline{F}_{act})}{\partial k} + \frac{\partial_g^0 \overline{F}_g}{\partial k} = \frac{\partial^0 R_v}{\partial k} \cdot {}_g^v \overline{F}_{act} + {}^0 R_v \cdot \frac{\partial_g^v \overline{F}_{act}}{\partial k} + \frac{\partial_g^0 \overline{F}_g}{\partial k} \qquad (12.26)$$

The actual calculation of the first order derivatives of all the components of equation (12.26) is presented in appendix J. The resulting first order Taylor series approximation (12.22) of the force vector in the operating point of the rotor (12.6) is given below.

$$\Delta_g^0 \overline{F}_{act}\Big|_{\substack{\overline{y}=\overline{y}_{op}\\ \overline{u}=\overline{u}_{op}}} = \begin{pmatrix} m_{ROTOR} g \cdot \Delta\beta \\ -m_{ROTOR} g \cdot \Delta\alpha \\ 0 \end{pmatrix} + \begin{pmatrix} C_1 \cdot \Delta x - \frac{1}{2} m_{ROTOR} g \cdot \Delta\beta + A_1 \cdot \Delta I_x \\ C_1 \cdot \Delta y + \frac{1}{2} m_{ROTOR} g \cdot \Delta\alpha + A_1 \cdot \Delta I_y \\ D_1 \cdot \Delta I_z \end{pmatrix} + \begin{pmatrix} 0 \\ 0 \\ 0 \end{pmatrix} \qquad (12.27)$$

12.1.9.3 Linear approximation of the torque vector

The chain rule (12.25) can be applied to calculate the first order derivatives of the torque vector (J.5):

$$\frac{\partial {}^0_g\bar{T}}{\partial k} = \frac{\partial({}^0R_v \cdot {}^v_g\bar{T}_{act})}{\partial k} = \frac{\partial {}^0R_v}{\partial k} \cdot {}^v_g\bar{T}_{act} + {}^0R_v \cdot \frac{\partial {}^v_g\bar{T}_{act}}{\partial k} \tag{12.28}$$

The actual calculation of the first order derivatives of all the components of equation (12.28) is presented in appendix J. The resulting first order Taylor series approximation (12.22) of the torque vector in the operating point of the rotor (12.6) is given below.

$$\Delta {}^0_g\bar{T}\Big|_{\substack{\bar{y}=\bar{y}_{op} \\ \bar{u}=\bar{u}_{op}}} = \begin{pmatrix} -I_{uv}C_1 \cdot \Delta y - \frac{1}{2}I_z m_{ROTOR}g \cdot \Delta\alpha - I_{uv}A_1 \cdot \Delta I_y + E_1 \cdot \Delta I_\alpha \\ I_{uv}C_1 \cdot \Delta x - \frac{1}{2}I_z m_{ROTOR}g \cdot \Delta\beta + I_{uv}A_1 \cdot \Delta I_x + E_1 \cdot \Delta I_\beta \\ 0 \end{pmatrix} \tag{12.29}$$

12.1.10 State Variable Model expressed in device parameters

Now the first order Taylor series approximations of the force vector (12.27) and the torque vector (12.29), both acting on the center of gravity of the rotor, can be filled in the equations of motion (12.12) and (12.13) of the rotor. The result is a linear model approximation of the device in its operating point. Since the operating point (12.6) is $\bar{0}$, the Δ-parameters can be replaced by the actual parameters, except for ΔI_z, which is indicated in (12.30) and (12.31).

$$\Delta\bar{x} = (\Delta x, \Delta y, \Delta z, \Delta\alpha, \Delta\beta)^T = \bar{x} - \bar{x}_{op} \stackrel{\triangle}{=} (x, y, z, \alpha, \beta)^T \tag{12.30}$$

$$\Delta\bar{u} = (\Delta I_x, \Delta I_y, \Delta I_z, \Delta I_\alpha, \Delta I_\beta)^T = \bar{u} - \bar{u}_{op} \stackrel{\triangle}{=} (I_x, I_y, \hat{I}_z = I_z - I_{z0}, I_\alpha, I_\beta)^T \tag{12.31}$$

The resulting model is presented below (12.32) in the standard State Space Model format.

$$\dot{\bar{x}} = A\bar{x} + B\bar{u}$$
$$\bar{y} = C\bar{x} + D\bar{u} \tag{12.32}$$

Where the State Space Matrices (**A**, **B**, **C** and **D**) are:

A =

$$\begin{bmatrix} 0 & 0 & 0 & 0 & 0 & 1 & 0 & 0 & 0 & 0 \\ 0 & 0 & 0 & 0 & 0 & 0 & 1 & 0 & 0 & 0 \\ 0 & 0 & 0 & 0 & 0 & 0 & 0 & 1 & 0 & 0 \\ 0 & 0 & 0 & 0 & 0 & 0 & 0 & 0 & 1 & 0 \\ 0 & 0 & 0 & 0 & 0 & 0 & 0 & 0 & 0 & 1 \\ {}_xK_x & 0 & 0 & 0 & {}_xK_\beta & 0 & 0 & 0 & 0 & 0 \\ 0 & {}_yK_y & 0 & {}_yK_\alpha & 0 & 0 & 0 & 0 & 0 & 0 \\ 0 & 0 & 0 & 0 & 0 & 0 & 0 & 0 & 0 & 0 \\ 0 & {}_\alpha K_y & 0 & {}_\alpha K_\alpha & 0 & 0 & 0 & 0 & 0 & 0 \\ {}_\beta K_x & 0 & 0 & 0 & {}_\beta K_\beta & 0 & 0 & 0 & 0 & 0 \end{bmatrix} =$$

$$\begin{bmatrix} 0 & 0 & 0 & 0 & 0 & 1 & 0 & 0 & 0 & 0 \\ 0 & 0 & 0 & 0 & 0 & 0 & 1 & 0 & 0 & 0 \\ 0 & 0 & 0 & 0 & 0 & 0 & 0 & 1 & 0 & 0 \\ 0 & 0 & 0 & 0 & 0 & 0 & 0 & 0 & 1 & 0 \\ 0 & 0 & 0 & 0 & 0 & 0 & 0 & 0 & 0 & 1 \\ \dfrac{2J^2}{\mu_0 A_{HC} d_{plus} m_{ROTOR}} & 0 & 0 & 0 & g/2 & 0 & 0 & 0 & 0 & 0 \\ 0 & \dfrac{2J^2}{\mu_0 A_{HC} d_{plus} m_{ROTOR}} & 0 & -g/2 & 0 & 0 & 0 & 0 & 0 & 0 \\ 0 & 0 & 0 & 0 & 0 & 0 & 0 & 0 & 0 & 0 \\ 0 & \dfrac{-2I_{uv}J^2}{\mu_0 A_{HC} d_{plus} J_x} & 0 & \dfrac{-I_z m_{ROTOR}g}{2J_x} & 0 & 0 & 0 & 0 & 0 & 0 \\ \dfrac{2I_{uv}J^2}{\mu_0 A_{HC} d_{plus} J_y} & 0 & 0 & 0 & \dfrac{-I_z m_{ROTOR}g}{2J_y} & 0 & 0 & 0 & 0 & 0 \end{bmatrix}$$

$$\tag{12.33}$$

$$
B = \begin{bmatrix}
0 & 0 & 0 & 0 & 0 \\
0 & 0 & 0 & 0 & 0 \\
0 & 0 & 0 & 0 & 0 \\
0 & 0 & 0 & 0 & 0 \\
0 & 0 & 0 & 0 & 0 \\
_xK_{Ix} & 0 & 0 & 0 & 0 \\
0 & _yK_{Iy} & 0 & 0 & 0 \\
0 & 0 & _zK_{Iz} & 0 & 0 \\
0 & _\alpha K_{Iy} & 0 & _\alpha K_{I\alpha} & 0 \\
_\beta K_{Ix} & 0 & 0 & 0 & _\beta K_{I\beta}
\end{bmatrix}
=
\begin{bmatrix}
0 & 0 & 0 & 0 & 0 \\
0 & 0 & 0 & 0 & 0 \\
0 & 0 & 0 & 0 & 0 \\
0 & 0 & 0 & 0 & 0 \\
0 & 0 & 0 & 0 & 0 \\
\dfrac{2JN_{HC}}{d_{plus}{}^m ROTOR} & 0 & 0 & 0 & 0 \\
0 & \dfrac{2JN_{HC}}{d_{plus}{}^m ROTOR} & 0 & 0 & 0 \\
0 & 0 & \dfrac{4JN_{VC}}{^l vc^m ROTOR} & 0 & 0 \\
0 & \dfrac{-2JN_{HC}{}^l uv}{d_{plus}{}^J x} & 0 & \dfrac{2RJN_{VC}}{^l vc^J x} & 0 \\
\dfrac{2JN_{HC}{}^l uv}{d_{plus}{}^J y} & 0 & 0 & 0 & \dfrac{2RJN_{VC}}{^l vc^J y}
\end{bmatrix}
\tag{12.34}
$$

$$
C = \begin{bmatrix}
1 & 0 & 0 & 0 & -l_{cg} & 0 & 0 & 0 & 0 & 0 \\
0 & 1 & 0 & l_{cg} & 0 & 0 & 0 & 0 & 0 & 0 \\
0 & 0 & 1 & 0 & 0 & 0 & 0 & 0 & 0 & 0 \\
0 & 0 & 0 & 1 & 0 & 0 & 0 & 0 & 0 & 0 \\
0 & 0 & 0 & 0 & 1 & 0 & 0 & 0 & 0 & 0
\end{bmatrix}
\tag{12.35}
$$

$$
D = \begin{bmatrix}
0 & 0 & 0 & 0 & 0 \\
0 & 0 & 0 & 0 & 0 \\
0 & 0 & 0 & 0 & 0 \\
0 & 0 & 0 & 0 & 0 \\
0 & 0 & 0 & 0 & 0
\end{bmatrix}
\tag{12.36}
$$

The used device parameters are presented in table 12.1.

12.1.11 Resulting transfer functions in the Laplace domain

The transfer functions from the inputs of the system $\bar{u} = (I_x, I_y, \hat{I_z}, I_\alpha, I_\beta)$ to the outputs of the system $\bar{y} = (_o^0 x, _o^0 y, _o^0 z, _o^0 \alpha, _o^0 \beta)$ can be derived from the State Space Model above (12.32)-(12.36), using the *Laplace* transform with the initial conditions (start values in the time domain) of these parameters.

The initial conditions of the optical center point of the mirror are:

$$
(_o^0 x(0) = 0, _o^0 y(0) = 0, _o^0 z(0) = 0, _o^0 \alpha(0) = 0, _o^0 \beta(0) = 0)
\tag{12.37}
$$

The initial conditions of the center of gravity of the rotor are:

$$
(_g^0 x(0) = 0, _g^0 y(0) = 0, _g^0 z(0) = l_{cg}, _g^0 \alpha(0) = 0, _g^0 \beta(0) = 0)
\tag{12.38}
$$

and

$$
(_g^0 \dot{x}(0) = 0, _g^0 \dot{y}(0) = 0, _g^0 \dot{z}(0) = 0, _g^0 \dot{\alpha}(0) = 0, _g^0 \dot{\beta}(0) = 0)
\tag{12.39}
$$

The resulting transfer functions in the *Laplace* domain are presented next.

The x-coordinate of the optical center point of the mirror:

$$
X(s) = \frac{_xK_{Ix}}{(s^2 - _xK_x)} I_x(s) + \left(\frac{_xK_\beta}{(s^2 - _xK_x)} - l_{cg} \right) \beta(s)
\tag{12.40}
$$

Equation (12.40) expressed in device parameters (table 12.1) is:

$$X(s) = \frac{\left(\dfrac{2JN_{HC}}{d_{plus}m_{ROTOR}}\right)}{\left(s^2 - \dfrac{2J^2}{\mu_0 A_{HC} d_{plus} m_{ROTOR}}\right)}I_x(s) + \left[\frac{\left(\dfrac{g}{2}\right)}{\left(s^2 - \dfrac{2J^2}{\mu_0 A_{HC} d_{plus} m_{ROTOR}}\right)} - I_{cg}\right]\beta(s) \tag{12.41}$$

The y-coordinate of the optical center point of the mirror:

$$Y(s) = \frac{{}_yK_{ly}}{(s^2 - {}_yK_y)}I_y(s) + \left(\frac{{}_yK_\alpha}{(s^2 - {}_yK_y)} + I_{cg}\right)\alpha(s) \tag{12.42}$$

Equation (12.42) expressed in device parameters (table 12.1) is:

$$Y(s) = \frac{\left(\dfrac{2JN_{HC}}{d_{plus}m_{ROTOR}}\right)}{\left(s^2 - \dfrac{2J^2}{\mu_0 A_{HC} d_{plus} m_{ROTOR}}\right)}I_y(s) - \left[\frac{\left(\dfrac{g}{2}\right)}{\left(s^2 - \dfrac{2J^2}{\mu_0 A_{HC} d_{plus} m_{ROTOR}}\right)} - I_{cg}\right]\alpha(s) \tag{12.43}$$

The z-coordinate of the optical center point of the mirror:

$$Z(s) = \frac{{}_zK_{lz}}{s^2}\hat{I}_z(s) = \frac{\left(\dfrac{4JN_{VC}}{I_{VC}m_{ROTOR}}\right)}{s^2}\hat{I}_z(s) \tag{12.44}$$

The tilting angle α around the x-axis of the mirror:

$$\alpha(s) = \frac{{}_\alpha K_{I\alpha}}{(s^2 - {}_\alpha K_\alpha)}I_\alpha(s) + \frac{{}_\alpha K_y}{(s^2 - {}_\alpha K_\alpha)}Y(s) + \frac{{}_\alpha K_{ly}}{(s^2 - {}_\alpha K_\alpha)}I_y(s) \tag{12.45}$$

Equation (12.45) expressed in device parameters (table 12.1) is:

$$\alpha(s) = \frac{\left(\dfrac{2RJN_{VC}}{I_{VC}J_x}\right)}{\left(s^2 + \dfrac{I_z m_{ROTOR}g}{2J_x}\right)}I_\alpha(s) + \frac{\left(\dfrac{-2I_{uv}J^2}{\mu_0 A_{HC} d_{plus} J_x}\right)}{\left(s^2 + \dfrac{I_z m_{ROTOR}g}{2J_x}\right)}Y(s) + \frac{\left(\dfrac{-2JN_{HC}I_{uv}}{d_{plus}J_x}\right)}{\left(s^2 + \dfrac{I_z m_{ROTOR}g}{2J_x}\right)}I_y(s) \tag{12.46}$$

The tilting angle β around the y-axis of the mirror:

$$\beta(s) = \frac{{}_\beta K_{I\beta}}{(s^2 - {}_\beta K_\beta)}I_\beta(s) + \frac{{}_\beta K_x}{(s^2 - {}_\beta K_\beta)}X(s) + \frac{{}_\beta K_{lx}}{(s^2 - {}_\beta K_\beta)}I_x(s) \tag{12.47}$$

Equation (12.47) expressed in device parameters (table 12.1) is:

$$\beta(s) = \frac{\left(\dfrac{2RJN_{VC}}{I_{VC}J_y}\right)}{\left(s^2 + \dfrac{I_z m_{ROTOR}g}{2J_y}\right)}I_\beta(s) + \frac{\left(\dfrac{2I_{uv}J^2}{\mu_0 A_{HC} d_{plus} J_y}\right)}{\left(s^2 + \dfrac{I_z m_{ROTOR}g}{2J_y}\right)}X(s) + \frac{\left(\dfrac{2JN_{HC}I_{uv}}{d_{plus}J_y}\right)}{\left(s^2 + \dfrac{I_z m_{ROTOR}g}{2J_y}\right)}I_x(s) \tag{12.48}$$

12.1.12 Linear model transfer function matrix

The transfer functions in the previous section (12.40)-(12.48) can be rewritten in the structure of (12.49), where all outputs (12.2) are expressed solely in inputs (12.1).

$$\overline{Y}(s) = G(s)\overline{U}(s) \tag{12.49}$$

The result is (12.50):

$$
\begin{pmatrix} X(s) \\ Y(s) \\ Z(s) \\ \alpha(s) \\ \beta(s) \end{pmatrix} =
\begin{pmatrix}
G_{11}(s) & 0 & 0 & 0 & G_{15}(s) \\
0 & G_{22}(s) & 0 & G_{24}(s) & 0 \\
0 & 0 & G_{33}(s) & 0 & 0 \\
0 & G_{42}(s) & 0 & G_{44}(s) & 0 \\
G_{51}(s) & 0 & 0 & 0 & G_{55}(s)
\end{pmatrix}
\cdot
\begin{pmatrix} I_x(s) \\ I_y(s) \\ \hat{I}_z(s) \\ I_\alpha(s) \\ I_\beta(s) \end{pmatrix}
\tag{12.50}
$$

Where

$$
G_{11}(s) = \frac{s^2\left({}_xK_{Ix} - I_{cg\cdot\beta}K_{Ix}\right) + \left(-{}_xK_{Ix\cdot\beta}K_\beta + {}_xK_{\beta\cdot\beta}K_{Ix} + I_{cg\cdot x}K_{x\cdot\beta}K_{Ix}\right)}{s^4 + s^2\left(-{}_xK_x - {}_\beta K_\beta + I_{cg\cdot\beta}K_x\right) + \left({}_xK_{x\cdot\beta}K_\beta - {}_xK_{\beta\cdot\beta}K_x - I_{cg\cdot x}K_{x\cdot\beta}K_x\right)}
\tag{12.51}
$$

$$
G_{15}(s) = \frac{s^2\left(-I_{cg\cdot\beta}K_{I\beta}\right) + \left({}_xK_{\beta\cdot\beta}K_{I\beta} + I_{cg\cdot x}K_{x\cdot\beta}K_{I\beta}\right)}{s^4 + s^2\left(-{}_xK_x - {}_\beta K_\beta + I_{cg\cdot\beta}K_x\right) + \left({}_xK_{x\cdot\beta}K_\beta - {}_xK_{\beta\cdot\beta}K_x - I_{cg\cdot x}K_{x\cdot\beta}K_x\right)}
\tag{12.52}
$$

$$
G_{22}(s) = \frac{s^2\left({}_yK_{Iy} + I_{cg\cdot\alpha}K_{Iy}\right) + \left(-{}_yK_{Iy\cdot\alpha}K_\alpha + {}_yK_{\alpha\cdot\alpha}K_{Iy} - I_{cg\cdot y}K_{y\cdot\alpha}K_{Iy}\right)}{s^4 + s^2\left(-{}_yK_y - {}_\alpha K_\alpha - I_{cg\cdot\alpha}K_y\right) + \left({}_yK_{y\cdot\alpha}K_\alpha - {}_yK_{\alpha\cdot\alpha}K_y + I_{cg\cdot y}K_{y\cdot\alpha}K_y\right)}
\tag{12.53}
$$

$$
G_{24}(s) = \frac{s^2\left(I_{cg\cdot\alpha}K_{I\alpha}\right) + \left({}_yK_{\alpha\cdot\alpha}K_{I\alpha} - I_{cg\cdot y}K_{y\cdot\alpha}K_{I\alpha}\right)}{s^4 + s^2\left(-{}_yK_y - {}_\alpha K_\alpha - I_{cg\cdot\alpha}K_y\right) + \left({}_yK_{y\cdot\alpha}K_\alpha - {}_yK_{\alpha\cdot\alpha}K_y + I_{cg\cdot y}K_{y\cdot\alpha}K_y\right)}
\tag{12.54}
$$

$$
G_{33}(s) = \frac{{}_zK_{Iz}}{s^2}
\tag{12.55}
$$

$$
G_{42}(s) = \frac{1}{\left(s^2 - {}_\alpha K_\alpha\right)}\left[{}_\alpha K_{Iy} + {}_\alpha K_y \cdot G_{22}(s)\right]
\tag{12.56}
$$

$$
G_{44}(s) = \frac{1}{\left(s^2 - {}_\alpha K_\alpha\right)}\left[{}_\alpha K_{I\alpha} + {}_\alpha K_y \cdot G_{24}(s)\right]
\tag{12.57}
$$

$$
G_{51}(s) = \frac{1}{\left(s^2 - {}_\beta K_\beta\right)}\left[{}_\beta K_{Ix} + {}_\beta K_x \cdot G_{11}(s)\right]
\tag{12.58}
$$

$$
G_{55}(s) = \frac{1}{\left(s^2 - {}_\beta K_\beta\right)}\left[{}_\beta K_{I\beta} + {}_\beta K_x \cdot G_{15}(s)\right]
\tag{12.59}
$$

In appendix L, three sets of numerical values of the transfer functions (12.51)-(12.59), the elements of G(s), can be found. Each set belongs to one of the three actuator models as described in Part 1 of this thesis: the ideal model in [1], the corrected ideal model (Part 1, chapter 3) and the model based on the actuator calibration measurement in [1] (expected model in Part 1, chapter 7). See table 12.2.

12.2 Coupled MIMO system analysis

When a system has multiple inputs that can influence multiple of its outputs, it is a coupled MIMO system. The analysis of controlled MIMO systems is the subject of [10], from which the information in this subsection is largely taken from.

12.2.1 Control design methods

For MIMO systems it is not always necessary to use more than one input to control one output of a system, like with **full multivariable control** or **centralized control**. Under certain conditions (e.g. when a system is approximately diagonal dominant), decentralized control can be used.

Decentralized control is defined in [10] as when the control system consists of independent feedback controllers which interconnect a subset of the output measurements/commands with a subset of manipulated inputs. These subsets should not be used by any other controller.

When the transfer matrix G(s) of a system is not a diagonal matrix, decentralized control becomes a two step controller design method:

Step ❶ a) Design pre-compensators for decoupling control; or
   b) An appropriate input-output pairing must be chosen (e.g. by using the RGA matrix (section 12.2.2) to decide which output is to be controlled by which input).

Step ❷ Design decentralized feedback controllers to control the system.

There are three controller design strategies [10] for decentralized control:
① *Fully coordinated design:* all controllers are designed simultaneously.
② *Independent design:* all the controllers are designed one by one.
③ *Sequential design:* The controllers are designed one at the time with the previous controllers implemented.

A number of conditions for stability[v] and performance[vv] of decentralized control systems can be found in [10], along with sensitivity and controllability analyses.

12.2.2 Relative Gain Array (RGA) matrix

The Relative Gain Array (RGA) matrix is a tool to evaluate a MIMO system. The mathematical formula to calculate the RGA matrix is given by [10]:

$$RGA(G(s)) = \Lambda(G) \triangleq G \times (G^{-1})^T \tag{12.60}$$

Where $\times$ denotes element-by-element multiplication (the Hadamard or Schur product). With MATLAB®, (12.60) is written as:

$$RGA = G.*inv(G).' \tag{12.61}$$

The original interpretation of the RGA matrix (12.60) is to see its elements as an interaction measure between the various inputs and outputs of a multivariable plant. The elements of the RGA matrix (12.61) are:

$$\lambda_{ij} = g_{ij}/\hat{g}_{ij} \tag{12.62}$$

---

[v] **Stability** questions are:
- Is stability guaranteed for the complete operating range of the system?
- Does the system remain stable as the gain in various loops is reduced (detuned) by an arbitrary factor? (Complete detunability)
- Does the complete system remain stable when one or more controllers fall-out (e.g. by input saturation)?

[vv] **Performance** loss by not directly controlling the non-diagonal elements in G(s).

Each RGA matrix element λ_{ij} (12.62) is the ratio between the open-loop gain (g_{ij}) and the closed-loop gain ($\hat{g}_{ij}$) for the corresponding input-output pair. Where in this application "closed-loop" means partial control with the other outputs perfectly controlled.

The elements of the RGA matrix have the following properties:
- Large RGA elements indicate strong interactions.
- Negative RGA elements indicate a gain change between the open-loop and closed-loop transfer functions, which is incompatible with integral action.
- RGA elements that are close to 1 indicate the best input-output pairing for decentralized control[v].

12.2.3 Performance Relative Gain Array (PRGA)

Especially for analyzing decentralized control systems based on independent controller design(e.g. stability and sensitivity), the Performance Relative Gain Array (PRGA) can be used. The mathematical definition of the PRGA matrix is:

$$\Gamma = \tilde{G}G^{-1} \qquad \text{where} \quad \tilde{G} = \text{diag}\{g_{ii}\} \qquad\qquad (12.63)$$

Matrix $\tilde{G}(s)$ is the same as the transfer function matrix $G(s)$, except that it only contains the diagonal elements of $G(s)$. Γ is the normalized inverse of a plant (system). It is called the Performance RGA, because its calculation is similar to that of the RGA matrix (12.60) and the fact that a large element in the PRGA matrix indicates that fast control is needed to get acceptable reference tracking (performance).

12.2.4 Diagonal dominance

Two methods are mentioned in [10], to investigate the diagonal dominance of a MIMO system.

The first method involves using the RGA number, which is a norm that is used as a measure of diagonal dominance and is defined for diagonal input-output paring as:

$$\text{RGA number} \triangleq \left\| \Lambda(G) - I \right\|_{\text{sum}} \qquad\qquad (12.64)$$

The RGA number is equal to the sum of all the elements of the matrix that results from subtracting the Identity matrix from the equally sized RGA matrix (12.60). Unfortunately, there is no guarantee for systems larger than 3x3 that a small RGA number (close to 0) indicates diagonal dominance.

The second method uses the singular values of the error matrix E, defined in (12.65).

$$E \triangleq (G - \tilde{G})\tilde{G}^{-1} \qquad\qquad (12.65)$$

Where the matrix $\tilde{G}(s)$ is already defined in (12.63). The magnitude of the error matrix E is commonly used as an "interaction measure". The transfer function matrix $G(s)$ is generalized diagonally dominant if and only if:

$$\mu(E) < 1 \qquad\qquad (12.66)$$

Where $\mu(E)$ is a structured singular value of matrix E (12.65).

---

[v] In general, there are some exceptions, see [10].

12.3 Application of MIMO system analysis on the linear model of the prototype

The (linear model) transfer function matrix G(s) (12.50) of the prototype shows that it is a two way interactive system for the coupled position and orientation parameters (x, β) and (y, α) of the optical center point of the mirror.

12.3.1 Calculation of the RGA matrix

The Relative Gain Array matrix (12.60) of the linear model transfer function matrix G(s) (12.50) is calculated for the frequencies within the operating range of the tilting mirror prototype and for all three actuator models (see PART 1).

The results in figure 12.1, show that:
- The diagonal RGA matrix elements are all ≥1 and typically 1.
- The non-diagonal RGA matrix elements are all ≤0 and typically 0.

So, the RGA matrix is (close to) the Identity matrix for the complete frequency range of the prototype. This means that the system is diagonal dominant, because the RGA number (12.64) is close to 0.

The RGA matrix analysis also suggests that the best input-output pairing (for the analyzed frequency range) for decentralized control is the diagonal pairing.

12.4 Controller adjustment

In part 1 of this thesis, the corrections for the ideal actuator model of the prototype resulted in adjustment of the actuator gains and additional gravitational components. Also the actuator calibration measurement in [1], although flawed, indicated that the actuator gains of the real device probably are much smaller than the corrected ideally modeled gains. So now there are three models (table 12.2). The setup of these models is basically the same, only the actuator gains are different. The controllers designed for the original model (1) can be optimized for the corrected (COR) and the measured (MES) model. This will be the subject of investigation of this section.

Table 12.2 Three different models that are distinguished in this section.

Model	Description
1	The ideal actuator model that contained some errors and was incomplete, but was used in [1, chapter 7] to design the five original controllers for the prototype.
COR	The corrected ideal model (part 1, chapter 3). This is also the model for which the linear model approximation has been done in section 12.1.
MES	The model that is based on the (flawed) horizontal actuator calibration measurements carried out in [1]. For this model the expected actuator gains, calculated and presented in table 7.6 (part 1), are used.
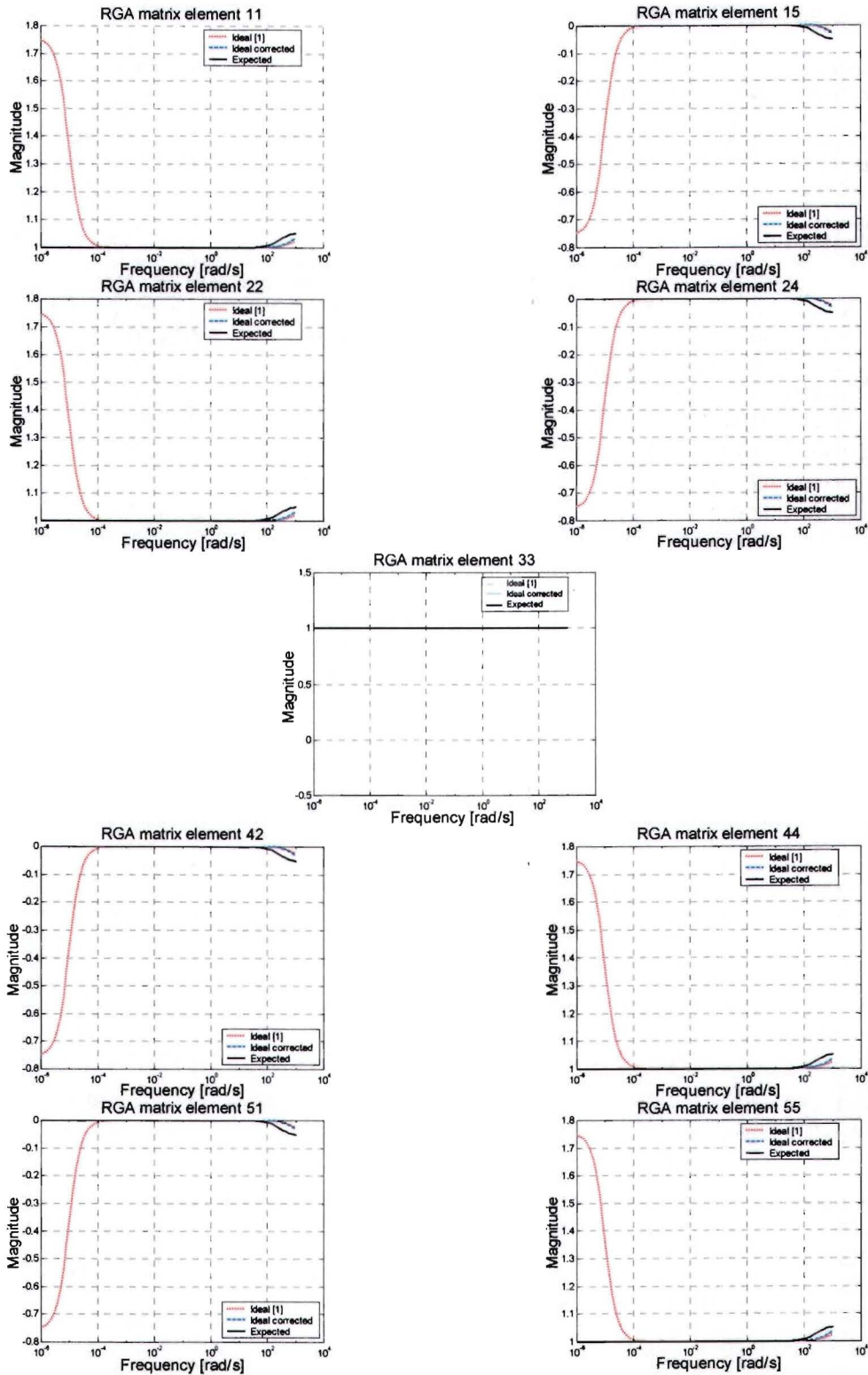
Figure 12.1 RGA matrix elements of G(s) (12.50) that are not equal to 0 for every frequency. The three lines in each plot represent the three (actuator) models, see table 12.2.

12.4.1 Original and adapted controllers

The original PID controllers (1) for all 5 DOF that are presented in [1, chapter 7] are principally the same. They all consist of a gain, two zeros and three poles.

The original controllers (1) are adapted (section 12.4.2) for the corrected ideal model (COR) and the model based on the horizontal actuator calibration measurement results (MES). The original and the adapted controllers are presented in table 12.3.

Table 12.3 Compensators for the three ideal actuator models.

Controller	Gain K_c	Zeros		Poles		
		z1	z2	p1	p2	p3
Cxy_1	$-2.25 \cdot 10^{11}$	-500	$-4 \cdot 10^3$	0	$-3 \cdot 10^4$	$-3 \cdot 10^5$
Cxy_{COR}	$-1.036 \cdot 10^{12}$	-500	-6170	0	-52813	$-3 \cdot 10^5$
Cxy_{MES}	$-2.1896 \cdot 10^{12}$	-500	-3847	0	-56885	$-3 \cdot 10^5$
Cz_1	$-5.41 \cdot 10^{11}$	-300	-500	0	$-3 \cdot 10^4$	$-3 \cdot 10^5$
Cz_{COR}	$-9.34 \cdot 10^{11}$	-300	-500	0	$-3 \cdot 10^4$	$-3 \cdot 10^5$
Cz_{MES}	$-7.27 \cdot 10^{12}$	-300	-500	0	$-3 \cdot 10^4$	$-3 \cdot 10^5$
$C\alpha\beta_1$	$-2.43 \cdot 10^9$	-300	-500	0	$-3 \cdot 10^4$	$-3 \cdot 10^5$
$C\alpha\beta_{COR}$	$-6.23 \cdot 10^9$	-300	-800	0	$-3 \cdot 10^4$	$-3 \cdot 10^5$
$C\alpha\beta_{MES}$	$-2.6 \cdot 10^{10}$	-300	-788	0	$-3 \cdot 10^4$	$-3 \cdot 10^5$

12.4.2 Controller adaptation

Since the difference between the original model (1) and the corrected- (COR) and "measured" model (MES) is only the modified actuator gains, the controller design strategy (pole and zero placement) from [1] can still be used:

Zero z1 neutralizes the system pole close to the origin of the s-plane.
Zero z2 is necessary because there are two active poles near the origin of the s-plane. This second zero helps to pull the root locus of the closed loop system (actuator and controller) to the stable left side of the s-plane.

Pole p1 is placed in the origin of s-plane, this pole has an integrator function that realizes a zero steady state error.
Pole p2 reduces the damping effect of zero z2 and increases the bandwidth of the closed loop system.
Pole p3 is placed far away on the real axis in the stable left side of the s-plane. It only has the function of making the controller strictly proper. It has no influence on the system behavior for low frequencies.

For the execution of the controller adaptation the MATLAB® root locus-tool is used to check the following criteria:

- Find a balance between the maximum overshoot and a fast settling time for the step response of the five main actuator transfers that are controlled.
- Prevent oscillation in the step response. Keep the response smooth to reduce the negative effect of the coupled transfers that are not directly controlled.
- Make sure that the root locus indicates enough gain margin to prevent stability problems when the actuator gains of the real model differ from the expected ones or are not constant.

Table 12.4 Step response characteristics for different controllers tested on the three ideal actuator models (H_1, H_{COR} and H_{MES}).

Transfer	Controller	Overshoot max [%]	Overshoot at [ms]	Settling time [ms]
Hxy_1	Cxy_1	45	0.138	3.94
Hxy_{COR}	Cxy_1	57	0.345	3.49
	Cxy_{COR}	35	0.12	2.7
Hxy_{MES}	Cxy_1	60	0.685	3.04
	Cxy_{MES}	22	0.18	0.8
Hz_1	Cz_1	17	1.2	3.49
Hz_{COR}	Cz_1	12	0.79	3.02
	Cz_{COR}	9	0.403	2.33
Hz_{MES}	Cz_1	43	3.18	14.0
	Cz_{MES}	8	0.34	2.16
$H\alpha\beta_1$	$C\alpha\beta_1$	17	1.2	3.54
$H\alpha\beta_{COR}$	$C\alpha\beta_1$	12	1.2	2.4
	$C\alpha\beta_{COR}$	11	0.27	1.72
$H\alpha\beta_{MES}$	$C\alpha\beta_1$	35	2.62	9.31
	$C\alpha\beta_{MES}$	11	0.29	1.74

Two characteristics of the step responses (the overshoot and the settling time) of the five systems are shown in table 12.4. First the original controllers are tested on the three models, so that the effect of the modified actuator gains can be investigated.

To obtain better control results, the original controllers are not significantly changed. Only the position of one zero (z2) and one pole (p2) as well as the controller gain (K_c) are adjusted. The resulting adapted controllers for the corrected ideal model (COR) and the model based on the actuator calibration measurements (MES) are presented in table 12.3.

Table 12.4 shows that the adaptation of the controllers resulted in closed loop step responses that are faster and have less overshoot compared to the step responses obtained with the original controllers.

Chapter 13

Conclusions of PART 2

This final chapter of part 2 of this M.Sc.-thesis contains the conclusions of chapters 10, 11 and 12 and the overall conclusions for the complete graduation work.

13.1 Processing the calibration measurement data of the test setup sensor

Two sets of measurement expectation values are now available for the 25 linear sensor model parameters of the prototype. The first set was calculated with the ideal sensor model in [1], the other set was extracted from the available calibration measurement data of the test setup sensor. The latter set showed significant couplings from the vertical rotor position (z) to all sensor outputs. These couplings are not present in the ideal set. The 5 sensor offset voltages can be easily extracted from calibration measurement data, but they cannot be predicted, because they depend on the used sensor electronics.

Position estimation tests have proven that a linear sensor model is applicable, at least for the static measurements performed on the sensor replica. There are three main differences between the sensor replica and the sensor system of the prototype:
• The horizontal coil cores are the orientation sensor electrodes of the prototype.
• The electromagnetic actuator system is present and active in the prototype.
• The sensor system of the prototype must be able to measure rotor movements (horizontal lift-off and mirror tilting). So it is used dynamic instead of just static.
These differences could influence the functioning of the sensor system of the prototype.

The sensitivity of the orientation sensors must be improved. Luckily the rotation sensor electrodes of the prototype are shaped differently as the ones of the replica, which will probably result in better functionality.

It was discovered that the sensitivity for vertical translations of the horizontal sensor output voltages can be used to find the horizontal coordinates of the operating point of the rotor: the center of the stator.

For the optimization of the linear sensor model that is based on the static calibration measurements, two choices must be made:
• Extract the linear sensor coupling parameters by hand or use an automatic extraction method.
• Optimize the linear sensor model for the full sensor range or only near the operating point of the rotor.

13.2 Design of a calibration setup for the prototype

A lack of means (people and money) forced to start with a simple calibration setup for the sensor of the prototype, where the rotor is fixated by a clamping device: the expansion gripper.
Micromanipulators can be used to perform static sensor calibration measurements for 4 sensors (u, v, z and α). For calibration of the other rotation angle (β) the device has to be reinstalled, rotated over a 90° angle around the z-axis of the stator frame.

Extra options for the calibration setup are discussed, like:
• Various (flexible) connection links.
• The integration of a Force/Torque sensor for full actuator calibration.
• A rotor release mechanism that avoids the lift-off problem of the rotor and could be used for controller testing.

Instructions for the installation and use of the calibration setup are given. Also the maximum range (horizontal, vertical and rotation) of the rotor in the setup is calculated.

13.3 Control

A linear model approximation for the rotor in its operating point, the center of the stator, has been calculated, based on the corrected and improved ideal model (Part 1) of the prototype with gravity added to the system. The linear model is expressed in device parameters, which provides insight for control engineering and facilitates the implementation of improvements for possible future prototype designs. The linear model is presented in the standard State Space Model notation and shows which device parameters cause transfers between the inputs and outputs of the system.

Also the transfer function matrix of the linear model was calculated. It contains four non-diagonal elements, which represent (unwanted) couplings between the inputs and outputs of the system. These unwanted couplings have three causes:
• The optical center point of the mirror and the center of gravity of the rotor do not coincide.
• The work-lines through the points of attack of actuator forces do not cross the center of gravity of the rotor.
• The actuators that have to compensate gravity act in the direction of the normal axis of the mirror. When the rotor is tilted, this normal axis does not lie on the work-line of the gravity.

Relative Gain Array (RGA) matrices are calculated to investigate the effect of the couplings, for the frequency domain of the system. Because the RGA matrices are almost equal to the Identity matrix for the whole frequency domain of the system, it can be concluded that the choice in [1] to consider the system as fully decoupled, was justified.

Lastly, the original controllers proposed for the prototype in [1] were tested on the corrected ideal model and the expected model (based on the actuator calibration in [1] that indicated even weaker actuators). The controllers seemed robust enough to cope with the possible smaller actuator gains and the added gravity. However, adaptation of the controllers resulted in faster feedback systems with less overshoot in the step-response compared to the original control results.

13.4 Main conclusions

No crucial theoretical mistakes were found in the design and modeling of the prototype of the magnetically levitated tilting mirror presented in [1]. So in theory the system could be operational.

However, several theoretical- and sloppy mistakes were corrected. Also some analyses were supplemented. Together these improvements resulted in a more accurate and complete modeling and calibration of the system.

The essential (re)calibration of the capacitive sensor system has been prepared with:
• The design and production of a calibration setup.
• The investigation of how to process the calibration measurement data, to obtain an optimal linear sensor model.

With the RGA analysis performed on a calculated approximating linear model, it is shown that this MIMO system can be contemplated as a decoupled system in its intended frequency domain. Via simulations with an ideal nonlinear model of the system, it is shown that five simple SISO controllers can keep the rotor in the middle of stator, but are also capable of performing the rotor lift-off at the

start up of the prototype. The five SISO controllers proposed in [1] are slightly adapted (for mistakes, added gravity and expected weaker actuators) to get a better performance.

Despite the thorough preparations, the necessary practical execution on the prototype did not take place (by a lack of time and means). So the sensor system of the prototype hasn't been recalibrated yet and therefore the adapted controllers could not be tested on the real device. This means that the prototype still isn't operational.

13.5 Additional commentary

This thesis doesn't contain radical suggestions for improvements of the prototype design, or the proposed calibration procedures in [1], because the emphasis was on making the available prototype operational, not redesigning it.

However, a proposal for two simple improvements would be:
- For the next design, try to let the point to be controlled (the optical center point of the mirror) coincide with the center of gravity of the rotor. Also let the actuator forces act on the center of gravity, so that unwanted couplings (torques) are avoided.
- The long flat-cable that transports high frequency digital modulation signals of the sensor system could be replaced by short coaxial cable, to reduce signal noise and other disturbances.

Possible practical problems that can be expected are:
- The double function of the vertical actuators, lifting the rotor (against gravity) and rotating the rotor to get a preferred mirror orientation, combined with the expected smaller actuator gains, could lead to instability when the rotor is tilted.
- When the sensitivity of the rotation sensors is not improved by the differently shaped sensor electrodes of the prototype, there could be a problem with the sensor electronics.
- The ambiguous use of reference frames has probably led to at least one faulty electrical wire connection, so it would be smart to check the wiring of the complete prototype.

Chapter 14

Literature and Software

14.1 Used literature

[1]   Van Acht, V.M.G.
       ELECTROMAGNETIC CONTROL OF A FREE BODY: DESIGN AND CONTROL OF A 6 DOF MAGNETICALLY
       LEVITATED SPHERICAL LASER DEFLECTION SYSTEM.
       Eindhoven (The Netherlands): Technische Universiteit Eindhoven, 2001
       Doctoral dissertation.
       ISBN 90-386-1899-9

[2]   Roest, R.
       INLEIDING MECHANICA [Dutch for: INTRODUCTION TO MECHANICS].
       Delft (The Netherlands): Delftse Uitgevers Maatschappij b.v., 1993 (fourth print)
       ISBN 90 6562 127 X

[3]   Almering, J.H.J et al.
       ANALYSE.
       Delft (The Netherlands): Delftse Uitgevers Maatschappij b.v., 1993 (sixth print)
       ISBN 90-6562-078-8

[4]   James, G. et al.
       MODERN ENGINEERING MATHEMATHICS.
       Harlow (England): Addison-Wesley, 1996 (second edition)
       ISBN 0-201-87761-9

[5]   NVON-committee
       BINAS, Information book for secondary school science education.
       Groningen (The Netherlands): Wolters-Noordhoff, 1986 (second print)
       ISBN 90 01 89351 1

[6]   USING MATLAB version 5.
       The MathWorks Inc., 1999

[7]   Blachman, N.
       MATHEMATICA (Translation into Dutch).
       Hemel Hempstead (England): Pretence Hall, 1992
       Schoonhoven (The Netherlands): Academic Service, 1993
       ISBN 90-395-0016-9

[8]   McKerrow, P.J.
       INTRODUCTION TO ROBOTICS.
       Sydney (Australia): Addison-Wesley Publishing Company, 1991 (corrected 1995)
       ISBN 0-201-18240-8

[9]   Dorf, R.C. and Bishop, R.H.
       MODERN CONTROL SYSTEMS.
       Reading, Massachusetts: Addison-Wesley Publishing Company, 1995 (7th edition)
       ISBN 0-201-84559-8

[10]   Skogestad, S. and Postlethwaite, I.
       MULTIVARIABLE FEEDBACK CONTROL, Analysis and Design.
       Chichester (England): John Wiley & Sons Ltd, 2001 (second edition 2005)
       ISBN 13 978-0-470-01167-6

14.2 Literature survey

As part of the graduation process, a literature survey was carried out to support the work on the tilting mirror project. The survey was executed from August 1 till October 15 in the year 2002. The search focused on articles and papers that where directly available, either as hardcopy in the TU/e library or as a digital pdf-file.

An extensive report on the survey was written. Some parts of that report are also presented in this thesis. In particular the list of found literature (subsection 14.2.1), important publications (subsection 14.2.2) and a table showing the links between the contents of the publications and the main research subjects of the tilting mirror project and the prototype (subsection 14.2.3).

14.2.1 List of found literature

[L1]   Van-Acht, V.M.G.
        ELECTROMAGNETIC CONTROL OF A FREE BODY : DESIGN AND CONTROL OF A 6 DOF MAGNETICALLY
        LEVITATED SPHERICAL LASER DEFLECTION SYSTEM.
        Technische Universiteit Eindhoven, 2001
        Doctoral dissertation, ISBN 90-386-1899-9

[L2]   Lindlau, J.D. and C.R. Knospe
        FEEDBACK LINEARIZATION OF AN ACTIVE MAGNETIC BEARING WITH VOLTAGE CONTROL.
        IEEE-Transactions-on-Control-Systems-Technology. Vol.10, no.1; Jan. 2002; p.21-31.
        Useful; Full-text (00974335.pdf)

[L3a]   De-Queiroz, M.S. and D.M. Dawson, A. Suri (Dept. of Electr. & Comput. Eng., Clemson Univ., SC, USA)
        NONLINEAR CONTROL OF A LARGE-GAP 2-DOF MAGNETIC BEARING SYSTEM BASED ON A COUPLED
        FORCE MODEL.
        IEE-Proceedings-Control-Theory-and-Applications. Vol.145, no.3; May 1998; p.269-276.
        Useful; Full-text: (00685445.pdf)

[L3b]   De-Queiroz, M.S. and D.M. Dawson, A. Suri (Dept. of Electr. & Comput. Eng., Clemson Univ., SC, USA)
        NONLINEAR CONTROL OF A LARGE GAP 2-DOF MAGNETIC BEARING SYSTEM BASED ON A COUPLED
        FORCE MODEL.
        Proceedings-of-the-1997-American-Control-Conference-Cat.-No.97CH36041. 1997: 2165-2169 vol.3.
        PUBLISHER: American Autom. Control Council, Evanston, IL, USA
        Useful; Full-text see [3a]

[L4]   Suzuki, Y
        ACCELERATION FEEDFORWARD CONTROL FOR ACTIVE MAGNETIC BEARING SYSTEMS EXCITED BY
        GROUND MOTION.
        IEE-Proceedings-Control-Theory-and-Applications. Vol.145, no.2; March 1998; p.113-118.
        Might be Useful; Full-text: (00675617.pdf)

[L5]   Hada-Chang and Sung-Chong-Chung
        INTEGRATED DESIGN OF RADIAL ACTIVE MAGNETIC BEARING SYSTEMS USING GENETIC ALGORITHMS.
        Mechatronics-. Feb. 2002; 12(1): 19-36.
        Useful; Full-text: (science_1_2e_10.pdf)

[L6]   Lee, C.W., A.S. Jeong
        DYNAMIC MODELING AND OPTIMAL CONTROL OF CONE-SHAPED ACTIVE MAGNETIC BEARING SYSTEMS.
        Control-Engineering-Practice. Oct. 1996; 4(10): 1393-403.
        Useful

[L7]   Polajzer, B. (Fac. of Electr. Eng. & Comput. Sci., Maribor Univ., Slovenia)
        MODELING AND CONTROL OF HORIZONTAL-SHAFT MAGNETIC BEARING SYSTEM.
        ISIE-'99.-Proceedings-of-the-IEEE-International-Symposium-on-Industrial-Electronics-Cat.-No.99TH8465. 1999:
        1051-1055 vol.3.
        PUBLISHER: IEEE, Piscataway, NJ, USA
        Useful; Full-text: (00796775.pdf)

[L8]   Hughes, A. and J.M. Stephenson, C. Sloan (Sch. of Electron. & Electr. Eng., Leeds Univ., UK)
        DYNAMIC MODELLING AND CONTROL OF A NORMAL-FORCE ACTUATOR.
        IEE-Proceedings-Electric-Power-Applications. Sept. 1998; 145(5): 449-454.
        Useful; Full-text: (00725625.pdf)

[L9]   Ren, Z., A. Razek (Lab. de Genie Electrique de Paris, France)
         MODELLING OF DYNAMICAL BEHAVIOURS OF ELECTRO-MAGNETO-MAGNETICAL COUPLED SYSTEMS.
         Second-International-Conference-on-Computation-in-Electromagnetics-Conf.-Publ.-No.384. 1994: 20-23.
         PUBLISHER: IEE, London, UK
         Useful; Full-text: (00324116.pdf)

[L10]   Fabian, T and G. Brasseur, H. Hauser (Inst. of Appl. Electron. & Quantumelectron., Tech. Univ. Wien, Austria)
         IMPACT OF AXIAL AND RADIAL ROTOR OFFSET ON THE MEASUREMENT ERROR OF A CAPACITIVE
         ANGULAR-POSITION SENSOR WITH MODIFIED FRONT-END TOPOLOGY.
         IMTC/99. Proceedings of the 16th IEEE Instrumentation and Measurement Technology Conference (Cat.
         No.99CH36309). IEEE, Piscataway, NJ, USA; 1999; 3 vol.xl+1937 pp. p.1362-6 vol.3.
         Might be Useful; Full-text (00776028.pdf)

[L11]   LI, X. and G.C.M. Meijer, G.W. de-Jong (Dept. of Electr. Eng., Delft Univ. of Technol., Netherlands)
         A MICROCONTROLLER-BASED SELF-CALIBRATION TECHNIQUE FOR A SMART CAPACITIVE ANGULAR-
         POSITION SENSOR.
         IEEE-Transactions-on-Instrumentation-and-Measurement. vol.46, no.4; Aug. 1997; p.888-892.
         Might be Useful; Full-text (00650794.pdf)

[L12]   Boskovic, J.D. and Sai-Ming-Li, R.K. Mehra (Scientific Syst. Co. Inc., Wobum, MA, USA)
         RECONFIGURABLE FLIGHT CONTROL DESIGN USING MULTIPLE SWITCHING CONTROLLERS AND ONLINE
         ESTIMATION OF DAMAGE-RELATED PARAMETERS.
         Proceedings of the 2000. IEEE International Conference on Control Applications. Conference Proceedings (Cat.
         No.00CH37162). IEEE, Piscataway, NJ, USA; 2000; 995 pp. p.479-484.
         Might be Useful; Full-text: (00897470.pdf)

[L13]   Nounou, H.N. and K.M. Passino (Dept. of Electr. Eng., Ohio State Univ., Columbus, OH, USA)
         FUZZY MODEL PREDICTIVE CONTROL: TECHNIQUES, STABILITY ISSUES, AND EXAMPLES.
         Proceedings of the 1999 IEEE International Symposium on Intelligent Control Intelligent Systems and Semiotics (Cat.
         No.99CH37014). IEEE, Piscataway, NJ, USA; 1999; xiv+464 pp. p.423-288.
         Might be Useful; Full-text: (00796692.pdf)

[L14]   Maki, M. and K. Hagino (Dept. of Commun. & Syst. Eng., Univ. of Electro-Commun., Chofu, Japan)
         ADAPTIVE CONTROL FOR UNCERTAIN LINEAR SYSTEMS USING SWITCHING BETWEEN MULTIPLE
         CONTROLLERS.
         SICE '97. Proceedings of the 36th SICE Annual Conference. International Session Papers (IEEE Cat. No.97TH8323).
         Soc. Instrum. & Control Eng, Tokyo, Japan; 1997; 466 pp. p.1235-1240.
         Useful

[L15]   Yoon-Sik-Kim and Woong-Gie-Han, Tae-Yong-Kuc (Intelligent Control &
         Dynamic Simulation Lab., Sung Kyun Kwan Univ., Suwon, South Korea)
         AN INTELLIGENT MISSILE AUTOPILOT USING GENETIC ALGORITHM.
         1997 IEEE International Conference on Systems, Man, and Cybernetics. Computational Cybernetics and Simulation
         (Cat. No.97CH36088-5). IEEE, New York, NY, USA; 1997; 5 vol. 4535 pp. p.1954-1959 vol.2.
         Useful; Full-text: (00638363.pdf)

[L16]   Aenis, M. and E. Knopf, R. Nordmann
         ACTIVE MAGNETIC BEARINGS FOR THE IDENTIFICATION AND FAULT DIAGNOSIS IN TURBOMACHINERY.
         Mechatronics, Volume 12, Issue 8, October 2002, Pages 1011-1021
         Might be Useful; Full-text: (science1_2a_1.pdf)

[L17]   Schroder, P. and B. Green, N. Grum and P.J. Fleming
         ON-LINE EVOLUTION OF ROBUST CONTROL SYSTEMS: AN INDUSTRIAL ACTIVE MAGNETIC BEARING
         APPLICATION.
         Control Engineering Practice, Volume 9, Issue 1, January 2001, Pages 37-49
         Useful; Full-text (science_1_2c_5)

[L18]   Sung-Kyung Hong and R. Langari
         AN LMI-BASED H^∞ FUZZY CONTROL SYSTEM DESIGN WITH TS FRAMEWORK.
         Information Sciences, Volume 123, Issues 3-4, April 2000, Pages 163-179
         Useful; Full-text (science_1_2c_6 and science_1_2e_31)

[L19]   Sivrioglu, S. and K. Nonami
         LMI APPROACH TO GAIN SCHEDULED H$_{INFINITY}$ CONTROL BEYOND PID CONTROL FOR GYROSCOPIC
         ROTOR-MAGNETIC BEARING SYSTEM.
         Proceedings of the IEEE Conference on Decision and Control, Volume 4, 1996, Pages 3694-3699
         Useful; Full-text (00577221.pdf)

[L20]   Vischer, D. and H. Bleuler
         SELF-SENSING ACTIVE MAGNETIC LEVITATION.
         IEEE Transactions on Magnetics, Volume 29, Issue 2, March 1993, Pages 1276-1281
         Useful; Full-text: (00250632.pdf)

[L21]   Chen, K.S. and D.L. Trumper, S.T. Smith
         DESIGN AND CONTROL FOR AN ELECTROMAGNETICALLY DRIVEN X-Y-θ STAGE.
         Precision Engineering, Volume 26, Issue 4, October 2002, Pages 355-369
         Very Useful; Full-text: (design and control.pdf)

[L22]   Yu Sun and D. Piyabongkarn, A. Sezen, B.J. Nelson, R. Rajamani
         A HIGH-ASPECT-RATIO TWO-AXIS ELECTROSTATIC MICROACTUATOR WITH EXTENDED TRAVEL RANGE.
         Sensors and Actuators A: Physical, **In Press, Corrected Proof**, Available online 16 September 2002
         Might be Useful; Full-text (science_3_3_2.pdf)

[L23]   Horenstein, M.N. and J.A. Perreault, T.G. Bifano
         DIFFERENTIAL CAPACITIVE POSITION SENSOR FOR PLANAR MEMS STRUCTURES WITH VERTICAL
         MOTION.
         Sensors and Actuators A: Physical, Volume 80, Issue 1, 1 March 2000, Pages 53-61
         Might be Useful; Full-text (science_3_3_10.pdf)

[L24]   Fukuda, T. and H. Morita, F. Arai, H. Ishihara, H. Matsuura
         MICRO RESONATOR USING ELECTROMAGNETIC ACTUATOR FOR TACTILE DISPLAY
         Micromechatronics and Human Science, 1997. Proceedings of the 1997 International Symposium on , 1997 Page(s):
         143 -148
         Useful; Full-text: (00768872.pdf)

[L25]   Melgoza, E. and D. Rodger
         COMPARISON OF TABLE MODELS OF ELECTROMAGNETIC ACTUATORS.
         Magnetics, IEEE Transactions on , Volume: 38 Issue: 2 Part: 1 , March 2002
         Page(s): 953 –956
         Useful; Full-text: (00996245.pdf)

[L26]   Zhi Zhou and Kok-Meng Lee
         REAL-TIME MOTION CONTROL OF A MULTI-DEGREE-OF-FREEDOM VARIABLE RELUCTANCE SPHERICAL
         MOTOR.
         Robotics and Automation, 1996. Proceedings., 1996 IEEE International Conference on , Volume: 3 , 1996, Page(s):
         2859 -2864 vol.3
         Might be Useful; Full-text: (00506596.pdf)

[L27]   Kwang-Suk-Jung and Yoon-Su-Baek (Dept. of Mech. Eng., Yonsei Univ., Seoul, South Korea)
         DEVELOPMENT OF A NOVEL MAGLEV POSITIONER WITH SELF-STABILIZING PROPERTY.
         Mechatronics-. June 2002; 12(5): 771-90. (PUBLISHER: Elsevier)
         Useful; Full-text: (science_1_3b_1.pdf & science_1_3c_5.pdf)

[L28]   Kladas, A.G. and J.A. Tegopoulos (Dept. of Electr. & Comput. Eng., Nat. Tech. Univ. of Athens, Greece)
         3D EDDY CURRENTS MODELLING BY MEANS OF A PARTICULAR REDUCED SCALAR POTENTIAL
         TECHNIQUE.
         IEEE-Transactions-on-Magnetics. March 1997; 33(2) pt. 2: 1350-3.
         Might be Useful; Full-text: (00582506.pdf)

[L29]   Kim, Y.B. and W.G. Hwang, C.D. Kee, H.B.Yi (Dept. of Mech. Eng., Chonnam Nat. Univ., Kwangju, South Korea)
         ACTIVE VIBRATION CONTROL OF A SUSPENSION SYSTEM USING AN ELECTROMAGNETIC DAMPER.
         Proceedings-of-the-Institution-of-Mechanical-Engineers,-Part-D-Journal-of-Automobile-Engineering. 2001; 215(D8):
         865-73.
         PUBLISHER: Professional Engineering Publishing
         Useful; Full-text: (p865.pdf)

[L30]   Hanson, B.M. and M.D. Brown, J. Fisher (Sch. of Mech. Eng., Leeds Univ., UK)
         SELF SENSING: CLOSED-LOOP ESTIMATION FOR A LINEAR ELECTROMAGNETIC ACTUATOR.
         Proceedings-of-the-2001-American-Control-Conference.-Cat.-No.01CH37148. 2001: 1650-1655 vol.2.
         PUBLISHER: IEEE, Piscataway, NJ, USA
         Very Useful; Full-text: (00945965.pdf)

[L31]   Lai, H.C. and P.C. Coles, D. Rodger, P.J. Leonard (Bath Univ., UK)
         TRANSIENT ANALYSIS OF AN ELECTROMAGNETIC ACTUATOR USING AN OVERLAPPING FINITE ELEMENT
         SCHEME.
         IEEE-Transactions-on-Magnetics. July 2000; 36(4) pt. 1: 1462-7.
         Might be Useful; Full-text: (00877714.pdf)

[L32]   Xiujun-Li and G. de-Jong, G.C.M. Meijer (Dept. of Electr. Eng., Delft Univ. of Technol., Netherlands)
         THE APPLICATION OF THE CAPACITOR'S PHYSICS TO OPTIMIZE CAPACITIVE ANGULAR-POSITION
         SENSORS.
         IEEE-Transactions-on-Instrumentation-and-Measurement. vol.46, no.1; Feb. 1997; p.8-14.
         Might be Useful; Full-text: (00552149.pdf)

[L33] Xiujun-Li and G.C.M. **Meijer**, G.W. **de-Jong** (Dept. of Electr. Eng., Delft Univ. of Technol., Netherlands)
A SELF-CALIBRATION TECHNIQUE FOR A SMART CAPACITIVE ANGULAR-POSITION SENSOR.
Quality Measurements: The Indispensable Bridge between Theory and Reality (No Measurements? No Science!)
Joint Conference - 1996: IEEE Instrumentation and Measurement Technology Conference and IMEKO Technical
Committee 7. Conference Proceedings (Cat. No.96CH35936). IEEE, New York, NY, USA; 1996; 2 vol. xxxviii+1515
pp. p.774-7 vol.2.
Might be useful; Full-text: (00507273.pdf)

[L34] **Wang**, Z. and M.K. **Jouaneh**, D.A. **Dornfeld** (Dept. of Mech. Eng., California Univ., Berkeley, CA, USA)
DESIGN AND CHARACTERIZATION OF A LINEAR MOTION PIEZOELECTRIC MICROPOSITIONER.
IEEE-Control-Systems-Magazine. vol.10, no.2; Feb. 1990; p.10-15.
Might be Useful; Full-text:(00045788.pdf)

[L35] **Fen-Wu** (Dept. of Mech. & Aerosp. Eng., North Carolina State Univ., Raleigh, NC, USA)
SWITCHING LPV CONTROL DESIGN FOR MAGNETIC BEARING SYSTEMS.
Proceedings of the 2001 IEEE International Conference on Control Applications (CCA'01) (Cat. No.01CH37204).
IEEE, Piscataway, NJ, USA; 2001; 1207 pp. p.41-6.
Useful; Full-text: (00973835.pdf)

[L36] **Zanma**, T. and T. **Suzuki**, S. **Okuma** (Dept. of Electr. Eng., Nagoya Univ., Japan)
A DESIGN OF SWITCHED CONTROLLERS FOR FORCE CONTROL SYSTEM
6th International Workshop on Advanced Motion Control. Proceedings (Cat. No.00TH8494). IEEE, Piscataway, NJ,
USA; 2000; xxxviii+635 pp. p.258-63.
Useful; Full-text: (00862870.pdf)

[L37] **Inaba**, M. and **Hai-Jiao-Guo**, K. **Nakao**, K. **Abe** (Dept. of Electr. Eng., Tohoku Univ., Sendai, Japan)
ADAPTIVE CONTROL SYSTEMS SWITCHED BY CONTROL AND ROBUST PERFORMANCE CRITERIA.
Proceedings. 1996 IEEE Conference on Emerging Technologies and Factory Automation. EFTA '96 (Cat.
No.96TH8238). IEEE, New York, NY, USA; 1996; 2 vol. xiii+787 pp. p.690-696 vol.2.
Might be Useful; Full-text: (00573988.pdf)

[L38] **Ji**, J.C. and C.H. **Hansen**
NON-LINEAR OSCILLATIONS OF A ROTOR IN ACTIVE MAGNETIC BEARINGS. Journal of Sound and Vibration,
Volume 240, Issue 4, 1 March 2001, Pages 599-612
Might be Useful; Full-text: (science_1_2c_4.pdf)

[L39] **Gibson**, N.S. and G.D. **Buckner**
REAL-TIME ADAPTIVE CONTROL OF ACTIVE MAGNETIC BEARINGS USING LINEAR PARAMETER VARYING
MODELS.
Conference Proceedings - IEEE SOUTHEASTCON, 2002, Pages 268-272
Very Useful; Full-text: (00995603.pdf)

[L40] **Coey**, J.M.D.
PERMANENT MAGNET APPLICATIONS.
Journal of Magnetism and Magnetic Materials, Volume 248, Issue 3, August 2002, Pages 441-456
Might be Useful; Full-text: (science_1_3a_6.pdf)

[L41] **Sung-Q Lee** and **Dae-Gab Gweon**
A NEW 3-DOF Z-TILTS MICROPOSITIONING SYSTEM USING ELECTROMAGNETIC ACTUATORS AND AIR
BEARINGS.
Precision Engineering, Volume 24, Issue 1, January 2000, Pages 24-31
Useful; Full-text: (science_2_3d_30.pdf)

[L42] **Kee-Bong Choi** and **Soo Hyun Kim**, **Byung-Wook Choi**
MOVING-MAGNET TYPE PRECISION MINIATURE PLATFORM FOR FINE POSITIONING AND COMPLIANT
MOTION.
Mechatronics, Volume 11, Issue 7, October 2001, Pages 921-937
Useful; Full-text: (science_1_3b_2.pdf)

[L43] **Mei-Yung Chen** and **Kun-Nan Wu**, **Li-Chen Fu**
DESIGN, IMPLEMENTATION AND SELF-TUNING ADAPTIVE CONTROL OF MAGLEV GUIDING SYSTEM.
Mechatronics, Volume 10, Issues 1-2, February-March 2000, Pages 215-237
Useful; Full-text: (science_1_3c_15.pdf)

[L44] **Chen**, **Mei-Yung** and **Ming-Jyh Wang**, **Li-Chen Fu**
MODELING AND CONTROLLER DESIGN OF A MAGLEV GUIDING SYSTEM FOR APPLICATION IN PRECISION
POSITIONING.
Proceedings of the American Control Conference, Volume 5, 1999, Pages 3072-3076
Might be Useful; Full-text: (00782326.pdf)

[L45] **Mohamed**, A.M. and B. **Vestgaard**, I. **Busch-Vishniac**
REAL TIME IMPLEMENTATION OF A ROBUST H INFINITY CONTROLLER FOR A 2-DOF MAGNETIC MICRO-
LEVITATION POSITIONER.
Proceedings of the American Control Conference, Volume 3, 1994, Pages 3219-3223
Might be Useful; Full-text: (00735167.pdf)

[L46] Lee S.H., and H.K. Sung, J.T. Lim, Z. Bien
SELF-TUNING CONTROL OF ELECTROMAGNETIC LEVITATION SYSTEMS.
Control Engineering Practice, Volume 8, Issue 7, July 2000, Pages 749-756
Very Useful; full-text: (science_1_3c_14.pdf)

[L47] Kruusing, A.
ACTUATORS WITH PERMANENT MAGNETS HAVING VARIABLE IN SPACE ORIENTATION OF
MAGNETIZATION.
Sensors and Actuators A: Physical, Volume 101, Issues 1-2, 30 September 2002, Pages 168-174
Useful; Full-text: (science_2_3d_2.pdf)

[L48] Moses, A.J. and F. Al-Naemi, J. Hall
DESIGNING AND PROTOTYPING FOR PRODUCTION PRACTICAL APPLICATIONS OF ELECTROMAGNETIC
MODELLING.
Journal of Magnetism and Magnetic Materials, In Press, Uncorrected Proof, Available online 17 September 2002,
Useful; Full-text: (science_2_3d_3.pdf)

[L49] Kruusing, A.
OPTIMIZING MAGNETIZATION ORIENTATION OF PERMANENT MAGNETS FOR MAXIMAL GRADIENT FORCE.
Journal of Magnetism and Magnetic Materials, Volume 234, Issue 3, September 2001, Pages 545-555
Useful; Full-text: (science_2_3d_14.pdf)

[L50] Hafez, M. and T.C. Sidler, R.P. Salathé, G.L.M. Jansen, J.C. Compter
DESIGN, SIMULATIONS AND EXPERIMENTAL INVESTIGATIONS OF A COMPACT SINGLE MIRROR TIP/TILT
LASER SCANNER.
Mechatronics, Volume 10, Issue 7, 1 October 2000, Pages 741-760
Useful; Full-text: (science_2_3d_23.pdf)

[L51] Feeley, J.J.
SIMPLE DYNAMIC MODEL FOR EDDY CURRENTS IN A MAGNETIC ACTUATOR.
IEEE Transactions on Magnetics, Volume 32, Issue 2, March 1996, Pages 453-458
Very Useful; Full-text: (00486532.pdf)

[L52] Li, Xiujun; G. de Jong, G.C.M. Meijer
INFLUENCE OF ELECTRIC-FIELD BENDING ON THE NONLINEARITY OF CAPACITIVE SENSORS.
IEEE Transactions on Instrumentation and Measurement, Volume 49, Issue 2, 2000, Pages 256-259
Might be Useful; Full-text: (00843059.pdf)

[L53] Meijer, G.C.M. and G.W. De Jong
AN EFFICIENT RETRIEVING ALGORITHM FOR ACCURATE CAPACITIVE POSITION SENSORS.
Sensors and Actuators A: Physical, Volume 58, Issue 1, January 1997, Pages 75-84
Might be Useful; Full-text: (science_3_3_24.pdf)

[L54] Zaccarian, L. and A.R. Teel
A COMMON FRAMEWORK FOR ANTI-WINDUP, BUMPLESS TRANSFER AND RELIABLE DESIGNS.
Automatica, Volume 38, Issue 10, October 2002, Pages 1735-1744
Very Useful; Full-text: (science_4c_1.pdf)

[L55] Rodriguez, J.A. and J.A. Romagnoli, G.C. Goodwin
SUPERVISORY MULTIPLE REGIME CONTROL.
Journal of Process Control, In Press, Uncorrected Proof, Available online 12 February 2002,
Very Useful; Full-text: (science_4c_2.pdf)

[L56] Zuoxing Yang and Lei Zhao, Hongbin Zhao
GLOBAL LINEARIZATION AND MICROSYNTHESIS FOR HIGH-SPEED GRINDING SPINDLE WITH ACTIVE
MAGNETIC BEARINGS.
Magnetics, IEEE Transactions on , Volume: 38 Issue: 1 Part: 2 , Jan. 2002 Page(s): 250 -256
Useful; Full-text: (00990115.pdf)

[L57] Motee, N. and M.S. de Queiroz, Y. Fang, D.M. Dawson
ACTIVE MAGNETIC BEARING CONTROL WITH ZERO STEADY-STATE POWER LOSS.
American Control Conference, 2002. Proceedings of the 2002 , Volume: 1 , 2002
Page(s): 827 -832
Useful; Full-text: (01024917.pdf)

[L58] Chin-Teng Lin and Chong-Ping Jou
GA-BASED FUZZY REINFORCEMENT LEARNING FOR CONTROL OF A MAGNETIC BEARING SYSTEM.
Systems, Man and Cybernetics, Part B, IEEE Transactions on , Volume: 30 Issue: 2 , April 2000, Page(s): 276 -289
Might be Useful; Full-text: (00836376.pdf)

[L59] Tsiotras, P. and E. Velenis
LOW-BIAS CONTROL OF AMBS SUBJECT TO SATURATION CONSTRAINTS.
Control Applications, 2000. Proceedings of the 2000 IEEE International Conference on , 2000, Page(s): 138 -143
Might be Useful; Full-text: (00897413.pdf)

[L60]   Knospe, C.R.
         THE NONLINEAR CONTROL BENCHMARK EXPERIMENT.
         American Control Conference, 2000. Proceedings of the 2000 , Volume: 3 , 2000
         Page(s): 2134 -2138 vol.3
         Useful; Full-text: (00879578.pdf)

[L61]   Li, L. and J. Mao
         FEEDBACK LINEARISATION OF MAGNETIC BEARING ACTUATORS FOR A UNIFORM UPPER BOUND OF
         FORCE SLEW RATE.
         Electric Power Applications, IEE Proceedings- , Volume: 146 Issue: 4 , July 1999, Page(s): 378 -382
         Might be Useful; Full-text: (00796069.pdf)

[L62]   Duan, G.R. and Z.Y. Wu, C.M. Bingham, D. Howe
         ROBUST ACTIVE MAGNETIC BEARING CONTROL USING STABILIZING DYNAMICAL COMPENSATORS.
         Electric Machines and Drives, 1999. International Conference IEMD '99 , 1999, Page(s): 493 -495
         Very Useful; Full-text: (00769156.pdf)

[L63]   Kai-Yew Lum and V.T. Coppola, D.S. Bernstein
         ADAPTIVE AUTOCENTERING CONTROL FOR AN ACTIVE MAGNETIC BEARING SUPPORTING A ROTOR WITH
         UNKNOWN MASS IMBALANCE.
         Control Systems Technology, IEEE Transactions on , Volume: 4 Issue: 5 , Sept. 1996, Page(s): 587 -597
         Very Useful; Full-text: (00531925.pdf)

[L64]   Zhang Siyi and Zhao Lei, Zhang Xiantong, Zhang qing chun
         IMPROVEMENT OF PHASE MARGIN OF AMB CONTROL SYSTEM BY FLUX TIME DERIVATIVE.
         Computer, Communication, Control and Power Engineering. Proceedings. TENCON '93., 1993 IEEE Region 10
         Conference on Part: 40000 , 1993, Page(s): 544 -547 vol.4
         Useful; Full-text: (00320552.pdf)

[L65]   Williams, R.D., F.J. Keith, P.E. Allaire
         DIGITAL CONTROL OF ACTIVE MAGNETIC BEARINGS.
         Industrial Electronics, IEEE Transactions on , Volume: 37 Issue: 1 , Feb. 1990, Page(s): 19 -27
         Might be Useful; Full-text: (00045839.pdf)

[L66]   Ming Cheng and K.T. Chau, C.C. Chan, E. Zhou, X. Huang
         NONLINEAR VARYING-NETWORK MAGNETIC CIRCUIT ANALYSIS FOR DOUBLY SALIENT PERMANENT-
         MAGNET MOTORS.
         Magnetics, IEEE Transactions on , Volume: 36 Issue: 1 Part: 2 , Jan. 2000, Page(s): 339 -348
         Useful; Full-text: (00822544.pdf)

[L67]   Morera, X.A. and A.G. Espinosa
         MODELING OF CONTACT BOUNCE OF AC CONTACTOR.
         Electrical Machines and Systems, 2001. ICEMS 2001. Proceedings of the Fifth International Conference on , Volume:
         1 , 2001, Page(s): 174 -177 vol.1
         Useful; Full-text: (00970637.pdf)

[L68]   Hung, J.Y.
         MAGNETIC BEARING CONTROL USING FUZZY LOGIC.
         Industry Applications, IEEE Transactions on , Volume: 31 Issue: 6 , Nov.-Dec. 1995, Page(s): 1492 -1497
         Useful; Full-text: (00475746.pdf)

[L69]   Wang, T.C. and Yeou-Kuang Tzeng
         A NEW ELECTROMAGNETIC LEVITATION SYSTEM FOR RAPID TRANSIT AND HIGH SPEED
         TRANSPORTATION.
         Magnetics, IEEE Transactions on , Volume: 30 Issue: 6 Part: 1-2 , Nov. 1994, Page(s): 4734 -4736
         Useful; Full-text: (00334205.pdf)

[L70]   Abri, A. and R. Nordgren, S. Kjellnas, L. Banghammar, S. Lindgren
         FINITE ELEMENT ANALYSIS OF ELECTROMAGNETS AND CONTACT SYSTEMS IN LOW VOLTAGE CURRENT
         LIMITING CIRCUIT BREAKERS.
         Magnetics, IEEE Transactions on , Volume: 26 Issue: 2 , March 1990, Page(s): 960 -963
         Might be Useful; Full-text: (00106478.pdf)

[L71]   Srairi, K. and M.Feliachi, Z. Ren
         ELECTROMAGNETIC ACTUATOR BEHAVIOR ANALYSIS USING FINITE ELEMENT AND PARAMETRIZATION
         METHODS.
         Magnetics, IEEE Transactions on , Volume: 31 Issue: 6 Part: 2 , Nov. 1995, Page(s): 3497 -3499
         Useful; Full-text: (00489548.pdf)

[L72]   Charara, A. and J. de Miras, B. Caron
         NONLINEAR CONTROL OF A MAGNETIC LEVITATION SYSTEM WITHOUT PREMAGNETIZATION.
         IEEE Transaction on Control Systems Technology., vol 4, pp.513-523, Sept. 1996
         Useful; Full-text; Source: Snowball method

[L73]   Levine, J. and J. Lottin, J.C. Ponsart
A NONLINEAR APPROACH TO THE CONTROL OF MAGNETIC BEARINGS.
IEEE Transaction on Control Systems Technology., vol 4, pp.524-544, Sept. 1996
Useful; Full-text; Source: Snowball method

[L74]   Namerikawa, T and M. Fujita
MODELING AND ROBUSTNESS ANALYSIS OF A MAGNETIC SUSPENSION SYSTEM CONSIDERING
STRUCTURED UNCERTAINTIES.
Proc. 36th IEEE Conf.Decision Contr., 1997, pp. 2559-2564
Very Useful; Full-text; Source: Snowball method

[L75]   Nakashima, K. and T. Tsujino, T. Fujii
MULTIVARIABLE CONTROL OF A MAGNETIC LEVITATION SYSTEM USING CLOSED LOOP IDENTIFICATION
AND H_∞ CONTROL THEORY.
Proc. 35th IEEE Conf. Decision Contr., 1996, pp. 3668-3673
Useful; Full-text; Source: Snowball method

[L76]   Trumper, D. and S. Olson, P. Subrahmanyan
LINEARIZING CONTROL OF MAGNETIC SUSPENSION SYSTEMS.
IEEE Transaction on Control Systems Technology., vol 5, pp.427-437, July. 1997
Very Useful; Full-text; Source: Snowball method

[L77]   Charara, A and B. Caron, G. Lemarquand
MODELLING AND NONINTERACTIVE CONTROL OF AN ACTIVE MAGNETIC BEARING.
International-Journal-of-Applied-Electromagnetics-in-Materials. vol.2, no.4; April 1992; p.359-68.
Check on TU/e campus

[L78]   KwangSuk-Jung and YoonSu-Baek (Dept. of Mech. Eng., Yonsei Univ., Seoul, South Korea)
DESIGN, MODELING, AND CONTROL OF A NOVEL SIX D.O.F POSITIONING SYSTEM USING MAGNETIC
LEVITATION.
IEICE-Transactions-on-Electronics. Dec. 2000; E83-C(12): 1937-49.
Inst. Electron. Inf. & Commun. Eng
Check on TU/e campus

[L79]   Chin-E.—Lin and Jinn-Yin-Wang (Inst. of Aeronaut. & Astronaut., Cheng Kung Univ., Tainan, Taiwan)
DESIGN AND IMPLEMENTATION OF A 5-DOF MAGNETIC LEVITATED PLATFORM.
Proceedings-of-the-National-Science-Council,-Republic-of-China,-Part-A-Physical-Science-and-Engineering. Sept.
1997; 21(5): 428-436.
PUBLISHER: Natl. Sci. Council, Taiwan
Check on TU/e campus

[L80]   Fouad, F.A. and T.W. Nehl, N.A. Demerdash (Virginia Polytech. Inst. & State Univ., Blacksburg, VA, USA)
MAGNETIC FIELD MODELING OF PERMANENT MAGNET TYPE ELECTRONICALLY OPERATED
SYNCHRONOUS MACHINES USING FINITE ELEMENTS.
IEEE-Transactions-on-Power-Apparatus-and-Systems. vol.PAS-100, no.9; Sept. 1981; p.4125-4135.
Check on TU/e campus

[L81]   Gaspalou, B. and F. Colamartino, C. Marchand, Z. Ren (CNRS, Paris Univ. VI-XI, Gif-sur-Yvette, France)
SIMULATION OF AN ELECTROMAGNETIC ACTUATOR BY A COUPLED MAGNETOMECHANICAL MODELLING.
COMPEL-The-International-Journal-for-Computation-and-Mathematics-in-Electrical-and-Electronic-Engineering. Dec.
1995; 14(4): 203-6.
PUBLISHER: MCB University Press
Check on TU/e campus

[L82]   Gazi, E. and W.D. Seider, L.H. Ungar (Dept. of Chem. Eng., Pennsylvania Univ., Philadelphia, PA, USA)
CONTROL OF NONLINEAR PROCESSES USING QUALITATIVE REASONING.
Computers-&-Chemical-Engineering. vol.18, suppl.issue; 1994; p.S189-93.
Check on TU/e campus

[L83]   D. Lynch and A. Alleyne (Dept. of Mech. & Ind. Eng., Illinois Univ., Urbana, IL, USA)
VELOCITY SCHEDULED DRIVER ASSISTED CONTROL.
International-Journal-of-Vehicle-Design. vol.29, no.1-2; 2002; p.1-22.
Check on TU/e campus

[L84]   Nonami, K. and H. Ueyama, Y. Segawa
H CONTROL OF MILLING AMB SPINDLE.
JSME International Journal, Series C: Dynamics, Control, Robotics, Design and Manufacturing, Volume 39, Issue 3,
September 1996, Pages 502-508
Check on TU/e campus

[L85]   Antila, M
ELECTROMECHANICAL PROPERTIES OF RADIAL ACTIVE MAGNETIC BEARINGS.
Acta Polytechnica Scandinavica, Electrical Engineering Series, 1998, Pages 2-94
Check on TU/e campus

[L86]   Doi, T. and K. Yoshida, Y. Tamai, K. Kono, K. Naito, T. Ono
         FEEDBACK CONTROL FOR ELECTROMAGNETIC VIBRATION FEEDER (APPLICATION OF TWO-DEGREES-OF-
         FREEDOM PROPORTIONAL PLUS INTEGRAL PLUS DERIVATIVE CONTROLLER WITH NONLINEAR ELEMENT).
         JSME International Journal, Series C: Mechanical Systems, Machine Elements and Manufacturing, Volume 44, Issue
         1, 2001, Pages 44-52
         Check on TU/e campus

[L87]   Foggia, A. and N. Burais, L. Krahenbuhl, A. Nicolas (Dept. d'Electrotech., CNRS, Ecully, France)
         FINITE ELEMENT ANALYSIS OF A FAST ELECTROMAGNETIC ACTUATOR.
         IEEE-Transactions-on-Magnetics. Sept. 1984; MAG-20(5) pt. 2: 1942-4.
         Check on TU/e campus

[L88]   Kasarda, M. and J. Imlach, P.A. Balaji, J.T. Marshall
         CONCURRENT USE OF MAGNETIC BEARINGS FOR ROTOR SUPPORT AND FORCE SENSING FOR THE
         NONDESTRUCTIVE EVALUATION OF MANUFACTURING PROCESSES.
         Proceedings-of-the-SPIE --The-International-Society-for-Optical-Engineering. vol.3985; 2000; p.352-363.
         Could be useful, but no (hard)copy directly available

[L89]   Shyh-Leh-Chen and Ting-Chyi-Yeh
         MODELING AND ROBUST CONTROL OF A 4-POLE MAGNETIC ROTOR-BEARING SYSTEM WITH OPTIMAL
         BIAS CURRENTS.
         Journal-of-the-Chinese-Society-of-Mechanical-Engineers. April 2002; 23(2): 173-83.
         Could be useful, but no (hard)copy directly available

[L90]   Shi, J.
         MODELLING AND FUZZY LOGIC CONTROL OF AN ACTIVE MAGNETIC BEARING SYSTEM.
         MS'97.-Proceedings-of-the-Third-International-Conference-on-Modelling-and-Simulation. 1997: 194-9. Ed. by A.
         Zayegh.
         Dept. of Electr. & Electron. Eng., Victoria Univ. of Technol., Melbourne, Vic., Australia
         Could be useful, but no (hard)copy directly available

[L91]   Chin-E.-Lin and Huei-Long-Jou (Inst. of Aeronaut. & Astronaut., Nat. Cheng Kung Univ., Tainan, Taiwan)
         MODEL ATTITUDE CONTROL FOR MAGNETIC SUSPENSION WIND TUNNEL.
         Proceedings-of-the-National-Science-Council,-Republic-of-China,-Part-A-Physical-Science-and-Engineering. May
         1997; 21(3): 222-32.
         PUBLISHER: Natl. Sci. Council, Taiwan
         Could be useful, but no (hard)copy directly available

[L92]   Tchaban, V. and Y. Kovivchak, V. Maday (Lviv Polytech. Nat. Univ., Ukraine)
         SIMULATION OF ELECTROMAGNETIC FIELD OF ELECTROMAGNET.
         MA'2001-Lviv.-International-Conference-on-Modeling-and-Simulation.-Proceedings. 2001: 19-20.
         PUBLISHER: Lviv Polytechnic National Univeristy, Lviv, Ukraine
         Could be useful, but no (hard)copy directly available

[L93]   Shagirov, E.A..
         SIMULATION OF THE MAGNETIC FIELD AND ION TRAJECTORIES IN A DEFLECTING ELECTROMAGNET.
         Computational-Mathematics-and-Modeling. July-Sept. 1992; 3(3): 347-51.
         Could be useful, but no (hard)copy directly available

[L94]   Sadowski, N. and Y. Lefevre, M. Lajoie-Mazenc, J.P.A. Bastos (Lab. d'Electrotech. et d'Electron. CNRS, Toulouse,
         France)
         CALCULATION OF TRANSIENT ELECTROMAGNETIC FORCES IN AN AXISYMMETRICAL ELECTROMAGNET
         WITH CONDUCTIVE SOLID PARTS.
         COMPEL-The-International-Journal-for-Computation-and-Mathematics-in-Electrical-and-Electronic-Engineering.
         March 1992; 11(1): 173-6.
         Could be useful, but no (hard)copy directly available

[L95]   Chiampi, M., A. Piazzoli, E. Serra, M. Tartaglia (Istituto Elettrotechnico Nazionale Galileo Ferraris, Torino, Italy)
         MODELLING ANALYSIS OF A DC ELECTROMAGNETIC CONTACTOR.
         International-Journal-of-Modelling-and-Simulation. 1990; 10(1): 22-6.
         Could be useful, but no (hard)copy directly available

[L96]   Chiampi, M. and M. Tartaglia (Istituto Elettrotecnico Nazionale Galileo Ferraris, Torino, Italy)
         ELECTROMAGNET MODEL THROUGH MAGNETIC FIELD ANALYSIS.
         International-Journal-of-Modelling-and-Simulation. 1987; 7(1): 43-6.
         Could be useful, but no (hard)copy directly available

[L97]   Germann, L.M.; D.R. Lutter (Left Hand Design Corp., Longmont, CO, USA)
         ELECTRO-MAGNETIC ACTUATOR WITH SIMPLE MAGNETIC PATH INCREASES EFFICIENCY AND REDUCES
         COST.
         Proceedings-of-the-SPIE-The-International-Society-for-Optical-Engineering. 1996; 2865: 84-92.
         PUBLISHER: SPIE-Int. Soc. Opt. Eng
         Could be useful, but no (hard)copy directly available

[L98]   Boukhtache, S. and Z. Ren, A. Razek (CNRS, Paris VI Univ., France)
          MODELLING OF MECHANICAL BEHAVIOUR OF AN ELECTROMAGNETIC ACTUATOR ACCOUNTING FOR
          DAMPER EFFECT.
          ICEM-94.-International-Conference-on-Electrical-Machines. 1994: 134-9 vol.3.
          PUBLISHER: Soc. Electr. Electron, Paris, France
          Could be useful, but no (hard)copy directly available

[L99]   Nowak, L.(Inst. of Ind. Electr. Eng., Poznan Tech. Univ., Poland)
          DYNAMIC OPERATION OF AN ELECTROMAGNETIC ACTUATOR TAKING NONLINEARITY AND EDDY
          CURRENTS INTO ACCOUNT.
          15th-Symposium.-Electromagnetic-Phenomena-in-Nonlinear-Circuits.-Proceedings.-EPNC'98. 1998: 26-9.
          PUBLISHER: Polish Soc. Theoretical & Appl. Electr. Eng, Poznan, Poland
          Could be useful, but no (hard)copy directly available

[L100]   Ying, T.F. and H.H. Chiu, C.L. Liang, Y.T. Huang, H.H. Cheng, C.D. Wu (Mater. Res. Lab., Ind. Technol. Res. Inst.,
          Hsinchu, Taiwan)
          DYNAMIC MODELING OF EM ACTUATOR FOR CAMERA SHUTTER.
          MRL-Bulletin-of-Research-and-Development. Oct. 1991; 5(2): 27-30.
          Could be useful, but no (hard)copy directly available

[L101]   Wagner, N.G. and K. Steff
          DYNAMIC LABYRINTH COEFFICIENTS FROM A HIGH-PRESSURE FULL-SCALE TEST RIG USING MAGNETIC
          BEARINGS.
          NASA Conference Publication, 1997, Pages 95-111
          Could be useful, but no (hard)copy directly available

[L102]   Wang, H. and Z. Wu
          EFFECTS OF AMB PARAMETERS ON THE DYNAMIC STABILITY OF THE ROTOR.
          Applied Mathematics and Mechanics (English Edition), Volume 15, Issue 4, April 1994, Pages 347-351
          Not available on TU/e campus (series only got to 1986, searched by ISSN number)
          Could be useful, but no (hard)copy directly available

[L103]   Sheu, Jia-Shing and Tyng-Ych Wu, Jyh-Ching Juang
          MODELING AND ROBUST CONTROL OF A MAGNETIC BEARING SYSTEM.
          Journal of the Chinese Institute of Engineers, Transactions of the Chinese Institute of Engineers,Series A/Chung-kuo
          Kung Ch'eng Hsuch K'an, Volume 22, Issue 2, 1999, Pages 139-148
          Could be useful, but no (hard)copy directly available

[L104]   Chen, Shyh-Leh and Ting-Chyi Yeh
          MODELING AND ROBUST CONTROL OF A 4-POLE MAGNETIC ROTOR-BEARING SYSTEM WITH OPTIMAL
          BIAS CURRENTS.
          Journal of the Chinese Society of Mechanical Engineers, Transactions of the Chinese Institute of Engineers, Series
          C/Chung-Kuo Chi Hsueh Kung Ch'eng Hsuebo Pao, Volume 23, Issue 2, 2002 April, Pages 173-183
          Could be useful, but no (hard)copy directly available

[L105]   Tsunashima, H. and T. Fujioka, M. Abe, K. Sasaki
          INFLUENCE OF GUIDEWAY SURFACE ROUGHNESS ON A MAGNETICALLY LEVITATED VEHICLE WITH
          MECHANICAL LEVITATION CONTROL (4TH REPORT, INFLUENCE OF NONLINEAR CHARACTERISTICS OF
          MAGNET).
          Nippon Kikai Gakkai Ronbunshu, C Hen/Transactions of the Japan Society of Mechanical Engineers, Part C, Volume
          62, Issue 594, February 1996, Pages 530-535
          Could be useful, but no (hard)copy directly available

[L106]   Tsunashima, H. and T. Fujioka, M. Abe
          DYNAMICS OF A MECHANICALLY CONTROLLED PERMANENT MAGNET SUSPENSION FOR MAGLEV
          TRANSPORT VEHICLE.
          Transportation Systems; American Society of Mechanical Engineers, Dynamic Systems and Control Division
          (Publication) DSC, Volume 54, 1994, Pages 265-275
          Could be useful, but no (hard)copy directly available

[L107]   Roberts, P.W. and P. Tcheng
          STRAIN-GAGE BALANCE CALIBRATION OF A MAGNETIC SUSPENSION AND BALANCE SYSTEM.
          ICIASF Record, International Congress on Instrumentation in Aerospace Simulation Facilities, 1987, Pages 308-321
          Could be useful, but no (hard)copy directly available

[L108]   Brusa, G.and A. Riccardi, S. Ragland, S. Esposito, C. Del Vecchio, L. Fini, P. Stefanini, V. Biliotti, P. Ranfagni,
          P.; Salinari et al.
          ADAPTIVE SECONDARY P30 PROTOTYPE: LABORATORY RESULTS.
          Proceedings of SPIE - The International Society for Optical Engineering, Volume 3353, Issue 2, 1998, Pages 764-775
          Could be useful, but no (hard)copy directly available

[L109]   Durali, M. and H. Bateni
          NONLINEAR BEHAVIOUR AND CONTROL OF ACTIVE ELECTROMAGNETIC BEARINGS.
          International Journal of Modelling and Simulation, Volume 19, Issue 4, 1999, Pages 397-404
          Could be useful, but no (hard)copy directly available

[L110]   Brusa, G. and A. Riccardi, V. Biliotti, C. Del Vecchio, P. Salinari, P. Stefanini, P. Matengazza, R. Biasi, M.
         Andrighettoni, Franchini et al.
         ADAPTIVE SECONDARY MIRROR FOR THE 6.5M CONVERSION OF THE MULTIPLE MIRROR TELECOSPE:
         FIRST LABORATORY TESTING RESULTS.
         Proceedings of SPIE - The International Society for Optical Engineering, Volume 3762, 1999, Pages 38-49 (this paper
         is like 21CU)
         Could be useful, but no (hard)copy directly available

[L111]   Barrett, T.K. and D.G. Bruns, T.J. Brinkley, D.G. Sandler, B.C. FitzPatrick, J.R.P. Angel, T. Rhoadarmer
         ADAPTIVE SECONDARY MIRROR FOR THE 6.5-M MMT.
         Proceedings of SPIE - The International Society for Optical Engineering, Volume 3353, Issue 2, 1998, Pages 754-763
         Could be useful, but no (hard)copy directly available

[L112]   Liu, S.and H. Xu, L. Yu
         ROBUST PROPORTIONAL INTEGRAL DIFFERENTIAL CONTROLLER DESIGN BASED ON H INFINITY THEORY
         FOR ACTIVE MAGNETIC BEARING.
         Hsi-An Chiao Tung Ta Hsueh/Journal of Xi'an Jiaotong University, Volume 35, Issue 6, 2001 June, Pages 625-
         628+651
         Could be useful, but no (hard)copy directly available

14.2.2 Important literature survey results

Table 14.1 Publications rated as Very Useful.

Article	Year	Subject
L21	2002	An electro magnetically driven X-Y-θ stage.
L30	2001	The modelling of an electromagnetic actuator.
L39	2002	Real-time adaptive control of AMB's using LPV models.
L46	2000	Self-tuning control of electromagnetic levitation systems.
L51	1996	A simple dynamic model for Eddy currents in a magnetic actuator.
L54	2002	A framework for anti-windup, bumpless transfer and reliable designs.
L55	2002	Supervisory multiple regime control (controller switching).
L62	1999	Robust AMB control.
L63	1996	Adaptive autocentering control for an AMB.
L74	1997	Modeling and robustness analysis of a magnetic suspension system.
L76	1997	Linearizing control of magnetic suspension systems.

Table 14.2 Publications that contain information about a nearly similar device.

Article	Year	Subject
L21	2002	An electro magnetically driven X-Y-θ stage.
L27	2002	The design and control of a maglev positioner.
L41	2000	3-DOF micro-positioning system using EM actuators and air bearings.
L42	2001	A moving magnet type precision miniature platform for fine positioning and compliant motion.
L50	1999	A single mirror tip/tilt laser scanner.

Table 14.3 Publications that contain information about quite similar devices.

Article	Year	Subject
L22	2002	The design and control of an electrostatic micro-actuator.
L26	1996	Real-time motion control of a multi-DOF spherical motor.
L34	1990	The design and characterization of a linear motion piezo-electric micro-positioner.
L43	2000	The design, implementation and self-tuning adaptive control of a maglev guiding system.

14.2.3 Relation between literature contents and the main research topics

Matrix table 14.4 shows a summery of the relation between the contents of found literature and the main research subjects of the tilting mirror prototype.

Valuation of the literature: (VU = Very useful, U = useful, MU = Might be useful).

The publication's contents is marked in the corresponding columns:
(Black marking = subject is worked out in publication; Grey marking = subject is only mentioned in publication; Simulation: A = (Magnetic) Actuator, S = Sensor, C = Controller).

Table 14.4 Relation between the contents of found literature and the project.

Valuation*	Article	Year of Publication	1 dynamics	2a PM Modeling	2b Modeling	2c Modeling Dynamics	3a Sensor Calibration	3b Actuator Calibration	4 Sensors	5 Multiple Controllers	6 Simulation	7 FEM
VU	L1	2001									A	
U	L2	2002									A	
U	L3	1998									A	
MU	L4	1998										
U	L5	2002										
U	L6	1996										
U	L7	1999									AC	
U	L8	1998									A	
U	L9	1994									A	
MU	L10	1999									S	
MU	L11	1997										
MU	L12	2000									C	
MU	L13	1999										
U	L14	1997										
U	L15	1997									C	
MU	L16	2002										
U	L17	2001									AC	
U	L18	2000									C	
U	L19	1996										
U	L20	1993										
VU	L21	2002										
MU	L22	2002										
MU	L23	1999									S	
U	L24	1997										
U	L25	2002										
MU	L26	1996										
U	L27	2002										
MU	L28	1997									A	
U	L29	2001										
VU	L30	2001										
MU	L31	2000									A	
MU	L32	1997									S	
MU	L33	1996										
MU	L34	1990									A	

Valuation[♥]	Article	Year of Publication	1 Control	2a PM Modeling	2b EM Modeling	2c Modeling Dynamics	3a Sensor Calibration	3b Actuator Calibration	4 Sensors	5 Multiple Controllers[♥♥]	6 Simulation	7 FEM
U	L35	2001	■							■	C	
U	L36	2000				■				■	C	
MU	L37	1996	■			■					C	
MU	L38	2001	■		■	■						
VU	L39	2002		■	■	■					AC	
MU	L40	2002		■	■	■			■			
U	L41	2000	■		■							
U	L42	2001	■			■						
U	L43	2000				■		■	■		AC	
MU	L44	1999	■	■		■						
MU	L45	1994	■			■					AC	
VU	L46	1999	■		■	■					AC	
U	L47	2002		■				■			A	
U	L48	2002		■	■						A	■
U	L49	2001		■	■						A	■
U	L50	1999			■						(AC)	■
VU	L51	1996			■							
MU	L52	2000							■		S	
MU	L53	1996							■		S	
VU	L54	2002	■							■	C	
VU	L55	2002	■									
U	L56	2002	■		■	■					AC	
U	L57	2002	■		■	■					(AC)	
MU	L58	2000		■	■	■						
MU	L59	2000	■		■	■					C	
U	L60	2000			■	■						■
MU	L61	1999	■		■						A	
VU	L62	1999	■		■	■						
VU	L63	1996	■			■					(A)C	
U	L64	1993	■		■						A	
MU	L65	1990	■									
U	L66	2000			■							■
U	L67	2001			■	■					A	
U	L68	1995	■		■	■					AC	
U	L69	1994	■									
MU	L70	1990			■	■					A	■
U	L71	1995			■							
U	L72	1996	■		■	■					AC	
U	L73	1996	■		■	■			■		AC	
VU	L74	1997	■		■	■					AC	
U	L75	1996	■		■	■				■	AC	
VU	L76	1997	■		■	■					EXP.	

♥ The valuation is based on the complete paper. The columns 4-13 are marked when a paper contains information about the subject belonging to it. It doesn't necessarily mean the content of that subject is valuated.

♥♥ Multiple controllers working together to control one device, not multiple controllers that are being compared, controlling the same device separately.

14.3 Used Internet web-pages

[W1]   Festo AG & Co. KG
        Manufacturer of amongst other things: vacuum systems, suction cups and suction grippers.
        www.festo.com

[W2]   Sensor Show
        Sorted links to all kinds of sensor manufacturers.
        www.sensorshow.com

[W3]   Bokam Engineering Inc.
        Producer of multi-axis Force sensors.
        www.bokam.com

[W4]   ATI Industrial Automation
        Producer of multi-axis Force/Torque transducers.
        www.ati.com

14.4 Used software

[S1]   MATLAB® 5.3 R11
        The MathWorks Inc., 1999
        Mathematical software package (especially for matrix manipulations and control engineering).

[S2]   Mathematica 2.2.3 For Windows
        Wolfram Research Inc, 1994
        Mathematical software package (especially for computer algebra).

[S3]   DesignCAD 3DMAX
        2001
        Mechanical engineering design tool.

Postscript

After reading the Ph.D.-thesis [1], I was impressed by how relative simple techniques were combined to form a complex whole: the prototype of the magnetically levitated tilting mirror.

What I found was an intelligent design merging several fields of electrical engineering (electromagnetism, electronics, modeling and control).

Unfortunately, the Ph.D.-thesis proved not to be flawless. It is my impression that one person alone working on a complex project makes the work vulnerable for (unintentional) mistakes. Reviewing of the work [1] by others would have saved me a lot of work and time and it might even resulted in an operational device at the end of the Ph.D. period.

Although the device still is not operational, I think I have made a step forward towards making it stable, after first setting a step back, making the Ph.D.-thesis corrections and supplements (Part 1).

In general, with my work I hope to have made a valuable contribution to the research of the MBS-CS division.

Acknowledgements

APPENDICES

Appendix A Corrected expressions

A.1 Corrected formula for $I_{A,x}^V$ [1, (D.16)]

Rotor-part A is part of a sphere with radius R. When the sphere is thought of as a stack of horizontal flat discs, its moment of inertia can be calculated with the standard inertia of a disc and the Steiner rule [2]:

$$I_{DISC} = \tfrac{1}{4}(dm)r^2 + (dm)z^2 \tag{A.1}$$

r is radius of a disc at height z: $r = \sqrt{R^2 - z^2}$ $\tag{A.2}$

dm is the mass of the disc: $dm = m_{DISC} = \rho_{Al}\cdot\pi r^2 \cdot dz = \rho_{Al}\cdot\pi \, (R^2 - z^2)dz$ $\tag{A.3}$

Combining (A.1), (A.2) and (A.3) yields:

$$I_{DISC} = \tfrac{1}{4}\cdot\rho_{Al}\cdot\pi \, (R^4 + 2R^2z^2 - 3z^4)dz \tag{A.4}$$

Now the total moment of inertia (around the x-axis of the rotor) of part A can be calculated taking the sum of all horizontal discs between z = -R and z = -a, together forming the spherical shape A:

$$I_{A,x}^V = \int_{z=-R}^{z=-a} I_{DISC} = \frac{\pi\rho_{Al}}{4}\int_{z=-R}^{z=-a}(R^4 + 2R^2z^2 - 3z^4)\,dz = \frac{\pi\rho_{Al}}{4}\left[R^4z + \tfrac{2}{3}R^2z^3 - \tfrac{3}{5}z^5\right]_{z=-R}^{z=-a} =$$

$$= \frac{\pi\rho_{Al}}{4}\left[-aR^4 - \tfrac{2}{3}R^2a^3 + \tfrac{3}{5}a^5 + R^5 + \tfrac{2}{3}R^5 - \tfrac{3}{5}R^5\right] = \frac{\pi\rho_{Al}}{4}\left[\tfrac{16}{15}R^5 - aR^4 - \tfrac{2}{3}R^2a^3 + \tfrac{3}{5}a^5\right] =$$

$$= \pi\rho_{Al}\left[\tfrac{4}{15}R^5 - \tfrac{1}{4}aR^4 - \tfrac{1}{6}R^2a^3 + \tfrac{3}{20}a^5\right] \tag{A.5}$$

A.2 Corrected formula for $I_{C,x}^V$ [1, (D.18)]

Proposed corrections for this formula are:
Parameter b should be r_1. Parameter h_{PM} should be replaced by $a + h_2$. The last a in the formula should have a minus-sign. The last cylinder-term should have a minus-sign (caused by unnecessary and therefore only confusing nesting!!!)

The corrected formula:

$$I_{C,x}^V = \rho_{Fe}\left[\pi(a+h_2)(r_1^2 - r_2^2)\left\{\tfrac{1}{12}(3r_1^2 + 3r_2^2 + (a+h_2)^2 + \left(\frac{a-h_2}{2}\right)^2\right\} - \tfrac{1}{5}h_2\pi r_1^2\left\{\frac{r_1^2}{4} + h_2^2\right\} + \right.$$

$$\left. + \tfrac{1}{5}(h_1 - a)\pi r_2^2\left\{\frac{r_2^2}{4} + (h_1 - a)^2\right\} + \pi r_2^2(h_2 - h_1 + a)\left\{\frac{r_2^2}{4} + \tfrac{1}{12}(h_2 - h_1 + a)^2 + \left(\frac{h_1 + h_2 - a}{2}\right)^2\right\}\right]$$

$$\tag{A.6}$$

A.3 Corrected formula for $I_{D,x}^V$ [1, (D.19)]

Besides the typo (ρ_{Fe} switched for m_D) the outcome of the calculation in [1] differs from mine:

$$I_{D,x}^V = 4\rho_{Fe} \int_{h=-a}^{h_2} \int_{\varphi=22.5°}^{67.5°} \int_{r=r_1}^{b} (h^2 + r^2 \sin^2\varphi)\, r\, dr\, d\varphi\, dh =$$

$$= 4\rho_{Fe} \int_{h=-a}^{h_2} \int_{\varphi=22.5°}^{67.5°} \left[\frac{r^2 h^2}{2} + \tfrac{1}{4}r^4 \sin^2\varphi\right]_{r=r_1}^{r=b} d\varphi\, dh = \quad \{\text{with } \sin^2\varphi = \tfrac{1}{2}(1-\cos2\varphi)\}$$

$$= 4\rho_{Fe} \int_{h=-a}^{h_2} \int_{\varphi=22.5°}^{67.5°} \left[\frac{(b^2 - r_1^2)}{2}h^2 + \tfrac{1}{8}(b^4 - r_1^4)(1-\cos2\varphi)\right] d\varphi\, dh =$$

$$= 4\rho_{Fe} \int_{h=-a}^{h_2} \left[\frac{(b^2 - r_1^2)}{2}h^2\varphi + \tfrac{1}{8}(b^4 - r_1^4)(\varphi - \tfrac{1}{2}\sin2\varphi)\right]_{\varphi_1=22.5°}^{\varphi_2=67.5°} dh =$$

$$= 4\rho_{Fe}(\varphi_2 - \varphi_1) \int_{h=-a}^{h_2} \left(\frac{(b^2 - r_1^2)}{2}h^2 + \tfrac{1}{8}(b^4 - r_1^4)\right) dh =$$

$$= 4\rho_{Fe}(\varphi_2 - \varphi_1)\left[\frac{(b^2 - r_1^2)}{6}h^3 + \tfrac{1}{8}h(b^4 - r_1^4)\right]_{h=-a}^{h_2} =$$

$$= 4\rho_{Fe}(\varphi_2 - \varphi_1)\left(\frac{(b^2 - r_1^2)}{6}(h_2^3 + a^3) + \tfrac{1}{8}(h_2 + a)(b^4 - r_1^4)\right) = \underline{\underline{2.69 \cdot 10^{-8}}}\ [\text{kgm}^2] \tag{A.7}$$

Remember this formula is just an approximation and the uncorrected Ph.D.-thesis parameter values are used!

A.4 Corrected formula for $I_{E,x}^V$ [1, (D.20)]

The permanent magnets on the y-axis also have a Steiner distance of $(a - h_{PM}/2)$ in the –z-direction. Together with their displacement in the y-direction (R) the total Steiner distance is $\sqrt{R^2 + (a - h_{PM}/2)^2}$ instead of only R. For this reason, the last term in the formula should be doubled:

$$I_{E,x}^V = 2\rho_{PM}h_{PM}w_{PM}l_{PM}\left[\frac{l_{PM}^2}{12} + \frac{w_{PM}^2}{12} + \frac{h_{PM}^2}{6} + R^2 + \underline{2}\left(a - \frac{h_{PM}}{2}\right)^2\right] = 9.0616 \cdot 10^{-8}\ [\text{kgm}^2] \tag{A.8}$$

A.5 Corrected formulae for generated torques by vertical coils

Formulae (3.14) are the corrections for division by the angle α of the total coil length over the top- and bottom-part of a vertical coil. Together with the permanent magnet flux distribution, (3.14) can be used to calculate the generated torques by the vertical coils. This is the magnitudes, not the directions!

+α coil

Top part +α1: permanent magnet flux = -J/2 and is coupled $N_{VC}\left(\dfrac{k-\alpha}{2k}\right)$ times.

Bottom part +α2: permanent magnet flux = J/2 and is coupled $N_{VC}\left(\dfrac{k+\alpha}{2k}\right)$ times.

Together this gives for the +α coil:

$$\Phi_{coupled,0,+\alpha} = -\frac{J}{2}N_{VC}\left(\left(\frac{k-\alpha}{2k}\right)-\left(\frac{k+\alpha}{2k}\right)\right) = \frac{JN_{VC}}{2k}\alpha \qquad (A.9)$$

The contribution to the total torque T_α by the +α coil alone can now be calculated:

$$T_{+\alpha} = \frac{d\Phi_{coupled,0,+\alpha}}{d\alpha}(I_\alpha + I_z) = \frac{JN_{VC}}{2k}(I_\alpha + I_z) \qquad (A.10)$$

-α coil

Top part -α1: permanent magnet flux = -J/2 and is coupled $N_{VC}\left(\dfrac{k+\alpha}{2k}\right)$ times.

Bottom part -α2: permanent magnet flux = J/2 and is coupled $N_{VC}\left(\dfrac{k-\alpha}{2k}\right)$ times.

Together this gives for the -α coil:

$$\Phi_{coupled,0,-\alpha} = -\frac{J}{2}N_{VC}\left(\left(\frac{k+\alpha}{2k}\right)-\left(\frac{k-\alpha}{2k}\right)\right) = -\frac{JN_{VC}}{2k}\alpha \qquad (A.11)$$

The contribution to the total torque T_α by the -α coil alone can now be calculated:

$$T_{-\alpha} = \frac{d\Phi_{coupled,0,-\alpha}}{d\alpha}(-I_\alpha + I_z) = -\frac{JN_{VC}}{2k}(-I_\alpha + I_z) \qquad (A.12)$$

Combining (A.10) and (A.12) gives the total torque T_α :

$$T_\alpha = T_{+\alpha} + T_{-\alpha} = -\frac{JN_{VC}}{2k}(-2I_\alpha - I_z + I_z) = \frac{JN_{VC}}{k}I_\alpha \qquad (A.13)$$

The derivation of the magnitude of torque T_β is equivalent.

Appendix B   Exact formulae for approximated rotor parameters

The properties of rotor-part C and D can be calculated exactly using cylinder coordinates. To do this properly, first the definition of the rotor dimensions has slightly been changed (section B.1). These dimensions are only used in this appendix and the MATLAB®-file in which the numerical values of all the rotor parameters are calculated. The results of the MATLAB®-calculations are presented in table 5.1 (see chapter 5).

B.1 Altered rotor dimensions

The illogical choice (for me) of rotor dimensions in [1] has been changed to simplify the correcting and reviewing of found expressions. The altered definition of dimensions of the rotor is presented below.
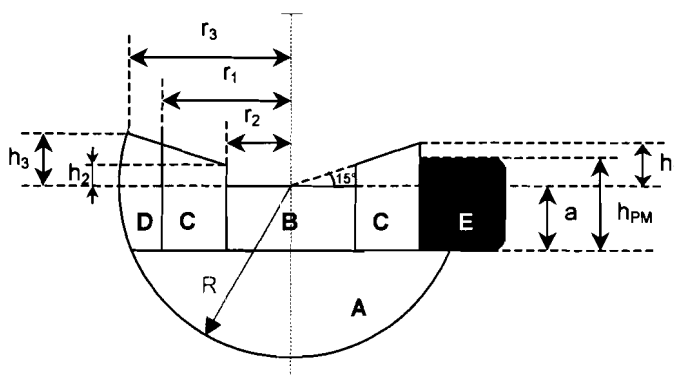

Table B.1 Rotor dimensions.

Parameter	Value
a [mm]	2.8
R [mm]	8
r_1 [mm]	6
r_2 [mm]	3
r_3 [mm]	$R\cos15° \approx 7.73$
h_1 [mm]	$r_1\tan15° \approx 1.61$
h_2 [mm]	$r_2\tan15° \approx 0.80$
h_3 [mm]	$R\sin15° \approx 2.07$
x_1 [mm]	$2.5/\tan26.5° \approx 5.01$
x_2 [mm]	$r_1 - x_1 \approx 0.96$
w_{PM} [mm]	5
l_{PM} [mm]	4
h_{PM} [mm]	4.3
φ_2	26.5°
R_{PM} [mm]	$r_1 + l_{PM} = 10$

Figure B.1
Double cross-section of the rotor showing the dimensions of the rotor. Left side: uz-plane with X-shaped rotor leg. Right side: xz-plane with a permanent magnet.

B.2 Derivation of the z-coordinate of the center of gravity

As figure B.1 and [1] show, the rotor is composed of parts that are positioned symmetrical around the z-axis of the rotor. This means that the center of gravity of these separate parts (A, B, C and D) and the composition of the four permanent magnets (E) are all located on the z-axis. Because of this property, the center of gravity of the complete rotor is positioned on the z-axis too.

For the derivation of the (z-coordinate of the) center of gravity of an object, a mathematical integration technique can be applied.
The following two properties are used:

①   The parts in which the integration is done are homogenous▼, so the mass density ρ is constant.

②   The total is the sum of the parts, so $l_{TOT}\, m_{TOT} = \sum l\, dm$ (B.1)

▼ In reality the rotor-parts C and D consist of thin layers of iron (with a high magnetic permeability) that are glued together. The layers of glue can and will be left out of consideration here.

Because I is equal to the z-coordinate (B.1) can also be written as:

$$I_{TOT}\, m_{TOT} = \sum z\, dm \tag{B.2}$$

Since ① is valid, the masses in (B.2) can be converted to volumes:

$$I_{TOT}\, \rho V_{TOT} = \sum z\, dm = \sum z\rho\, dV = \sum z\rho\, dxdydz = \sum z\rho r\, drd\varphi dz \tag{B.3}$$

When both sides of equation (B.3) are divided by ρ, the result is:

$$I_{TOT}\, V_{TOT} = \sum (z\, dxdy)dz = \sum zr\, drd\varphi dz \Leftrightarrow I_{TOT} = \frac{\sum (z\, dxdy)dz}{V_{TOT}} = \frac{\sum (zr\, drd\varphi)dz}{V_{TOT}} \tag{B.4}$$

Formula (B.4) can be interpreted as follows:
$\sum dxdy$ (or $\sum rdrd\varphi$) is the surface of the horizontal cross-section of an object at height z. This quantity is multiplied by the height z. Subsequently these values are calculated and summarized over the total height of the object. To get the wanted z-coordinate, this last sum must be divided by the total volume of the object.

B.3 Exact formula for I_c

Parameter I_c is the z-coordinate of the center of gravity of rotor-part C. It is expressed with respect to the plane z = 0. For calculation purposes, rotor-part C will be divided in two parts, see figure B.2. For these parts the z-coefficient of the center of gravity (I_{botc} and I_{topC}) will be calculated separately. Subsequently these values are used to calculate the height of the center of gravity of the complete part C.
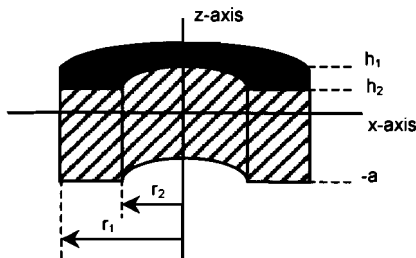

Figure B.2
Half of rotor-part C with its dimensions drawn at the vertical cross-section. The green bottom-part is a tube and the red top-part is also a tube, cut off at an angle of 15°.

Bottom-part of C

The volume of the bottom-part of C is:

$$V_{botC} = \pi \int_{z=-a}^{h_2} (r_1^2 - r_2^2)dz = \left[\pi(r_1^2 - r_2^2)z\right]_{z=-a}^{h_2} = \pi(r_1^2 - r_2^2)(h_2 + a) = 3.5689 \cdot 10^{-7}\,[m^3] \tag{B.5}$$

The center of gravity of bottom-part C is positioned on the z-axis. A horizontal plane at half the height would split this part in two equal halves. Consequently the center of gravity is located in this plane and on the z-axis, so calculated with respect to the plane z = 0 this is:

$$I_{botC} = \left(\frac{a+h_2}{2} - a\right) = \left(\frac{h_2-a}{2}\right) = -9.9808 \cdot 10^{-4}\,[m] \tag{B.6}$$

Top-part of C

The outer radius of this part is constant and equal to r_1.
The inner radius is dependent on the height z: $r_{in} = (z / \tan 15°)$.   (B.7)

The volume of the top-part of C is:

$$V_{topC} = \pi \int_{z=h_2}^{h_1} \left(r_1^2 - \left(\frac{z}{\tan 15°} \right)^2 \right) dz = \pi \left[r_1^2 z - \tfrac{1}{3} z^3 \left(\frac{1}{\tan^2 15°} \right) \right]_{z=h_2}^{h_1} =$$

$$= \pi \left[r_1^2 [h_1 - h_2] - \tfrac{1}{3} \left(\frac{1}{\tan^2 15°} \right) [h_1^3 - h_2^3] \right] = 3.7880 \cdot 10^{-8} \, [m^3]$$ (B.8)

The z-coordinate of the center of gravity of the top-part of C can be calculated by substituting $r_{out} = r_1$, $r_{in} = (z / \tan 15°)$, $(h_2 \leq z \leq h_1)$ and (B.8) in formula (B.4):

$$l_{topC} = \frac{\pi}{V_{topC}} \int_{z=h_2}^{h_1} z \left(r_1^2 - \left(\frac{z}{\tan 15°} \right)^2 \right) dz = \frac{\pi}{V_{topC}} \left[\tfrac{1}{2} r_1^2 z^2 - \tfrac{1}{4} z^4 \left(\frac{1}{\tan^2 15°} \right) \right]_{z=h_2}^{h_1} =$$

$$= \frac{\pi}{V_{topC}} \left[\tfrac{1}{2} r_1^2 [h_1^2 - h_2^2] - \tfrac{1}{4} \left(\frac{1}{\tan^2 15°} \right) [h_1^4 - h_2^4] \right] = 1.0852 \cdot 10^{-3} \, [m]$$ (B.9)

Total part C

Using formula (B.1) and filling in (B.5), (B.6), (B.8) and (B.9) gives the z-coordinate of the center of gravity of whole part C:

$$l_C = \frac{l_{botC} \cdot V_{botC} + l_{topC} \cdot V_{topC}}{V_{botC} + V_{topC}} = -7.6838 \cdot 10^{-4} \, [m]$$ (B.10)

B.4 Exact formula for m_D

For calculation purposes, rotor-part D will be divided up in several parts. First the mass of the total D-ring (m_{DT}) is calculated (see figure B.3). After that, the mass of the four cut-outs for the permanent magnets (m_{Dcut}) is calculated (see figure B.4). These two values are subtracted to obtain the mass of rotor-part D: ($m_D = m_{DT} - m_{Dcut}$).

Figure B.3
Half of the total D-ring, so with the cut-outs
for the permanent magnets. Its dimensions
are drawn at the vertical cross-section.
The black bottom-part is a tube with a
spherical outer surface. The gray top-part
is also a tube with a spherical outer
surface, cut off at an angle of 15°.
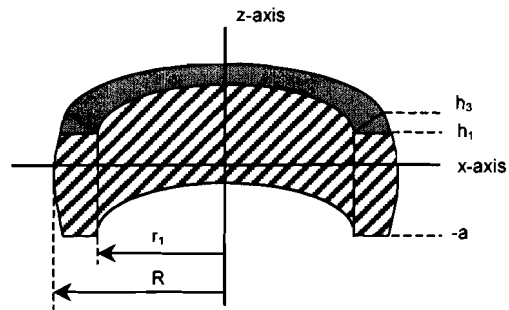
The surface of a horizontal cross-section of the total D-ring at height z =

$$\int_{\varphi=0}^{2\pi}\int_{r=r_{in}}^{r_{out}} r\,dr\,d\varphi = \tfrac{1}{2}\int_{\varphi=0}^{2\pi}\left[r^2\right]_{r=r_{in}}^{r_{out}} d\varphi = \tfrac{1}{2}\int_{\varphi=0}^{2\pi}(r_{out}^2 - r_{in}^2)\,d\varphi = \tfrac{1}{2}\left[(r_{out}^2 - r_{in}^2)\varphi\right]_{\varphi=0}^{2\pi} = \pi(r_{out}^2 - r_{in}^2)$$ (B.11)

The outer radius of this part is dependent on the height z: $r_{out} = \sqrt{R^2 - z^2}$ (B.12)

Bottom-part D-ring

The inner radius of this part is constant: $r_{in} = r_1$.
Using (B.11) and (B.12), the volume of the bottom-part of the total D-ring is:

$$V_{botDT} = \sum_{z=-a}^{z=h_1}\text{cross} - \text{sections} = \int_{z=-a}^{h_1}\pi\,(r_{out}^2 - r_{in}^2)\,dz = \pi\int_{z=-a}^{h_1}(R^2 - z^2 - r_1^2)\,dz =$$

$$= \pi\left[(R^2 - r_1^2)z - \tfrac{1}{3}z^3\right]_{z=-a}^{h_1} = \pi\left[(R^2 - r_1^2)(h_1 + a) - \tfrac{1}{3}(h_1^3 + a^3)\right] = 3.6038\cdot10^{-7}\ [\text{m}^3]$$ (B.13)

Top-part D-ring

The inner radius of this part is dependent on the height z: $r_{in} = (z / \tan15°)$.

Using (B.11) and (B.12), the volume of the top-part of the total D-ring is:

$$V_{topDT} = \sum_{z=h_1}^{z=h_3}\text{cross} - \text{sections} = \int_{z=h_1}^{h_3}\pi(r_{out}^2 - r_{in}^2)\,dz = \pi\int_{z=h_1}^{h_3}\left(R^2 - z^2 - \left(\frac{z}{\tan15°}\right)^2\right)dz =$$

$$= \pi\int_{z=h_1}^{h_3}\left(R^2 - z^2\left(1 + \frac{1}{\tan^215°}\right)\right)dz = \pi\left[R^2 z - \tfrac{1}{3}z^3\left(1 + \frac{1}{\tan^215°}\right)\right]_{z=h_1}^{h_3} =$$

$$= \pi\left[R^2(h_3 - h_1) - \tfrac{1}{3}\left(1 + \frac{1}{\tan^215°}\right)(h_3^3 - h_1^3)\right] = 1.9253\cdot10^{-8}\ [\text{m}^3]$$ (B.14)

Total D-ring

The mass of the total D-ring can now be calculated using (B.13) and (B.14):

$$m_{DT} = \rho_{Fe}\,(V_{botDT} + V_{topDT}) = 2.9991\cdot10^{-3}\ [\text{kg}]$$ (B.15)

Cut-outs for permanent magnets

To get the mass of the four cut-outs for the permanent magnets, the same strategy is used as for the calculation of m_{DT} (since the cut-outs are imaginary parts of the D-ring). The cut-outs will also be split up in two parts: a bottom-part (botDcut) and a top-part (topDcut). For both parts the surface of the horizontal cross-section at height z will be determined. These surfaces will then be summarized over the total height of the bottom- and top-part.

The resulting volumes of these calculations will be multiplied with the mass-density of the iron, to obtain the total mass of the cut-outs (m_{Dcut}).

However, there are two main differences with the previous calculations:

①   The integration is not done with respect to the z-axis of the rotor, but with respect to the cross-line of the two cut-out planes making an angle of 53°. This line is shifted over a distance x_2 on the x-axis of the rotor (see figure B.4b).

②   The integration radius of the bottom-part doesn't start at $r = r_1$, but at the straight inner border of the cut-out: $r = r_\varphi$ (see figure B.5).

Because the four cut-outs have the same shape and are symmetrical with respect to the vertical plane ($y = 0$ for cut-outs on x-axis and $x = 0$ for cut-outs on y-axis), only 1/8 part of the total cut-outs will be calculated. Later the outcome will be multiplied by 8 to obtain the total value.

Bottom-part Cut-outs

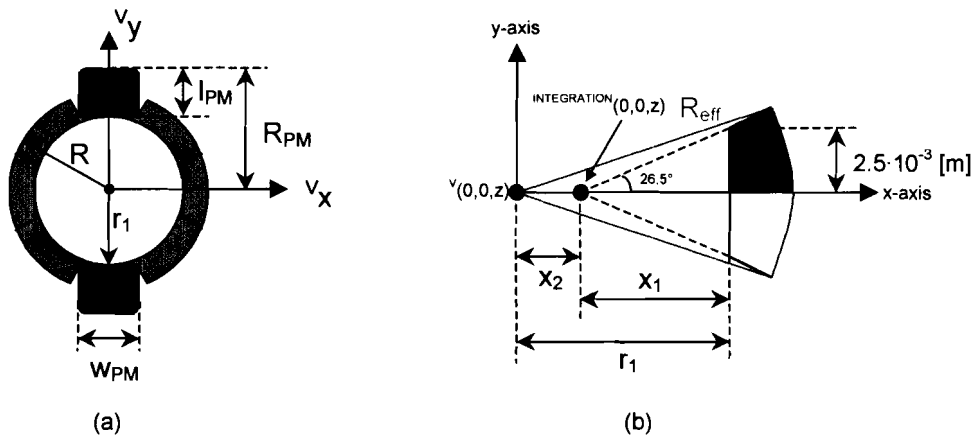(a)   (b)

Figure B.4
a) Horizontal cross-section in plane $z = 0$ of D-ring. On the y-axis the two cut-outs are removed and the permanent magnets are placed. On the x-axis the borders of the cut-outs are drawn. In reality all four cut-outs are replaced by permanent magnets. This drawing is only meant to give an idea of what is going to be calculated.
b) Horizontal cross-section of one cut-out for a permanent magnet, showing the dimensions. The red surface is 1/8 of the total surface of the cut-outs at a certain height z.

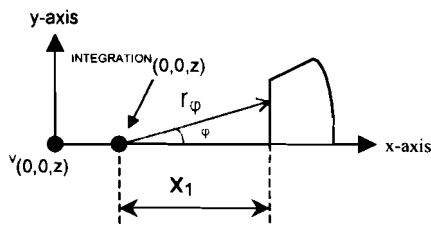The inner radius of botDcut must be defined with respect to the new integration z-axis:

Figure B.5
Partial horizontal cross-section (like figure B.4b), defining the inner radius r_φ, used for integration:

$$r_\varphi = x_1 / \cos\varphi \tag{B.16}$$

The outer radius of botDcut must also be expressed with respect to the new integration z-axis. The outer radius is a circle with the z-axis of the rotor perpendicular through its center-point. This circle can be expressed with respect to the new integration z-axis using the following formula:

$$(x+x_2)^2 + y^2 = R_{circle}^2 \Rightarrow x^2 + 2xx_2 + x_2^2 + y^2 = R_{circle}^2 \Rightarrow$$

$$\Rightarrow x^2 + y^2 + 2xx_2 + x_2^2 - R_{circle}^2 = 0 \Rightarrow \{with: x^2 + y^2 = r^2 \text{ and } x = r\cos\varphi\} \Rightarrow$$

$$\Rightarrow r^2 + 2rx_2\cos\varphi + x_2^2 - R_{circle}^2 = 0 \Rightarrow r_{I,II} = \frac{-2x_2\cos\varphi \pm \sqrt{4x_2^2\cos^2\varphi - 4(x_2^2 - R_{circle}^2)}}{2} \Rightarrow$$

$$\{with: \sin^2\varphi + \cos^2\varphi = 1\} \Rightarrow r = -x_2\cos\varphi + \sqrt{R_{circle}^2 - x_2^2\sin^2\varphi} \tag{B.17}$$

Formula (B.17) can be used to convert the outer radius of the rotor-part D (B.12) to the integration z-axis:

$$r_{out} = -x_2\cos\varphi + \sqrt{R^2 - z^2 - x_2^2\sin^2\varphi} \tag{B.18}$$

Now (1/8 part of) the surface of a horizontal cross-section at height z of botDcut can be determined using the formulae for r_φ (B.16) and r_{out} (B.18):

$$S_{botDcut} = \int_{\varphi=0}^{\varphi_2=26.5°} \left(\int_{r=r_\varphi}^{r_{out}} r\,dr \right) d\varphi = \frac{1}{2} \int_{\varphi=0}^{\varphi_2=26.5°} \left[r^2 \right]_{r=r_\varphi}^{r_{out}} d\varphi = \frac{1}{2} \int_{\varphi=0}^{\varphi_2=26.5°} (r_{out}^2 - r_\varphi^2)\,d\varphi =$$

$$= \frac{1}{2} \int_{\varphi=0}^{\varphi_2=26.5°} \left(\left(-x_2\cos\varphi + \sqrt{R^2-z^2-x_2^2\sin^2\varphi} \right)^2 - \frac{x_1^2}{\cos^2\varphi} \right) d\varphi =$$

$$= \frac{1}{2} \int_{\varphi=0}^{\varphi_2=26.5°} \left(x_2^2\cos^2\varphi - 2x_2\cos\varphi\sqrt{R^2-z^2-x_2^2\sin^2\varphi} + R^2 - z^2 - x_2^2\sin^2\varphi - \frac{x_1^2}{\cos^2\varphi} \right) d\varphi =$$

$$= \{with: -x_2^2\sin^2\varphi = x_2^2\cos^2\varphi - x_2^2\} = S_1 + S_2 + S_3 + S_4 = \int_{\varphi=0}^{\varphi_2} x_2^2\cos^2\varphi\,d\varphi +$$

$$- \int_{\varphi=0}^{\varphi_2} \left(x_2\cos\varphi\sqrt{R^2-z^2-x_2^2\sin^2\varphi} \right) d\varphi + \frac{1}{2}\int_{\varphi=0}^{\varphi_2}(R^2-z^2-x_2^2)d\varphi - \frac{1}{2}\int_{\varphi=0}^{\varphi_2} \frac{x_1^2}{\cos^2\varphi} d\varphi$$

These four integrals can be calculated one by one:

$$S_1 = \int_{\varphi=0}^{\varphi_2} x_2^2\cos^2\varphi\,d\varphi = \frac{1}{2}x_2^2 \int_{\varphi=0}^{\varphi_2}(1+\cos2\varphi)d\varphi = \frac{1}{2}x_2^2 \left[\varphi + \frac{1}{2}\sin2\varphi\right]_{\varphi=0}^{\varphi_2} = \frac{1}{2}x_2^2\left[\varphi_2 + \frac{1}{2}\sin2\varphi_2\right]$$

$$S_2 = -\int_{\varphi=0}^{\varphi_2} \left(x_2\cos\varphi\sqrt{R^2-z^2-x_2^2\sin^2\varphi} \right) d\varphi = -\int_{u=0}^{u_2=x_2\sin\varphi_2} \left(\sqrt{R^2-z^2-x_2^2\sin^2\varphi} \right) d(x_2\sin\varphi) =$$

$$= -\int_{u=0}^{u_2=x_2\sin\varphi_2} \left(\sqrt{R^2-z^2-u^2} \right) du = \left\{ \begin{bmatrix} 3, \text{Standard} \\ \text{integral (t.24)} \end{bmatrix} \right\} =$$

$$= -\left[\frac{u}{2}\sqrt{R^2-z^2-u^2} + \frac{R^2-z^2}{2}\arcsin\left(\frac{u}{\sqrt{R^2-z^2}} \right) \right]_{u=0}^{u_2=x_2\sin\varphi_2} =$$

$$= -\frac{1}{2}x_2\sin\varphi_2\sqrt{R^2-z^2-x_2^2\sin^2\varphi_2} - \frac{1}{2}(R^2-z^2)\arcsin\left(\frac{x_2\sin\varphi_2}{\sqrt{R^2-z^2}} \right)$$

$$S_3 = \tfrac{1}{2} \int_{\varphi=0}^{\varphi_2} (R^2 - z^2 - x_2^2) d\varphi = \tfrac{1}{2} \left[(R^2 - z^2 - x_2^2)\varphi \right]_{\varphi=0}^{\varphi_2} = \tfrac{1}{2}(R^2 - z^2 - x_2^2)\varphi_2$$

$$S_4 = -\tfrac{1}{2} \int_{\varphi=0}^{\varphi_2} \frac{x_1^2}{\cos^2 \varphi} d\varphi = -\tfrac{1}{2} x_1^2 \left[\tan\varphi \right]_{\varphi=0}^{\varphi_2} = -\tfrac{1}{2} x_1^2 \tan\varphi_2$$

Finally, the surface (of 1/8 part) of a horizontal cross-section at height z of botDcut is:

$$S_{botDcut} = S_1 + S_2 + S_3 + S_4 = \tfrac{1}{2}\left(x_2^2\left[\varphi_2 + \tfrac{1}{2}\sin2\varphi_2\right] - x_2\sin\varphi_2\sqrt{R^2 - z^2 - x_2^2\sin^2\varphi_2} \right.$$

$$\left. -(R^2 - z^2)\arcsin\left(\frac{x_2\sin\varphi_2}{\sqrt{R^2-z^2}}\right) + (R^2 - z^2 - x_2^2)\varphi_2 - x_1^2\tan\varphi_2 \right) \qquad (B.19)$$

(1/8 part of) the total volume of the bottom-parts of the cut-outs of the D-ring is calculated by summarizing all the surfaces of the cross-sections (B.19) between the heights $z = -a$ and $z = h_1$:

$$V_{botDcut} = \sum_{z=-a}^{h_1} S_{botDcut} \cdot dz = \tfrac{1}{2} \int_{z=-a}^{h_1} \left(x_2^2\left[\varphi_2 + \tfrac{1}{2}\sin2\varphi_2\right] - x_2\sin\varphi_2\sqrt{R^2 - z^2 - x_2^2\sin^2\varphi_2} \right.$$

$$\left. - (R^2 - z^2)\arcsin\left(\frac{x_2\sin\varphi_2}{\sqrt{R^2-z^2}}\right) + (R^2 - z^2 - x_2^2)\varphi_2 - x_1^2\tan\varphi_2 \right) dz =$$

$$= 2.11932909 \cdot 10^{-8}\ [m^3] \qquad \text{(MATLAB}^\circledR \text{ approximation)} \qquad (B.20)$$

The integral is numerically approximated using the MATLAB$^\circledR$ quad-function. An analytical working-out of the integral is presented in appendix E. This is done to compare the approximated value (B.20) with the exact outcome.

It turns out that the quad-function returns an answer with an accuracy of 5 decimals, which is enough for this application. From now on complex integrals won't be worked out analytically to save time and avoid mistakes in (for humans) unmanageable large algebraic expressions.

Top-part Cut-outs

Both the outer and the inner radius of the top-part have to be converted to the new integration z-axis. For the outer radius this was already done in (B.18) which is repeated below:

$$r_{out} = -x_2\cos\varphi + \sqrt{R^2 - z^2 - x_2^2\sin^2\varphi}$$

Formula (B.17) can be used to convert the inner radius of the top-part of the cut-outs
($r_{in} = (z\ /\ \tan15°)$) to the new integration z-axis:

$$r_{in} = -x_2\cos\varphi + \sqrt{\left(\frac{z}{\tan15°}\right)^2 - x_2^2\sin^2\varphi} \qquad (B.21)$$

(1/8 part of) the total volume of the top-parts of the cut-outs of the D-ring is calculated with a standard volume integral using cylinder coordinates and the radii (B.18) and (B.21):

$$V_{topDcut} = \int\limits_{z=h_1}^{h_3} \int\limits_{\varphi=0}^{\varphi_2} \int\limits_{r=r_{in}}^{r_{out}} r\,dr\,d\varphi\,dz = \tfrac{1}{2} \int\limits_{z=h_1}^{h_3} \int\limits_{\varphi=0}^{\varphi_2} [r^2]_{r=r_{in}}^{r_{out}} d\varphi\,dz = \tfrac{1}{2} \int\limits_{z=h_1}^{h_3} \int\limits_{\varphi=0}^{\varphi_2} [r_{out}^2 - r_{in}^2]d\varphi\,dz =$$

$$= \tfrac{1}{2} \int\limits_{z=h_1}^{h_3} \int\limits_{\varphi=0}^{\varphi_2} \left(\underline{x_2^2\cos^2\varphi - 2x_2\cos\varphi\sqrt{R^2-z^2-x_2^2\sin^2\varphi} + R^2 - z^2} - x_2^2\sin^2\varphi + \right.$$

$$\left. -\underline{x_2^2\cos^2\varphi} + 2x_2\cos\varphi\sqrt{\left(\frac{z}{\tan15°}\right)^2 - x_2^2\sin^2\varphi} - \left(\frac{z}{\tan15°}\right)^2 + \underline{x_2^2\sin^2\varphi} \right)d\varphi\,dz =$$

$$= \tfrac{1}{2} \int\limits_{z=h_1}^{h_3} \int\limits_{\varphi=0}^{\varphi_2} \left[R^2 + 2x_2\cos\varphi\left(\sqrt{\left(\frac{z}{\tan15°}\right)^2 - x_2^2\sin^2\varphi} - \sqrt{R^2-z^2-x_2^2\sin^2\varphi} \right) + \right.$$

$$\left. -z^2\left(1+\frac{1}{\tan^2 15°}\right)\right]d\varphi\,dz = 1.2298\cdot 10^{-9}\,[m^3] \quad \text{(MATLAB}^\circledR\text{ approximation)} \quad \text{(B.22)}$$

Total Cut-outs

The total mass of the four cut-outs from the D-ring is found by combining the volume of the bottom-part (B.20) and the volume of the top-part (B.22):

$$m_{Dcut} = 8\cdot\rho_{Fe}\cdot(V_{botDcut} + V_{topDcut}) = 1.4171\cdot 10^{-3}\,[kg] \tag{B.23}$$

Total part D

Total mass of rotor-part D is calculated using (B.15) and (B.23):

$$m_D = m_{DT} - m_{Dcut} = 1.5820\cdot 10^{-3}\,[kg] \tag{B.24}$$

The four cut-outs are $\dfrac{m_{Dcut}}{m_{DT}}\cdot 100\% = 47.25\%$ of the total D-ring. $\tag{B.25}$

B.5 Exact formula for I_D

Parameter I_D is the z-coordinate of the center of gravity of rotor-part D. It is expressed with respect to the plane z = 0. The technique to calculate the z-coordinate of the center of gravity of an object has been described in section B.2, resulting in formula (B.4). This formula consists of two integrals. The denominator is an integral calculating the volume of the object. The numerator is the same integral, only the integrand is multiplied with the height z, before it is calculated.

For calculation purposes, rotor-part D will be divided up in the same parts as in the previous section, see figure B.3 and B.4.

Bottom-part D-ring

The volume of this part is calculated in the previous section. Using the result and the integrand in (B.13), the z-coordinate of the center of gravity of this part can now be calculated with formula (B.4):

$$
I_{botDT} = \frac{\int_{z=-a}^{h_1} z\pi(R^2 - z^2 - r_1^2)\,dz}{V_{botDT}} = \frac{\pi}{V_{botDT}} \int_{z=-a}^{h_1} \left(z(R^2 - r_1^2) - z^3\right)dz = \frac{\pi}{V_{botDT}} \left[\tfrac{1}{2}z^2(R^2 - r_1^2) - \tfrac{1}{4}z^4\right]_{z=-a}^{h_1} =
$$

$$
= \frac{\pi}{V_{botDT}} \left[\tfrac{1}{2}(R^2 - r_1^2)(h_1^2 - a^2) - \tfrac{1}{4}(h_1^4 - a^4)\right] = -5.2198 \cdot 10^{-4} \text{ [m]} \tag{B.26}
$$

Top-part D-ring

The volume of this part is calculated in the previous section. Using the result and the integrand in (B.14), the z-coordinate of the center of gravity of this part can now be calculated with formula (B.4):

$$
I_{topDT} = \frac{\int_{z=h_1}^{h_3} z\pi\left(R^2 - z^2 - \left(\frac{z}{\tan 15°}\right)^2\right)dz}{V_{topDT}} = \frac{\pi}{V_{topDT}} \int_{z=h_1}^{h_3} \left(zR^2 - z^3\left(1 + \frac{1}{\tan^2 15°}\right)\right)dz =
$$

$$
= \frac{\pi}{V_{topDT}} \left[\tfrac{1}{2}R^2 z^2 - \tfrac{1}{4}z^4\left(1 + \frac{1}{\tan^2 15°}\right)\right]_{z=h_1}^{h_3} =
$$

$$
= \frac{\pi}{V_{topDT}} \left[\tfrac{1}{2}R^2(h_3^2 - h_1^2) - \tfrac{1}{4}\left(1 + \frac{1}{\tan^2 15°}\right)(h_3^4 - h_1^4)\right] = 1.7651 \cdot 10^{-3} \text{ [m]} \tag{B.27}
$$

Total D-ring

Using formula (B.1) and inserting (B.13), (B.14), (B.26) and (B.27) gives the z-coordinate of the center of gravity of whole D-ring:

$$
I_{DT} = \frac{I_{botDT} \cdot V_{botDT} + I_{topDT} \cdot V_{topDT}}{V_{botDT} + V_{topDT}} = -4.0599 \cdot 10^{-4} \text{ [m]} \tag{B.28}
$$

Cut-outs for permanent magnets

The calculation of the z-coordinate of the center of gravity of the four cut-outs is actually done on one half of a cut-out. This is 1/8 part of the total volume of cut-outs. Due to the symmetrical shape of one cut-out and the symmetrical composition of the four cut-outs, the calculated z-coordinate is the same as for one whole cut-out and for the four cut-outs together.

Because of the nasty integrands, the integrals for the cut-outs have again been numerically approximated with MATLAB®. As shown in appendix E, the approximation has an negligible effect on the total outcome.

Bottom-part Cut-outs

The volume of this part is calculated in the previous section. Using the result and the integrand in (B.20), the z-coordinate of the center of gravity of this part can now be calculated with formula (B.4):

$$I_{botDcut} = \frac{1}{V_{botDcut}} \int_{z=-a}^{h_1} z \left(\frac{1}{2} x_2^2 [\varphi_2 + \frac{1}{2}\sin 2\varphi_2] - \frac{1}{2} x_2 \sin \varphi_2 \sqrt{R^2 - z^2 - x_2^2 \sin^2 \varphi_2} \right. +$$

$$\left. - \frac{1}{2}(R^2 - z^2) \arcsin\left(\frac{x_2 \sin \varphi_2}{\sqrt{R^2 - z^2}} \right) + \frac{1}{2}(R^2 - z^2 - x_2^2)\varphi_2 - \frac{1}{2} x_1^2 \tan \varphi_2 \right) dz =$$

$$= -5.1465 \cdot 10^{-4} \text{ [m]} \qquad (\text{MATLAB}^{\circledR} \text{ approximation}) \tag{B.29}$$

Top-part Cut-outs

The volume of this part is calculated in the previous section. Using the result and the integrand in (B.22), the z-coordinate of the center of gravity of this part can now be calculated with formula (B.4):

$$I_{topDcut} = \frac{1}{2V_{topDcut}} \int_{z=h_1}^{h_3} \int_{\varphi=0}^{\varphi_2} z \left[R^2 + 2x_2 \cos\varphi \left(\sqrt{\left(\frac{z}{\tan 15°}\right)^2 - x_2^2 \sin^2 \varphi} - \sqrt{R^2 - z^2 - x_2^2 \sin^2 \varphi} \right) \right. +$$

$$\left. - z^2 \left(1 + \frac{1}{\tan^2 15°} \right) \right] d\varphi dz = 1.7655 \cdot 10^{-3} \text{ [m]} \qquad (\text{MATLAB}^{\circledR} \text{ approximation}) \tag{B.30}$$

Total Cut-outs

Using formula (B.1) and inserting (B.20), (B.22), (B.29) and (B.30) gives the z-coordinate of the center of gravity of the cut-outs for the permanent magnets:

$$I_{Dcut} = \frac{I_{botDcut} \cdot V_{botDcut} + I_{topDcut} \cdot V_{topDcut}}{V_{botDcut} + V_{topDcut}} = -4.8701 \cdot 10^{-5} \text{ [m]} \tag{B.31}$$

Total part D

Filling in formula (B.1) with the values of m_D (B.24), m_{DT} (B.15), I_{DT} (B.28), m_{Dcut} (B.23) and I_{Dcut} (B.31) gives the z-coordinate of the center of gravity of rotor-part D:

$$I_{DT} \cdot m_{DT} = I_D \cdot m_D + I_{Dcut} \cdot m_{Dcut} \Leftrightarrow I_D = \frac{I_{DT} \cdot m_{DT} - I_{Dcut} \cdot m_{Dcut}}{m_D} = -7.2605 \cdot 10^{-4} \text{ [m]} \tag{B.32}$$

B.6 Exact formula for $I_{D,z}^V$

Parameter $I_{D,z}^V$ is the moment of inertia of rotor-part D around the z-axis of the rotor-frame (rotating V-frame). The general formula to calculate this moment of inertia is stated below (B.33). The use of cylinder-coordinates for the calculation has the benefit that the length of the integration radius r is also the distance between a small piece of mass (dm) of the D-ring and the z-axis, at least for now.

For calculation purposes, rotor-part D will be divided up in the same parts as in the previous sections, see figure B.3 and B.4.

The moment of inertia around the z-axis of both the bottom-part and the top-part of the total D-ring can be calculated with:

$$I_{DT,^Vz} = \sum r^2 dm = \rho_{Fe}\sum r^2 dV = \rho_{Fe}\int_{z=z_1}\int_{\varphi=0}^{2\pi}\int_{r=r_{in}}^{r_{out}} r^3 dr d\varphi dz = \tfrac{1}{4}\rho_{Fe}\int_{z=z_1}^{z_2}\int_{\varphi=0}^{2\pi}(r_{out}^4-r_{in}^4)d\varphi dz = \tfrac{\pi}{2}\rho_{Fe}\int_{z=z_1}^{z_2}(r_{out}^4-r_{in}^4)dz$$

(B.33)

Bottom-part D-ring

The moment of inertia of this part around the z-axis of the rotor can be calculated with

$r_{out} = \sqrt{R^2-z^2}$, $r_{in} = r_1$ and $(-a \le z \le h_1)$ substituted in (B.33):

$$I_{botDT,^Vz} = \tfrac{\pi}{2}\rho_{Fe}\int_{z=-a}^{h_1}((R^2-z^2)^2-r_1^4)dz = \tfrac{\pi}{2}\rho_{Fe}\int_{z=-a}^{h_1}(R^4-2R^2z^2+z^4-r_1^4)dz =$$

$$= \tfrac{\pi}{2}\rho_{Fe}\left[(R^4-r_1^4)z-\tfrac{2}{3}R^2z^3+\tfrac{1}{5}z^5\right]_{z=-a}^{h_1} = \tfrac{\pi}{2}\rho_{Fe}\left[(R^4-r_1^4)(h_1+a)-\tfrac{2}{3}R^2(h_1^3+a^3)+\tfrac{1}{5}(h_1^5+a^5)\right] =$$

$$= 1.3978 \cdot 10^{-7} \text{ [kgm}^2\text{]}$$

(B.34)

Top-part D-ring

The moment of inertia of this part around the z-axis of the rotor can be calculated with

$r_{out} = \sqrt{R^2-z^2}$, $r_{in} = \dfrac{z}{\tan 15°}$ and $(h_1 \le z \le h_3)$ substituted in (B.33):

$$I_{topDT,^Vz} = \tfrac{\pi}{2}\rho_{Fe}\int_{z=h_1}^{h_3}\left((R^2-z^2)^2-\left(\frac{z}{\tan 15°}\right)^4\right)dz = \tfrac{\pi}{2}\rho_{Fe}\int_{z=h_1}^{h_3}\left(R^4-2R^2z^2+z^4-\frac{z^4}{\tan^4 15°}\right)dz =$$

$$= \tfrac{\pi}{2}\rho_{Fe}\int_{z=h_1}^{h_3}\left(R^4-2R^2z^2+z^4\left(1-\frac{1}{\tan^4 15°}\right)\right)dz = \tfrac{\pi}{2}\rho_{Fe}\left[R^4z-\tfrac{2}{3}R^2z^3+\tfrac{1}{5}\left(1-\frac{1}{\tan^4 15°}\right)z^5\right]_{z=h_1}^{h_3} =$$

$$= \tfrac{\pi}{2}\rho_{Fe}\left[R^4(h_3-h_1)-\tfrac{2}{3}R^2(h_3^3-h_1^3)+\tfrac{1}{5}\left(1-\frac{1}{\tan^4 15°}\right)(h_3^5-h_1^5)\right] = 7.9423 \cdot 10^{-9} \text{ [kgm}^2\text{]}$$

(B.35)

Total D-ring

The moment of inertia of the complete D-ring around the z-axis of the rotor can be calculated by adding (B.34) and (B.35):

$$I_{DT,^Vz} = I_{botDT,^Vz} + I_{topDT,^Vz} = 1.4772 \cdot 10^{-7} \text{ [kgm}^2\text{]}$$

(B.36)

Next the moment of inertia of the four cut-outs for the permanent magnets (around the z-axis of the rotor) will be calculated. The result of that computation will be subtracted from $I_{DT,^Vz}$ (B.36) to obtain the wanted inertia of rotor-part D.

Cut-outs for permanent magnets

Now the moment of inertia of the four cut-outs for the permanent magnets around the z-axis of the rotor must be calculated. First the distance vector r_z is determined. This is necessary because the integration vector r doesn't start on the z-axis of the rotor (see figure B.6), like before. The length of r_z (B.37) is the distance between a small piece of mass (dm) of the cut-out and the z-axis of the rotor. It is used in the general formula for calculation of the moment of inertia of an object around a rotation axis (B.38).
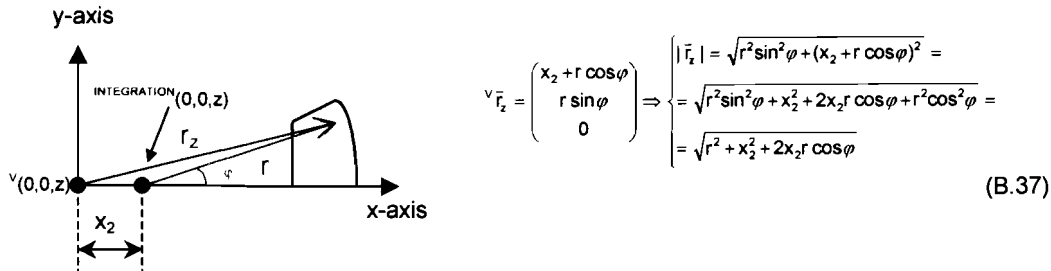

$$\left| \vec{r}_z \right| = \sqrt{r^2 \sin^2\varphi + (x_2 + r\cos\varphi)^2} =$$

$$^{v}\vec{r}_z = \begin{pmatrix} x_2 + r\cos\varphi \\ r\sin\varphi \\ 0 \end{pmatrix} \Rightarrow = \sqrt{r^2\sin^2\varphi + x_2^2 + 2x_2 r\cos\varphi + r^2\cos^2\varphi} =$$

$$= \sqrt{r^2 + x_2^2 + 2x_2 r\cos\varphi}$$

(B.37)

Figure B.6

½ part of a horizontal cross-section of one cut-out (like figure B.4b) with the definition of the inertia distance vector r_z. This vector lies in the horizontal plane of the cross-section. It starts on the z-axis of the rotor and it ends on the same piece of mass (dm) as the integration vector r.

Again, the symmetrical shape allows that the integration is done for only ½ part of one cut-out. The integral will be multiplied with 8 to obtain the value for the four cut-outs together. For both the bottom-part and the top-part of the cut-out, the moment of inertia around the z-axis of the rotor can now be calculated using (B.37):

$$I_{Dcut,^vz} = \sum |r_z|^2 \, dm = \rho_{Fe}\sum |r_z|^2 \, dV = 8 \cdot \rho_{Fe} \int\limits_{z=z_1}^{z_2} \int\limits_{\varphi=0}^{\varphi_2} \int\limits_{r=r_{in}}^{r_{out}} |r_z|^2 \, r \, dr \, d\varphi \, dz =$$

$$= 8 \cdot \rho_{Fe} \int\limits_{z=z_1}^{z_2} \int\limits_{\varphi=0}^{\varphi_2} \int\limits_{r=r_{in}}^{r_{out}} (r^2 + x_2^2 + 2x_2 r \cos\varphi) \, r \, dr \, d\varphi \, dz =$$

$$= 8 \cdot \rho_{Fe} \int\limits_{z=z_1}^{z_2} \int\limits_{\varphi=0}^{\varphi_2} \int\limits_{r=r_{in}}^{r_{out}} (r^3 + x_2^2 r + 2x_2 r^2 \cos\varphi) \, dr \, d\varphi \, dz =$$

$$= 8 \cdot \rho_{Fe} \int\limits_{z=z_1}^{z_2} \int\limits_{\varphi=0}^{\varphi_2} \left[\tfrac{1}{4}r^4 + \tfrac{1}{2}x_2^2 r^2 + \tfrac{2}{3}x_2 r^3 \cos\varphi \right]_{r=r_{in}}^{r_{out}} d\varphi \, dz =$$

$$= 8 \cdot \rho_{Fe} \int\limits_{z=z_1}^{z_2} \int\limits_{\varphi=0}^{\varphi_2} \left(\tfrac{1}{4}\left[r_{out}^4 - r_{in}^4\right] + \tfrac{1}{2}x_2^2\left[r_{out}^2 - r_{in}^2\right] + \tfrac{2}{3}x_2\cos\varphi\left[r_{out}^3 - r_{in}^3\right] \right) d\varphi \, dz$$

(B.38)

Bottom-part Cut-outs

The moment of inertia of this part around the z-axis of the rotor can be calculated with

$$r_{out} = -x_2\cos\varphi + \sqrt{R^2 - z^2 - x_2^2\sin^2\varphi}, \quad r_{in} = \frac{x_1}{\cos\varphi} \text{ and } (-a \le z \le h_1)$$

substituted in (B.38):

$$I_{botDcut,}{}^{v}{}_{z} = 8\rho_{Fe} \int_{z=-a}^{h_1} \int_{\varphi=0}^{\varphi_2} \left(\tfrac{1}{4}\left[\left(-x_2\cos\varphi + \sqrt{R^2 - z^2 - x_2^2\sin^2\varphi}\right)^4 - \left(\frac{x_1}{\cos\varphi}\right)^4\right] + \right.$$

$$+ \tfrac{1}{2}x_2^2\left[\left(-x_2\cos\varphi + \sqrt{R^2 - z^2 - x_2^2\sin^2\varphi}\right)^2 - \left(\frac{x_1}{\cos\varphi}\right)^2\right] +$$

$$\left. + \tfrac{2}{3}x_2\cos\varphi\left[\left(-x_2\cos\varphi + \sqrt{R^2 - z^2 - x_2^2\sin^2\varphi}\right)^3 - \left(\frac{x_1}{\cos\varphi}\right)^3\right]\right)d\varphi dz =$$

$$= 6.7109 \cdot 10^{-8} \text{ [kgm}^2\text{]} \quad \text{(MATLAB}^{\circledR}\text{ approximation)} \tag{B.39}$$

Top-part Cut-outs

The moment of inertia of this part around the z-axis of the rotor can be calculated with

$$r_{out} = -x_2\cos\varphi + \sqrt{R^2 - z^2 - x_2^2\sin^2\varphi}, \quad r_{in} = -x_2\cos\varphi + \sqrt{\left(\frac{z}{\tan 15°}\right)^2 - x_2^2\sin^2\varphi}$$

and ($h_1 \le z \le h_3$) substituted in (B.38):

$$I_{topDcut,}{}^{v}{}_{z} = 8\rho_{Fe} \int_{z=h_1}^{h_3} \int_{\varphi=0}^{\varphi_2} \left(\tfrac{1}{4}\left[\left(-x_2\cos\varphi + \sqrt{R^2 - z^2 - x_2^2\sin^2\varphi}\right)^4 - \left(-x_2\cos\varphi + \sqrt{\left(\frac{z}{\tan 15°}\right)^2 - x_2^2\sin^2\varphi}\right)^4\right] + \right.$$

$$+ \tfrac{1}{2}x_2^2\left[\left(-x_2\cos\varphi + \sqrt{R^2 - z^2 - x_2^2\sin^2\varphi}\right)^2 - \left(-x_2\cos\varphi + \sqrt{\left(\frac{z}{\tan 15°}\right)^2 - x_2^2\sin^2\varphi}\right)^2\right] +$$

$$\left. + \tfrac{2}{3}x_2\cos\varphi\left[\left(-x_2\cos\varphi + \sqrt{R^2 - z^2 - x_2^2\sin^2\varphi}\right)^3 - \left(-x_2\cos\varphi + \sqrt{\left(\frac{z}{\tan 15°}\right)^2 - x_2^2\sin^2\varphi}\right)^3\right]\right)d\varphi dz =$$

$$= 4.0622 \cdot 10^{-9} \text{ [kgm}^2\text{]} \quad \text{(MATLAB}^{\circledR}\text{ approximation)} \tag{B.40}$$

Total Cut-outs

The moment of inertia of the four cut-outs combined around the z-axis of the rotor can be calculated by adding (B.39) and (B.40):

$$I_{Dcut,}{}^{v}{}_{z} = I_{botDcut,}{}^{v}{}_{z} + I_{topDcut,}{}^{v}{}_{z} = 7.1172 \cdot 10^{-8} \text{ [kgm}^2\text{]} \tag{B.41}$$

Total part D

Finally, the moment of inertia of rotor-part D around the z-axis can be found by combining (B.36) and (B.41):

$$I_{D,}{}^{v}{}_{z} = I_{DT,}{}^{v}{}_{z} - I_{Dcut,}{}^{v}{}_{z} = 7.6552 \cdot 10^{-8} \text{ [kgm}^2\text{]} \tag{B.42}$$

B.7 Exact formula for $I_{D,x}^V$

Parameter $I_{D,x}^V$ is the moment of inertia of rotor-part D around the x-axis of the rotor-frame (rotating V-frame). The general formula to calculate this moment of inertia is stated below (B.44). Because cylinder-coordinates are used for the integration over the volumes in this section, the distance between the small piece of mass (dm) and the x-axis ($|r_x|$ in (B.43)) must also be expressed in the cylinder-coordinates (r, φ, z). This is done in figure B.7c.

For calculation purposes, rotor-part D will be divided up in the same parts as in the previous sections, see figure B.3 and B.4.
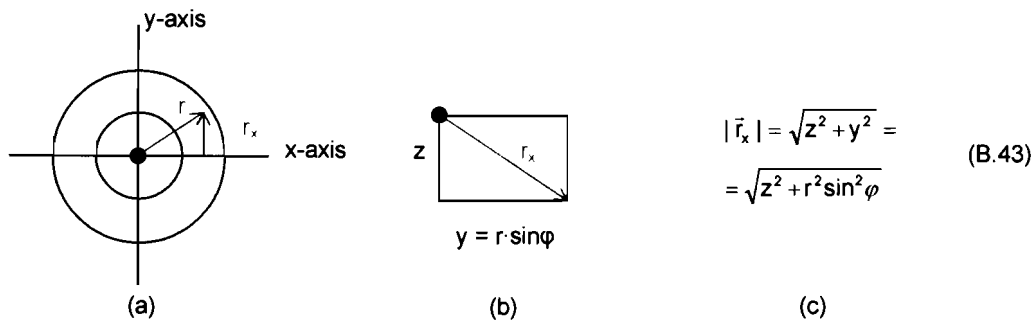

$$|\vec{r}_x| = \sqrt{z^2 + y^2} =$$
$$= \sqrt{z^2 + r^2\sin^2\varphi}$$

(B.43)

$$y = r\cdot\sin\varphi$$

(a)   (b)   (c)

Figure B.7

a) Horizontal cross-section of the complete D-ring, with the definition of the inertia distance vector $\vec{r}_x$.

b) Vector $\vec{r}_x$ doesn't lie in the horizontal plane of the cross-section (except for z = 0). It starts on the x-axis of the rotor and it ends on the same piece of mass (dm) as the integration vector $\vec{r}$.

c) The length of vector $\vec{r}_x$ (B.43) is the distance between the x-axis and the piece of mass (dm).

The moment of inertia around the x-axis of both the bottom-part and the top-part of the total D-ring can be calculated with:

$$I_{DT,x}^V = \sum |r_x|^2\, dm = \rho_{Fe}\sum |r_x|^2\, dV = \rho_{Fe}\int_{z=z_1}^{z_2}\int_{\varphi=0}^{2\pi}\int_{r=r_{in}}^{r_{out}} |r_x|^2\, r\, dr\, d\varphi\, dz =$$

$$= \rho_{Fe}\int_{z=z_1}^{z_2}\int_{\varphi=0}^{2\pi}\int_{r=r_{in}}^{r_{out}} (z^2 r + r^3\sin^2\varphi)\, dr\, d\varphi\, dz = \rho_{Fe}\int_{z=z_1}^{z_2}\int_{\varphi=0}^{2\pi} \left[\tfrac{1}{2}z^2 r^2 + \tfrac{1}{4}r^4\sin^2\varphi\right]_{r=r_{in}}^{r_{out}} d\varphi\, dz =$$

$$= \rho_{Fe}\int_{z=z_1}^{z_2}\int_{\varphi=0}^{2\pi} \left(\tfrac{1}{2}z^2[r_{out}^2 - r_{in}^2] + \tfrac{1}{4}\sin^2\varphi[r_{out}^4 - r_{in}^4]\right) d\varphi\, dz =$$

$$\left\{\text{with: } \int_{\varphi=0}^{2\pi}\sin^2\varphi\, d\varphi = \tfrac{1}{2}\int_{\varphi=0}^{2\pi}(1-\cos2\varphi)\, d\varphi = \tfrac{1}{2}[\varphi - \tfrac{1}{2}\sin2\varphi]_{\varphi=0}^{2\pi} = \pi\right\}$$

$$= \pi\cdot\rho_{Fe}\int_{z=z_1}^{z_2}\left(z^2[r_{out}^2 - r_{in}^2] + \tfrac{1}{4}[r_{out}^4 - r_{in}^4]\right) dz$$

(B.44)

Bottom-part D-ring

The moment of inertia of this part around the x-axis of the rotor can be calculated

with $r_{out} = \sqrt{R^2 - z^2}$, $r_{in} = r_1$ and $(-a \le z \le h_1)$ substituted in (B.44):

$$I_{botDT,^{\vee}x} = \pi \cdot \rho_{Fe} \int_{z=-a}^{h_1} \left(z^2[r_{out}^2 - r_{in}^2] + \tfrac{1}{4}[r_{out}^4 - r_{in}^4]\right)dz = \frac{\pi \cdot \rho_{Fe}}{4} \int_{z=-a}^{h_1} \left(4z^2[R^2 - z^2 - r_1^2] + [(R^2 - z^2)^2 - r_1^4]\right)dz =$$

$$= \frac{\pi \cdot \rho_{Fe}}{4} \int_{z=-a}^{h_1} \left([4R^2z^2 - 4z^4 - 4r_1^2z^2] + [R^4 - 2R^2z^2 + z^4 - r_1^4]\right)dz = \frac{\pi \cdot \rho_{Fe}}{4} \int_{z=-a}^{h_1} \left(R^4 + 2R^2z^2 - 3z^4 - 4r_1^2z^2 - r_1^4\right)dz =$$

$$= \frac{\pi \cdot \rho_{Fe}}{4} \int_{z=-a}^{h_1} \left[(R^4 - r_1^4) + (2R^2 - 4r_1^2)z^2 - 3z^4\right]dz = \frac{\pi \cdot \rho_{Fe}}{4} \left[(R^4 - r_1^4)z + \tfrac{2}{3}(R^2 - 2r_1^2)z^3 - \tfrac{3}{5}z^5\right]_{z=-a}^{h_1} =$$

$$= \frac{\pi \cdot \rho_{Fe}}{4} \left[(R^4 - r_1^4)(h_1 + a) + \tfrac{2}{3}(R^2 - 2r_1^2)(h_1^3 + a^3) - \tfrac{3}{5}(h_1^5 + a^5)\right] = 7.5030 \cdot 10^{-8} \; [kgm^2] \qquad (B.45)$$

Top-part D-ring

The moment of inertia of this part around the x-axis of the rotor can be calculated

with $r_{out} = \sqrt{R^2 - z^2}$, $r_{in} = \dfrac{z}{\tan 15°}$ and $(h_1 \le z \le h_3)$ substituted in (B.44):

$$I_{topDT,^{\vee}x} = \pi \cdot \rho_{Fe} \int_{z=h_1}^{h_3} \left(z^2[r_{out}^2 - r_{in}^2] + \tfrac{1}{4}[r_{out}^4 - r_{in}^4]\right)dz =$$

$$= \pi \cdot \rho_{Fe} \int_{z=h_1}^{h_3} \left(z^2\left[(R^2 - z^2) - \left(\frac{z}{\tan 15°}\right)^2\right] + \tfrac{1}{4}\left[(R^2 - z^2)^2 - \left(\frac{z}{\tan 15°}\right)^4\right] \right)dz =$$

$$= \pi \cdot \rho_{Fe} \int_{z=h_1}^{h_3} \left(z^2\left[R^2 - z^2\left(1 + \left(\frac{1}{\tan 15°}\right)^2\right)\right] + \tfrac{1}{4}\left[R^4 - 2R^2z^2 + z^4\left(1 - \left(\frac{1}{\tan 15°}\right)^4\right)\right] \right)dz =$$

$$= \frac{\pi \cdot \rho_{Fe}}{4} \int_{z=h_1}^{h_3} \left[R^4 + 2R^2z^2 - z^4\left(3 + 4\left(\frac{1}{\tan 15°}\right)^2 + \left(\frac{1}{\tan 15°}\right)^4\right)\right]dz =$$

$$= \frac{\pi \cdot \rho_{Fe}}{4} \left[R^4z + \tfrac{2}{3}R^2z^3 - \tfrac{1}{5}z^5\left(3 + 4\left(\frac{1}{\tan 15°}\right)^2 + \left(\frac{1}{\tan 15°}\right)^4\right)\right]_{z=h_1}^{h_3} =$$

$$= \frac{\pi \cdot \rho_{Fe}}{4} \left[R^4(h_3 - h_1) + \tfrac{2}{3}R^2(h_3^3 - h_1^3) - \tfrac{1}{5}\left(3 + 4\left(\frac{1}{\tan 15°}\right)^2 + \left(\frac{1}{\tan 15°}\right)^4\right)(h_3^5 - h_1^5)\right] =$$

$$= 4.4469 \cdot 10^{-9} \; [kgm^2] \qquad (B.46)$$

Total D-ring

The moment of inertia of the complete D-ring around the x-axis of the rotor can be calculated by adding (B.45) and (B.46):

$$I_{DT,^{\vee}x} = I_{botDT,^{\vee}x} + I_{topDT,^{\vee}x} = 7.9477 \cdot 10^{-8} \; [kgm^2] \qquad (B.47)$$

Next the moment of inertia of the four cut-outs for the permanent magnets (around the x-axis of the rotor) will be calculated. The result of that computation will be subtracted from $I_{DT,}{}^V{}_x$ (B.47) to obtain the wanted inertia of rotor-part D.

Cut-outs for permanent magnets

Now the moment of inertia of the four cut-outs for the permanent magnets around the x-axis of the rotor must be calculated. This time, the determination of the inertia distance vector is more complicated, because the position of the four cut-outs with respect to the x-axis is not symmetrical as it is with respect to the z-axis. This problem is solved by splitting up the four cut-outs in four equal quadrants (see figure B.8a) and the definition of two distance vectors: one for the cut-outs on the x-axis ($\vec{r}_{DCX}$) and one for the cut-outs on the y-axis ($\vec{r}_{DCY}$).

Because cylinder-coordinates are used for the integration over the volumes in this section, the distance between the point mass (dm) and the x-axis must also be expressed in the cylinder-coordinates (r, φ, z). This is done in figure B.8b.

$$| \vec{r}_{DCX} | = \sqrt{z^2 + y^2} = \sqrt{z^2 + r^2 \sin^2 \varphi} \qquad (B.48)$$

$$| \vec{r}_{DCY} | = \sqrt{z^2 + x^2} = \sqrt{z^2 + (x_2 + r \cos \varphi)^2} \qquad (B.49)$$
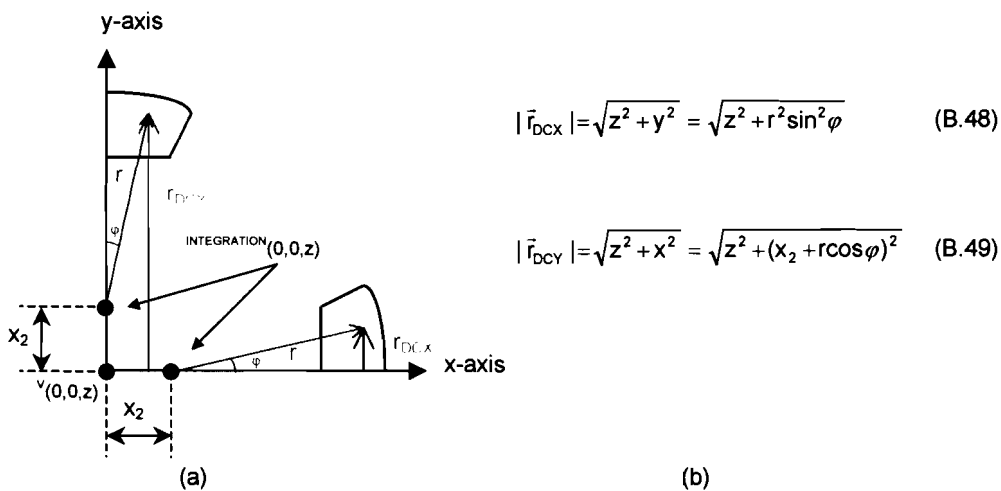
Figure B.8
a) One quadrant of a horizontal cross-section of the four cut-outs, with the definition of the inertia distance vectors $\vec{r}_{DCX}$ and $\vec{r}_{DCY}$. These vectors don't lie in the horizontal plane of the cross-section (except for z = 0). Both vectors start on the x-axis of the rotor and end on the same point mass (dm) as the integration vector r.
b) The length of vectors $\vec{r}_{DCX}$ (B.48) and $\vec{r}_{DCY}$ (B.49), which is the distance between the x-axis and the point mass (dm).
Note that $| \vec{r}_{DCY} |$ is expressed as if it was also pointing at (dm) in the cut-out part on the x-axis, because this is how it has been used in the calculation (B.50) !!!

The symmetrical shape allows that the integration is done for only one quadrant. The integral will be multiplied with 4 to obtain the value for the four cut-outs together.

In fact, the integration still is done over ½ part of one cut-out only now the integrand contains two different inertia-distances. This is shown on the next page.

For both the bottom-part and the top-part of the cut-out the moment of inertia around the x-axis can be calculated with:

$$I_{Quadrant,^v x} = \sum |\vec{r}_{DCX}|^2 \, dm + \sum |\vec{r}_{DCY}|^2 \, dm = \sum (|\vec{r}_{DCX}|^2 + |\vec{r}_{DCY}|^2) \, dm =$$

$$= \rho_{Fe} \sum (|\vec{r}_{DCX}|^2 + |\vec{r}_{DCY}|^2) \, dV = \rho_{Fe} \int\limits_{z=z_1}^{z_2} \int\limits_{\varphi=0}^{\varphi_2} \int\limits_{r=r_{in}}^{r_{out}} (|\vec{r}_{DCX}|^2 + |\vec{r}_{DCY}|^2) \, r \, dr \, d\varphi \, dz =$$

$$= \rho_{Fe} \int\limits_{z=z_1}^{z_2} \int\limits_{\varphi=0}^{\varphi_2} \int\limits_{r=r_{in}}^{r_{out}} (z^2 + r^2 \sin^2 \varphi + z^2 + x_2^2 + 2x_2 r \cos\varphi + r^2 \cos^2 \varphi) \, r \, dr \, d\varphi \, dz =$$

$$= \rho_{Fe} \int\limits_{z=z_1}^{z_2} \int\limits_{\varphi=0}^{\varphi_2} \int\limits_{r=r_{in}}^{r_{out}} (2z^2 + x_2^2 + 2x_2 r \cos\varphi + r^2) \, r \, dr \, d\varphi \, dz =$$

$$= \rho_{Fe} \int\limits_{z=z_1}^{z_2} \int\limits_{\varphi=0}^{\varphi_2} \int\limits_{r=r_{in}}^{r_{out}} \left((2z^2 + x_2^2) r + 2x_2 r^2 \cos\varphi + r^3 \right) dr \, d\varphi \, dz =$$

$$= \rho_{Fe} \int\limits_{z=z_1}^{z_2} \int\limits_{\varphi=0}^{\varphi_2} \left[\tfrac{1}{2}(2z^2 + x_2^2) r^2 + \tfrac{2}{3} x_2 r^3 \cos\varphi + \tfrac{1}{4} r^4 \right]_{r=r_{in}}^{r_{out}} d\varphi \, dz =$$

$$= \rho_{Fe} \int\limits_{z=z_1}^{z_2} \int\limits_{\varphi=0}^{\varphi_2} \left((z^2 + \tfrac{1}{2} x_2^2)\left[r_{out}^2 - r_{in}^2\right] + \tfrac{2}{3} x_2 \cos\varphi \left[r_{out}^3 - r_{in}^3\right] + \tfrac{1}{4} \left[r_{out}^4 - r_{in}^4\right] \right) d\varphi \, dz \qquad (B.50)$$

Bottom-part Cut-outs

The moment of inertia of this part around the x-axis of the rotor can be calculated

with $r_{out} = -x_2 \cos\varphi + \sqrt{R^2 - z^2 - x_2^2 \sin^2\varphi}$, $r_{in} = \dfrac{x_1}{\cos\varphi}$ and $(-a \le z \le h_1)$

substituted in (B.50):

$$I_{botDcut,^v x} = 4 \cdot \rho_{Fe} \int\limits_{z=-a}^{h_1} \int\limits_{\varphi=0}^{\varphi_2} \left((z^2 + \tfrac{1}{2} x_2^2) \left[\left(-x_2 \cos\varphi + \sqrt{R^2 - z^2 - x_2^2 \sin^2\varphi} \right)^2 - \left(\frac{x_1}{\cos\varphi} \right)^2 \right] + \right.$$

$$+ \tfrac{2}{3} x_2 \cos\varphi \left[\left(-x_2 \cos\varphi + \sqrt{R^2 - z^2 - x_2^2 \sin^2\varphi} \right)^2 - \left(\frac{x_1}{\cos\varphi} \right)^2 \right] +$$

$$\left. + \tfrac{1}{4} \left[\left(-x_2 \cos\varphi + \sqrt{R^2 - z^2 - x_2^2 \sin^2\varphi} \right)^4 - \left(\frac{x_1}{\cos\varphi} \right)^4 \right] \right) d\varphi \, dz =$$

$$= 3.2906 \cdot 10^{-8} \ [kgm^2] \quad (\text{MATLAB}^\circledR \text{ approximation}) \qquad (B.51)$$

Top-part Cut-outs

The moment of inertia of this part around the x-axis of the rotor can be calculated

with $r_{out} = -x_2\cos\varphi + \sqrt{R^2 - z^2 - x_2^2\sin^2\varphi}$, $r_{in} = -x_2\cos\varphi + \sqrt{\left(\dfrac{z}{\tan15°}\right)^2 - x_2^2\sin^2\varphi}$

and ($h_1 \le z \le h_3$) substituted in (B.50):

$$I_{topDcut,^V x} = 4 \cdot \rho_{Fe} \int_{z=h_1}^{h_3} \int_{\varphi=0}^{\varphi_2} \left((z^2 + \tfrac{1}{2}x_2^2) \left[\left(-x_2\cos\varphi + \sqrt{R^2 - z^2 - x_2^2\sin^2\varphi}\right)^2 - \left(-x_2\cos\varphi + \sqrt{\left(\dfrac{z}{\tan15°}\right)^2 - x_2^2\sin^2\varphi}\right)^2 \right] + \right.$$

$$+ \tfrac{2}{3}x_2\cos\varphi \left[\left(-x_2\cos\varphi + \sqrt{R^2 - z^2 - x_2^2\sin^2\varphi}\right)^3 - \left(-x_2\cos\varphi + \sqrt{\left(\dfrac{z}{\tan15°}\right)^2 - x_2^2\sin^2\varphi}\right)^3 \right] +$$

$$\left. + \tfrac{1}{4} \left[\left(-x_2\cos\varphi + \sqrt{R^2 - z^2 - x_2^2\sin^2\varphi}\right)^4 - \left(-x_2\cos\varphi + \sqrt{\left(\dfrac{z}{\tan15°}\right)^2 - x_2^2\sin^2\varphi}\right)^4 \right] \right) d\varphi dz =$$

$$= 2.2743 \cdot 10^{-9} \text{ [kgm}^2\text{]} \quad \text{(MATLAB}^\circledR \text{ approximation)} \tag{B.52}$$

Total Cut-outs

The moment of inertia of the four cut-outs combined around the x-axis of the rotor can be calculated by adding (B.51) and (B.52):

$$I_{Dcut,^V x} = I_{botDcut,^V x} + I_{topDcut,^V x} = 3.5180 \cdot 10^{-8} \text{ [kgm}^2\text{]} \tag{B.53}$$

Total part D

Finally, the moment of inertia of rotor-part D around the x-axis can be found by combining (B.47) and (B.53):

$$I_{D,^V x} = I_{DT,^V x} - I_{Dcut,^V x} = 4.4297 \cdot 10^{-8} \text{ [kgm}^2\text{]} \tag{B.54}$$

Appendix C   Weighted average function

Goal of this analysis is to investigate the behavior of the "weighted average" function in section 5.2. First the formula is converted into a standard mathematical notation:

$$I_{C+D} = \frac{I_C m_C + I_D m_D}{m_C + m_D} \qquad \Leftrightarrow \qquad f(x,y) = \frac{I_x x + I_y y}{x + y} \tag{C.1}$$

This formula is valid on the physical domain (m stands for mass and I for length), so $m_C = x \geq 0$, $m_D = y \geq 0$, $I_C = I_x \geq 0$ and $I_D = I_y \geq 0$.

The extreme values of function $f(x,y)$ can be found using the gradient $\nabla f(x,y)$:

$$\nabla f(x,y) = \left(\frac{\partial f}{\partial x}, \frac{\partial f}{\partial y} \right) = \left(\frac{(I_x - I_y)y}{(x+y)^2}, \frac{(I_y - I_x)x}{(x+y)^2} \right) \tag{C.2}$$

When $\nabla f(x,y) = (0,0)$ the function $f(x,y)$ has an extreme value. Here $[\partial f/\partial x = 0$ when $y = 0]$ and $[\partial f/\partial y = 0$ when $x = 0]$. Because of the denominator in both derivatives, x and y can't both be equal to zero at the same time. This situation would be trivial and without physical meaning. (When there are no masses, there is no center of gravity).

The only way to get $\nabla f(x,y) = (0,0)$ is when $I_x = I_y$. Again this is a trivial situation, because then $f(x,y) = I_x = I_y = I_{C+D}$ for every x and y.

Because $\nabla f(x,y) \neq (0,0)$ on the physical domain, the extreme values of $f(x,y)$ must be on the border of the domain. There are two borders, namely $x = 0$ and $y = 0$. With $\nabla f(x,y)$ the character of the extreme values can be determined:

Two situations can be distinguished:

① $I_x > I_y$

$$\left. \begin{array}{l} \text{Global minimum } I_{C+D} = f(0,y) = I_y = I_D \\ \text{Global maximum } I_{C+D} = f(x,0) = I_x = I_C \end{array} \right\} \qquad I_D \leq I_{C+D} \leq I_C \tag{C.3}$$

② $I_x < I_y$

$$\left. \begin{array}{l} \text{Global minimum } I_{C+D} = f(x,0) = I_x = I_C \\ \text{Global maximum } I_{C+D} = f(0,y) = I_y = I_D \end{array} \right\} \qquad I_C \leq I_{C+D} \leq I_D \tag{C.4}$$

So, the value of I_{C+D} is always bounded by the values of I_C and I_D.

Appendix D   Calculation of torques $_g^v\vec{T}_\alpha$ and $_g^v\vec{T}_\beta$

D.1 Torque produced by a single force

Before any torque can be calculated it must be clear how a torque can be generated by a single force. This is a common situation for all actuator-forces acting on the rotor, because non of them has a work-line that (always) goes through the center of gravity. Figure D.1 shows the basic principle.
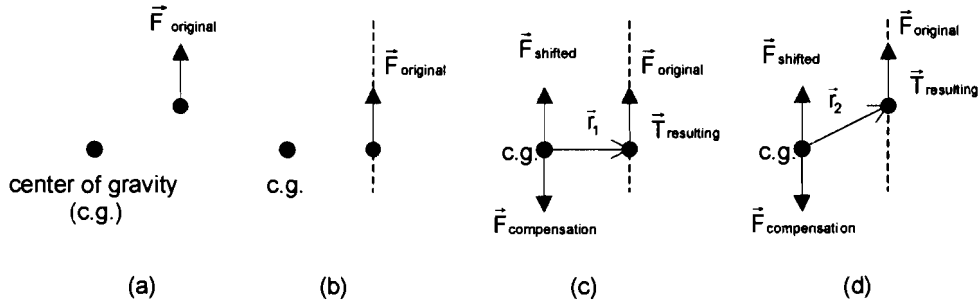

    (a)   (b)   (c)   (d)

Figure D.1
Simple two-dimensional (the plane of this piece of paper) explanation of how a torque T is generated by a force F with a work-line not going through the center of gravity.
a) The original force, its point of impact and the center of gravity.
b) The original force shifted along its work-line. This is allowed for a solid stiff body.
c) The original force shifted parallel to its work-line. A compensation force is needed to make the total force acting on the center of gravity the same as in situation a) (= 0 [N]), so $\vec{F}_{compensation} = -\vec{F}_{shifted}$. The resulting torque is formed by the original force and the (virtual) compensation force.
d) The resulting torque without first shifting the original force along its work-line. This resulting torque is equal to the torque in situation c), because the original forces are equal in size and the distance between their parallel work-lines is the same.

This last property is expressed in the general formula for calculating a torque:

$$\vec{T} = \vec{r} \times \vec{F} \tag{D.1}$$

Where $\vec{F}$ is one of the two equal (in size) forces and $\vec{r}$ is the vector between the two points of impact of the forces. In fact, a torque can be calculated using any arbitrary point as a reference point for the position vectors [2, p143]. In this thesis the center of gravity of the rotor is chosen as the reference point, so that:

$$\vec{T}_{resulting} = \vec{r}_{compensation} \times \vec{F}_{compensation} + \vec{r}_{original} \times \vec{F}_{original} = \vec{r}_1 \times \vec{F}_{original} = \vec{r}_2 \times \vec{F}_{original} \tag{D.2}$$

(Because $\vec{r}_{compensation} = \vec{0}$ with respect to the center of gravity)

Concluding: A force not acting on the center of gravity can be expressed in a force and a torque both acting on the center of gravity. Formula (D.1) can be used to calculate the torque, also in a three-dimensional situation.

D.2 Torques produced by the vertical coils

Formula (D.1) can be used to calculate the torques generated by the vertical coils.
For this, the direction of the forces and the position of their point of impact on the rotor (both defined in the rotating V-frame) are needed.
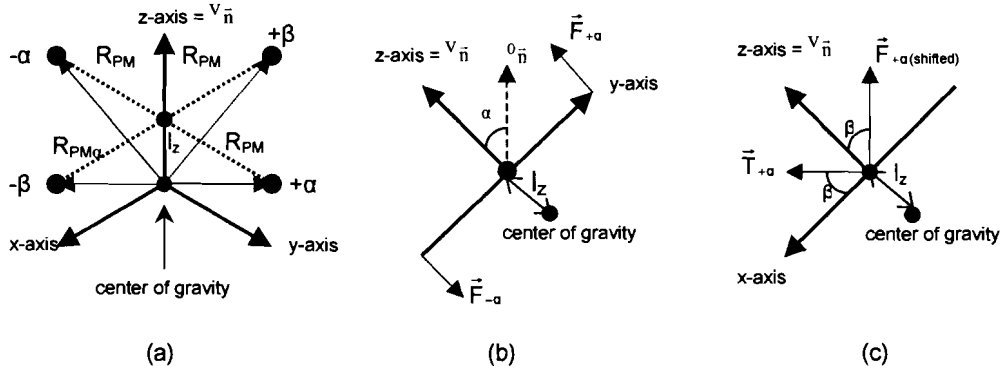

(a)   (b)   (c)

Figure D.2
a) Definition of the position vectors of the vertical forces in the rotor-frame (rotating V-frame). The points of attack of the vertical forces are chosen to be in the middle of the outside surfaces of the permanent magnets. These points are located at a distance l_z above the center of gravity and at a distance R_{PM} (= 10 [mm]) away from the normal-axis of the rotor. The position vectors expressed in the rotor-frame are:

$$
{}_g^V \vec{r}_{+\alpha} = \begin{pmatrix} 0 \\ R_{PM} \\ I_z \end{pmatrix}
\quad
{}_g^V \vec{r}_{-\alpha} = \begin{pmatrix} 0 \\ -R_{PM} \\ I_z \end{pmatrix}
\quad
{}_g^V \vec{r}_{+\beta} = \begin{pmatrix} -R_{PM} \\ 0 \\ I_z \end{pmatrix}
\quad
{}_g^V \vec{r}_{-\beta} = \begin{pmatrix} R_{PM} \\ 0 \\ I_z \end{pmatrix}
\tag{D.3}
$$

b) Cross-section ^{V}yz-plane. The rotor is tilted over an angle α. The work-lines of the α-forces remain parallel to the normal-axis of the rotor, independent of α.

c) Cross section ^{V}xz-plane. When the rotor is tilted over an angle β, the direction of the α-forces doesn't turn with the rotor-axes. So, the direction of the α-forces and α-torques in the rotor-frame is dependent of angle β.

The expressions for the α-forces were found by converting [1, (6.18)]. Together with the position vectors in (D.3) the α-torques can be calculated:

$$
{}_g^V \vec{T}_{+\alpha} = {}_g^V \vec{r}_{+\alpha} \times {}_g^V \vec{F}_{+\alpha} = \begin{pmatrix} 0 \\ R_{PM} \\ I_z \end{pmatrix} \times \begin{pmatrix} -\tfrac{1}{4}F_z \sin\beta \\ 0 \\ \tfrac{1}{4}F_z \cos\beta \end{pmatrix} = \begin{pmatrix} \tfrac{1}{4}R_{PM}F_z \cos\beta \\ -\tfrac{1}{4}I_z F_z \sin\beta \\ \tfrac{1}{4}R_{PM}F_z \sin\beta \end{pmatrix}
\tag{D.4}
$$

$$
{}_g^V \vec{T}_{-\alpha} = {}_g^V \vec{r}_{-\alpha} \times {}_g^V \vec{F}_{-\alpha} = \begin{pmatrix} 0 \\ -R_{PM} \\ I_z \end{pmatrix} \times \begin{pmatrix} \tfrac{1}{4}F_z \sin\beta \\ 0 \\ -\tfrac{1}{4}F_z \cos\beta \end{pmatrix} = \begin{pmatrix} \tfrac{1}{4}R_{PM}F_z \cos\beta \\ \tfrac{1}{4}I_z F_z \sin\beta \\ \tfrac{1}{4}R_{PM}F_z \sin\beta \end{pmatrix}
\tag{D.5}
$$

The total torque generated by the α-forces is:

$$
{}^V_g\vec{T}_\alpha = {}^V_g\vec{T}_{+\alpha} + {}^V_g\vec{T}_{-\alpha} = \begin{pmatrix} \frac{1}{2}R_{PM}F_z\cos\beta \\ 0 \\ \frac{1}{2}R_{PM}F_z\sin\beta \end{pmatrix} \tag{D.6}
$$

The expressions for the β-forces were found by converting [1, (6.19)]. Together with the position vectors in (D.3) the β-torques can be calculated in an equivalent way:

$$
{}^V_g\vec{T}_{+\beta} = {}^V_g\vec{r}_{+\beta} \times {}^V_g\vec{F}_{+\beta} = \begin{pmatrix} -R_{PM} \\ 0 \\ I_z \end{pmatrix} \times \begin{pmatrix} 0 \\ \frac{1}{4}F_z\sin\alpha \\ \frac{1}{4}F_z\cos\alpha \end{pmatrix} = \begin{pmatrix} -\frac{1}{4}I_zF_z\sin\alpha \\ \frac{1}{4}R_{PM}F_z\cos\alpha \\ -\frac{1}{4}R_{PM}F_z\sin\alpha \end{pmatrix} \tag{D.7}
$$

$$
{}^V_g\vec{T}_{-\beta} = {}^V_g\vec{r}_{-\beta} \times {}^V_g\vec{F}_{-\beta} = \begin{pmatrix} R_{PM} \\ 0 \\ I_z \end{pmatrix} \times \begin{pmatrix} 0 \\ -\frac{1}{4}F_z\sin\alpha \\ -\frac{1}{4}F_z\cos\alpha \end{pmatrix} = \begin{pmatrix} \frac{1}{4}I_zF_z\sin\alpha \\ \frac{1}{4}R_{PM}F_z\cos\alpha \\ -\frac{1}{4}R_{PM}F_z\sin\alpha \end{pmatrix} \tag{D.8}
$$

The total torque generated by the β-forces is:

$$
{}^V_g\vec{T}_\beta = {}^V_g\vec{T}_{+\beta} + {}^V_g\vec{T}_{-\beta} = \begin{pmatrix} 0 \\ \frac{1}{2}R_{PM}F_z\cos\alpha \\ -\frac{1}{2}R_{PM}F_z\sin\alpha \end{pmatrix} \tag{D.9}
$$

Appendix E   Analytical expression for $V_{botDcut}$

In section B.4 the integral for the volume of ½ bottom-part of the cut-out of the D-ring ($V_{botDcut}$) was numerically approximated. Stated below is the analytical working-out of the integral. This is not done for the mathematical die-hards, but to compare the result with the approximated outcome (B.20) to assess if further use of this approximation technique is justified. The integral under examination is repeated below:

$$V_{botDcut} = \sum_{z=-a}^{h_1} S_{botDcut} = \frac{1}{2} \int_{z=-a}^{h_1} \left(x_2^2 \left[\varphi_2 + \frac{1}{2}\sin2\varphi_2 \right] - x_2\sin\varphi_2\sqrt{R^2 - z^2 - x_2^2\sin^2\varphi_2} \right. +$$

$$\left. - (R^2 - z^2)\arcsin\left(\frac{x_2\sin\varphi_2}{\sqrt{R^2 - z^2}} \right) + (R^2 - z^2 - x_2^2)\varphi_2 - x_1^2\tan\varphi_2 \right)dz =$$

$$= 2.11932|909 \cdot 10^{-8} \text{ [m}^3\text{]} \qquad \text{(MATLAB}^{\circledR} \text{ approximation)} \qquad \text{(E.1)}$$

Integral (E.1) can be split up in four integrals that are analytically solved, namely:

$$V_{botDcut} = S_1 + S_2 + S_3 + S_4 \quad \Rightarrow$$

$$S_1 = \frac{1}{2} \int_{z=-a}^{h_1} \left(x_2^2(\varphi_2 + \frac{1}{2}\sin2\varphi_2) + \varphi_2(R^2 - x_2^2) - x_1^2\tan\varphi_2 \right)dz =$$

$$= \frac{1}{2} \left[\left(x_2^2(\varphi_2 + \frac{1}{2}\sin2\varphi_2) + \varphi_2(R^2 - x_2^2) - x_1^2\tan\varphi_2 \right)z \right]_{z=-a}^{h_1} =$$

$$= \frac{1}{2} \left[\left(x_2^2(\varphi_2 + \frac{1}{2}\sin2\varphi_2) + \varphi_2(R^2 - x_2^2) - x_1^2\tan\varphi_2 \right)(h_1 + a) \right] = 3.8464329 \cdot 10\text{-}8 \text{ [m}^3\text{]}$$

$$\text{(E.2)}$$

$$S_2 = \frac{-x_2\sin\varphi_2}{2} \int_{z=-a}^{h_1} \left(\sqrt{R^2 - x_2^2\sin^2\varphi_2 - z^2} \right)dz = \left\{ \begin{bmatrix} 3, \text{Standard} \\ \text{integral (t.24)} \end{bmatrix} \right\} =$$

$$= \frac{-x_2\sin\varphi_2}{2} \left[\frac{z}{2}\sqrt{R^2 - x_2^2\sin^2\varphi_2 - z^2} + \frac{R^2 - x_2^2\sin^2\varphi_2}{2}\arcsin\left(\frac{z}{\sqrt{R^2 - x_2^2\sin^2\varphi_2}} \right) \right]_{z=-a}^{h_1} =$$

$$= -7.6213254 \cdot 10^{-9} \text{ [m}^3\text{]} \qquad \text{(E.3)}$$

$$S_3 = \frac{-\varphi_2}{2} \int_{z=-a}^{h_1} z^2 \, dz = \frac{-\varphi_2}{2}\left[\frac{1}{3}z^3 \right]_{z=-a}^{h_1} = \frac{-\varphi_2}{6}(h_1^3 + a^3) = -2.0124975 \cdot 10^{-9} \text{ [m}^3\text{]} \qquad \text{(E.4)}$$

$$S_4 = -\frac{1}{2} \int_{z=-a}^{h_1} \left((R^2 - z^2)\arcsin\left(\frac{x_2\sin\varphi_2}{\sqrt{R^2 - z^2}} \right) \right)dz = -7.6372|19001560960 \cdot 10^{-8} \text{ [m}^3\text{]} \qquad \text{(E.5)}$$

Again, (E.5) is just a MATLAB® approximation. With the use of Mathematica 2.2.3 and
$u = x_2 \sin\varphi_2,$ S_4 can be expressed analytically:

$$S_4 = -\frac{1}{2}\left[\frac{uz\sqrt{R^2-z^2}\sqrt{\frac{u^2-R^2+z^2}{-R^2+z^2}}}{6} + \frac{z(3R^2-z^2)\arcsin\left(\frac{u}{\sqrt{R^2-z^2}}\right)}{3} + \right.$$

$$+ \frac{R^3\arctan\left(\frac{u(u^2-R^2+z^2)}{(u^2-R^2-Rz)\sqrt{R^2-z^2}\sqrt{\frac{u^2-R^2+z^2}{-R^2+z^2}}}\right)}{3} +$$

$$- \frac{R^3\arctan\left(\frac{u(u^2-R^2+z^2)}{(u^2-R^2+Rz)\sqrt{R^2-z^2}\sqrt{\frac{u^2-R^2+z^2}{-R^2+z^2}}}\right)}{3} +$$

$$\left. - \frac{u(u^2+3R^2)\arctan\left(\frac{z\sqrt{R^2-z^2}\sqrt{\frac{u^2-R^2+z^2}{-R^2+z^2}}}{(u^2-R^2+z^2)}\right)}{6}\right]^{h_1}_{z=-a} =$$

$$= -7.6372|22688496823 \cdot 10^{-9} \text{ [m}^3] \quad \text{(EXACT)} \tag{E.6}$$

$$V_{botDcut} = S_1 + S_2 + S_3 + S_4 = 2.11932|8354403535 \cdot 10^{-8} \text{ [m}^3] \quad \text{(EXACT)} \tag{E.7}$$

Comparing the approximations with the exact values in this section: (E.5) and (E.6) and also (E.1) and (E.7), the first 5 decimals match, which is enough for this application.

Appendix F Correction for Finite Element Model

F.1 Ideal model with stator air gaps

The neglected magnetic resistances (R_S) of the four small air gaps in the stator have been added to the ideal magnetic model (see section 3.3) scheme in figure F.1.

$$R_1 = \frac{d_1 - y}{\mu_0 A_{FC}} \Rightarrow \frac{dR_1}{dy} = \frac{-1}{\mu_0 A_{FC}}$$

$$R_2 = \frac{d_1 + y}{\mu_0 A_{FC}} \Rightarrow \frac{dR_2}{dy} = \frac{1}{\mu_0 A_{FC}}$$

$$R_1 + R_2 = \frac{2d_1}{\mu_0 A_{FC}} \tag{F.1}$$
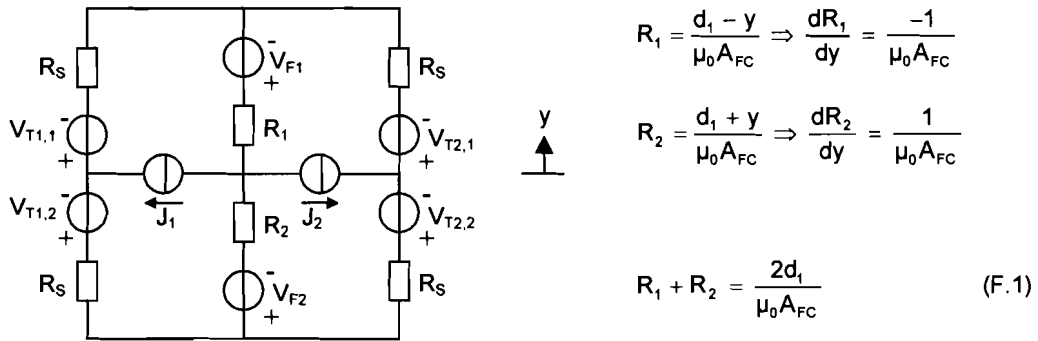
Figure F.1
Idealized magnetic scheme of the Finite Element Model [1, figure 4.12]. There are two torque-coils (V_{T1} and V_{T2}) both split-up by the permanent magnet fluxes, which in common mode can also generate a vertical force. Also present are two vertical force-coils (V_{F1} and V_{F2}). The expressions for the magnetic resistances [A/Wb] are presented next to figure F.1 in (F.1).

The following properties of the idealized model (figure F.1) can be derived.

The total magnetic resistance for one T-coil:

$$R_{TOT,T} = 2R_S + \frac{(R_1 + R_2) \cdot 2R_S}{(R_1 + R_2) + 2R_S} = 2R_S\left(1 + \frac{R_1 + R_2}{R_1 + R_2 + 2R_S}\right) \tag{F.2}$$

The total magnetic flux generated by the T-coils:

$$\Phi_{T1} = \frac{V_{T1}}{R_{TOT,T}} = \frac{N_{T1} \cdot I_{T1}}{R_{TOT,T}} \text{ [Wb]} \quad \text{and} \quad \Phi_{T2} = \frac{V_{T2}}{R_{TOT,T}} = \frac{N_{T2} \cdot I_{T2}}{R_{TOT,T}} \text{ [Wb]} \tag{F.3}$$

The total magnetic resistance for one F-coil:

$$R_{TOT,F} = R_1 + R_2 + \frac{2R_S \cdot 2R_S}{2R_S + 2R_S} = R_1 + R_2 + R_S \tag{F.4}$$

The total magnetic flux generated by the F-coils:

$$\Phi_{F1} = \frac{V_{F1}}{R_{TOT,F}} = \frac{N_{F1} \cdot I_{F1}}{R_{TOT,F}} \text{ [Wb]} \quad \text{and} \quad \Phi_{F2} = \frac{V_{F2}}{R_{TOT,F}} = \frac{N_{F2} \cdot I_{F2}}{R_{TOT,F}} \text{ [Wb]} \tag{F.5}$$

As (F.2) and (F.4) show, the magnetic resistive loads of both types of coils is constant and independent of the rotor position y. This combined with (F.3) and (F.5) means that the magnetic fluxes generated by the force- and torque-coils are only dependent on the current through those coils and not of the rotor position y. When also the flux paths of the coils are observed in figure F.1, it is evident that these are independent of the rotor position y. This means that the self-inductances and mutual inductances of the four coils are all constant (not dependent on the position y of the rotor). Ergo, all derivatives (to y) of the inductances are equal to 0.

This means that the second term in the force formula (3.1) is zero and the magnetic force in this circuit is solely generated by the interaction of the coils with the permanent magnet fluxes (first term in (3.1)) and the permanent magnets alone (third term in (3.1)). To calculate these two force types, first the flux distribution of the two permanent magnets in the circuit must be known. The permanent magnet flux distribution is drawn in figure F.2. In contradiction to the coil flux distribution, it is dependent on the rotor position y.
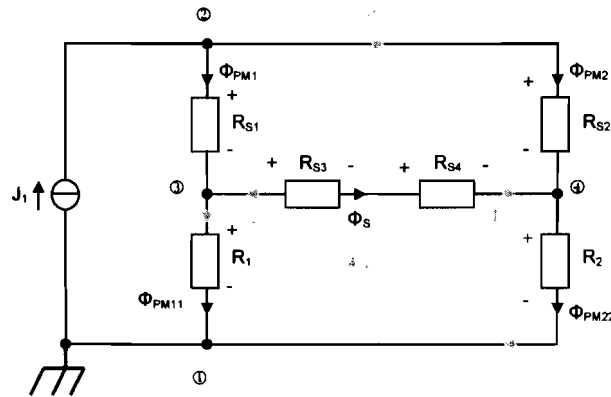
Figure F.2
Magnetic resistive load circuits of the permanent magnets (J_1 and), with flux directions, sign definitions and electrical node numbers.

The permanent magnets flux distribution through the magnetic scheme (figure F.1) can now be calculated using the definitions in figure F.2 and both *Kirchhoff* laws.

The *Kirchhoff* current equations are:

① $J_1 - \Phi_{PM11} - \Phi_{PM22} = 0$ (F.6)

② $-J_1 + \Phi_{PM1} + \Phi_{PM2} = 0$ $\Rightarrow$ $\Phi_{PM2} = J_1 - \Phi_{PM1}$ (F.7)

③ $\Phi_S - \Phi_{PM1} + \Phi_{PM11} = 0$ Combined with ❶ (F.12) $\Rightarrow$

$\Rightarrow$ $\Phi_{PM11} = \Phi_{PM1} - \Phi_S = \Phi_{PM1} - \frac{1}{2}\Phi_{PM2} + \frac{1}{2}\Phi_{PM1} = \frac{1}{2}(3\Phi_{PM1} - \Phi_{PM2})$ (F.8)

④ $-\Phi_S - \Phi_{PM2} + \Phi_{PM22} = 0$ Combined with ❶ (F.12) $\Rightarrow$

$\Rightarrow$ $\Phi_{PM22} = \Phi_S + \Phi_{PM2} = \frac{1}{2}\Phi_{PM2} - \frac{1}{2}\Phi_{PM1} + \Phi_{PM2} = \frac{1}{2}(3\Phi_{PM2} - \Phi_{PM1})$ (F.9)

Some *Kirchhoff* voltage equations are:

Potential difference between node ① and ②:
❶ $\Phi_{PM1}R_S + \Phi_{PM11}R_1 = \Phi_{PM2}R_S + \Phi_{PM22}R_2$ (F.10)
Potential difference between node ③ and ④:
❷ $\Phi_{PM11}R_1 - \Phi_{PM22}R_2 = \Phi_S2R_S$ (F.11)

Potential difference between node ③ and ④:
❸ $-\Phi_{PM1}R_S + \Phi_{PM2}R_S = \Phi_S2R_S$ $\Rightarrow$ $\Phi_S = \frac{1}{2}(\Phi_{PM2} - \Phi_{PM1})$ (F.12)

Combining ② and ❸ yields:
$\Phi_S = \frac{1}{2}(J_1 - 2\Phi_{PM1})$ (F.13)

Combining (F.7), (F.8), (F.9) and **O** (expressing all variables in Φ_{PM1}) yields:

$$\Phi_{PM1} = \frac{J_1}{4}\frac{(R_1 + 3R_2 + 2R_S)}{(R_1 + R_2 + R_S)} \tag{F.14}$$

$$\Phi_{PM2} = J_1 - \Phi_{PM1} = \frac{J_1}{4}\frac{(3R_1 + R_2 + 2R_S)}{(R_1 + R_2 + R_S)} \tag{F.15}$$

$$\Phi_{PM11} = \tfrac{1}{2}(3\Phi_{PM1} - \Phi_{PM2}) = J_1\frac{(R_2 + \tfrac{1}{2}R_S)}{(R_1 + R_2 + R_S)} \tag{F.16}$$

$$\Phi_{PM22} = \tfrac{1}{2}(3\Phi_{PM2} - \Phi_{PM1}) = J_1\frac{(R_1 + \tfrac{1}{2}R_S)}{(R_1 + R_2 + R_S)} \tag{F.17}$$

These are the fluxes caused by one permanent magnet (J_1). The total of fluxes by the two permanent magnets (J_1 and $\cdot$) through the magnetic resistors in the scheme can now be calculated (using $J_1 = $ and the fact that all partial fluxes, as calculated above, are the same):

$$\Phi_{RS1} = \Phi_{PM1} - \Phi = \tfrac{1}{2}(3\Phi_{PM1} - \Phi_{PM2}) = J_1\frac{(R_2 + \tfrac{1}{2}R_S)}{(R_1 + R_2 + R_S)} \tag{F.18}$$

$$\Phi_{RS2} = \Phi_{PM2} + \Phi = \tfrac{1}{2}(3\Phi_{PM2} - \Phi_{PM1}) = J_1\frac{(R_1 + \tfrac{1}{2}R_S)}{(R_1 + R_2 + R_S)} \tag{F.19}$$

$$\Phi_{RS3} = \Phi_S - \Phi = \tfrac{1}{2}(\Phi_{PM2} - 3\Phi_{PM1}) = -J_1\frac{(R_2 + \tfrac{1}{2}R_S)}{(R_1 + R_2 + R_S)} \tag{F.20}$$

$$\Phi_{RS4} = \Phi_S + \Phi = \tfrac{1}{2}(\Phi_{PM1} - 3\Phi_{PM2}) = -J_1\frac{(R_1 + \tfrac{1}{2}R_S)}{(R_1 + R_2 + R_S)} \tag{F.21}$$

$$\Phi_{R1} = \Phi_{PM11} + \Phi = 2\Phi_{PM11} = 2J_1\frac{(R_2 + \tfrac{1}{2}R_S)}{(R_1 + R_2 + R_S)} \tag{F.22}$$

$$\Phi_{R2} = \Phi_{PM22} + \Phi = 2\Phi_{PM22} = 2J_1\frac{(R_1 + \tfrac{1}{2}R_S)}{(R_1 + R_2 + R_S)} \tag{F.23}$$

Now that the permanent magnet flux distribution through the complete magnetic circuit is known, the forces and torques these fluxes generate, by interaction with the electromagnetic coils in the system, can be calculated.

First the numerical parameter values must be defined (taken from [1, section 4.4]):

$J_1 = B_{PM}h_{PM} = 1.11 \cdot 3.5 \cdot 10^{-3}$ [Wb/m]   (Flux of one permanent magnet)

$A_{FC} = A_1 \triangleq 2.5 \cdot 10^{-3}$ [m]   (Cross-section (width) of force coil-core)

$A_S \triangleq 6 \cdot 10^{-3}$ [m]   (Cross-section (width) of stator air gap)

$d_S = 0.4 \cdot 10^{-3}$ [m]   (Stator air gap length)

$d_1 = 0.5 \cdot 10^{-3}$ [m]   (Nominal air gap between stator and rotor)

$l_{FC} = 3.5 \cdot 10^{-3}$ [m]   (Length of force coil)

$d_{TC} = d_{FC} = 0.5 \cdot 10^{-3}$ [m]   (Thickness of coil wire cross-section)

$\tfrac{1}{2}l_{TC} = 5.0 \cdot 10^{-3}$ [m]   (**Half** the length of the torque-coil !!!)

$N_{TC}I_T = \frac{l_{TC}}{d_{TC}} \cdot J_T \cdot d_{TC}^2 = I_{TC}d_{TC}J_T$ [A]   (Square T-coil wires)

$N_{FC}I_F = \frac{l_{FC}}{d_{FC}} \cdot J_F \cdot d_{FC}^2 = I_{FC}d_{FC}J_F$ [A]   (Square F-coil wires)   (F.24)

(I_T and I_F are coil currents [A]; J_T and J_F are current densities in [A/m^2])

Note that some parameters have deviating dimensions because this analysis concerns an academic 2D-model which has no depth.

F.2 Torque-coils

To calculate the coupled permanent magnet flux through one T-coil (because of the symmetry in the circuit (figure F.1), it is the same for both coils), two things must be known: the size of and the permanent magnet flux through the upper- and bottom-part of one torque-coil.

The previously calculated permanent magnet flux distribution can now be used. Φ_{RS1} (F.18) goes through the upper-part of the coil ($T_{1,1}$) in the same direction as the coil-flux. Φ_{RS2} (F.19) goes through the bottom-part of the coil ($T_{1,2}$) in the opposite direction as the coil-flux.

The size of the upper-part and bottom-part of the torque-coils is determined by the position of the rotor y, which splits-up the total length of a torque-coil (= I_{TC}).

$$\Phi^{T1}_{coupled,0} = \Phi^{T2}_{coupled,0} = N_{TC}J_1 \left[\left(\frac{\frac{1}{2}I_{TC} - y}{I_{TC}} \right)\left(\frac{R_2 + \frac{1}{2}R_s}{R_1 + R_2 + R_s} \right) - \left(\frac{\frac{1}{2}I_{TC} + y}{I_{TC}} \right)\left(\frac{R_1 + \frac{1}{2}R_s}{R_1 + R_2 + R_s} \right) \right] \quad (F.25)$$

To calculate the generated force, the derivative of the coupled flux (F.25) to the rotor position (y) must be calculated:

$$\frac{d\Phi^{T}_{coupled,0}}{dy} = \frac{d\left(\Phi^{T1}_{coupled,0} + \Phi^{T2}_{coupled,0}\right)}{dy} = \frac{d\left(-\frac{J_1 N_{TC}}{I_{TC}}\left(2y + \frac{I_{TC}(R_1 - R_2)}{R_1 + R_2 + R_s} \right) \right)}{dy} = -\frac{N_{TC}J_1}{I_{TC}}\left(2 - \frac{I_{TC}}{\left(d_1 + \frac{d_s A_{FC}}{2A_s} \right)} \right) \quad (F.26)$$

With (F.26), the motor constant for the vertical force generated by the T-coils can be calculated:

$$\frac{d\Phi^{T}_{coupled,0}}{dy} = -\frac{N_{TC}J_1}{I_{TC}}\left(2 - \frac{I_{TC}}{d_1 + \frac{d_s A_{FC}}{2A_s}} \right) = K_F^T \frac{J_T}{I_T} \quad (F.27)$$

Substitution of (F.24) in (F.27) gives a numerical value of the motor constant.

$$K_F^T = -\frac{N_{TC}J_1 I_T}{I_{TC}J_T}\left(2 - \frac{I_{TC}}{d_1 + \frac{d_s A_{FC}}{2A_s}} \right) = -\frac{I_{TC}d_{TC}B_{PM}h_{PM}}{I_{TC}}\left(2 - \frac{I_{TC}}{d_1 + \frac{d_s A_{FC}}{2A_s}} \right) = -2d_{TC}B_{PM}h_{PM}\left(1 - \frac{I_{TC}}{2d_1 + \frac{d_s A_{FC}}{A_s}} \right) =$$

$$= -2 \cdot 0.5 \cdot 10^{-3} \cdot 1.11 \cdot 3.5 \cdot 10^{-3}\left(1 - \frac{10 \cdot 10^{-3}}{1.0 \cdot 10^{-3} + 0.4 \cdot 10^{-3}\left(\frac{2.5}{6}\right)} \right) = 2.942 \cdot 10^{-5} \text{ [Nm/A]} \quad (F.28)$$

F.3 Force-coils

To calculate the coupled permanent magnet flux through the F-coils, the previously calculated permanent magnet flux distribution can now be used. Φ_{R1} (F.22) goes through F-coil 1 in the same direction as the coil-flux.

$$\Phi^{F1}_{coupled,0} = 2J_1N_{FC}\left(\frac{R_2 + \frac{1}{2}R_s}{R_1 + R_2 + R_s}\right)$$ (F.29)

Φ_{R2} (F.23) goes through F-coil 2 in the opposite direction as the coil-flux.

$$\Phi^{F2}_{coupled,0} = -2J_1N_{FC}\left(\frac{R_1 + \frac{1}{2}R_s}{R_1 + R_2 + R_s}\right)$$ (F.30)

To calculate the generated force, the derivatives of the coupled fluxes (F.29) and (F.30) to the rotor position (y) must be calculated:

$$\frac{d\Phi^F_{coupled,0}}{dy} = \frac{d\left(\Phi^{F1}_{coupled,0} + \Phi^{F2}_{coupled,0}\right)}{dy} = \frac{d\left(2J_1N_{FC}\left(\frac{R_2 - R_1}{R_1 + R_2 + R_s}\right)\right)}{dy} = \frac{4J_1N_{FC}}{\left(2d_1 + d_s\left(\frac{A_{FC}}{A_s}\right)\right)}$$ (F.31)

With (F.31), the motor constant for the vertical force generated by the F-coils can be calculated:

$$\frac{d\Phi^F_{coupled,0}}{dy} = K^F_F \frac{J_F}{I_F}$$ (F.32)

Substitution of (F.24) in (F.32) gives a numerical value of the motor constant.

$$K^F_F = \frac{4J_1N_{FC}I_F}{J_F\left(2d_1 + d_s\left(\frac{A_{FC}}{A_s}\right)\right)} = \frac{4B_{PM}h_{PM}I_{FC}d_{FC}}{\left(2d_1 + d_s\left(\frac{A_{FC}}{A_s}\right)\right)} = \frac{4 \cdot 1.11 \cdot 3.5 \cdot 10^{-3} \cdot 3.5 \cdot 10^{-3} \cdot 0.5 \cdot 10^{-3}}{\left(1.0 \cdot 10^{-3} + \cdot 0.4 \cdot 10^{-3}\left(\frac{2.5}{6}\right)\right)} = 2.331 \cdot 10^{-5}\ [\text{Nm/A}]$$ (F.33)

The numerical values of the motor constants will be compared in section 3.4 with the ones calculated via FEM analysis in [1, section 4.4].

The third term in force formula (3.1) can be calculated using (3.21):

$$W_{m0} = \frac{1}{2}R_1\Phi^2_{R1} + \frac{1}{2}R_2\Phi^2_{R2} + \frac{1}{2}R_s(\Phi^2_{RS1} + \Phi^2_{RS2} + \Phi^2_{RS3} + \Phi^2_{RS4})$$ (F.34)

The calculation of this term is not necessary because is doesn't result in a motor constant (is not dependant of a current). This is left to do for a devoted reader.

Appendix G

Maximum actuator forces and torques (numerical values)

G.1 Forces by horizontal coils

The corrected formula for the horizontal force actuator in the u-direction (3.31) is repeated below:

$$F_u = \frac{2JN_{HC}}{d_{plus}}I_u + I_u^2\frac{\mu_0 A_{HC}N_{HC}^2}{d_{plus}^3}u - I_uI_v\frac{\mu_0 A_{HC}N_{HC}^2}{d_{plus}^3}v + \frac{2J^2}{\mu_0 A_{HC}d_{plus}}u \qquad (G.1)$$

Formula (G.1) can now be numerically given by filling in the parameters from the thesis [1, p107] and the corrected value d_{plus} (3.8):

$J = B_{PM}A_{PM} = 0.74 \cdot 4.3 \cdot 10^{-3} \cdot 5 \cdot 10^{-3} = 1.6 \cdot 10^{-5}$ [Wb] Permanent magnet flux.
$A_{HC} = d_{HC} \cdot h_X = 2.88 \cdot 10^{-3} \cdot 4.8 \cdot 10^{-3} = 1.4 \cdot 10^{-5}$ [m^2] Horizontal coil core surface.
$N_{HC} = 30$ [Windings]
$\mu_0 = 4\pi \cdot 10^{-7}$ [H/m]
$d_{plus} = 2.77 \cdot 10^{-4}$ [m] $\qquad\qquad\qquad\qquad\qquad\qquad\qquad\qquad\qquad$ (G.2)

Combining (G.2) and (G.1) results in:

$$F_u = 3.47 \cdot I_u + I_u^2 \cdot 745 \cdot u - I_uI_v \cdot 745 \cdot v + 1.05 \cdot 10^5 \cdot u \qquad (G.3)$$

Substitution of the maximum values for the four variables in (G.3),

$$I_{u,max} = I_{v,max} = \pm 2.5 \text{ [A] and } u_{max} = v_{max} = \pm 0.05 \cdot 10^{-3} \text{ [m] see (3.52)} \qquad (G.4)$$

gives:

$$F_{u,max} = 3.47 \cdot 2.5 + (2.5)^2 \cdot 745 \cdot 5 \cdot 10^{-5} + (2.5)^2 \cdot 745 \cdot 5 \cdot 10^{-5} + 1.05 \cdot 10^5 \cdot 5 \cdot 10^{-5} =$$

$$= 8.6643 + 0.2328 + 0.2328 + 5.25 = 14.38 \text{ [N]} \qquad (G.5)$$

Only the first term of F_u is really the generated force for the neutral position of the rotor:

$$F_{u,generated,max} = 3.47 \cdot I_{u,max} = 8.66 \text{ [N]} \qquad (G.6)$$

G.2 Force by vertical coils

Starting with the formula for the generated force in the z-direction [1, formula (4.81)]:

$$F_z = 2J\frac{N_{VC}}{I}I_z \qquad (G.7)$$

The vertical coil parameters are:

$I = \frac{1}{2}I_{VC}$ This is **half** the length of the vertical coil !!!

D_{VC}^2 The cross-section of vertical coil wire (is presumed to be square)

$N_{VC} = \frac{d_W I_{VC}}{D_{VC}^2} \approx 150$ [Windings]

$J_{T,max} = 10^7$ [A/m²]   The maximum current density through the coil wire.

$I_{z,max} = J_{T,max} D_{VC}^2 = \pm 2.5$ [A]   The maximum current through the coil wire.   (G.8)

Substituting (G.8) in (G.7) gives the maximum force generated by the vertical coils in the z-direction:

$$F_{z,max} = 2J\frac{2d_W I_{VC}}{I_{VC}D_{VC}^2}J_{T,max}D_{VC}^2 = 4Jd_W J_{T,max} = 4 \cdot 1.6 \cdot 10^{-5} \cdot 3 \cdot 10^{-3} \cdot 10^7 = 1.92 \text{ [N]} \qquad (G.9)$$

G.3 Torques by vertical coils

A similar calculation can be executed for the maximum torque in the α- or β-direction with [1, formula (4.150)] or (A.13):

$$T_{\alpha/\beta} = J\frac{N_{VC}}{k}I_{\alpha/\beta} \qquad (G.10)$$

And the vertical coil parameters:

The length of the vertical coil $I_{VC} = 2I = 2kR \iff k = \frac{I}{R} = \frac{I_{VC}}{2R}$

$I_{\alpha/\beta,max} = J_{T,max}D_{VC}^2 = \pm 2.5$ [A]   (G.11)

Substituting (G.8), (G.11) and R = $10 \cdot 10^{-3}$ [m] in (G.10) gives the maximum torque generated by the vertical coils in the α- or β-direction:

$$T_{\alpha/\beta,max} = J\frac{2Rd_W I_{VC}}{I_{VC}D_{VC}^2}J_{T,max}D_{VC}^2 = 2JRd_W J_{T,max} = 2 \cdot 1.6 \cdot 10^{-5} \cdot 10^{-2} \cdot 3 \cdot 10^{-3} \cdot 10^7 = 9.6 \cdot 10^{-3} \text{ [Nm]} \qquad (G.12)$$

G.4 Torques around the z-axis (T$_\gamma$)

These parameters for the toroidal coil are taken from [1]:

$N_{TC} = 12$ [Windings] $R_{PM} = 10^{-2}$ [m]   (rotor radius)
$B_{PM} = 0.74$ [T] $I_{TC} = 8 \cdot 10^{-3}$ [m]   (coil length)
$A_{PM} = w_{PM} \cdot h_{PM} = 5 \cdot 10^{-3} \cdot 4.3 \cdot 10^{-3}$ [m²] $I_z = 3.41 \cdot 10^{-7}$ [kgm²]   (corrected)
$J = B_{PM} \cdot A_{PM} = 1.6 \cdot 10^{-5}$ [Wb] $c_{HC} = 7.71$ [1/rad²]
$A_{HC} = w_{HC} \cdot h_x = 2.88 \cdot 10^{-3} \cdot 4.8 \cdot 10^{-3}$ [m²] $c_{VC} = 2.84$ [1/rad²]
$d = 0.25 \cdot 10^{-3}$ [m] (air gap)   (G.13)

Appendix H Vertical rotor position
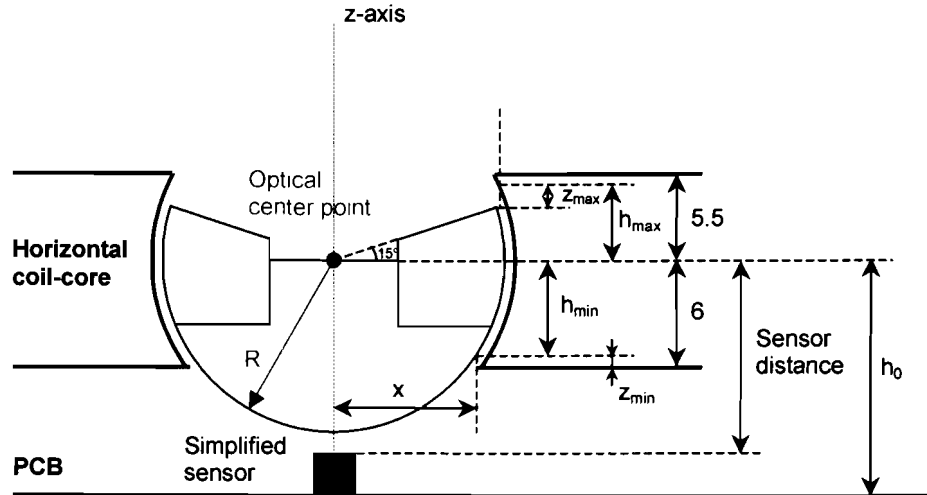
Figure H.1
A simplified vertical cross-section of the rotor, a part of the stator (horizontal coil-cores) and the sensor on the printed circuit board (PCB). The distance parameters are indicated in millimeters.

H.1 Vertical rotor range

When the windings of the vertical coils are fitted properly around their cores, the range of the rotor in the vertical direction (z-direction) is limited by the horizontal coil-cores and the layer of coating (0.2 [mm] thick) on it.

The distance parameters defined in figure H.1 in combination with the rotor radius (R = 8 [mm]) and the nominal air gap between the rotor and stator (d = 0.25 [mm]) can be used to calculate the vertical rotor range in case no coating is applied. In that situation the rotor range is imposed by the solid horizontal coil-cores, which becomes reality when the coating (locally) starts to wear.

$$h_{max} = \sqrt{(R+d)^2 - (R \cdot \cos 15°)^2} = \sqrt{(8.25)^2 - (8 \cdot \cos 15°)^2} = 2.89 \text{ [mm]} \tag{H.1}$$

$$z_{max} = h_{max} - R \cdot \sin 15° = h_{max} - 8 \cdot \sin 15° = 819 \text{ [µm]} \tag{H.2}$$

$$x = \sqrt{(R + d)^2 - 6^2} = \sqrt{(8.25)^2 - 6^2} \approx 5.66 \text{ [mm]} \tag{H.3}$$

$$h_{min} = \sqrt{R^2 - x^2} = \sqrt{8^2 - x^2} \approx 5.65 \text{ [mm]} \tag{H.4}$$

$$z_{min} = h_{min} - 6 \approx -349 \text{ [µm]} \tag{H.5}$$

With the coating, the vertical rotor range becomes even more limited, as the slightly adjusted calculations show:

$$h_{max} = \sqrt{(8.05)^2 - (8 \cdot \cos 15°)^2} = 2.26 \text{ [mm]} \tag{H.6}$$

$$z_{max} = h_{max} - 8 \cdot \sin 15° = 185.48 \text{ [µm]} \tag{H.7}$$

$$x = \sqrt{(8.05)^2 - 6^2} \approx 5.37 \text{ [mm]} \tag{H.8}$$

$$h_{min} = \sqrt{R^2 - x^2} = \sqrt{8^2 - x^2} \approx 5.93 \text{ [mm]} \tag{H.9}$$

$$z_{min} = h_{min} - 6 \approx -67.25 \text{ [µm]} \tag{H.10}$$

The results are summarized in table H.1.

Table H.1 Vertical rotor range.

Parameter	Without coating on horizontal coil-cores	With coating on horizontal coil-cores
z_{min} [µm]	-349	-67.25
z_{max} [µm]	819	185.48

H.2 Sensor bowl distance

The distance between the capacitive sensor electrodes and the rotor determines the sensitivity of the sensor for rotor positions/orientations, see Observation ② in section 4.5.1.

Evaluation of the blue-prints of the system [1, appendix E] shows that the nominal distance between the sensor and rotor might be more than the expected nominal air gap of d = 0.25 [mm]. Some possible design- and manufacturing inaccuracies will be investigated next.

The distance h_0 (see figure H.1) between the horizontal plane through the optical center point of the rotor and the printed circuit board (PCB) can be calculated on three locations in the stator:

$h_{0,\text{Horizontal coil}}$:   Stator bottom ring (2.8 + glue) + Electrical insulation layer (0.1) +
                            Bottom coil-core part (7.3) = **10.2 + glue [mm]**   (H.11)

$h_{0,\text{Vertical coil}}$:   Stator bottom ring (2.8 + glue) + Insulation layer (0.5) +
                            Bottom coil-core part (6.8) = **10.1 + glue [mm]**   (H.12)

$h_{0,\text{Sensor}}$:   Sensing electrode (1.75) + Air gap + Rotor (8.0) = **9.75 + Air gap [mm]** (H.13)

One of the design rules for a perfectly aligned system is:

$$h_{0,\text{Horizontal coil}} = h_{0,\text{Vertical coil}} = h_{0,\text{Sensor}} \tag{H.14}$$

The intention was to create a nominal air gap of 0.25 [mm] between the sensing electrode and the rotor. Then $h_{0,Sensor}$ (H.13) would be equal to 10.0 [mm]. Combining (H.11 – H.14) illustrates that the design- and manufacturing inaccuracies can add an extra 0.2 [mm] (+ glue thickness) to the sensor air gap. This almost doubles the intended nominal air gap size, and therefore decreases the sensor sensitivity.

Besides the possible increased nominal sensor air gap, the blue-print dimensions [1, appendix E] reveal two other things:

❶ According to (H.14), $h_{0,Horizontal\ coil}$ (H.11) and $h_{0,Vertical\ coil}$ (H.12) should be equal to have a perfect alignment. Now the difference seems to be 0.1 [mm].

❷ The space between the two stator rings should be the same at both the horizontal- and the vertical coil positions, but it isn't:

Horizontal coil:	Two electrical insulation layers (2·0.1) + Horizontal coil-core height (7.3 + 6.5) = **14.0 [mm]**	(H.15)
Vertical coil:	Two insulation layers (2·0.5) + Vertical coil-core height (6.8 + 6.0) = **13.8 [mm]**	(H.16)

The total height of the stator is indicated as 19.6 [mm], which means that the heights of the stator rings are counted as 2.8 [mm] when the glue is omitted. This leaves a space of 14.0 [mm] between the rings (or 13.8 [mm] when the lamellae-glue is taken into account).

Hopefully, the constructor of the system has made sure that the alignment of the vertical- and horizontal coils with the rotor is correct and that the deviation of the nominal air gap distance is minimal.

Appendix I   Blue-prints of the calibration setup
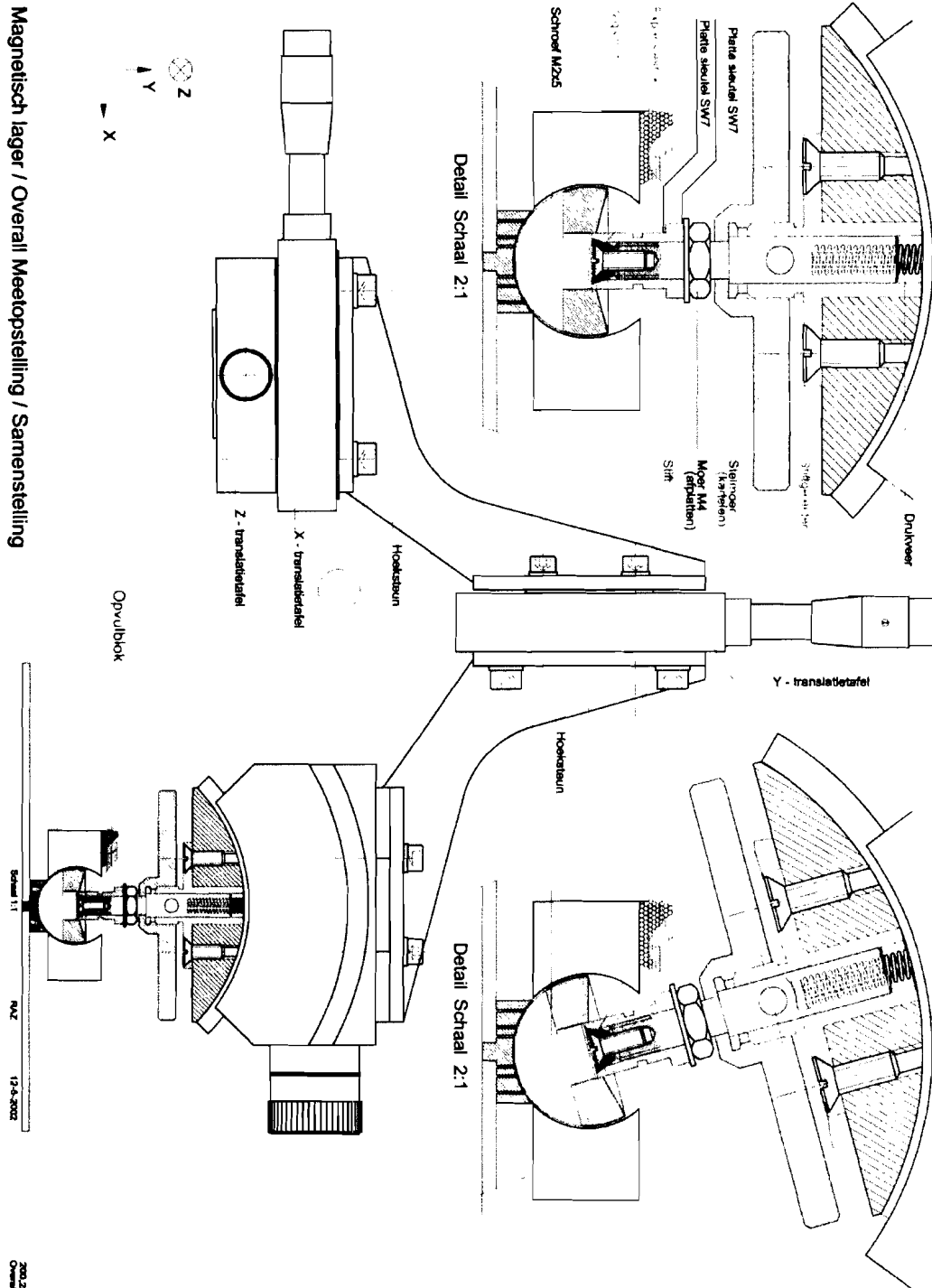
Figure I.1
Total sensor calibration measurement setup with micro-manipulation tables for the three translation directions and one rotation table for the α-direction.
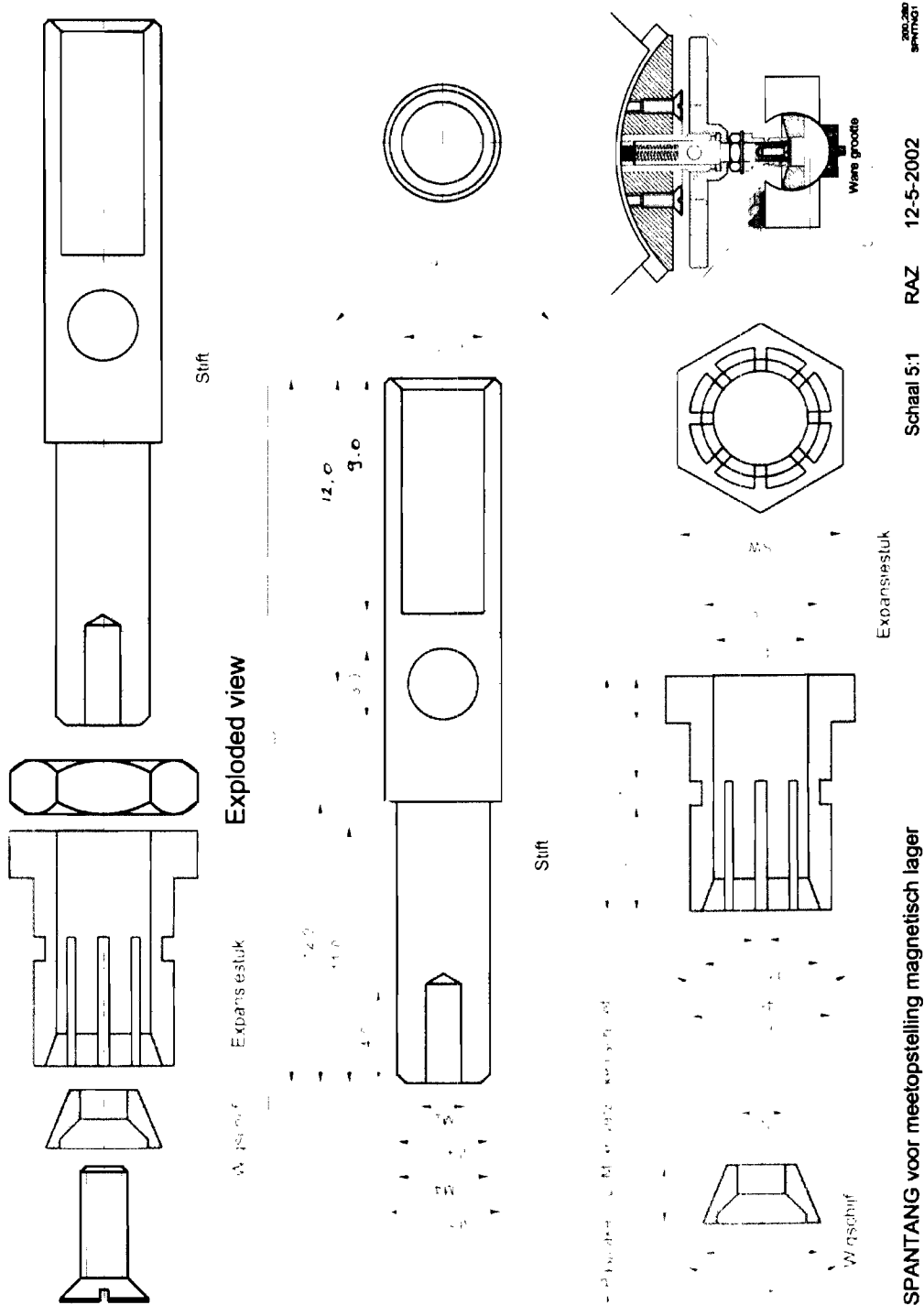
Figure I.2
Blue-print (in Dutch) of the expansion-gripper (section 11.3) to fixate the rotor inside the prototype, as
is indicated in the small upper right corner (also see figure I.1).
Notice that the last corrections are also visible.
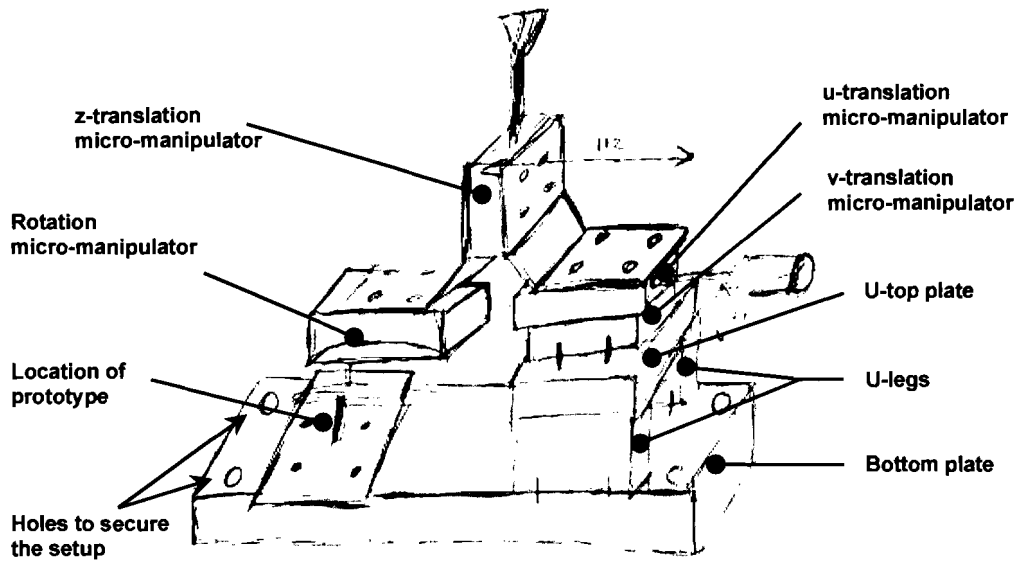
Figure I.3
3D sketch of the support for the sensor calibration setup, that indicates the position and the function of the bottom plate and the U-shaped support.
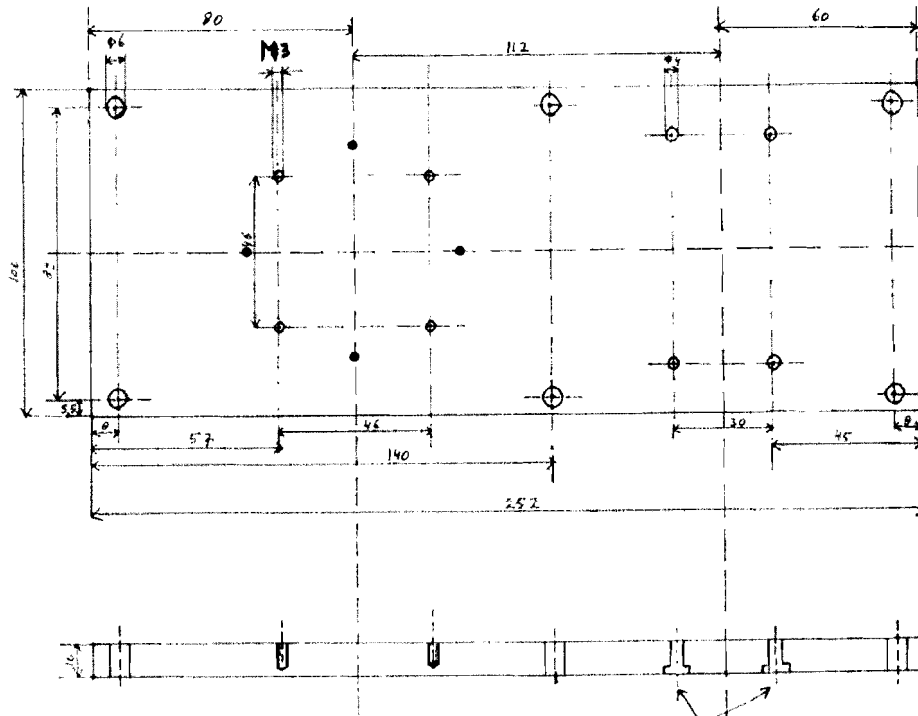
Figure I.4
Bottom plate of calibration setup.
The green dots are screw holes to mount the prototype 45° rotated.

BOUEN PLAAT

Φ3   Φ4

SCHROEUEN
VERZINKEN

U-BEEN
(2X)

Figure I.5
Blue-print of the U-shaped support for the calibration setup, to compensate for the height of the prototype.

$\phi 50.0$

M8 Fijn

kartelen

$\phi 4.0$

$\phi 9.0$

$\phi 12.0$

4.0

6.5

8.0

Figure I.6
Adjustment wheel.

$\phi 35$

$\phi 8.0$

$\phi 5.0$

M8 Fijn

20.0

Figure I.7
Pin-guider.

Appendix J Calculation of the first order derivatives (for the linear model)

J.1 Ideal actuator formulae

The sum vector of all forces acting on the center of gravity of the rotor is:

$$\,^{0}_{g}\vec{F} = \,^{0}R_{V}\cdot\,^{V}_{g}\vec{F}_{act} + \,^{0}_{g}\vec{F}_{g} \tag{J.1}$$

Where:
$\,^{0}R_{V}$ is the transformation matrix from the rotating V-frame to the static world frame (0-frame). With the rotation around z-axis omitted ($\psi = 0$) it is:

$$\,^{0}R_{V} = \begin{pmatrix} \cos\Theta & 0 & \sin\Theta \\ \sin\Theta\sin\Phi & \cos\Phi & -\cos\Theta\sin\Phi \\ -\sin\Theta\cos\Phi & \sin\Phi & \cos\Theta\cos\Phi \end{pmatrix} \quad\Rightarrow\quad \,^{0}R_{V}\big|_{\substack{\bar{y}=\bar{y}_{op}\\ \bar{u}=\bar{u}_{op}}} = \begin{pmatrix} 1 & 0 & 0 \\ 0 & 1 & 0 \\ 0 & 0 & 1 \end{pmatrix} \tag{J.2}$$

The sum vector of all actuator forces acting on the center of gravity of the rotor is:

$$\,^{V}_{g}\vec{F}_{act} = \begin{pmatrix} \frac{1}{2}\sqrt{2}F_{u} - \frac{1}{2}\sqrt{2}F_{v} - \frac{1}{2}F_{z}\sin\beta \\ \frac{1}{2}\sqrt{2}F_{u} + \frac{1}{2}\sqrt{2}F_{v} + \frac{1}{2}F_{z}\sin\alpha \\ \frac{1}{2}F_{z}(\cos\alpha + \cos\beta) \end{pmatrix} \quad\Rightarrow\quad \,^{V}_{g}\vec{F}_{act}\big|_{\substack{\bar{y}=\bar{y}_{op}\\ \bar{u}=\bar{u}_{op}}} = \begin{pmatrix} 0 \\ 0 \\ D_{1}I_{z0} \end{pmatrix} = \begin{pmatrix} 0 \\ 0 \\ m_{ROTOR}g \end{pmatrix} \tag{J.3}$$

The gravity acting on the rotor:

$$\,^{0}_{g}\vec{F}_{g} = \begin{pmatrix} 0 \\ 0 \\ -F_{g} \end{pmatrix} = \begin{pmatrix} 0 \\ 0 \\ -m_{ROTOR}g \end{pmatrix} \tag{J.4}$$

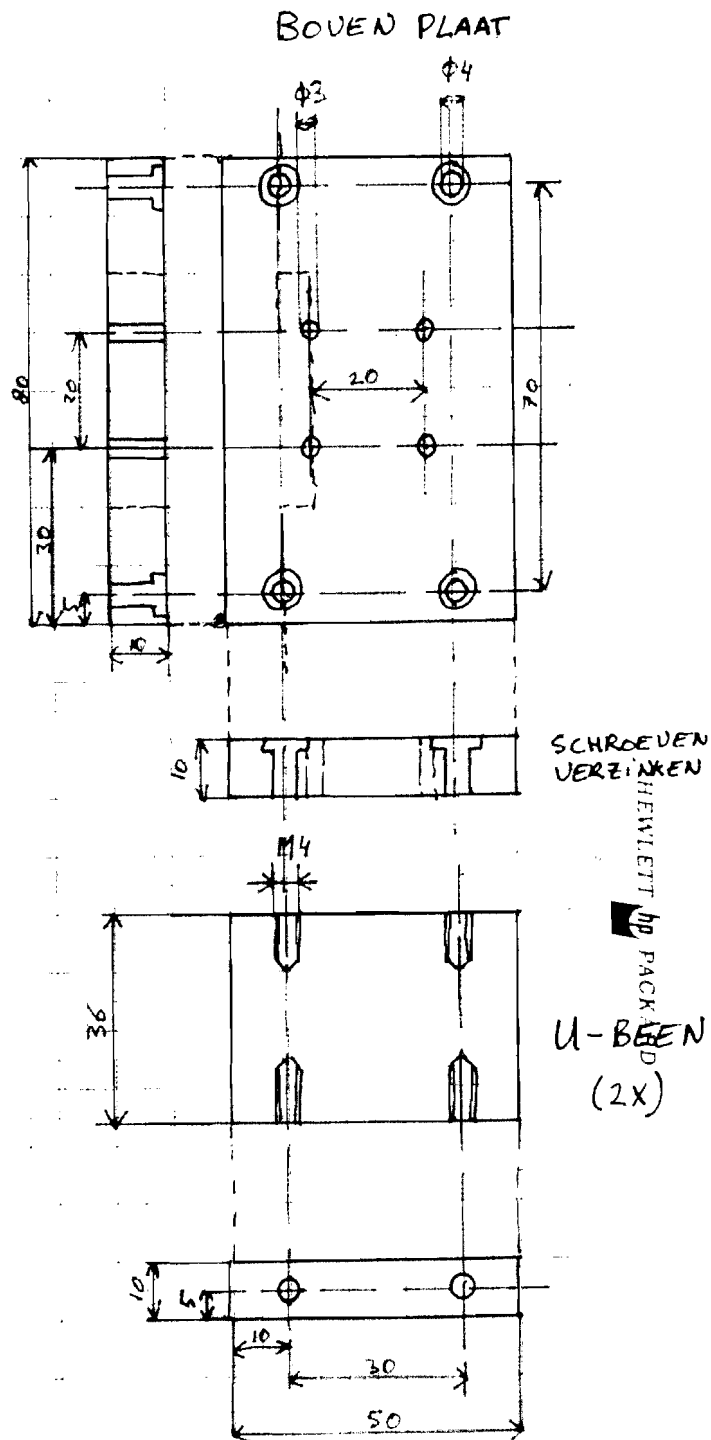The sum vector of all actuator torques acting on the center of gravity of the rotor is:

$$\,^{0}_{g}\vec{T} = \,^{0}R_{V}\cdot\,^{V}_{g}\vec{T}_{act} \tag{J.5}$$

Where:

$$\,^{V}_{g}\vec{T}_{act} = \begin{pmatrix} T_{\alpha}\cos\beta - \frac{1}{2}I_{z}F_{z}\sin\alpha - \frac{1}{2}\sqrt{2}I_{uv}F_{u} - \frac{1}{2}\sqrt{2}I_{uv}F_{v} \\ T_{\beta}\cos\alpha - \frac{1}{2}I_{z}F_{z}\sin\beta + \frac{1}{2}\sqrt{2}I_{uv}F_{u} - \frac{1}{2}\sqrt{2}I_{uv}F_{v} \\ T_{\alpha}\sin\beta - T_{\beta}\sin\alpha \end{pmatrix} \quad\Rightarrow\quad \,^{V}_{g}\vec{T}_{act}\big|_{\substack{\bar{y}=\bar{y}_{op}\\ \bar{u}=\bar{u}_{op}}} = \begin{pmatrix} 0 \\ 0 \\ 0 \end{pmatrix} \tag{J.6}$$

The equations for the magnitudes and signs of the actuator forces and torques (F_{u}, F_{v}, F_{z}, T_{α} and T_{β}) are repeated below. They are presented with the device parameters bundled in parameters (A_{1} till E_{1}) to promote convenient calculation.

Horizontal force actuators (equation (G.1)):

$$F_{u} = A_{1}I_{u} + B_{1}(I_{u}^{2}\cdot u - I_{u}I_{v}\cdot v) + C_{1}u \tag{J.7}$$

$$F_{v} = A_{1}I_{v} + B_{1}(I_{v}^{2}\cdot v - I_{u}I_{v}\cdot u) + C_{1}v \tag{J.8}$$

$$\text{Where: } A_{1} = \frac{2JN_{HC}}{d_{plus}}; \quad B_{1} = \frac{\mu_{0}A_{HC}N_{HC}^{2}}{d_{plus}^{3}}; \quad C_{1} = \frac{2J^{2}}{\mu_{0}A_{HC}d_{plus}} \tag{J.9}$$

Vertical force actuator (equation (G.7)):

$$F_z = D_1 I_z$$ (J.10)

Where: $D_1 = 4J\dfrac{N_{VC}}{I_{VC}}$ (J.11)

Torque actuators (equation (G.10)):

$$T_\alpha = E_1 I_\alpha$$ (J.12)
$$T_\beta = E_1 I_\beta$$ (J.13)

Where: $E_1 = J\dfrac{N_{VC}}{k} = 2JR\dfrac{N_{VC}}{I_{VC}}$ (J.14)

The device parameters used in the equations above are summarized in table 12.1.

J.2 Actuator current and coordinate transformations

The controller for the x- and y-position need some transformations for the controlled positions (x, y ⇒ u, v) [1, (2.9)] and the controlling currents (I_x, I_y ⇒ I_u, I_v) [1, (7.1)]. The horizontal actuator coordinate and current transformations and their derivatives are:

$u = \frac{1}{\sqrt{2}}(x + y)$ ⇒ $\dfrac{\partial u}{\partial x} = \dfrac{1}{\sqrt{2}}$ and $\dfrac{\partial u}{\partial y} = \dfrac{1}{\sqrt{2}}$ (J.15)

$v = \frac{1}{\sqrt{2}}(-x + y)$ ⇒ $\dfrac{\partial v}{\partial x} = -\dfrac{1}{\sqrt{2}}$ and $\dfrac{\partial v}{\partial y} = \dfrac{1}{\sqrt{2}}$ (J.16)

$I_u = \frac{1}{\sqrt{2}}(I_x + I_y)$ ⇒ $\dfrac{\partial I_u}{\partial I_x} = \dfrac{1}{\sqrt{2}}$ and $\dfrac{\partial I_u}{\partial I_y} = \dfrac{1}{\sqrt{2}}$ (J.17)

$I_v = \frac{1}{\sqrt{2}}(-I_x + I_y)$ ⇒ $\dfrac{\partial I_v}{\partial I_x} = -\dfrac{1}{\sqrt{2}}$ and $\dfrac{\partial I_v}{\partial I_y} = \dfrac{1}{\sqrt{2}}$ (J.18)

J.3 Bryant angles

Equation (12.8) and (12.9) are repeated:

$\Phi = \alpha$
$\theta = \arctan(\tan\beta\cos\alpha)$
$\Psi = 0$ (The rotation around the z-axis of the rotor will be neglected in this analysis)

Then

$$\dfrac{d\Phi}{d\alpha} = 1$$ (J.19)

$$\dfrac{d\Phi}{d\beta} = 0$$ (J.20)

$\dfrac{d\theta}{d\alpha} = \dfrac{-\tan\beta\sin\alpha}{1 + (\tan\beta\cos\alpha)^2}$ ⇒ $\left.\dfrac{d\theta}{d\alpha}\right|_{\substack{\bar{y}=\bar{y}_{op}\\ \bar{u}=\bar{u}_{op}}} = 0$ (J.21)

$\dfrac{d\theta}{d\beta} = \left(\dfrac{\cos\alpha}{\cos^2\beta}\right)\cdot\dfrac{1}{1 + (\tan\beta\cos\alpha)^2}$ ⇒ $\left.\dfrac{d\theta}{d\beta}\right|_{\substack{\bar{y}=\bar{y}_{op}\\ \bar{u}=\bar{u}_{op}}} = 1$ (J.22)

J.4 Transformation matrix ^0R_v

$$\frac{\partial^0 R_v}{\partial x} = \overline{0}; \qquad \frac{\partial^0 R_v}{\partial y} = \overline{0}; \qquad \frac{\partial^0 R_v}{\partial z} = \overline{0} \tag{J.23}$$

$$\frac{\partial^0 R_v}{\partial \Phi} = \begin{pmatrix} 0 & 0 & 0 \\ \sin\Theta\cos\Phi & -\sin\Phi & -\cos\Theta\cos\Phi \\ \sin\Theta\sin\Phi & \cos\Phi & -\cos\Theta\sin\Phi \end{pmatrix} \quad \Rightarrow \quad \left.\frac{\partial^0 R_v}{\partial \Phi}\right|_{\substack{\bar{y}=\bar{y}_{op} \\ \bar{u}=\bar{u}_{op}}} = \begin{pmatrix} 0 & 0 & 0 \\ 0 & 0 & -1 \\ 0 & 1 & 0 \end{pmatrix} \tag{J.24}$$

$$\frac{\partial^0 R_v}{\partial \Theta} = \begin{pmatrix} -\sin\Theta & 0 & \cos\Theta \\ \cos\Theta\sin\Phi & 0 & \sin\Theta\sin\Phi \\ -\cos\Theta\cos\Phi & 0 & -\sin\Theta\cos\Phi \end{pmatrix} \quad \Rightarrow \quad \left.\frac{\partial^0 R_v}{\partial \Theta}\right|_{\substack{\bar{y}=\bar{y}_{op} \\ \bar{u}=\bar{u}_{op}}} = \begin{pmatrix} 0 & 0 & 1 \\ 0 & 0 & 0 \\ -1 & 0 & 0 \end{pmatrix} \tag{J.25}$$

$$\frac{\partial^0 R_v}{\partial \alpha} = \frac{\partial^0 R_v}{\partial \Phi}\cdot\frac{\partial \Phi}{\partial \alpha} + \frac{\partial^0 R_v}{\partial \Theta}\cdot\frac{\partial \Theta}{\partial \alpha} \quad \Rightarrow \quad \left.\frac{\partial^0 R_v}{\partial \alpha}\right|_{\substack{\bar{y}=\bar{y}_{op} \\ \bar{u}=\bar{u}_{op}}} = \begin{pmatrix} 0 & 0 & 0 \\ 0 & 0 & -1 \\ 0 & 1 & 0 \end{pmatrix} \tag{J.26}$$

$$\frac{\partial^0 R_v}{\partial \beta} = \frac{\partial^0 R_v}{\partial \Phi}\cdot\frac{\partial \Phi}{\partial \beta} + \frac{\partial^0 R_v}{\partial \Theta}\cdot\frac{\partial \Theta}{\partial \beta} \quad \Rightarrow \quad \left.\frac{\partial^0 R_v}{\partial \beta}\right|_{\substack{\bar{y}=\bar{y}_{op} \\ \bar{u}=\bar{u}_{op}}} = \begin{pmatrix} 0 & 0 & 1 \\ 0 & 0 & 0 \\ -1 & 0 & 0 \end{pmatrix} \tag{J.27}$$

$$\frac{\partial^0 R_v}{\partial l_x} = \overline{0}; \qquad \frac{\partial^0 R_v}{\partial l_y} = \overline{0}; \qquad \frac{\partial^0 R_v}{\partial l_z} = \overline{0}; \qquad \frac{\partial^0 R_v}{\partial l_\alpha} = \overline{0}; \qquad \frac{\partial^0 R_v}{\partial l_\beta} = \overline{0} \tag{J.28}$$

J.5 Actuator formulae

$$\frac{\partial F_u}{\partial u} = B_1 l_u^2 + C_1 \quad \Rightarrow \quad \left.\frac{\partial F_u}{\partial u}\right|_{\substack{\bar{y}=\bar{y}_{op} \\ \bar{u}=\bar{u}_{op}}} = C_1 \tag{J.29}$$

$$\frac{\partial F_u}{\partial v} = -B_1 l_u l_v \quad \Rightarrow \quad \left.\frac{\partial F_u}{\partial v}\right|_{\substack{\bar{y}=\bar{y}_{op} \\ \bar{u}=\bar{u}_{op}}} = 0 \tag{J.30}$$

$$\frac{\partial F_u}{\partial l_u} = A_1 + 2B_1 l_u u - B_1 l_v v \quad \Rightarrow \quad \left.\frac{\partial F_u}{\partial l_u}\right|_{\substack{\bar{y}=\bar{y}_{op} \\ \bar{u}=\bar{u}_{op}}} = A_1 \tag{J.31}$$

$$\frac{\partial F_u}{\partial l_v} = -B_1 l_u v \quad \Rightarrow \quad \left.\frac{\partial F_u}{\partial l_v}\right|_{\substack{\bar{y}=\bar{y}_{op} \\ \bar{u}=\bar{u}_{op}}} = 0 \tag{J.32}$$

$$\frac{\partial F_u}{\partial x} = \frac{\partial F_u}{\partial u}\cdot\frac{\partial u}{\partial x} + \frac{\partial F_u}{\partial v}\cdot\frac{\partial v}{\partial x} \quad \Rightarrow \quad \left.\frac{\partial F_u}{\partial x}\right|_{\substack{\bar{y}=\bar{y}_{op} \\ \bar{u}=\bar{u}_{op}}} = \frac{C_1}{\sqrt{2}} \tag{J.33}$$

$$\frac{\partial F_u}{\partial y} = \frac{\partial F_u}{\partial u}\cdot\frac{\partial u}{\partial y} + \frac{\partial F_u}{\partial v}\cdot\frac{\partial v}{\partial y} \quad \Rightarrow \quad \left.\frac{\partial F_u}{\partial y}\right|_{\substack{\bar{y}=\bar{y}_{op} \\ \bar{u}=\bar{u}_{op}}} = \frac{C_1}{\sqrt{2}} \tag{J.34}$$

$$\frac{\partial F_u}{\partial z} = 0; \qquad \frac{\partial F_u}{\partial \alpha} = 0; \qquad \frac{\partial F_u}{\partial \beta} = 0 \tag{J.35}$$

$$\frac{\partial F_u}{\partial l_x} = \frac{\partial F_u}{\partial l_u} \cdot \frac{\partial l_u}{\partial l_x} + \frac{\partial F_u}{\partial l_v} \cdot \frac{\partial l_v}{\partial l_x} \quad \Rightarrow \quad \left.\frac{\partial F_u}{\partial l_x}\right|_{\substack{\bar{y}=\bar{y}_{op} \\ \bar{u}=\bar{u}_{op}}} = \frac{A_1}{\sqrt{2}} \tag{J.36}$$

$$\frac{\partial F_u}{\partial l_y} = \frac{\partial F_u}{\partial l_u} \cdot \frac{\partial l_u}{\partial l_y} + \frac{\partial F_u}{\partial l_v} \cdot \frac{\partial l_v}{\partial l_y} \quad \Rightarrow \quad \left.\frac{\partial F_u}{\partial l_y}\right|_{\substack{\bar{y}=\bar{y}_{op} \\ \bar{u}=\bar{u}_{op}}} = \frac{A_1}{\sqrt{2}} \tag{J.37}$$

$$\frac{\partial F_u}{\partial l_z} = 0; \qquad \frac{\partial F_u}{\partial l_\alpha} = 0; \qquad \frac{\partial F_u}{\partial l_\beta} = 0 \tag{J.38}$$

$$\frac{\partial F_v}{\partial u} = -B_1 l_u l_v \quad \Rightarrow \quad \left.\frac{\partial F_v}{\partial u}\right|_{\substack{\bar{y}=\bar{y}_{op} \\ \bar{u}=\bar{u}_{op}}} = 0 \tag{J.39}$$

$$\frac{\partial F_v}{\partial v} = B_1 l_v^2 + C_1 \quad \Rightarrow \quad \left.\frac{\partial F_v}{\partial v}\right|_{\substack{\bar{y}=\bar{y}_{op} \\ \bar{u}=\bar{u}_{op}}} = C_1 \tag{J.40}$$

$$\frac{\partial F_v}{\partial l_u} = -B_1 l_v u \quad \Rightarrow \quad \left.\frac{\partial F_v}{\partial l_u}\right|_{\substack{\bar{y}=\bar{y}_{op} \\ \bar{u}=\bar{u}_{op}}} = 0 \tag{J.41}$$

$$\frac{\partial F_v}{\partial l_v} = A_1 + 2B_1 l_v v - B_1 l_u u \quad \Rightarrow \quad \left.\frac{\partial F_v}{\partial l_v}\right|_{\substack{\bar{y}=\bar{y}_{op} \\ \bar{u}=\bar{u}_{op}}} = A_1 \tag{J.42}$$

$$\frac{\partial F_v}{\partial x} = \frac{\partial F_v}{\partial u} \cdot \frac{\partial u}{\partial x} + \frac{\partial F_v}{\partial v} \cdot \frac{\partial v}{\partial x} \quad \Rightarrow \quad \left.\frac{\partial F_v}{\partial x}\right|_{\substack{\bar{y}=\bar{y}_{op} \\ \bar{u}=\bar{u}_{op}}} = -\frac{C_1}{\sqrt{2}} \tag{J.43}$$

$$\frac{\partial F_v}{\partial y} = \frac{\partial F_v}{\partial u} \cdot \frac{\partial u}{\partial y} + \frac{\partial F_v}{\partial v} \cdot \frac{\partial v}{\partial y} \quad \Rightarrow \quad \left.\frac{\partial F_v}{\partial y}\right|_{\substack{\bar{y}=\bar{y}_{op} \\ \bar{u}=\bar{u}_{op}}} = \frac{C_1}{\sqrt{2}} \tag{J.44}$$

$$\frac{\partial F_v}{\partial z} = 0; \qquad \frac{\partial F_v}{\partial \alpha} = 0; \qquad \frac{\partial F_v}{\partial \beta} = 0 \tag{J.45}$$

$$\frac{\partial F_v}{\partial l_x} = \frac{\partial F_v}{\partial l_u} \cdot \frac{\partial l_u}{\partial l_x} + \frac{\partial F_v}{\partial l_v} \cdot \frac{\partial l_v}{\partial l_x} \quad \Rightarrow \quad \left.\frac{\partial F_v}{\partial l_x}\right|_{\substack{\bar{y}=\bar{y}_{op} \\ \bar{u}=\bar{u}_{op}}} = -\frac{A_1}{\sqrt{2}} \tag{J.46}$$

$$\frac{\partial F_v}{\partial l_y} = \frac{\partial F_v}{\partial l_u} \cdot \frac{\partial l_u}{\partial l_y} + \frac{\partial F_v}{\partial l_v} \cdot \frac{\partial l_v}{\partial l_y} \quad \Rightarrow \quad \left.\frac{\partial F_v}{\partial l_y}\right|_{\substack{\bar{y}=\bar{y}_{op} \\ \bar{u}=\bar{u}_{op}}} = \frac{A_1}{\sqrt{2}} \tag{J.47}$$

$$\frac{\partial F_v}{\partial l_z} = 0; \qquad \frac{\partial F_v}{\partial l_\alpha} = 0; \qquad \frac{\partial F_v}{\partial l_\beta} = 0 \tag{J.48}$$

$$\frac{\partial F_z}{\partial l_z} = D_1; \qquad \frac{\partial T_\alpha}{\partial l_\alpha} = E_1; \qquad \frac{\partial T_\beta}{\partial l_\beta} = E_1 \tag{J.49}$$

J.6 Actuator force vector (J.3) expressed in the rotating rotor frame (V-frame)

$$\frac{\partial^V_g \bar{F}_{act}}{\partial x} = \begin{pmatrix} \frac{1}{2}\sqrt{2}\frac{\partial F_u}{\partial x} - \frac{1}{2}\sqrt{2}\frac{\partial F_v}{\partial x} - \frac{1}{2}\sin\beta\frac{\partial F_z}{\partial x} \\ \frac{1}{2}\sqrt{2}\frac{\partial F_u}{\partial x} + \frac{1}{2}\sqrt{2}\frac{\partial F_v}{\partial x} + \frac{1}{2}\sin\alpha\frac{\partial F_z}{\partial x} \\ \frac{1}{2}(\cos\alpha + \cos\beta)\frac{\partial F_z}{\partial x} \end{pmatrix} \quad \Rightarrow \quad \left.\frac{\partial^V_g \bar{F}_{act}}{\partial x}\right|_{\substack{\bar{y}=\bar{y}_{op} \\ \bar{u}=\bar{u}_{op}}} = \begin{pmatrix} C_1 \\ 0 \\ 0 \end{pmatrix} \tag{J.50}$$

$$\frac{\partial \, _g^V\vec{F}_{act}}{\partial y} = \begin{pmatrix} \frac{1}{2}\sqrt{2}\,\frac{\partial F_u}{\partial y} - \frac{1}{2}\sqrt{2}\,\frac{\partial F_v}{\partial y} - \frac{1}{2}\sin\beta\,\frac{\partial F_z}{\partial y} \\ \frac{1}{2}\sqrt{2}\,\frac{\partial F_u}{\partial y} + \frac{1}{2}\sqrt{2}\,\frac{\partial F_v}{\partial y} + \frac{1}{2}\sin\alpha\,\frac{\partial F_z}{\partial y} \\ \frac{1}{2}(\cos\alpha + \cos\beta)\frac{\partial F_z}{\partial y} \end{pmatrix} \quad \Rightarrow \quad \left.\frac{\partial \, _g^V\vec{F}_{act}}{\partial y}\right|_{\substack{\bar{y}=\bar{y}_{op}\\ \bar{u}=\bar{u}_{op}}} = \begin{pmatrix} 0 \\ C_1 \\ 0 \end{pmatrix} \qquad (J.51)$$

$$\frac{\partial \, _g^V\vec{F}_{act}}{\partial z} = \bar{0} \qquad (J.52)$$

$$\frac{\partial \, _g^V\vec{F}_{act}}{\partial \alpha} = \begin{pmatrix} 0 \\ \frac{1}{2}F_z\cos\alpha \\ -\frac{1}{2}F_z\sin\alpha \end{pmatrix} \quad \Rightarrow \quad \left.\frac{\partial \, _g^V\vec{F}_{act}}{\partial \alpha}\right|_{\substack{\bar{y}=\bar{y}_{op}\\ \bar{u}=\bar{u}_{op}}} = \begin{pmatrix} 0 \\ \frac{1}{2}F_z \\ 0 \end{pmatrix} = \begin{pmatrix} 0 \\ \frac{1}{2}m_{ROTOR}g \\ 0 \end{pmatrix} \qquad (J.53)$$

$$\frac{\partial \, _g^V\vec{F}_{act}}{\partial \beta} = \begin{pmatrix} -\frac{1}{2}F_z\cos\beta \\ 0 \\ -\frac{1}{2}F_z\sin\beta \end{pmatrix} \quad \Rightarrow \quad \left.\frac{\partial \, _g^V\vec{F}_{act}}{\partial \beta}\right|_{\substack{\bar{y}=\bar{y}_{op}\\ \bar{u}=\bar{u}_{op}}} = \begin{pmatrix} -\frac{1}{2}F_z \\ 0 \\ 0 \end{pmatrix} = \begin{pmatrix} -\frac{1}{2}m_{ROTOR}g \\ 0 \\ 0 \end{pmatrix} \qquad (J.54)$$

$$\frac{\partial \, _g^V\vec{F}_{act}}{\partial l_x} = \begin{pmatrix} \frac{1}{2}\sqrt{2}\,\frac{\partial F_u}{\partial l_x} - \frac{1}{2}\sqrt{2}\,\frac{\partial F_v}{\partial l_x} - \frac{1}{2}\sin\beta\,\frac{\partial F_z}{\partial l_x} \\ \frac{1}{2}\sqrt{2}\,\frac{\partial F_u}{\partial l_x} + \frac{1}{2}\sqrt{2}\,\frac{\partial F_v}{\partial l_x} + \frac{1}{2}\sin\alpha\,\frac{\partial F_z}{\partial l_x} \\ \frac{1}{2}(\cos\alpha + \cos\beta)\frac{\partial F_z}{\partial l_x} \end{pmatrix} \quad \Rightarrow \quad \left.\frac{\partial \, _g^V\vec{F}_{act}}{\partial l_x}\right|_{\substack{\bar{y}=\bar{y}_{op}\\ \bar{u}=\bar{u}_{op}}} = \begin{pmatrix} A_1 \\ 0 \\ 0 \end{pmatrix} \qquad (J.55)$$

$$\frac{\partial \, _g^V\vec{F}_{act}}{\partial l_y} = \begin{pmatrix} \frac{1}{2}\sqrt{2}\,\frac{\partial F_u}{\partial l_y} - \frac{1}{2}\sqrt{2}\,\frac{\partial F_v}{\partial l_y} - \frac{1}{2}\sin\beta\,\frac{\partial F_z}{\partial l_y} \\ \frac{1}{2}\sqrt{2}\,\frac{\partial F_u}{\partial l_y} + \frac{1}{2}\sqrt{2}\,\frac{\partial F_v}{\partial l_y} + \frac{1}{2}\sin\alpha\,\frac{\partial F_z}{\partial l_y} \\ \frac{1}{2}(\cos\alpha + \cos\beta)\frac{\partial F_z}{\partial l_y} \end{pmatrix} \quad \Rightarrow \quad \left.\frac{\partial \, _g^V\vec{F}_{act}}{\partial l_y}\right|_{\substack{\bar{y}=\bar{y}_{op}\\ \bar{u}=\bar{u}_{op}}} = \begin{pmatrix} 0 \\ A_1 \\ 0 \end{pmatrix} \qquad (J.56)$$

$$\frac{\partial \, _g^V\vec{F}_{act}}{\partial l_z} = \begin{pmatrix} -\frac{1}{2}\sin\beta\,\frac{\partial F_z}{\partial l_z} \\ \frac{1}{2}\sin\alpha\,\frac{\partial F_z}{\partial l_z} \\ \frac{1}{2}(\cos\alpha + \cos\beta)\frac{\partial F_z}{\partial l_z} \end{pmatrix} \quad \Rightarrow \quad \left.\frac{\partial \, _g^V\vec{F}_{act}}{\partial l_z}\right|_{\substack{\bar{y}=\bar{y}_{op}\\ \bar{u}=\bar{u}_{op}}} = \begin{pmatrix} 0 \\ 0 \\ D_1 \end{pmatrix} \qquad (J.57)$$

$$\frac{\partial \, _g^V\vec{F}_{act}}{\partial l_\alpha} = \bar{0}; \qquad \left.\frac{\partial \, _g^V\vec{F}_{act}}{\partial l_\beta}\right|_{\substack{\bar{y}=\bar{y}_{op}\\ \bar{u}=\bar{u}_{op}}} = \bar{0} \qquad (J.58)$$

J.7 Gravity vector

$$\frac{\partial \, {}^0_g\vec{F}_g}{\partial k} = \begin{pmatrix} 0 \\ 0 \\ 0 \end{pmatrix} \qquad \forall\, k \in \{x, y, z, \alpha, \beta, I_x, I_y, I_z, I_\alpha, I_\beta\} \tag{J.59}$$

J.8 Actuator torque vector (J.6) expressed in the rotating rotor frame (V-frame)

$$\frac{\partial \, {}^V_g\vec{T}_{act}}{\partial x} = \begin{pmatrix} \cos\beta\dfrac{\partial T_\alpha}{\partial x} - \tfrac{1}{2}I_z\sin\alpha\dfrac{\partial F_z}{\partial x} - \tfrac{1}{2}\sqrt{2}I_{uv}\dfrac{\partial F_u}{\partial x} - \tfrac{1}{2}\sqrt{2}I_{uv}\dfrac{\partial F_v}{\partial x} \\[4pt] \cos\alpha\dfrac{\partial T_\beta}{\partial x} - \tfrac{1}{2}I_z\sin\beta\dfrac{\partial F_z}{\partial x} + \tfrac{1}{2}\sqrt{2}I_{uv}\dfrac{\partial F_u}{\partial x} - \tfrac{1}{2}\sqrt{2}I_{uv}\dfrac{\partial F_v}{\partial x} \\[4pt] \sin\beta\dfrac{\partial T_\alpha}{\partial x} - \sin\alpha\dfrac{\partial T_\beta}{\partial x} \end{pmatrix} \Rightarrow \left.\frac{\partial \, {}^V_g\vec{T}_{act}}{\partial x}\right|_{\substack{\vec{y}=\vec{y}_{op}\\ \vec{u}=\vec{u}_{op}}} = \begin{pmatrix} 0 \\ I_{uv}C_1 \\ 0 \end{pmatrix} \tag{J.60}$$

$$\frac{\partial \, {}^V_g\vec{T}_{act}}{\partial y} = \begin{pmatrix} \cos\beta\dfrac{\partial T_\alpha}{\partial y} - \tfrac{1}{2}I_z\sin\alpha\dfrac{\partial F_z}{\partial y} - \tfrac{1}{2}\sqrt{2}I_{uv}\dfrac{\partial F_u}{\partial y} - \tfrac{1}{2}\sqrt{2}I_{uv}\dfrac{\partial F_v}{\partial y} \\[4pt] \cos\alpha\dfrac{\partial T_\beta}{\partial y} - \tfrac{1}{2}I_z\sin\beta\dfrac{\partial F_z}{\partial y} + \tfrac{1}{2}\sqrt{2}I_{uv}\dfrac{\partial F_u}{\partial y} - \tfrac{1}{2}\sqrt{2}I_{uv}\dfrac{\partial F_v}{\partial y} \\[4pt] \sin\beta\dfrac{\partial T_\alpha}{\partial y} - \sin\alpha\dfrac{\partial T_\beta}{\partial y} \end{pmatrix} \Rightarrow \left.\frac{\partial \, {}^V_g\vec{T}_{act}}{\partial y}\right|_{\substack{\vec{y}=\vec{y}_{op}\\ \vec{u}=\vec{u}_{op}}} = \begin{pmatrix} -I_{uv}C_1 \\ 0 \\ 0 \end{pmatrix} \tag{J.61}$$

$$\frac{\partial \, {}^V_g\vec{T}_{act}}{\partial z} = \begin{pmatrix} \cos\beta\dfrac{\partial T_\alpha}{\partial z} - \tfrac{1}{2}I_z\sin\alpha\dfrac{\partial F_z}{\partial z} - \tfrac{1}{2}\sqrt{2}I_{uv}\dfrac{\partial F_u}{\partial z} - \tfrac{1}{2}\sqrt{2}I_{uv}\dfrac{\partial F_v}{\partial z} \\[4pt] \cos\alpha\dfrac{\partial T_\beta}{\partial z} - \tfrac{1}{2}I_z\sin\beta\dfrac{\partial F_z}{\partial z} + \tfrac{1}{2}\sqrt{2}I_{uv}\dfrac{\partial F_u}{\partial z} - \tfrac{1}{2}\sqrt{2}I_{uv}\dfrac{\partial F_v}{\partial z} \\[4pt] \sin\beta\dfrac{\partial T_\alpha}{\partial z} - \sin\alpha\dfrac{\partial T_\beta}{\partial z} \end{pmatrix} \Rightarrow \left.\frac{\partial \, {}^V_g\vec{T}_{act}}{\partial z}\right|_{\substack{\vec{y}=\vec{y}_{op}\\ \vec{u}=\vec{u}_{op}}} = \begin{pmatrix} 0 \\ 0 \\ 0 \end{pmatrix} \tag{J.62}$$

$$\frac{\partial \, {}^V_g\vec{T}_{act}}{\partial \alpha} = \begin{pmatrix} -\tfrac{1}{2}I_z F_z\cos\alpha \\ -T_\beta\sin\alpha \\ -T_\beta\cos\alpha \end{pmatrix} \Rightarrow \left.\frac{\partial \, {}^V_g\vec{T}_{act}}{\partial \alpha}\right|_{\substack{\vec{y}=\vec{y}_{op}\\ \vec{u}=\vec{u}_{op}}} = \begin{pmatrix} -\tfrac{1}{2}I_z D_i I_{z0} \\ 0 \\ 0 \end{pmatrix} = \begin{pmatrix} -\tfrac{1}{2}I_z m_{ROTOR}g \\ 0 \\ 0 \end{pmatrix} \tag{J.63}$$

$$\frac{\partial \, {}^V_g\vec{T}_{act}}{\partial \beta} = \begin{pmatrix} -T_\alpha\sin\beta \\ -\tfrac{1}{2}I_z F_z\cos\beta \\ T_\alpha\cos\beta \end{pmatrix} \Rightarrow \left.\frac{\partial \, {}^V_g\vec{T}_{act}}{\partial \beta}\right|_{\substack{\vec{y}=\vec{y}_{op}\\ \vec{u}=\vec{u}_{op}}} = \begin{pmatrix} 0 \\ -\tfrac{1}{2}I_z D_i I_{z0} \\ 0 \end{pmatrix} = \begin{pmatrix} 0 \\ -\tfrac{1}{2}I_z m_{ROTOR}g \\ 0 \end{pmatrix} \tag{J.64}$$

$$\frac{\partial\, ^V_g\vec{T}_{act}}{\partial I_x} = \begin{pmatrix} \cos\beta\frac{\partial T_\alpha}{\partial I_x} - \frac{1}{2}I_z\sin\alpha\frac{\partial F_z}{\partial I_x} - \frac{1}{2}\sqrt{2}I_{uv}\frac{\partial F_u}{\partial I_x} - \frac{1}{2}\sqrt{2}I_{uv}\frac{\partial F_v}{\partial I_x} \\ \cos\alpha\frac{\partial T_\beta}{\partial I_x} - \frac{1}{2}I_z\sin\beta\frac{\partial F_z}{\partial I_x} + \frac{1}{2}\sqrt{2}I_{uv}\frac{\partial F_u}{\partial I_x} - \frac{1}{2}\sqrt{2}I_{uv}\frac{\partial F_v}{\partial I_x} \\ \sin\beta\frac{\partial T_\alpha}{\partial I_x} - \sin\alpha\frac{\partial T_\beta}{\partial I_x} \end{pmatrix} \Rightarrow \left.\frac{\partial\, ^V_g\vec{T}_{act}}{\partial I_x}\right|_{\substack{\vec{y}=\vec{y}_{op}\\ \vec{u}=\vec{u}_{op}}} = \begin{pmatrix} 0 \\ I_{uv}A_1 \\ 0 \end{pmatrix} \qquad (J.65)$$

$$\frac{\partial\, ^V_g\vec{T}_{act}}{\partial I_y} = \begin{pmatrix} \cos\beta\frac{\partial T_\alpha}{\partial I_y} - \frac{1}{2}I_z\sin\alpha\frac{\partial F_z}{\partial I_y} - \frac{1}{2}\sqrt{2}I_{uv}\frac{\partial F_u}{\partial I_y} - \frac{1}{2}\sqrt{2}I_{uv}\frac{\partial F_v}{\partial I_y} \\ \cos\alpha\frac{\partial T_\beta}{\partial I_y} - \frac{1}{2}I_z\sin\beta\frac{\partial F_z}{\partial I_y} + \frac{1}{2}\sqrt{2}I_{uv}\frac{\partial F_u}{\partial I_y} - \frac{1}{2}\sqrt{2}I_{uv}\frac{\partial F_v}{\partial I_y} \\ \sin\beta\frac{\partial T_\alpha}{\partial I_y} - \sin\alpha\frac{\partial T_\beta}{\partial I_y} \end{pmatrix} \Rightarrow \left.\frac{\partial\, ^V_g\vec{T}_{act}}{\partial I_y}\right|_{\substack{\vec{y}=\vec{y}_{op}\\ \vec{u}=\vec{u}_{op}}} = \begin{pmatrix} -I_{uv}A_1 \\ 0 \\ 0 \end{pmatrix} \qquad (J.66)$$

$$\frac{\partial\, ^V_g\vec{T}_{act}}{\partial I_z} = \begin{pmatrix} -\frac{1}{2}I_zD_1\sin\alpha \\ -\frac{1}{2}I_zD_1\sin\beta \\ 0 \end{pmatrix} \qquad \Rightarrow \qquad \left.\frac{\partial\, ^V_g\vec{T}_{act}}{\partial I_z}\right|_{\substack{\vec{y}=\vec{y}_{op}\\ \vec{u}=\vec{u}_{op}}} = \begin{pmatrix} 0 \\ 0 \\ 0 \end{pmatrix} \qquad (J.67)$$

$$\frac{\partial\, ^V_g\vec{T}_{act}}{\partial I_\alpha} = \begin{pmatrix} E_1\cos\beta \\ 0 \\ E_1\sin\beta \end{pmatrix} \qquad \Rightarrow \qquad \left.\frac{\partial\, ^V_g\vec{T}_{act}}{\partial I_\alpha}\right|_{\substack{\vec{y}=\vec{y}_{op}\\ \vec{u}=\vec{u}_{op}}} = \begin{pmatrix} E_1 \\ 0 \\ 0 \end{pmatrix} \qquad (J.68)$$

$$\frac{\partial\, ^V_g\vec{T}_{act}}{\partial I_\beta} = \begin{pmatrix} 0 \\ E_1\cos\alpha \\ -E_1\sin\alpha \end{pmatrix} \qquad \Rightarrow \qquad \left.\frac{\partial\, ^V_g\vec{T}_{act}}{\partial I_\beta}\right|_{\substack{\vec{y}=\vec{y}_{op}\\ \vec{u}=\vec{u}_{op}}} = \begin{pmatrix} 0 \\ E_1 \\ 0 \end{pmatrix} \qquad (J.69)$$

J.9 Linear model gains expressed in device parameters

Table J.1 Linear model gains expressed in device parameters.

Gain	Symbolic function	Parameter function	Unit
$_xK_x$ and $_yK_y$	C_1/m_{ROTOR}	$\dfrac{2J^2}{\mu_0 A_{HC} d_{plus} m_{ROTOR}}$	$\dfrac{1}{s^2}$
$_xK_{Ix}$ and $_yK_{Iy}$	A_1/m_{ROTOR}	$\dfrac{2JN_{HC}}{d_{plus} m_{ROTOR}}$	$\dfrac{m}{s^2 A}$
$_xK_\beta$	$-(D_1 \cdot I_{z0}/m_{ROTOR}) + g$	$g/2$	$\dfrac{m}{s^2 rad}$
$_yK_\alpha$	$(D_1 \cdot I_{z0}/m_{ROTOR}) - g$	$-g/2$	$\dfrac{m}{s^2 rad}$
$_zK_{Iz}$	D_1/m_{ROTOR}	$\dfrac{4JN_{VC}}{I_{VC} m_{ROTOR}}$	$\dfrac{m}{s^2 A}$
$_\alpha K_y$	$-I_{uv} \cdot C_1/J_x$	$\dfrac{-2I_{uv}J^2}{\mu_0 A_{HC} d_{plus} J_x}$	$\dfrac{rad}{ms^2}$
$_\alpha K_\alpha$	$-I_z \cdot m_{ROTOR} \cdot g/(2J_x)$	$\dfrac{-I_z m_{ROTOR} g}{2J_x}$	$\dfrac{rad}{s^2}$
$_\alpha K_{Iy}$	$-I_{uv} \cdot A_1/J_x$	$\dfrac{-2JN_{HC}I_{uv}}{d_{plus}J_x}$	$\dfrac{rad}{s^2 A}$
$_\alpha K_{Ia}$	E_1/J_x	$\dfrac{2RJN_{VC}}{I_{VC}J_x}$	$\dfrac{rad}{s^2 A}$
$_\beta K_x$	$I_{uv} \cdot C_1/J_y$	$\dfrac{2I_{uv}J^2}{\mu_0 A_{HC} d_{plus}J_y}$	$\dfrac{rad}{s^2 m}$
$_\beta K_\beta$	$-I_z \cdot m_{ROTOR} \cdot g/(2J_y)$	$\dfrac{-I_z m_{ROTOR} g}{2J_y}$	$\dfrac{rad}{s^2}$
$_\beta K_{Ix}$	$I_{uv} \cdot A_1/J_y$	$\dfrac{2JN_{HC}I_{uv}}{d_{plus}J_y}$	$\dfrac{rad}{s^2 A}$
$_\beta K_{I\beta}$	E_1/J_y	$\dfrac{2RJN_{VC}}{I_{VC}J_y}$	$\dfrac{rad}{s^2 A}$

The used device parameters can be found in table 12.1 in section 12.1.

Appendix K

Datasheet of the Nano17 multi-axis Force/Torque sensor of ATI
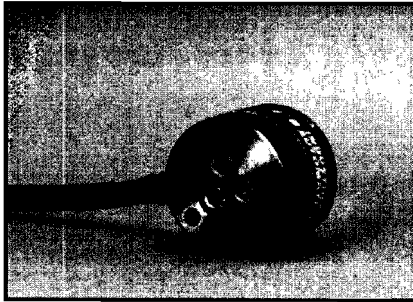
The Nano17 F/T transducer
The transducer is made of hardened stainless steel, with integral interface plates made from high-strength aircraft aluminum

Peter W. Johnson, PhD, President
Ergonomic Research and Consulting, Inc., Seattle, WA

One of the Smallest 6-axis Sensors in the World
The Nano17 fits into restricted spaces of research applications.
Extremely High Strength
* EDM wire-cut from high yield-strength stainless steel
* Maximum allowable single-axis overload values are 5.2 to 23 times rated capacities
**High Signal-to-Noise Ratio**
Silicon strain gauges provide a signal 75 times stronger than conventional foil gauges. This signal is amplified, resulting in near-zero noise distortion

* **Dental research**
* **Robotic hand research**
* **Robotic Surgery**
* **Finger-force Research**

English-Calibrated Sensing Ranges	US-3-1		US-6-2		US-12-4	
Fx, Fy (±lb)	3		6		12	
Fz (±lb)	4.25		8.5		17	
Tx, Ty (±in-lb)	1		2		4	
Tz (±in-lb)	1		2		4	
Resolution						
F/T System Type †	CON	DAQ	CON	DAQ	CON	DAQ
Fx, Fy (lb)	1/320	1/5120	1/160	1/2560	1/80	1/1280
Fz (lb)	1/320	1/5120	1/160	1/2560	1/80	1/1280
Tx, Ty (in-lb)	1/2000	1/32000	1/1000	1/16000	1/500	1/8000
Tz (in-lb)	1/2000	1/32000	1/1000	1/16000	1/500	1/8000

Metric-Calibrated Sensing Ranges	SI-12-0.12		SI-25-0.25		SI-50-0.5	
Fx, Fy (±N)	12		25		50	
Fz (±N)	17		35		70	
Tx, Ty (±N-mm)	120		250		500	
Tz (±N-mm)	120		250		500	
Resolution						
F/T System Type †	CON	DAQ	CON	DAQ	CON	DAQ
Fx, Fy (N)	1/80	1/1280	1/20	1/320	1/10	1/160
Fz (N)	1/80	1/1280	1/40	1/640	1/20	1/320
Tx, Ty (N-mm)	1/16	1/256	1/8	1/128	1/4	1/64
Tz (N-mm)	1/16	1/256	1/8	1/128	1/4	1/64

Contact ATI for complex loading information. Resolutions are typical. † *CON = Controller F/T System, DAQ = 16-bit DAQ F/T System*
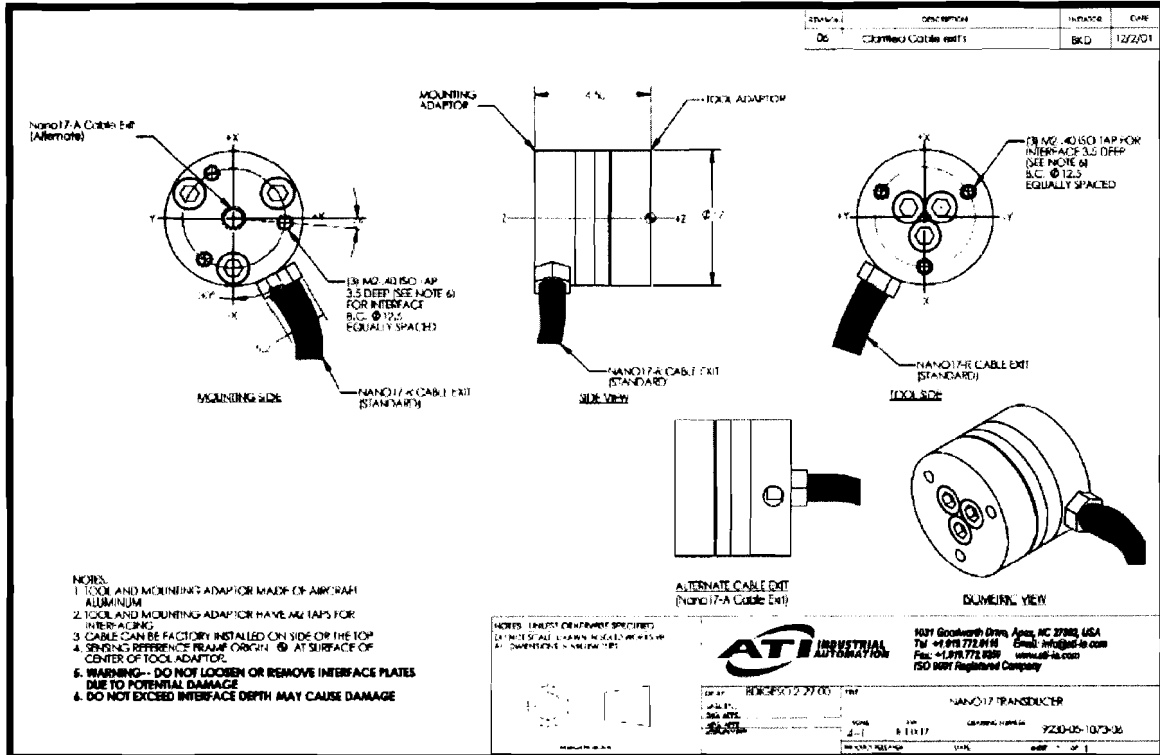
Single-Axis Overload	English	Metric
Fxy	±79 lb	±350 N
Fz	±180 lb	±820 N
Txy	±23 in-lb	±2.6 N-m
Tz	±28 in-lb	±3.1 N-m
Stiffness (Calculated)	**English**	**Metric**
X-axis & Y-axis force (Kx, Ky)	53×10^3 lb/in	9.3×10^6 N/m
Z-axis force (Kz)	69×10^3 lb/in	12×10^6 N/m
X-axis & Y-axis torque (Ktx, Kty)	2.2×10^3 in-lb/rad	250 N-m/rad
Z-axis torque (Ktz)	3.5×10^3 in-lb/rad	400 N-m/rad
Resonant Frequency (Measured)		
Fx, Fy, Tz	7200 Hz	
Fz, Tx, Ty	7200 Hz	
Physical Specifications	**English**	**Metric**
Weight †	0.020 lb	9.1 g
Diameter †	0.669 in	17 mm
Height †	0.571 in	14.5 mm

† *Specifications include standard interface plates.*

Appendix L   Numerical values

L.1 Numerical values of the transfer function matrix G(s) elements

In table L.1, three sets of numerical values of the transfer functions (12.51)-(12.60), the elements of G(s) (12.50), can be found. Each set belongs to one of the three actuator models as described in part 1 of this thesis: the ideal model in [1], the corrected ideal model (PART 1, chapter 3) and the model based on the actuator calibration measurement in [1] (the expected model in PART 1, chapter 7).

Table L.1 Numerical transfer functions of matrix G(s) for the three actuator models in MATLAB®
notation.

Parameter	Ideal Model [1]	Corrected Ideal Model	Expected from Measurements
$G_{11}(s)$	$\dfrac{1107\ s^2 - 6.547e8}{s^4 - 1.672e7\ s^2 + 9.889e12}$	$\dfrac{603.2\ s^2 - 3.966e8}{s^4 - 1.323e7\ s^2 + 8.697e12}$	$\dfrac{138.2\ s^2 - 9.459e6}{s^4 - 1.382e6\ s^2 + 9.459e10}$
$G_{15}(s)$	$\dfrac{17.48\ s^2 - 2.817e8}{s^4 - 1.672e7\ s^2 + 9.889e12}$	$\dfrac{15.71\ s^2 - 1.969e008}{s^4 - 1.323e007\ s^2 + 8.697e012}$	$\dfrac{5.587\ s^2 - 7.299e006}{s^4 - 1.382e006\ s^2 + 9.459e10}$
$G_{22}(s)$	$\dfrac{1107\ s^2 - 6.547e8}{s^4 - 1.672e7\ s^2 + 9.889e12}$	$\dfrac{603.2\ s^2 - 3.966e8}{s^4 - 1.323e7\ s^2 + 8.697e12}$	$\dfrac{138.2\ s^2 - 9.459e6}{s^4 - 1.382e6\ s^2 + 9.459e10}$
$G_{24}(s)$	$\dfrac{-17.48\ s^2 + 2.817e8}{s^4 - 1.672e7\ s^2 + 9.889e12}$	$\dfrac{-15.71\ s^2 + 1.969e8}{s^4 - 1.323e7\ s^2 + 8.697e12}$	$\dfrac{-5.587\ s^2 + 7.299e6}{s^4 - 1.382e6\ s^2 + 9.459e10}$
$G_{33}(s)$	$\dfrac{52.78}{s^2}$	$\dfrac{58.44}{s^2}$	$\dfrac{12.6}{s^2}$
$G_{42}(s)$	$\dfrac{-2.709e4\ s^4 - 6.104e\text{-}5\ s^2 - 32}{s^6 - 1.672e7\ s^4 + 9.889e12\ s^2}$	$\dfrac{-2.261e4\ s^4 - 3.196e6\ s^2 + 32}{s^6 - 1.323e7\ s^4 + 8.695e12\ s^2 + 1.229e15}$	$\dfrac{-5183\ s^4 - 7.324e5\ s^2 + 0.0625}{s^6 - 1.382e6\ s^4 + 9.44e10\ s^2 + 1.337e13}$
$G_{44}(s)$	$\dfrac{1.166e4\ s^4 - 1.878e11\ s^2 + 32}{s^6 - 1.672e7\ s^4 + 9.889e12\ s^2}$	$\dfrac{1.122e4\ s^4 - 1.407e11\ s^2 - 1.988e13}{s^6 - 1.323e7\ s^4 + 8.695e12\ s^2 + 1.229e15}$	$\dfrac{3991\ s^4 - 5.227e9\ s^2 - 7.387e11}{s^6 - 1.382e6\ s^4 + 9.44e10\ s^2 + 1.337e13}$
$G_{51}(s)$	$\dfrac{2.709e4\ s^4 + 6.104e\text{-}5\ s^2 + 32}{s^6 - 1.672e7\ s^4 + 9.889e12\ s^2}$	$\dfrac{2.261e4\ s^4 + 3.196e6\ s^2 - 32}{s^6 - 1.323e7\ s^4 + 8.695e12\ s^2 + 1.229e15}$	$\dfrac{5183\ s^4 + 7.324e5\ s^2 - 0.0625}{s^6 - 1.382e6\ s^4 + 9.44e10\ s^2 + 1.337e13}$
$G_{55}(s)$	$\dfrac{1.166e4\ s^4 - 1.878e11\ s^2 + 32}{s^6 - 1.672e7\ s^4 + 9.889e12\ s^2}$	$\dfrac{1.122e4\ s^4 - 1.407e11\ s^2 - 1.988e13}{s^6 - 1.323e7\ s^4 + 8.695e12\ s^2 + 1.229e15}$	$\dfrac{3991\ s^4 - 5.227e9\ s^2 - 7.387e11}{s^6 - 1.382e6\ s^4 + 9.44e10\ s^2 + 1.337e13}$

L.2 Numerical values of the linear model gains

Table L.2 Numerical parameter values for the three actuator models.

Parameter	Ideal Model [1]	Ideal Model [Corrected]	Model expected from Measurements
A1	7.6800	4.8520	1.1120
B1	2026	1441.8	185
C1	116000	106400	11120
D1	0.38000	0.49612	0.10700
E1	$3.8000 \cdot 10^{-3}$	$2.4806 \cdot 10^{-3}$	$8.8200 \cdot 10^{-4}$
$_xK_x$	$1.6111 \cdot 10^7$	$1.2533 \cdot 10^7$	$1.3098 \cdot 10^6$
$_yK_y$	$1.6111 \cdot 10^7$	$1.2533 \cdot 10^7$	$1.3098 \cdot 10^6$
$_xKl_x$	$1.0667 \cdot 10^3$	$5.7149 \cdot 10^2$	$1.3098 \cdot 10^2$
$_yKl_y$	$1.0667 \cdot 10^3$	$5.7149 \cdot 10^2$	$1.3098 \cdot 10^2$
$_xK_\beta$	0	4.9050	4.9050
$_yK_\alpha$	0	-4.9050	-4.9050
$_zK_{lz}$	52.778	58.436	12.603
$_\alpha K_y$	$-4.0920 \cdot 10^8$	$-4.9590 \cdot 10^8$	$-5.1826 \cdot 10^7$
$_\alpha K_\alpha$	0	$-1.4132 \cdot 10^2$	$-1.4132 \cdot 10^2$
$_\alpha K_{ly}$	$-2.7092 \cdot 10^4$	$-2.2613 \cdot 10^4$	$-5.1826 \cdot 10^3$
$_\alpha K_{l\alpha}$	$1.1656 \cdot 10^4$	$1.1225 \cdot 10^4$	$3.9910 \cdot 10^3$
$_\beta K_x$	$4.0920 \cdot 10^8$	$4.9590 \cdot 10^8$	$5.1826 \cdot 10^7$
$_\beta K_\beta$	0	$-1.4132 \cdot 10^2$	$-1.4132 \cdot 10^2$
$_\beta K_{lx}$	$2.7092 \cdot 10^4$	$2.2613 \cdot 10^4$	$5.1826 \cdot 10^3$
$_\beta K_{l\beta}$	$1.1656 \cdot 10^4$	$1.1225 \cdot 10^4$	$3.9910 \cdot 10^3$